Université de Toulouse

THÈSE

En vue de l'obtention du

DOCTORAT DE L'UNIVERSITÉ DE TOULOUSE

Délivré par :
Institut National Polytechnique de Toulouse (INP Toulouse)

Discipline ou spécialité :
Dynamique des Fluides

Présentée et soutenue par :
Nicolas NOUYRIGAT

le : mercredi 28 mars 2012

Titre :
Hydrodynamic modeling of poly-solid reactive circulating fluidized beds: Application to Chemical Looping Combustion

---

Ecole doctorale :
Mécanique, Energétique, Génie civil et Procédés (MEGeP)

Unité de recherche :
IMFT - UMR 5502

Directeur(s) de Thèse :
Olivier Simonin (IMFT-INPT)
Virginie Lalam (Alstom Power Systems)

Rapporteurs :
Bjorn H. Hjertager (Stavanger University)
Juray de Wilde (Université Catholique de Louvain)

Membre(s) du jury :
Eric Climent (IMFT-INPT)
Olivier Authier (EDF R&D)
Bjorn H. Hjertager (Stavanger University)
Juray de Wilde (Université Catholique de Louvain)
Olivier Simonin (IMFT-INPT)
Virginie Lalam (Alstom Power Systems)

Ce travail a été réalisé à l'IMFT au sein du groupe PSC et en collaboration avec Alstom Power Systems. Je tiens à remercier Olivier Simonin, mon directeur de thèse, qui m'a fait confiance et m'a fait profiter de ses compétences scientifiques. Je remercie également ma co-directrice de thèse, Virginie Lalam, pour sa présence et son soutien tout au long de ma thèse.
Je remercie tout particulièrement Renaud Ansart et Pascal Fede, pour tout le temps qu'ils m'ont consacré pendant ces trois ans, les connaissances qu'ils m'ont transmises et l'intérêt qu'ils ont porté à mon travail.
Merci à Ali, Zafer, Arthurs et les autres pour leurs conseils précieux et leurs travaux sans lesquels ma thèse ne serait pas.

Je remercie l'ensemble des membres du jury, et tout particulièrement les rapporteurs, Pr. de Wilde et Pr. Hjertager, d'avoir relu avec attention ce manuscrit. Je remercie également Pr. Climent et Olivier Authier pour l'intérêt qu'ils ont trouvé à ce travail.

Je tiens à remercier l'équipe d'Alstom qui développe le Chemical Looping et qui a financé cette étude : Corinne Béal et Eric Bouquet. Les échanges fréquents que nous avons eu m'ont permis de mener à bien cette thèse.

Ce travail n'aurait pas été possible sans l'aide quotidienne d'Hervé Neau et du service CoSiNUs, du service informatique, de Suzy et Florence.

Enfin, ceux que j'ai pu côtoyer durant ma thèse ont rendu cette expérience plaisante et inoubliable :
- Mes mutliples co-bureaux qui ont rendu la vie au laboratoire chaleureuse, tropicale, cosmopolite, gourmande, porcine, polyglote, convalescente, monétisée, pictionarisée, agitée, sportive, caféinée et parfois studieuse.
- Le groupe PSC et tout particulièrement ceux qui ont rendu vivants les déjeuners et autres pots : Jeunette, Marion, Enrica, Laurent, J-F, Florian, Pascal, Olivier, Renaud, Hervé, Annaig, Adriens, Erics, Thierry, Romain, Alice, Marco, Dirk, Mehdis, Aurélien, Mambo, Anne, Moe's et tous les stagiaires et thésards qui font vivre ce groupe.
- Les Matmeca de Toulouse qui sont partout et reliés à tout le monde de façon incroyable : Arnaud, Cypy, Thomas, Christian, Jérôme...
- La Compagnie des Chercheurs d'Etoiles qui m'a permis de garder les pieds sur terre et d'occuper mes semaines.
- L'AIFOMEJ, Dominique, J-F et Florian qui m'ont fait découvrir le plaisir qu'il y a à faire découvrir les sciences.
- Romain, Florian, J-F pour plein de choses.
- Feu notre appart de St-Cyprien dans lequel on a passé de bons moments et qui a su m'occuper pendant l'été consacré à la rédaction.
- Miles Davis, Nina Simone, Léo Ferré et Pink Floyd qui ne m'ont pas lâché.

Enfin, rien n'aurait été possible sans ma Zouze, mes amis, ma famille.

Mais que diable allait-il faire dans cette galère ?

Contents

List of symbols

Greek letters

α_i	Volume fraction of phase i	$(-)$
α_s	Total fraction of solid	$(-)$
α_{max}	Maximum random packing of identical hard spheres	$(-)$
χ_{pq}	Exchange of agitation between classes due to collisions	$(kg \cdot m^{-1} \cdot s^{-3})$
Γ_g	Mass transfer between species	$(kg \cdot m^{-2} \cdot s^{-3})$
Γ_k	Reaction rate of the specie k	$(kg \cdot m^{-3} \cdot s^{-1})$
λ_p	Bulk viscosity	$(Pa \cdot s)$
μ_g	Dynamic viscosity of the fluid phase	$(Pa \cdot s)$
μ_p	Particle dynamic viscosity of the particle phase	$(Pa \cdot s)$
ν_g	Gas kinematic viscosity	$(m^2 \cdot s^{-1})$
ν_g^t	Turbulent viscosity of the gas phase	$(m^2 \cdot s^{-1})$
ν_p^{col}	Particle collisional viscosity of the particle phase	$(m^2 \cdot s^{-1})$
ν_p^{kin}	Particle kinetic viscosity of the particle phase	$(m^2 \cdot s^{-1})$
$\Pi_{p\to g}^k$	Exchange term of turbulent kinetic energy k coming from the fluctuating motion of particles	$(kg \cdot m^2 \cdot s^{-3})$
$\Pi_{p\to g}^\varepsilon$	Influence of the fluctuating motion of particles on k in ε equation	$(kg \cdot m^2 \cdot s^{-4})$
ρ_g	Density of the gas phase	$(kg \cdot m^{-3})$
ρ_p	Density of the particle phase	$(kg \cdot m^{-3})$
σ_k	Constant of the $(k-\varepsilon)$ model	$(-)$
σ_ε	Variable of the $(k-\varepsilon)$ model	$(-)$
τ	Characteristic reaction time	(s)
τ_{pq}^c	Characteristic collision time of a binary mixture of particles p and q	(s)
τ_{gp}^F	Mean particle relaxation time	(s)

τ_g^t	Fluide turbulent time scale	(s)
τ_{gp}^t	Eddy particle interaction time	(s)
Θ_g	Viscous tensor of the gas phase	$(kg \cdot m^{-2} \cdot s^{-2})$
ε	Turbulent dissipation of the gas phase	$(m^2 \cdot s^{-3})$
$\widehat{\alpha_p}$	Modified polydisperse volume fraction of solid	$(-)$
$\widehat{\tau_p^c}$	Modified polydisperse collision timescale	(s)
q_2	Constant of the $(q_p^2 - q_{fp})$ model	$(-)$

Roman Letters

$< C_D >$	Drag coefficient	$(-)$
$< u'_{g,i} u'_{p,j} >$	Fluid-particle velocity correlations tensor components	$(m^2 \cdot s^{-2})$
$\dot{Q}$	Molar reaction rate of the specie k	$(kg \cdot m^{-3} \cdot s^{-1})$
$\widehat{d_p}$	Modified polydisperse collision diameter	(μm)
c_p	Velocity of the p-particle	$(m \cdot s^{-1})$
C_{12}	Variable of the $(k - \varepsilon)$ model	$(-)$
C_μ	Variable of the $(k - \varepsilon)$ model	$(-)$
C_{ε_i}	Variable of the $(k - \varepsilon)$ model	$(-)$
C_q	Constant of the $(q_p^2 - q_{fp})$ model	$(-)$
D	Molecular and turbulent diffusivity coefficient	$(m^2 \cdot s^{-1})$
d_p	d_{50} of the particle phase p	(μm)
$D_{gp,ij}$	Fluid-particle turbulent dispersion tensor	$(m^2 \cdot s^{-1})$
d_{pq}	Diameter representative from	$(-)$
e_c	Inelastic restitution coefficient	$(-)$
$f_p^{(1)}$	Single phase p-particle velocity distribution function	$(-)$
g_{pq}	Autocorrelation function	$(-)$
k	Turbulent kinetic energy of the gas phase	$(m^2 \cdot s^{-2})$
K_p^t	Turbulent diffusivity coefficient	$(m^2 \cdot s^{-1})$
L_p	Scalar representing the number of particles	$(-)$
M_c	Total mass of carbon in the bed	(kg)
m_p	Mass of the p-particle	(kg)

P_g	Mean pressure of the gas phase	$(kg \cdot m^{-1} \cdot s^{-2})$
P_p	Granular pressure	$(kg \cdot m^{-2} \cdot s^{-2})$
Q_z^k	Mass flow rate of the specie k at z	$(m^3 \cdot s^{-1})$
q_{gp}	Fluid-particle velocity correlation	$(m^2 \cdot s^{-2})$
R	Universal gas constant	$(J \cdot mol^{-1} \cdot K^{-1})$
$R_{g,ij}$	Reynolds stress tensor of the gas phase	$(m^2 \cdot s^{-2})$
Re_p	Particulate Reynolds number	$(-)$
T	Temperature	$(K$ or $^\circ C)$
V	Volume of the domain	(m^3)
V_d	Drift velocity	$(m \cdot s^{-1})$
V_f	Fluidization velocity in the main section	$(m \cdot s^{-1})$
$V_{r,i}$	i^{th} component of the mean relative velocity between the particle and the undisturbed fluid	$(m \cdot s^{-1})$
W_k	Molecular weight of specie k	$(kg \cdot mol^{-1})$
Y_k	Mass fraction of specie k	$(-)$
Z_{pq}	Parameter representative from collisions between solid phases	$(-)$

Summary

This work deals with the development, validation and application of a model of Chemical Looping Combustion (CLC) in a circulating fluidized bed system.

Chapter 1 is an introduction on Chemical Looping Combustion. It first presents the most important utilizations of coal in the energy industry. Then, it shows that because of the CO_2 capture policy, new technologies have been developed in the frame of post-combustion, pre-combustion and oxy-combustion. Then, the Chemical Looping Combustion technology is presented. It introduces multiple challenges: the choice of the Metal Oxide or the definition of the operating point for the fuel reactor. Finally, it shows that there are two specificities for CFD modeling: the influence of the collisions between particles of different species and the local production of gas in the reactor due to the gasification of coal particles.

Chapter 2 outlines the CFD modeling approach: the Eulerian-Eulerian approach extended to flows involving different types of particles and coupled with the chemical reactions.

Chapter 3 consists in the validation of the CFD model on mono-solid (monodisperse and poly-disperse) and poly-solid flows with the experimental results coming from an ALSTOM pilot plant based at the Université Tchnologique de Compiègne (France). The relevance of modeling the polydispersity of a solid phase is shown and the influence of small particles in a CFB of large particles is characterized. This chapter shows that the pilot plant hydrodynamics can be predicted by an Eulerian-Eulerian approach.

Chapter 4 consists in the validation of the CFD model on an extreme bi-solid CFB of particles of same density but whith a large particle diameter ratio. Moreover, the terminal settling velocity of the largest particles are twice bigger than the fluidization velocity: the hydrodynamics of the large particles are given by the hydrodynamics of the smallest. An experiment performed by Fabre (1995) showed that large particles can circulate through the bed in those operating conditions. Our simulations predicted a circulation of large particles, but underestimated it. It is shown that it can be due to mesh size effect. Finally, a simulation in a periodic box of this case was defined and allowed us to show the major influence of collisions between species.

Chapter 5 presents the simulation of a hot reactive CLC pilot plant under construction in Darmstadt (Germany). The simulations account for the chemical reactions and describe its effect on the hydrodynamics. Different geometries and operating conditions are tested.

Introduction

The global consumption of energy keeps increasing with the growth of population and the increasing standard of living. Coupled with the climate change new issues, it became of paramount importance to rethink our energy production processes : today, an economic and environmentally viable process must control its greenhouse gases and pollution release and run under stable conditions.
Today, three groups of power plant exist:

- Nuclear power is constantly questioned as it seems that guarantying the safety of the fission process is no longer evident. It represents about 14% of the world's electricity and according to the current political context, it is complicated to predict its evolution in the next few years.

- Renewable energy coming from sunlight, wind, rain, tides or geothermal heat: the share of renewable in electricity generation is around 19% (16% hydroelectricity / 3% other renewable). Its share is expected to increase a lot in the next few decades.

- Thermal power, mostly based on the combustion of natural gas, coal or petroleum remains a major source of energy for developing countries: about one thermal power station is built each week in China. Thermal power energy represents 67% of the world's electricity and is responsible for about 30% of the world CO_2 release in the atmosphere. The use of thermal energy by developing countries is intensive and keeps increasing with time.

It is then obvious that major stakes lie on the development of clean thermal power processes. Usually, the energy is produced thanks to the exothermic combustion of the fossil fuel with the oxygen present in air. The major drawback of this method is the production of CO_2 inside the air-flow: at the outlet of a classical thermal power plant, carbon dioxide is mixed with air. A solution to decrease the CO_2 emitted by thermal power plants is to store it. Because storing a huge amount of gas will have an important cost, it is crucial to collect the purest CO_2 possible. To do so, existing power plant should add Gas Separation Units to extract CO_2 from the exhaust fumes. These units generate an energetic cost that decreases the global efficiency of the process and add an extra economic cost.
During the 90's came the idea to burn the fossil fuel with another source of oxygen than air. It is referred to as oxy-combustion. This technology is developed in multiple processes to adapt to each fuel specificity.
In the frame of the coal combustion, chemical looping combustion process seems appropriate: it consists in two inter-connected circulating fluidized beds - the air reactor (AR) and the fuel reactor (FR)-. In the FR, coal is oxidized by a metal oxide in a steam fluidization flow. This often endothermic reaction produced at the outlet of the

FR is made of CO_2 and steam. Carbon dioxide can then be easily separated. In the AR, the reduced (in the FR) metal oxide is re-oxidized by air. This exothermic reaction produced at the outlet of the AR a flow of lean oxygen air. This concept seems promising since it intrinsically isolates the CO_2. In order to materialize this concept into a technical solution, a process was defined to build pilot plants. The validation of this process is in progress. Building a pilot plant and performing experiments on the fuel, metal oxide, geometries is very costly, then the CFD seems to be an appropriate tool to help in the design of such processes. CFD is already useful to predict and support the design of coal-powered circulating fluidized beds plants.
Indeed, lots of experiment were accumulated in the modeling of circulating fluidized beds (CFB) since the 80's. Two major modeling approaches exist to predict the hydrodynamics of such flows:

Eulerian - Lagrangian approaches

The gas phase is modeled with the classical Navier-Stokes equations and each particle of the solid phase is transported through its momentum equation. This approach is very costly for industrial applications were billions of particles need to be modeled.
or
The gas phase is modeled with the classical Navier-Stokes equations. For the solid phase numerical particles are defined to represent a part of the solid phase. Each numerical particle is then transported through its momentum equation.

Eulerian-Eulerian approach

The gas phase is modeled with the classical Navier-Stokes equations. The solid phase transport equation comes from the kinetic theory of granular flows resulting in three transport equations per solid phase : volume fraction, momentum and kinetic energy.

Combine with experiments, the hydrodynamics of CFB was investigated and different regimes were defined regarding the size of the fluidized particles, the fluidization velocity and the geometries. Nevertheless, the chemical looping combustion process introduces two essential characteristics that differ from usual coal powered CFB:

- First, in the fuel reactor, two solid species are fluidized by a gas flow. This two solid species have very different characteristics: coal particles are smaller and lighter than the metal oxide particles. What is the influence of the polydispersion on the hydrodynamics of the flow ? Does particle-particle interactions have macroscopic influence on the process ?

- Secondly, the reaction occurs between coal particles and metal oxide particles after gasification of coal particles. It means that the mass of carbon and oxygen contained in the reactants goes from solid state to gaseous state. This results in the local production of a large amount of gas. What is the influence of this gas stream on the fluidization of particles ?

In this work, an effort was made to answer those questions and give leads to predict the complex flow of 3D reactive polysolid circulating fluidized beds applied to Chemical Looping Combustion.

The first Chemical Looping Combustion pilot plant working with solid fuel and metal oxide is beeing built in Darmstadt University (Germany). The first results corresponding to CLC experiments are expected in a few months.

This thesis is organized as follow:
The first chapter consists in an introduction to the chemical looping process. The main frame of the coal combustion in industry, its environmental impact and its challenges to take up are presented.

Chapter two deals with the modeling of reactive circulating fluidized beds. After an introduction to CFB modeling, the main equations of the Eulerian-Eulerian approach solved in $NEPTUNE\_CFD$ are presented. Then, the closure laws for the interphase coupling and the stress tensors of the solid and gas phases are introduced. Finally, a proposition for the modeling of coal/metal oxide combustion is submitted.

The third chapter concerns the application of the previous modeling on non-reactive circulating fluidized beds. Mono-solid simulations were validated regarding experiments performed at the Université Technologique de Compiègne. Then, the introduction of a second solid phase was modeled and compared to experiments. The influence of the mean diameter of the particle phase and of the position of the secondary injector is investigated.

The fourth chapter concerns the modeling of Fabre's experiment at CERCHAR. The specificity of this configuration is that it consists in a bi-solid circulating fluidized bed where the mean diameter ratio between the solid species is equal to 5. Moreover, the fluidization velocity is twice less than the terminal settling velocity of the largest particles. It was found that large particles can circulate in the bed under specific conditions (ratio between large and small particles). To investigate this phenomenon, we simulate those experiments. Our results lead us to perform periodic simulations of a bi-solid mixture of particles in order to understand how the polydispersion can modify the global hydrodynamics of the flow.

The last part deals with the conclusions and perspectives of this work.

Résumé du Chapitre 1

Le premier chapitre est une présentation du procédé de Boucle chimique appliqué à la combustion du charbon.

La première section est un résumé des principales utilisations du charbon comme combustible: la principale valorisation énergétique du charbon est la combustion. Ainsi, la méthode la plus utilisée à l'échelle industrielle est la gazéification, principalement réalisée en lit entrainé.
Au cours de la gazéification, le charbon solide est transformé majoritairement en monoxyde de carbone, hydrogène et méthane. Dans le cadre de la production d'électricité, les gaz produits sont brûlés, et la chaleur dégagée par leur combustion est récupérée. L'inconvénient principal de cette méthode est qu'elle produit des NOx et des suies qui polluent l'atmosphère. De plus, ce procédé rejette dans l'atmosphère du dioxyde de carbone mélangé à l'azote de l'air. Il est donc très coûteux de séparer le CO_2 de l'air en vue de sa séquestration.

La deuxième section replace l'industrie du charbon par rapport à la politique actuelle de séquestration des gaz à effet de serre. Afin de remplir les objectifs fixés par le protocole de Kyoto, différentes techniques ont été développées:

- La post-combustion classique: le CO_2 est séparé des autres gaz en sortie de centrale à l'aide d'une unité de séparation des gaz.
- La post-combustion de type Chemical Looping: ce procédé prometteur basé sur des cycles de carbonatation/calcination (aussi appelé Carbonate Looping) qui permettent de séparer de façon intrinsèque le CO_2 des autres gaz est en cours de développement.
- La pré-combustion: ce procédé est basé sur la gazéification du charbon en présence de vapeur d'eau ou d'oxygène pure afin de produire du Monoxyde de carbon qui au contact avec la vapeur d'eau et/ou l'oxygène pur va produire du CO_2 et/ou du H_2. Le CO_2 est ensuite aisément séparé du dihydrogène.
- L'oxy-combustion: Le charbon est brûlé dans un environnement riche en oxygène. Ainsi, les gaz de sortie sont composés majoritairement de CO_2. Deux méthodes sont actuellement développées. La première utilise une unité de séparation des gaz pour extraire l'oxygène de l'air qui servira à brûler le charbon. La seconde est fondée sur le concept de Boucle Chimique: le charbon est brûlé en présence d'un oxyde métallique dans un flux de CO_2 et de vapeur d'eau.

Ensuite, la technologie appelée Chemical Looping Combustion (Combustion en Boucle Chimique) est présentée. Elle concerne des centrales thermiques neuves dont la

puissance à l'échelle industrielle doit s'approcher de celles des centrales LFC actuelles pour être compétitive. Le procédé date d'un brevet déposé en 1954 par Lewis et Gilliland. Il avait pour objectif de produire du CO_2 quasi-pur. Une centrale de type Chemical Looping est composée de deux réacteurs interconnectés: l'Air Reactor est un lit fluidisé au sein duquel un métal est oxydé au contact de l'air. En sortie de ce réacteur, on trouve du gaz composé d'air appauvri en oxygène contenant peu de NOx et des particles de métal oxydées. Dans le second réacteur, le Fuel Reactor, les particules de charbon et de métal oxydé sont fluidisés par un courant chaud de vapeur d'eau et de CO_2. Le charbon s'oxyde au contact de l'oxyde métallique et produit du CO_2. En sortie de ce réacteur, on trouve un gaz composé majoritairement de CO_2 et de vapeur d'eau, et des particules d'oxyde métallique réduites.

Le choix de l'oxyde métallique dans ce procédé est primordial. Il doit supporter les multiples cycles d'oxydo/réduction, être fluidisable, ne pas être dommageable pour l'environnement et enfin être bon marché. De nombreuses études ont été menées pour sélectionner le meilleur candidat. L'équipe d'ALSTOM Power Systems développant le prototype de CLC de 1 MWth à Darmstadt a choisi d'utiliser l'ilmenite.

Le dimensionnement d'une centrale de type CLC présente des défis nouveaux par rapport à celui de centrale à lits fluidisés circulants classiques. En effet, le Fuel Reactor présentent deux particularités:

- Deux espèces de solides doivent circuler: les particules de charbon (plutôt petites et légères) et les particules d'ilmenite (plutôt grandes et lourdes).
- La réaction a lieu entre deux solides. Il en résulte une production de gaz conséquente au sein de l'écoulement.

Etant donné le coût élevé de la construction d'un prototype et l'évolution des moyens de calculs, l'utilisation de la CFD représente un atout considérable pour tenter de prédire le fonctionnement de de type de centrales. Ainsi, il sera possible de définir un point de fonctionnement stable: le flux circulant de chaque espèce ainsi que leur temps de séjour dans le lit doivent être suffisants pour assurer le bon fonctionnement du procédé.

Chapter 1

Chemical looping combustion

Contents

The overwhelming majority of the world's climate scientists and governments agree that climate change is occurring and that the main cause is human use of fossil fuels. That is why a protocol to the United Nations Framework Convention on Climate Change (UNFCCC) was adopted, aiming at fighting global warming. The UNFCCC is an international environmental treaty with the goal of achieving the "stabilization of greenhouse gas concentrations in the atmosphere at a level that would prevent dangerous anthropogenic interference with the climate system."
The Protocol was initially adopted on 11 December 1997 in Kyoto, Japan, and entered into force on 16 February 2005. As of August 2011, 191 states have signed and ratified the protocol. Lots of countries committed themselves to reduce the emission of greenhouse gases.

To fulfill their commitments, governments are funding research and development of new technologies to reduce the emissions of greenhouse gases and to capture and store industrially produced CO_2.

As an example, at their Hokkaido Summit in 2008, G8 leaders:

- agreed to establish an international initiative with the support of the IEA to develop CCS (Carbon Capture and Storage) technology road maps and co-operate through existing and new partnerships and strongly supported the launching of 20 large-scale CCS demonstration projects globally by 2010 taking into account various national circumstances with a view to beginning broad deployment of CCS by 2020

- committed to increase investment in clean energy technology research and development (R& D), and the promotion of commercialization including through direct government funding and fiscal measures to encourage private sector investment

- agreed to take various policy and regulatory measures to provide incentives for commercializing these technologies.

1.1 Industrial use of charcoal

According to the World Coal Institute Website, an increase in the use of coal of 53% is expected over the next 20 years as shown in figure 1.1. These figures are just estimations but it already shows that the production of China should control the overall production during that time. Every week to 10 days, a coal-fired power plant opens in China, partly because charcoal is far more available than oil or gas. Moreover it is admitted that over 120 years of coal are remaining worldwide. Because of the renewal of this industrial field, a lot of breakthrough are expected to increase the efficiency, and decrease the environmental impact of the coal combustion. The 21st century coal power plants emit 40% less CO_2 than the average 20th century coal plants. But it might not be sufficient to fulfill the commitment of 1997's Kyoto Protocol to reduce drastically CO_2 gas release coming from human activity.
Lots of international programs regroup multiple industrial and research teams to find ways to increase the efficiency of coal power plants while capturing and storing the CO_2.

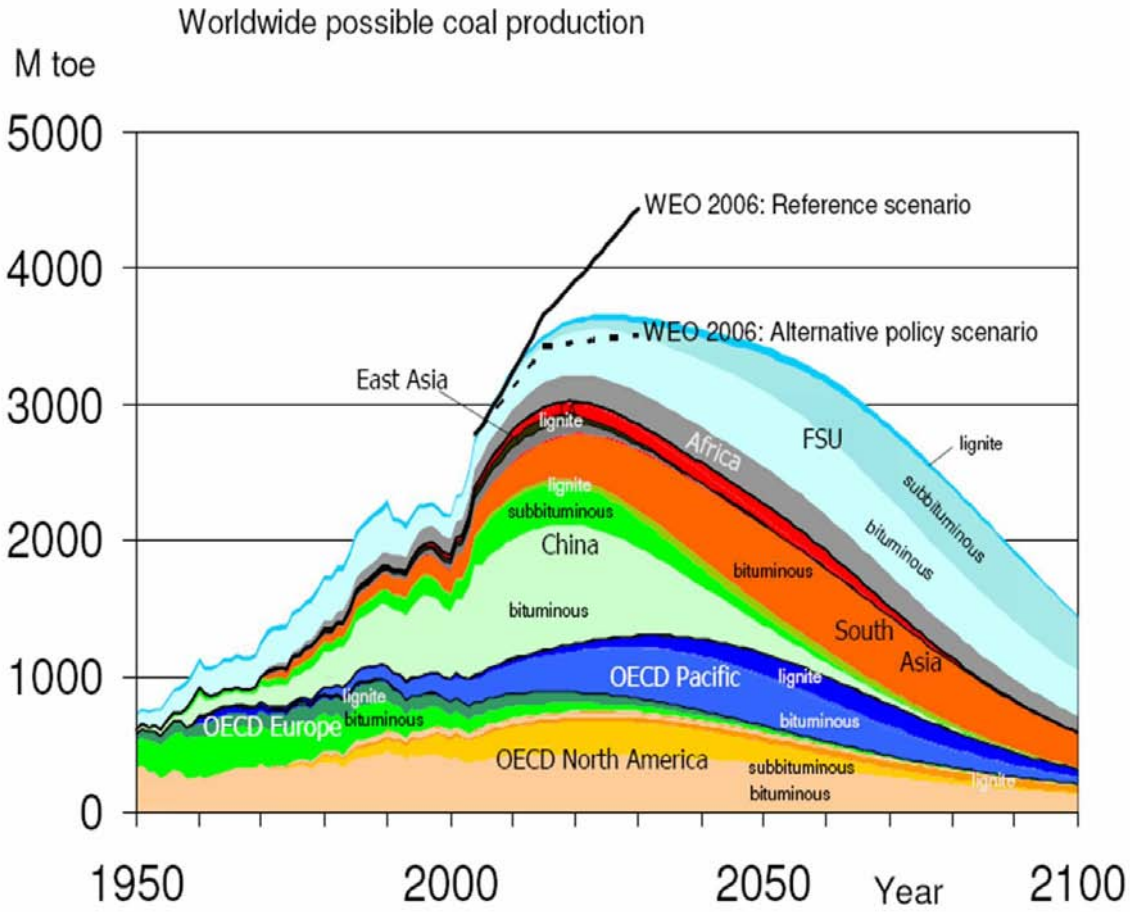

Figure 1.1: Worldwide estimated coal production by EWG (2007)

At the moment, several industrial ways to use the energy trapped in charcoal particles have been developed. This section aims at succinctly presenting the major industrial technologies implying coal.

1.1.1 Carbonization

It consists in heating coal to high temperature and then creating coking coal. It is 'The destructive distillation of organic substances in the absence of air, accompanied by the production of carbon and liquid and gaseous products (Menendez and Alvarez (1989)). The coke produced by carbonization of coal is used in the iron and steel industry and as a domestic smokeless fuel.

1.1.2 Liquefaction

The conversion of coal into liquid fuels involves the addition of hydrogen.

- The Bergius process: it consists in converting coal into oil. To do so, coal particles are ground and placed under high pressures ranging from 200 to 700 atmospheres. It finally reacts with hydrogen. This process was too costly and is no more developed by industry.

- Fischer-Tropsch process: in the first-generation, coal is gasified first in a high-pressure Lurgi gasifier. The resulting synthesis gas is reacted over an iron-based catalyst either in a fixed-bed or fluidized-bed reactor. Since the increase in the price of petrol, Fischer-Tropsch plants are being developed to produce liquid oil and thus reduce the dependency of some countries toward Middle East oil.

1.1.3 Gasification

The goal of gasification is to convert most of the combustible solids into combustible gases such as carbon monoxide, hydrogen, and methane.
The combustion of thoses gaseous species generates heat used to produce steam, and then to produce electricity through turbines. There are three main steps in the gasification process:

- 1. Diffusion of oxygen from the bulk gas to the charcoal particle surface.

- 2. Reaction between oxygen and the surface of the charcoal particle.

- 3. Diffusion of reaction products from the surface of the charcoal particle into the bulk gas.

Large scale coal gasification often occurs in a fixed or fluidized bed (dense, bubbling, circulating, etc). More than ten different processes have industrial use and an excellent description is given by Kunii and Levenspiel (1991). The most common are :

- Fixed beds: relatively large coal particles are burning in a reactor. The particle size that can be used in fixed-bed systems limits the rate of heating of the particles.

- Pulverized coal: coal is ground into very fine particles and pulverized inside a combustion chamber. This process is highly efficient but very costly due to the fine-particle-collection equipment needed to limit the emission of dangerous particles in the atmosphere.

- Cyclone: transported in a fluid at high temperature, coal melts and flows along the inclined wall of the furnace and is removed as a liquid slag.

- Coal-water slurry fuel: it consists in a mixture of small coal particles and water. It could be used in classical liquid fuel burning units. The commercial viability of this process depends on the price and availability of naturally occurring liquid fuels.

- Magnetohydrodynamics (MHD): it uses coal to generate a high-temperature combustion gas.

- Fluidized bed: the fluidization gas is increasing the circulation of oxygen through coal particles.

The major drawback of these processes is the fact that charcoal is not pure carbon (it is mainly composed of C,H,O,N,S, Ash). So its combustion with air produces NOx and soots that pollute the atmosphere and result in an efficiency loss of energy used to convert other species than carbon or hydrogen. Moreover, these technologies are not easily compatible with the Carbon Dioxide sequestration policy because CO_2 at the outlet is mixed with air. Capturing it requires Air Separation Units resulting in the reduction of the process global efficiency. Moreover, typical CFB units needs pollution control devices to limit the release of NOx and SOx.
That is why it became necessary to develop new technologies to be able to separate air and CO_2 before the combustion and to limit the production of pollutants..

1.2 Capturing the carbon dioxide

Because the cost of the secured storage of CO_2 will be expansive, it is of paramount importance to store the purest CO_2 possible: it means that new technologies have to be developed to filter the CO_2 at the outlet of the fossil fired power plants. There are three main pathways seriously considered to fulfill that goal.

1.2.1 Post-combustion

Classical units

It refers to the separation of CO_2 from the flue gas of a combustion process. Fuel sources can be any hydrocarbon, such as coal, natural gas, or oil. For coal plants, post-combustion capture is typically associated with pulverized coal (PC) and circulating fluidized bed (CFB) plants. A major drawback of this technique is the weak concentration of CO_2 in the exhaust fumes. Its main advantage is that this technology do not need major transformation of the industrial process to capture the carbon dioxide: an energy-consuming gas separation unit is added in the process.

Chemical looping applied to post-combustion

A process based on a carbonation/calcination cycle is currently developed. The main steps of the process are the following:
In a first fluidized bed, coal is burnt with the oxygen present in the fluidization gas: air. The resulting outlet gas is composed of mostly CO_2, N_2, O_2 and SO_2.
In a second fluidized bed, CaO is fluidized by the outlet gas of the previous reactor. Then, the following reactions occur:

$$CaO + CO_2 \rightarrow CaCO_3 \tag{1.1}$$

$$CaO + SO_2 + 1/2O_2 \rightarrow CaSO_4 \tag{1.2}$$

In a third fluidized bed, $CaCO_3$ is decomposed in a steam flow:

$$CaCO_3 \rightarrow CaO + CO_2 \tag{1.3}$$

Therefore, the CO_2 is filtered at the outlet of the process.
The overall process is presented on figures 1.2 and 1.3.

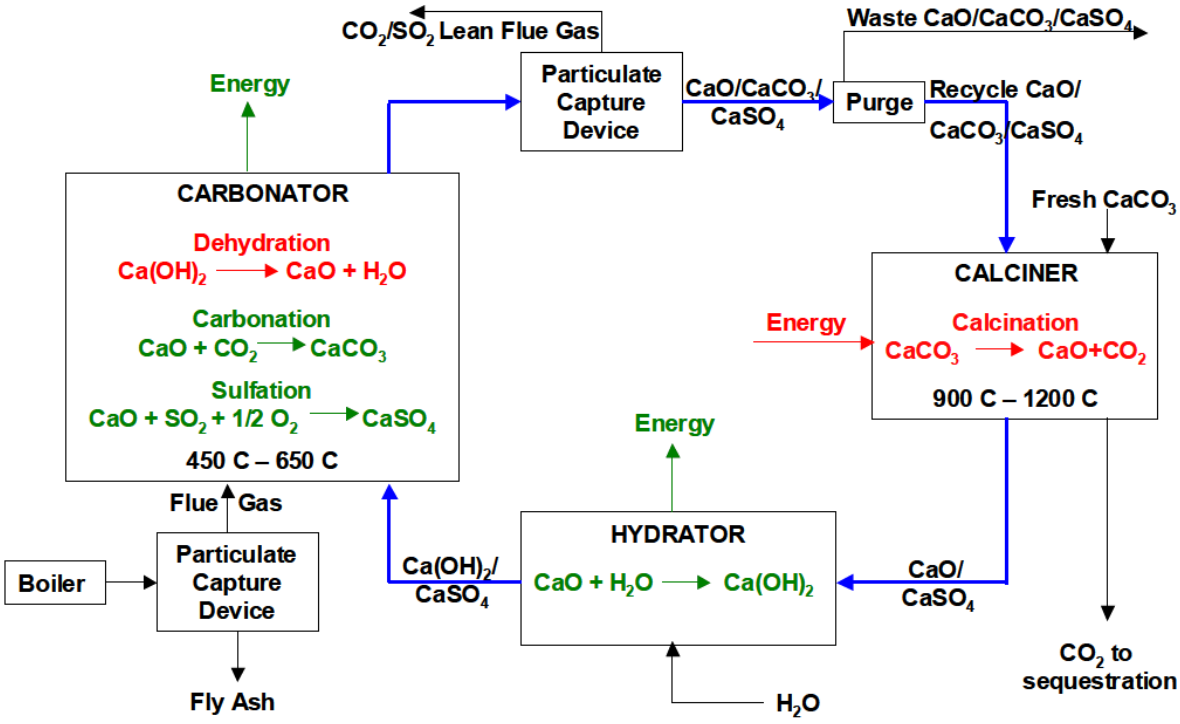

Figure 1.2: Presentation of the reactions occurring in a $CaO/CaCO_3$ chemical looping

This developing technology is currently being tested on a pilot plant in Darmstadt (Germany).

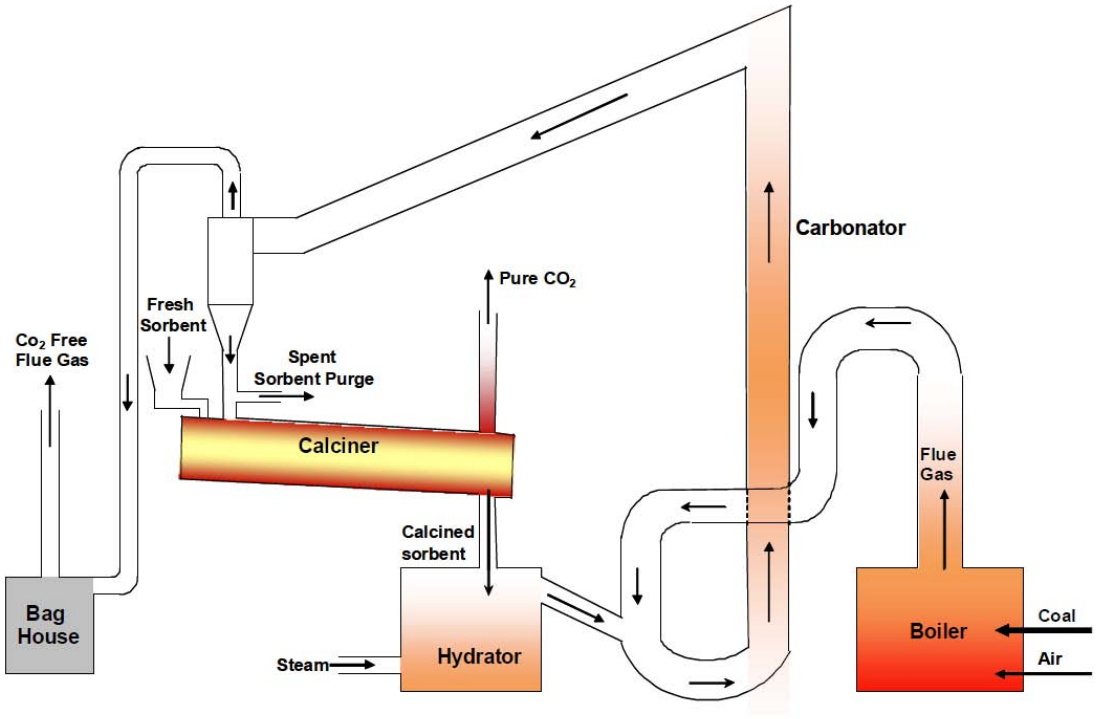

Figure 1.3: Summary of the $CaO/CaCO_3$ chemical looping process

1.2.2 Pre-combustion

It involves the generation of syngas (carbon monoxide plus hydrogen ($CO + H_2$)), followed by the shift reactions to convert the CO to CO_2. CO_2 is then separated from hydrogen, and the hydrogen can be burned in a turbine or used as fuel in a heater. Pre-combustion capture is often associated with integrated gasification combined cycle (IGCC) technology. Most studies suggest it is more cost-effective to use pre-combustion technologies with IGCC because the CO_2 can be captured at higher pressures compared to post-combustion (IPCC 2005).

1.2.3 Oxy-fuel combustion

The technology in the demonstration stage involves the combustion of fuel in an oxygen-rich environment to dramatically increase the CO_2 concentration of the resulting flue gases. The increased CO_2 concentration ($> 80\%$) of the flue gas stream facilitates CO_2 separation. Oxyfiring produces lower emissions of nitrogen oxides (NOx) compared to air-blown combustion. After combustion, the flue gas can be captured and compressed, although some cleaning to remove contaminants is necessary before compression. Two options exist for oxy-fuel combustion:
Using a separation gas unit to extract O_2 from air.
Using a chemical looping process based on the introduction of an oxygen carrier. This oxy-combustion process is presented in section 1.3.

As a conclusion on capturing the carbon dioxide technologies, the figure 1.4 presents a state of the art review of the promising CCS technologies.

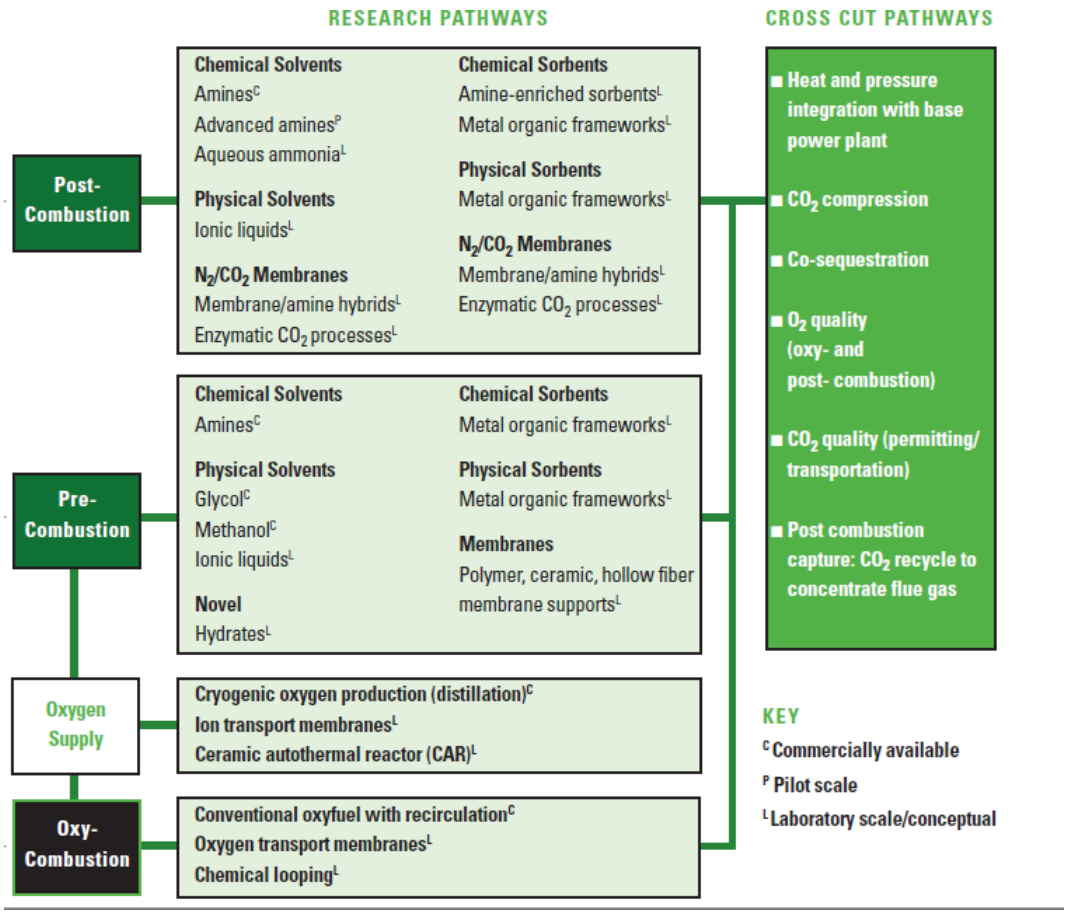

Figure 1.4: "Carbon sequestration technology road-map and program plan 2007" DOE /Office of Fossil Energy/NETL, April 2007

1.2.4 Storing the CO_2

In 1996, at the Norwegian Sleipner site in the North Sea, the first geological storage of CO_2 was installed. It involved the injection of one million tons of CO_2 each year in a deep aquifer. A European research project (Saline Aquifer CO_2 Storage) was created in 1998 to gather the experience earned on this pilot installation. In 2000, at Weyburn (Canada) an installation for CO_2 geological storage in an oil reservoir was built. The objective is to store 1.8 millions tons of CO_2 each year for fifteen years. In 2001, an international research program was created (IEA Weyburn CO_2 Monitoring and Storage Project) to study the efficiency of this plant. In the next few years, developing channels for CO_2 storage are :

- storage in deep aquifers
- storage in depleted or declining oil and natural gas reservoirs
- deep unmineable coal seams

But time is still necessary to ensure that those technologies allow CO_2 to be stored over several hundreds of years without endangering the local environment.

1.3 Chemical Looping Combustion technology

In this section, we will only focus on CLC technology as oxy-combustion technology. Among all alternative ways to use coal as a source of energy, Chemical Looping Combustion is a disruptive technology because the Oxygen is no more stored in a gaseous phase but in a solid phase. At the moment, it is still in development, but it is one of the most promising ways to burn coal and fulfill the environmental challenges of the next few years.
Chemical looping Combustion was first aimed to be used for pure CO_2 production (cf. Lewis and Gilliland (1954)). Its development really started thanks to the fossil industry in the 90's to build a technology that would filter carbon dioxide release.
While this development is still performed by the fossil industry, environmental industry is starting to study it, as a potential way to burn biomass or various waste.
A non-exhaustive list of companies funding research on CLC and academics partners working on this new technology is proposed at the end of this chapter.

1.3.1 General presentation of the process

In 1949, Lewis and Gilliland proposed a method to produce pure Carbon Dioxide resulting in a patent Lewis and Gilliland (1954).
"*[...]the invention is concerned with the oxidation of carbonaceous material by means of solid oxidizing agents, such as metallic oxides as the source of oxygen. [...] A more specific object of this invention is to provide a process of the type specified which will permit oxidation of the carbonaceous material by metallic oxides, without contaminating the carbon dioxide with inert gases, such as nitrogen.*"
The basics of Chemical Looping Combustion (CLC) were set.

Ironically, since the last decade, this technology represents a major possible breakthrough in the capture of Carbon Dioxide exhaust of charcoal power plants. As introduced by Lewis and Gilliland (1954), the chemical-looping combustion involves the use of a metal oxide (MeOx) as an oxygen carrier which transfers oxygen to coal during combustion, thus avoiding direct contact between air and coal. Therefore, two interconnected fluidized beds - a fuel reactor and an air reactor - are used in the process (cf. Figure 1.5). In the fuel reactor, the coal particle gasification allows the Metal Oxide reduction. In the air reactor, the Metal is oxidized by air. The element joining the two reactors can be a coal separation device or a loop seal.

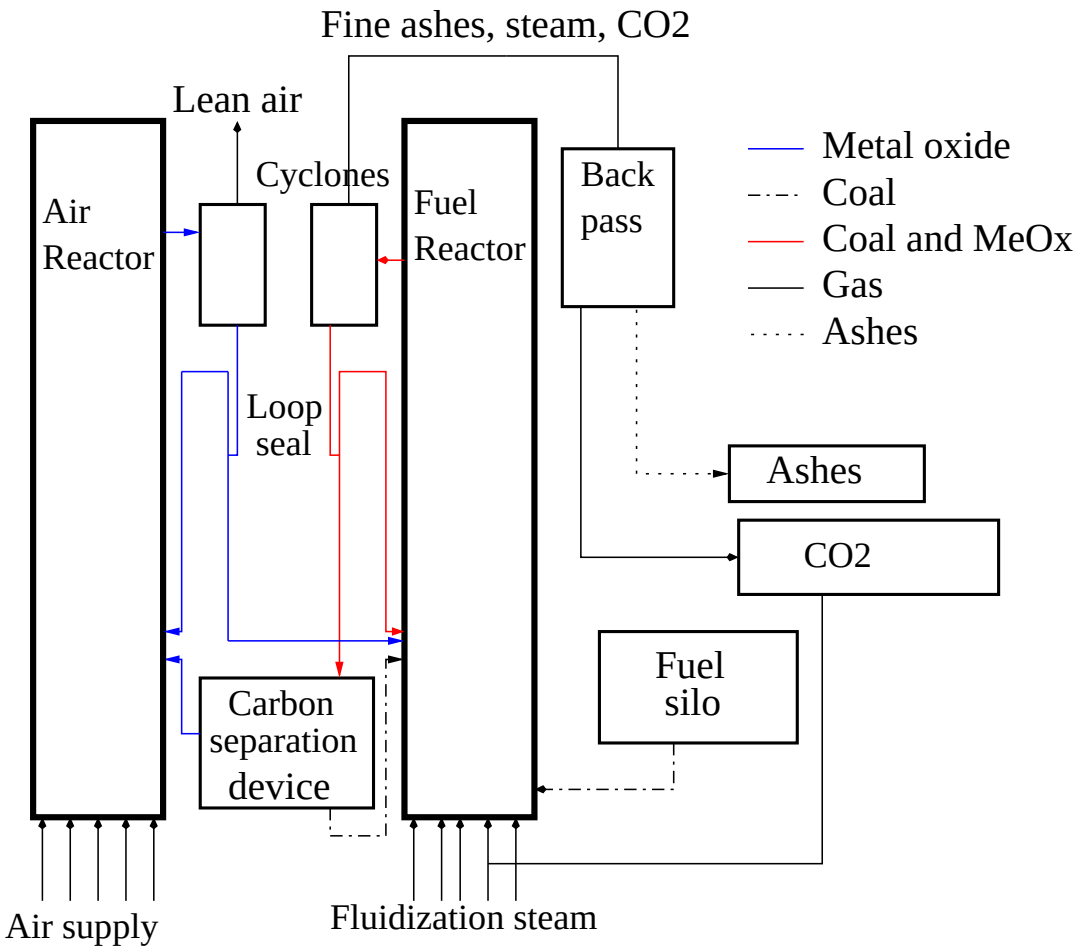

Figure 1.5: General sketch of a CLC process

1.3.2 Reactors

The air reactor often consists in a circulating fluidized bed in which the reduced oxygen carrier is fluidized by air: Shuai et al. (2010) showed that the circulating fluidized bed technology might be a preferred candidate for CLC because it does not generate large bubbles that decrease the fuel conversion speed. The metal oxidation is an exothermic reaction. Indeed, most of the heat production in a CLC power plant comes from the air reactor. This reactor is needed to avoid contact between carbon and nitrogen. The metal oxidation changes flue gas into exhaust fumes by consuming part of its oxygen. Finally, this reaction does not produce any carbon dioxide or NOx due to the nitrogen contained in charcoal particles. A few Thermal NOx are expected because of the operating temperatures.
In the air reactor, the predominant reaction is:

$$Me + 1/2O_2 \rightarrow MeO \tag{1.4}$$

The fuel reactor consists in a circulating fluidized bed in which the oxygen carrier particles and coal particles are fluidized by a mixture of steam and carbon dioxide. The coal particles are gasified and then oxidized by MeOx particles. It produces a large amount of carbon dioxide as a gaseous species, and reduced MeOx and ashes solid particles. This reaction is endothermic if the oxygen carrier is ilmenite and exothermic if the oxygen carrier is copper based. Then, in some configurations, the heat coming from the flue gas enable the reaction.
The gas phase at the outlet of the fuel reactor is expected to be composed mainly of carbon dioxide and steam so as to be able to capture a quasi-pure carbon dioxide flow by condensing the steam: more than 90% efficiency is expected.
In the fuel reactor, the predominant reaction is:

$$C_xH_y + \delta MeO \rightarrow \alpha Me + \beta CO_2 + \gamma H_20 \tag{1.5}$$

Both reactors need excellent gas-solids contact and sufficient solids circulation rate. It is then of paramount importance to understand and control the hydrodynamics of the flow.

1.3.3 Cyclones

A centrifugal flow is separating the different solid phases. Each cyclone has a cut-off diameter. The role of the cyclones is to separate the different solid species (Coal, ashes, Metal Oxide). Indeed, the CLC process efficiency is based on the assumption that there is no fuel inside the air reactor. Another technological issue is the design of those cyclones that has to be sized to fit in a large scale power plant, considering the increase in the number of cyclones needed to filter the important mass flow rate of coal, ashes and oxygen carrier.

1.3.4 Carbon separation device

It is located between the two reactors and its role is to separate the coal particles coming out of the fuel reactor from oxygen carrier reduced particles. The challenge is to re-inject the oxygen carrier in the air reactor without any carbon particle.

The confidentiality and the economic stakes behind this element explain the lack of publications on its conception. In the confidential section (**??**), the carbon separation device developed by Alstom is presented.

1.3.5 Gasification process

When the coal particles arrive in the fuel reactor, it first devolatilizes. The non-negligible part of volatile species contained in coal particles is released. Then the gasification occurs producing a syn-gas composed of mostly CO and H_2. Charcoal particles are gasified in an environment of oxidizing gas ($H_2O + CO_2$) with rapid removal of gasification products (CO, H_2) already inside the particle phase. Dennis et al. (2006) showed that gasification occurs in the Fuel Reactor expected operating conditions.

1.3.6 Oxygen carrier selection

Lots of experiments on Metal Oxide as oxygen carriers were performed to determine the best candidates for CLC utilization. This work regroups an important number of industrial partners and researchers. It is due to the fact that CLC technology is new and only a few pilot plants were operational in the early 00's.

The oxygen carrier needs to fulfill restrictive conditions to be considered as a good candidate for CLC:

- Be stable under repeated oxidation/reduction cycles and offer mechanical resistance to friction: the oxygen carrier will be used for thousands of hours before being replaced.
- Be fluidizable and resistant to agglomeration: the circulation of both solid species is necessary from the beginning to the end of the process.
- Be environmentally benign in case of massive use in coal industry. This criterium is restrictive because the toxicity of Metal Oxides is difficult to characterize.
- Be economically feasible: the technology has to be cheap enough to stay under the CO_2 exhaust market.

Richter and Knoche (1983) first study on oxygen carriers showed the reversibility of combustion processes in CLC-like units. Later an important number of worldwide research teams focused on the research of the best oxygen carrier regarding the previous four physical, environmental and economical constraints.

Lots of experiments were performed on gaseous, solid and liquid fuels. Villa et al. (2003) from Politecnico di Milano, Readman et al. (2006) and Kolbitsch et al. (2009) performed experiments on Nickel based oxygen carriers. In 2004, Adanez et al. (2004) from Instituto de Carboquimica (CSIC) in Zaragoza, experimented on oxygen carriers based on Cu, Fe, Mn, or Ni oxides on Al2O3, sepiolite, SiO2, TiO2, or ZrO2 for CLC. Shen et al. (2010) from South East Nanjing worked on Iron ore as oxygen carrier.

Eyring et al. (2011) performed experiments with Copper Oxide as carrier and Coal as Fuel. It showed that 'the gasification rate of carbon is no longer a major constraint in the sizing of the fuel reactor as the burnout times for carbon are comparable or smaller than the decomposition times of CuO'. The main advantage of copper oxide is that its reaction with coal is exothermic. The main drawbacks are its price and toxicity.

Adanez et al. (2004) conclude that ilmenite was a good oxygen carrier regarding its price, reactivity and performance in fluidized beds.

It is also of paramount importance to determine the optimum conditions for the conversions of the fuel reactor and the air reactor: the mass ratio of the Oxygen carrier has to be settled regarding it residence time in each reactor.

Ksepko et al. (2010) in the Institute for Chemical Processing for Coal of Poland showed that the reaction profile was changed by the presence of H_2S but there was no effect on the reaction rate due to the presence of H_2S in synthesis gases.

Ryu et al. (2004) from Korea Institute of Energy Research performed experiments on a 50 kWth pilot plant that showed continuous oxidation-reduction cycles and the absence of NOx at the outlet of the oxidizer. Hossain and de Lasa (2008) from Chemical Reactor Engineering Center at the University of Western Ontario, published a review on the work already done on Oxygen carrier selection.

Based on Adanez et al. (2004) work, ilmenite was selected to be the oxygen carrier for the 1 $MWth$ CLC pilot plant of Darmstadt.

Ilmenite characteristics

Ilmenite is a titanium-iron oxide mineral: $FeTiO_3$. It is known to be a black sharp, opaque crystal. Its density is between 4.5 and 5. Its magnetism is naturally weak but it will always becomes magnetic if heated Cui et al. (2002). World resources of ilmenite total more than 1.2 billion tons, as mentioned in the following report Survey (2006).

Even when ground, the shape of ilmenite particles is uneasy to define. Knowing the influence of the shape (sphericity) of the particle on the drag force and on the granulometric analysis, work has been done on the study of the grinding of particles Berthiaux and Dodds (1999). It is a major issue to control the distribution of the sizes of the particles that are fluidized to be able to predict the hydrodynamics of the process in order to size the power plants.

In 1962, Ciborowski and Wlodarski (1962) first studied the electrostatic effects in fluidized beds:
"The electric charges which accumulate on solid particles may cause:

- *1. the adhesion of a layer of solid particles to the walls of the fluidizing equipment.*
- *2. the agglomeration of particles into larger aggregates.*
- *3. the change of a fluidized bed into a channeling bed.*

Between the metal elements which are in contact with the fluidized bed there may arise considerable potential differences, reaching even more than 15 kV."

At the moment, the author did not find any review dealing with the effect of magnetism on the hydrodynamic, but it is well admitted that electric phenomena can alter the hydrodynamic of fluidized beds.

In CLC processes, this property can also be a way to separate reduced metal oxide particles from coal particles in the carbon separation device. No tests have yet been performed to see if the magnetic property of ilmenite would be sufficient to do so.

1.3.7 CLC with gaseous fuels

Ishida and Jin (1994); Jin and Ishida (2002) from Tokyo Institute of Technology propose CLC as a solution to solve environmental issues of industrial energy production. Experiments on a Metal Oxide have been performed with gaseous fuels. It showed good reactivity and mechanical strength.

Experiments performed by Lyngfelt et al. (2001) at Chalmers University of Technology showed that using interconnected fluidized beds was promising for CLC technologies. 100 h of experiments on a pilot scale plant (12 m high Fuel Reactor, 35 ton coal/day) have been performed by Lyngfelt et al. (2004). It showed the efficiency of the process: 99.5% of fuel conversion (gaseous fuel), 100% of CO_2 separated, no loss in particle reactivity during cycles.

Kronberger et al. (2005) work on a dual-fluidized bed reactor system representing a 10-kW CLC prototype. A scaled flow model was built and investigated: gas velocities and reactors designs were parameters, while solids circulation rate and gas leakage between the reactors as well as static pressure balance and residence time distribution of gas and particles were measured. Results showed that the solids circulation rates were sufficient and the gas leakage could be decreased to very low values.

1.3.8 CLC with solid and liquid fuels

In 2008 , 2800 h of operational experience were performed by Lyngfelt et al. on multiple CLC units. Many fuels (solid and liquid) and oxygen carriers were tested. It then was showed that:

- Solid fuels react after a gasification step.
- It is a major issue to ensure that no charcoal particles arrive in the AR.
- Gasification reaction is slow implying a large solid inventory in the fuel reactor.
- Ashes can influence the MeOx lifetime.

In 2010, experiments performed on the 100 kWth Vienna University of Technology prototype that gave interesting results on the influence of Oxygen carriers circulation rate, reactor temperature or fuel gas load. The influence of the solid inventory is planned to be studied. Ilmenite was proven to be a good oxygen carrier regarding its price, reactivity and performance in fluidized beds. Nevertheless, it provokes a very endothermic reaction reducing thus the main efficiency of the process.

1.3.9 Hydrodynamics issues

Circulating flow rate

A mixing of two different solid species is coexisting in the Fuel Reactor: on one hand, large and dense oxygen carriers particles and on the other hand smaller and lighter carbon particles. Fabre (1995) or Batrak (2005) Ph.D works showed the complexity of the prediction and understanding of the main hydrodynamic of such a flow. Batrak modeled the experiment of Fabre in which was introduced a binary mixture of:

- Large and dense particles with a terminal settling velocity twice bigger than the fluidization gas velocity.
- Small and light particles with a terminal settling velocity inferior to the fluidization gas velocity.

It was shown that both large and small particles were able to circulate through the bed. The main characteristic mechanisms triggering the circulation of the large particles are not yet understood. One of the purpose of this Ph.D work is to propose some explanations.

Production of gaseous species

Another specific issue of CLC process comes from the reaction between two solid species. Indeed, in classical gas-solid circulating fluidized beds, coal is oxidized by a gaseous phase: there is a change of density of the gas phase during the reaction, but hardly no production of gas inside the reactor. In solid-solid combustion, the production of gas inside the flow can be of the order of magnitude of the fluidization gas flux. There is no experimental data on the effect of this gas production on the circulation of solids inside the reactor available yet.
Nevertheless, the resulting increase of the gas phase velocity inside the reactor is expected to modify the global hydrodynamics of the bed. This work aimed at investigating and modeling the influence of this phenomenon in order to take it into account in the design of the CLC pilot plant of Darmstadt. This pilot plant is presented and described in Chapter **??**.

Scaling up

A few correlations exists to perform the scaling up of Circulating Fluidized Beds pilot plants to commercial scale. But it is known that the scaling up of fluidized bed is a tricky matter. Kronberger explained that the ratio between the solid mass flow rate and fuel reactor inventory must remain constant during the scaling up. So does the inter-phase mass transfer coefficient and the dimensionless reaction rate (cf. Kronberger et al. (2004)).

Recent studies performed by Parmentier et al. (2008) showed that the issues of fluidization of Geldart A particles at experimental scale can be found with Geldart B particles at commercial scale. This effect has to be taken into account before considering the scaling up of the pilot plant.

1.3.10 Review of pilots or experimental CLC units

In the Table 1.3.10, the different existing pilot plants of CLC are presented. The information is likely to change quite quickly because of the interests and expectations around this technology.

Location	**Unit**	MeOx/CaO tested	Operation hours	Fuel	Ref
Chalmers	10 kW	NiO, Fe_2O_3	1355	natural gas	Lyngfelt and Thunman (2005)
KIER, S korea	50 kW	NiO, CoO	28	natural gas	Ryu et al. (2004)
CSIC, Spain	10 kW	NiO, CuO	140	natural gas	Adanez et al. (2006)
Chalmers	300 W	NiO, Mn_3O_4 Fe_2O_3, Ilmenite	559	natural gas syngas	Johansson et al. (2006)
CSIC, Spain	500 W	NiO, CuO	660	natural gas	Adanez et al. (2008)
Chalmers	10 kW	Ilmenite	50	coal, petcoke	Berguerand and Lyngfelt (2008)
Daejong, S Korea	1 kW	NiO + Fe_2O_3	?	CH_4	Son and Kim (2006)
Vienna Techn. Univ.	120 kW	NiO, Ilmenite	50	natural gas, CO, H_2	Pröll et al. (2008)
Darmstadt	1 MWth	Ilmenite/CaO	-	coal	-
OSU	2.5 kWth, 25 kWth 250 kWth	-	-	coal, syngas	Lee et al. (2001)
IFP	10 kWth	NiAlO	-	liquid/solid fuels	Chandel et al. (2009)
Alstom	65 kWth	MeOx	100 h	natural gas	
Alstom, windsor	3 MWth	CaO	-	naturalgas, coal	
ICSET, Kentucky	10 kW	NiO	-	solid	Cao et al. (2004)
South East Univ Nanjing, Chine	1 kW	-	-	-	Song et al. (2008)

1.3.11 Companies and institutions working on CLC

- Funding for research on CLC are coming from multiple energy companies that are interested by Chemical Looping Combustion intrinsic CO_2 capture. For example,
  ALSTOM Power Systems, Air Liquide, IFP energies nouvelles, Sintef, Vattenfall, Shell, Total S.A., Gaz de France, EDF...

- National and International Institutions are funding projects such as: CO_2 Capture Project (CCP), GRACE project, ENCAP project, ECLAIR, CASTOR...

- Academic partners working on the subject are among others: Université Paul Sabatier (France), Institut National Polytechnique de Toulouse (France), Chalmers University (Sweden), Technische Univ. Darmstadt (Germany), CSIC (Spain), NETL (USA), University of Western Ontario (Canada), Ohio State University (USA), Vienna University of Technology (Austria), Southeast University (China), Cambridge University (UK), Univ. di Napoli Federico II (Italy), Hamburg Univ. of Technology (Germany), Univ. Henri Poincaré (France), Korean Institute of Energy (Korea)...

Résumé du Chapitre 2

Le chapitre 2 présente la modélisation des écoulements réactifs poly-solides.

Depuis les années 70, des scientifiques étudient le comportement des lits fluidisés. De nombreuses études ont été effectuées sur des installations expérimentales ou industrielles. Ainsi, les différents comportements de ces lits ont été classés en tenant compte des caractéristiques des particules transportées, de la vitesse et de la composition du gaz de fluidisation et en fonction de la géométrie étudiée.

Au cours des années 80, des approches empiriques ont été developpées pour dimensionner des lits fluidisés industriels. En raison des limitations de ce type d'approches, des scientifiques ont travaillé à modéliser le mouvement des particules transportées par un gaz. Ainsi, plusieurs approches sont nées:

- Euler-Lagrange: la phase gazeuse est modélisée à l'aide des équations de Navier-Stokes et l'équation du mouvement de chaque particule est résolue. Cette approche permet de résoudre très précisément l'écoulement autour de chaque particule mais a l'inconvénient d'être très coûteux.

- Euler-Euler: la phase gazeuse est modélisée à l'aide des équations de Navier-Stokes. La phase solide est modélisée en adaptant la théorie cinétique des gaz en prenant en compte la présence d'un gaz interstitiel. Cette approche nécessite la modélisation des couplages interfaciaux: trainée, collisions... mais présente l'avantage d'être beaucoup moins coûteuse que l'approche précédente.

L'approche Euler-Euler de type modèle à N-fluides a donné de bons résultats concernant la modélisation de lits fluidisés de particules de classe B selon Geldart. En revanche, certaines études ont montré les limites de cette approche lors de l'étude de lits fluidisés de particules de classe A. Il a été montré qu'il est nécessaire de développer des modèles de sous-mailles pour modéliser correctement la trainée exercée par le gaz sur ces particules. Il a également été montré que la taille de la géométrie peut avoir une influence conséquente sur la capacité des modèles à prédire l'hydrodynamique des LFC.

En ce qui concerne l'étude de lits fluidisés d'un mélange binaire de particules, des études ont montré que l'approche Euler-Euler prédisait correctement l'hydrodynamique des lits fluidisés bouillonnants. Des études concernant la ségrégation radiale et axiale ainsi que les profils radiaux de vitesses et de flux circulant de solide ont été menées. Ces études numériques et expérimentales sont souvent faites sur des géométries à l'échelle expérimentale. Il existe peu de simulations tridimensionnelles d'expériences à l'échelle du pilote industriel.

Ce travail a pour objectif de valider l'approche Euler-Euler implémentée dans NEPTUNE_CFD V1.08@Tlse sur des configurations expérimentales mono-solide puis bi-solide afin d'être en mesure de participer au dimensionnement d'un pilote de type CLC via des simulations 3D instationnaires isothermes poly-solides et réactives.

La deuxième partie de ce chapitre présente la mise en place des equations de transport des phases gazeuses et solides. Ensuite, sont présentés les lois de fermeture des équations implémentées dans NEPTUNE_CFD V1.08@Tlse ainsi qu'un modèle de réaction permettant de prendre en compte la production locale de gaz due à la combustion du charbon avec l'ilmenite.

Chapter 2

CFD modeling of poly-solid reacting flows

2.1 Introduction to circulating fluidized beds

2.1.1 Behavior of circulating fluidized beds

The circulating fluidized beds are utilized at industrial scale since the 40's in the frame of Fluid Catalytic Cracking. It means that lots of experience and experimental data have been accumulated about their behavior.

Geldart's Classification

The prediction of the behavior of a fluidized bed first requires to know the characteristics of the fluidized particles. In 1973, Geldart (1973) proposed a classification of the particles regarding their size and density. The conclusion of his study was:
"The behavior of powders fluidized by gases falls into four categories characterized by density difference ($\rho_p - \rho_g$) and mean size. Powders in group A exhibit dense phase expansion after minimum fluidization and prior to the commencement of bubbling; those in group B bubble at the minimum fluidization velocity; those in group C are difficult to fluidize at all and those in group D are of large size and/or density and spout readily. A criterion which distinguishes between groups A and B has been devised and is shown to agree well with published data. It also predicts that a change in pressure and/or gas viscosity may cause a change in the behavior of particles. A tentative criterion is also suggested for group D."
In 2007, Yang (2007) adapted this classification (cf. 2.1) of powders to make it valid for powders with different properties and fluidized at different pressures and temperatures.

Depending on the fluidization velocity, the particles of each Geldart group form a bubbling, circulating ... fluidized bed. Kunii and Levenspiel (1991) proposed a diagram summarizing the different sort of fluidized beds regarding the particle class and the fluidization velocity (cf. Figure 2.2).

Evolution of the volume fraction of solid

Considering the axial profiles, most of the existing experiments showed a "S-shape" solid fraction curve for the circulating fluidized beds due to:

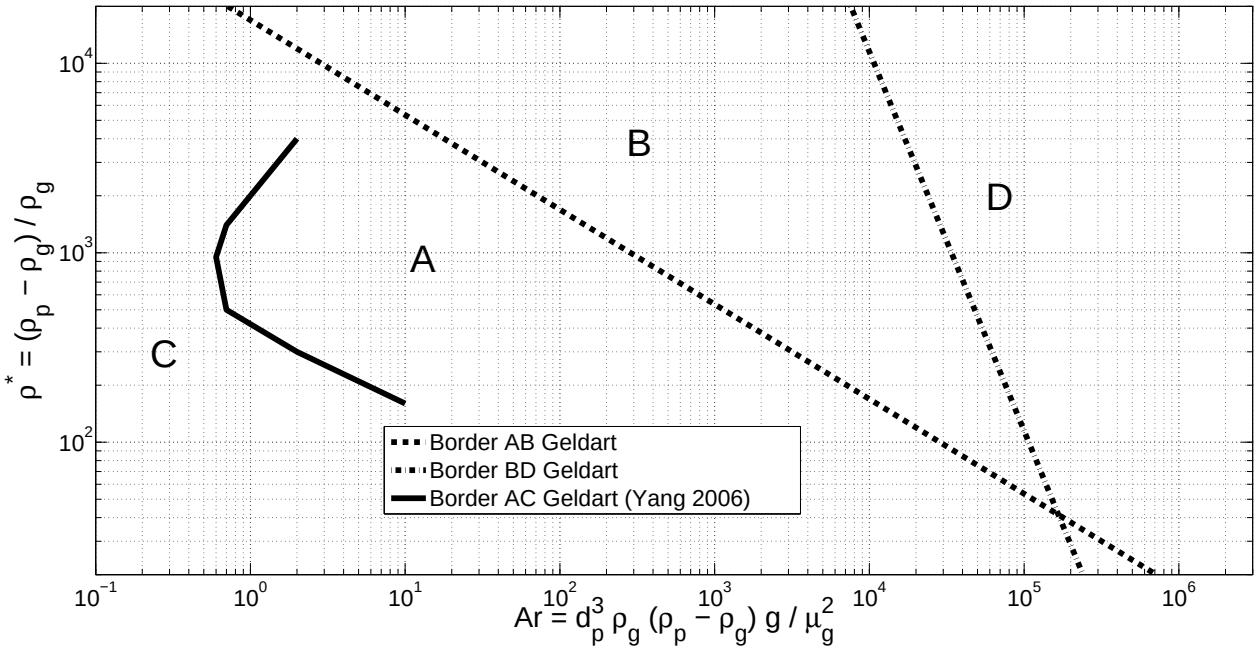

Figure 2.1: Geldart classification of powders modified by Yang

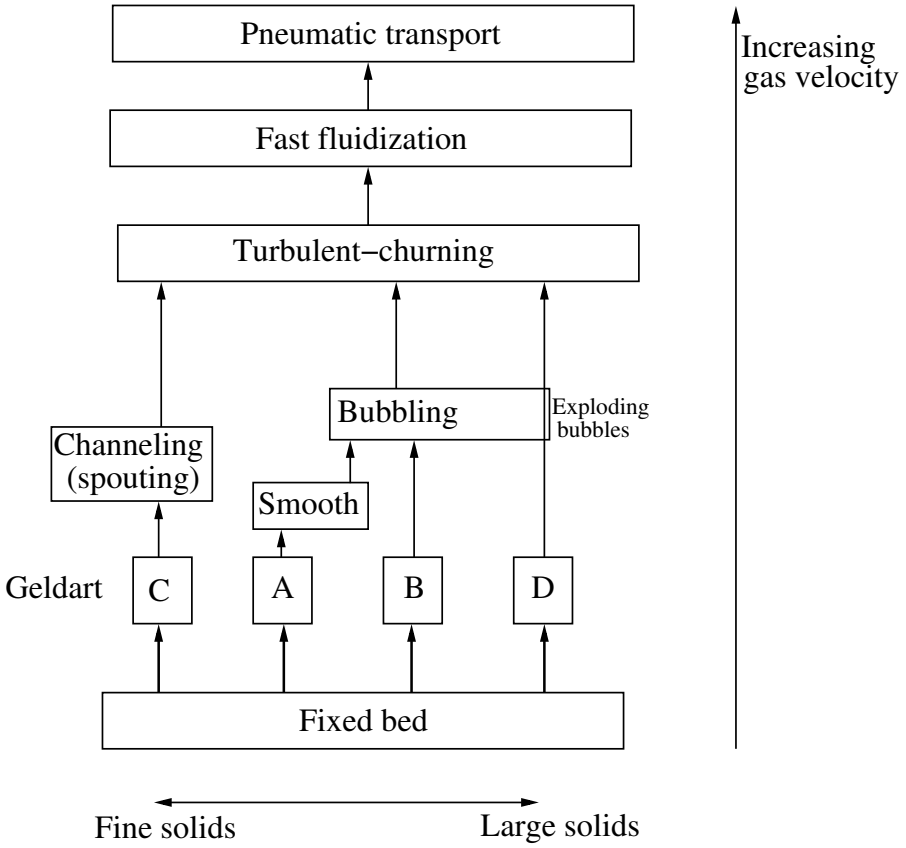

Figure 2.2: Progressive change in gas solid contacting with change in the gas velocity

- at the bottom: the short dense zone with $\overline{\alpha_s}$ = from 0.2 to 0.4
- in the intermediate region: a short part where $\overline{\alpha_s} \simeq 0.2$

- in the upper region: the solid volume fraction decreases until $\overline{\alpha_s}$ = from 0.02 to 0.05.

Mixing and segregation

The mixing and segregation of solids in a CFB strongly depends on the operating point studied. Nevertheless, a few general behaviors can be outlined:

- Vertical segregation is not likely to appear in fast fluidized beds: where the fluidization velocity is larger than the minimum fluidization velocity of the particles (Kunii and Levenspiel (1991)).
- A significant radial segregation of the mean diameter is observed in the riser (Mathiesen et al. (1999)).
- For binary mixture of particles, segregation occurs when the fluidization velocity comes close to the minimum fluidization velocity of largest/heaviest particles (Chiba et al. (1980)).

2.1.2 Numerical modeling of CFB

In the late 60's, scientists such as Wen and Yu (1966) started to develop theoretical tools to describe the motion of particles inside a gas phase.

Since the 80's, empirical approaches have been developed to predict the behavior of CFB's hydrodynamic (Schoenfelder et al. (1994) or Kunii and Levenspiel (1991)). The major drawback of this modeling approach is that it cannot be extended to any other operating point. Its use is then very limited.

The Eulerian modeling of the dispersed phase in dilute two-phase flows using models obtained in the framework of Tchen's therory of discrete particles supended in homogeneous turbulence was achieved and validated by Elghobashi and Abou-Arab (1983), Chen and Wood (1986) and Simonin and Viollet (1990). The modeling of dense gas-solid flows necessitates closures derived in the frame of the kinetic theory of dry granular flows (Lun et al. (1984), Jenkins and Mancini (1989),Ding and Gidaspow (1990)). Then, different approaches have been proposed to model the interaction between particles and turbulence and particles collisions (Derevich and Zaichik (1990), Reeks (1991), Simonin (1991)).

The Eulerian-Eulerian modeling gave relevant results for the simulation of fluidized beds: Enwald et al. (1999), Ferschneider and Mege (1996), Bouillard et al. (1991). The two-fluid modeling has been complemented by Balzer and Simonin (1994) and validated on multiple experimental set up for particles of Geldart B type: Patureaux and Barthod (2000), Neri and Gidaspow (2000), Andreux et al. (2003),Taghipour et al. (2005)... The order of magnitude of the height of the bed or the pressure gradient estimated compared quite well with the experiments.

When the influence of the size of the particles, or the mixing of solid particles with different characteristics is investigated, weaknesses of this modeling appear. The application of this method to bubbling or turbulent fluidized beds of fine Geldart A

particles leads to an overestimation of the bed expansion: (McKeen and Pugsley (2003), Zimmermann and Taghipour (2005)). Recently, Parmentier et al. (2008) showed that this overestimation might not be due to the van der Waals interaction only but to the refinement of the grid of the studied fluidized bed. Indeed, simulations on large dense fluidized bed with Geldart B type particles with a sufficiently refined grid predict the right bed height. Due to the cost of such simulations, it has become necessary to develop sub-grid models to predict the fine scale structures occuring in a CFB (Agrawal et al. (2001), Andrews IV et al. (2005) Igci et al. (2008)).

2.1.3 CFB with a binary mixture of solid

In the 80's, Squires et al. (1985) and Yates and Newton (1986) showed that adding fines to a monodisperse fluidized bed promote uniform fluidization. In 1991, Formisani (1991) performed experiments on dense fluidized beds of a binary mixture of particles with the same density. The conclusion was: "The considerable lowering of minimum fluidization velocity that the addition of a small amount of fines can promote in a bed of coarser particles can be explained by the resulting voidage reduction, which causes a corresponding increase in interstitial gas velocity." There is no mention of the possible influence of the collisions on this phenomena.

Other work on binary mixtures of particles have focused on fluidized beds and showed that both Euler-Euler and Euler-Lagrange approach can predict the axial segregation of the more massive particles towards the bottom of the riser (Mathiesen et al. (2000a), Mathiesen et al. (2000b), Huilin and Gidaspow (2003)). For the radial segregation, Benyahia (2008),He et al. (2009) or Hirschberg and Werther (1998) showed that the massive particles preferentially segregates to the wall. Moreover, it showed that increasing the solid loading tends to decrease the species segregation.
Fabre (1995) experimentally studied a circulating fluidized bed of a binary mixture of sand. The study showed that a binary mixture of solid fluidized bed can be a circulating fluidized bed, even if the terminal settling velocity of one of the two solid species is twice the fluidization velocity.
Batrak et al. (2005) showed that Eulerian-Eulerian modeling can predict this trend. But there is still an underestimation of the circulation of large particles through the bed.

2.1.4 CFD modeling of CLC processes

With such a young technology as CLC, there are only a few recent experimental data that can be used to validate its modeling. A few experiments have been performed specifically to design CLC power plants:

- Experiments on cold flow model circulating fluidized beds aiming at studying the main hydrodynamics phenomena due to the poly-solid flow characteristics.
- Small scale CLC experiments in order to investigate the reaction between the oxygen carrier and the charcoal.

For a few years, some experiments on the whole process have been performed at laboratory scale. Most of them aims at studying the process expected efficiency, the

pollutant emissions or the main hydrodynamics parameters such as the outlet mass flow rate of each species, the pressure profile along the reactors, the mass fluxes profiles...
The local hydrodynamic is seldom studied in such experiments because of the lack of non-intrusive measurement systems able to estimate important unknown parameters of the process such as for example the local production rate of gas inside the bed or the evolution of the volumetric fraction of each phase. In this area, CFD is needed to predict and understand the physical phenomena occurring in the main elements of the process: the fuel reactor, the carbon separation unit, the cyclones or the air reactor.

CFD developers are focusing on validating this modeling on cold flow experiment and on combustion experiments before modeling the entire CLC unit. Studies are mainly focused on:

- The combustion: the description of the kinetic mechanisms is complicated due to the composition and shapes of coal or oxygen carrier particles.
- The hydrodynamics: the fuel reactor is for example an unsteady three dimensional poly-solid reactive multiphase flow.
- The cyclones and the air reactor are better known because of their use in CFB units. Nevertheless the modeling of this kind of experiment at pilot scale remains a challenge.

Hydrodynamic studies of CLC working with gaseous fuel has successfully been performed and validated by Deng et al. (2008), Mahalatkar et al. (2011), Shuai et al. (2010), Kruggel-Emden et al. (2011),Jung and Gamwo (2008), Xu et al. (2007), Balaji et al. (2010), Rifflart et al. (2011).
At the moment, published simulations or experiments on the hydrodynamic study of a reactive circulating fluidized bed of a binary mixture of particles lacked.

Then, some points remain to be investigated:

Is Eulerian-Eulerian modeling able to predict the hydrodynamics of bisolid circulating fluidized beds of CLC plants ?

What is the source of the increase of solid circulation inside CFB's caused by polydispersion ?

Is there an influence of the local production of gas inside the bed on the global hydrodynamics of a circulating fluidized bed ?

2.2 Eulerian-Eulerian modeling of poly-solid reacting flows

Research in multiphase flows is very productive because of its wide range of applications such as fluidized beds, aeronautical engines, plankton transportation, pollutant dispersion, weather prediction, volcanoes eruptions...
Depending on the requirements of each utilization, different approaches were developed to understand and predict the transportation of particles and drops by a fluid phase.

The Direct Numerical Simulation (DNS)

The Navier-Stokes equations are solved around each inclusion, and the grid has to be adaptive to follow the movement of the particles (Hu (1996)). This approach requires minimal hypothesis and models the exact interactions between the fluid and the particles (cf. Wachmann and Schwarzer (1998)). It is sometimes referred to as "numerical experiment".
Despite the increase of the means of calculation, the Direct Numerical Simulation is still prohibitive to model pilot scale bi-solid flows where the interaction of millions of particles with the fluid must be predicted.

The Eulerian-Lagrangian approach

The fluid phase is solved using DNS (the time step and the mesh size must respectively be shorter than the time scale of the fastest fluctuations finer than the smallest length scale) or Large Eddy Simulation (using sub-grid models).
The trajectory of each particle is deduced from the integration of all the forces acting on the inclusion: Discrete Particle Simulation (DPS). This approach requires particle-particle collision algorithms and drag laws. It is also often too costly for industrial multiphase flow prediction.
Another approach is based on the transport of a numerical particle representing a part of the solid phase. Each numerical particle is then transported through its momentum equation. This approach needs more complex closure laws.

The Eulerian-Eulerian modeling approach

It consists in an Eulerian modeling of both solid and gas phases. For the fluid phase, the Navier-Stokes equations give averaged transport equation of volume fractions and velocities. The solid phase modeling is built on a kinetic approach based on a joint fluid-particle Probability Density Function (Simonin (2000)). The set of PDF's moment transport equations is derived from a Boltzmann-like kinetic equation of the PDF. The resulting mass, momentum and particle agitation transport equations needed closure laws. Multiple approaches have been developed to model the inter-particles collisions and the interaction between particles and turbulence (Jenkins and Richman (1985), Derevich and Zaichik (1990).

All these approaches are supplementary. For example, a Discrete Numerical Simulation performed on a few thousand particles can give data to model the interaction between the fluid and the particle resulting in drag laws. Then, a Eulerian-Lagrange

approach can use those drag laws to perform simulations with more particles and therefore investigate the transport of the gas turbulence and of the particles agitation. On the other hand, the statistical approach gives closure laws for the interaction between particles. Finally, the Eulerian-Eulerian approach uses the previous closure laws (drag law, gas turbulence, particle agitation or collision contribution) at mesoscopic to macroscopic scale and becomes able to predict the hydrodynamic of pilot or industrial scale processes.

Three different approaches based on the Eulerian-Eulerian approach are used for poly-solid flow modeling.

- Jenkins and Mancini (1989) proposed a model developed for binary mixture of particle in the vacuum. The transport equations of momentum and temperature are solved for the mixture. The transport equations of mass are solved for each particle species with a diffusion model.

- Lathouwers and Bellan (2000) proposed a model developed for dense binary mixture of particles in gas. The transport equations of mass, momentum and energy are solved for each particle species. The turbulent effect of gas is neglected. The kinetic contribution in the effective stress tensor is neglected and only the collisional part is taken into account.

- Gourdel et al. (1999) proposed a model developed for dilute binary mixture of settling particles in homogeneous isotropic gas turbulent flow. The transport equations of mass, momentum and energy are solved for each particle species. The model accounts simultaneously for dragging along the fluid turbulence and interstitial drag effect. The collisional flux in the effective stress tensor is neglected, and then only the kinetic part is taken into account.

2.2.1 Mean gas-phase transport equations

The phase-averaged transport equation in the frame of the multiphase approach was derived by Delhaye et al. (1981). Technically, the transport equations of the gas phase are deduced by multiplying the instantaneous local equations of mass and momentum by the function χ_g. The phase indicator function χ_g is equal to 1 if the gas phase is present, 0 otherwise. The average mass balance equation is:

$$\frac{\partial \alpha_g \ \rho_g}{\partial t} + \nabla \cdot \alpha_g \ \rho_g \mathbf{U_g} = \Gamma_g \tag{2.1}$$

where $\alpha_g =< \chi_g >$ representing the gas-phase mean-fraction rate. U_g is the gas phase mean velocity and Γ_g represents the mass transfer between phases.

The averaged momentum balance equation for the gas phase is written as:

$$\begin{aligned}\frac{\partial}{\partial t}(\alpha_g \rho_g \mathbf{U_g}) + \alpha_g \rho_g \mathbf{U_g} \nabla \cdot \mathbf{U_g} = -\alpha_g \nabla P_g + \alpha_g \rho_g \mathbf{g} - \nabla \cdot (\alpha_g \rho_g < \mathbf{u'_g u'_g} >_g) \\ + \nabla \cdot (\mathbf{\Theta_g}) + \mathbf{I'_g} + [\mathbf{U}_\sigma - \mathbf{U_g}]\Gamma_g\end{aligned} \tag{2.2}$$

(-$\mathbf{I'_g}$) represents the force exerted at the particle surface by the continuous phase due to viscous stress and pressure gradient fluctuations. P_g is the mean pressure, $\mathbf{\Theta_g}$

represents the mean viscous stress tensor on the gas phase. $\mathbf{U}_\sigma$ is the averaged velocity of the mass flux through the interface.

-$\mathbf{I'_g}$ will be developed during the writing of the dispersed phase momentum equation knowing that $\mathbf{I'_g} + \mathbf{I'_p} = 0$.

In the above equation, the molecular stress tensor writes:

$$\Theta_{g,ij} = \nu_g \left(\frac{\partial U_{g,i}}{\partial x_j} + \frac{\partial U_{g,j}}{\partial x_i} - \frac{2}{3} \frac{\partial U_{g,m}}{\partial x_m} \delta_{i,j} \right) \tag{2.3}$$

The averaging procedures lead to unknown terms proportional to $< \mathbf{u'_g} \mathbf{u'_g} >_g$. Closure laws must be defined to close the momentum equation of the gas phase.

Turbulence modeling

Our modeling is based on the work of Balzer and Simonin (1994) and Vermorel et al. (2003). It introduces the function q_{gp} that will be closed in the particle stress tensor closure section. In order to close the momentum equation of the gas phase, the Reynolds stress tensor must be modeled. Multiple approaches exist. The most common in the modeling of gas-solid flows is based on the writing of the transport equation of the Reynolds stress tensor. It is obtained by multiplying the non-conservative instantaneous momentum equation by $\mathbf{u'_g}$, followed by mathematical transformations and finally an averaging of the equation.
Writing the transport equation of Reynolds stress tensor lead to the introduction of new terms that also need to be closed. The transport equation of the gas kinetic energy can be easily deduced from the transport equation of the Reynolds stress tensor.

The approach developed in this chapter is based on the Boussinesq concept of turbulent viscosity. The Reynolds stress tensor is modeled as a function of the stresses and of the kinetic energy k:

$$< u'_{g,i} u'_{g,j} >= -\nu_g^t \left[\frac{\partial U_{g,i}}{\partial x_j} + \frac{\partial U_{g,j}}{\partial x_i} \right] + \frac{2}{3} \left[k + \nu_g^t \frac{\partial U_{g,m}}{\partial x_m} \right] \delta_{ij} \tag{2.4}$$

In order to close this equation, ν_g^t is modeled and the transport equation of k is solved (cf. equation 2.4), introducing the dissipation rate of the turbulent energy ε resulting in another equation to solve (cf. equation 2.8).

$$\nu_g^t = \frac{2}{3} k \tau_g^t \left[1 + \underbrace{\sum_p C_{12} \frac{\alpha_p \rho_p}{\alpha_g \rho_g} \frac{\tau_{gp}^t}{\tau_{gp}^F} \left(1 - \frac{q_{gp}}{2k} \right)}_{\text{Two-way coupling}} \right]^{-1} \tag{2.5}$$

with $\tau_g^t = C_\mu \frac{3}{2} \frac{k}{\varepsilon}$. A summary of all the important time scales in gas-particle flows can be found in 2.5 on page 63.

$$\begin{aligned}\alpha_g\rho_g\left[\frac{\partial}{\partial t}+U_{g,j}\frac{\partial}{\partial x_j}\right]k &= \underbrace{\frac{\partial}{\partial x_j}\left(\alpha_g\rho_g\frac{\nu_g^t}{\sigma_k}\frac{\partial k}{\partial x_j}\right)}_{\text{Diffusion}} \\ &- \underbrace{\alpha_g\rho_g < u'_{g,i}u'_{g,j} > \frac{\partial U_{g,i}}{\partial x_j}}_{\text{Production}} \\ &- \underbrace{\alpha_g\rho_g\varepsilon}_{\text{Dissipation}} \\ &+ \underbrace{\sum_p \Pi^k_{p\to g}}_{\text{Two-way coupling}}\end{aligned} \tag{2.6}$$

with $\Pi^k_{p\to g}$ representing the influence of the fluctuating motion of particles on the turbulence of the fluid.

$$\Pi^k_{p\to g} = \frac{\alpha_p\rho_p}{\tau^F_{gp}}(-2k + q_{gp} + V_{d,i}V_{r,i}) \tag{2.7}$$

$$\begin{aligned}\alpha_g\rho_g\left[\frac{\partial}{\partial t}+U_{g,j}\frac{\partial}{\partial x_j}\right]\varepsilon &= \underbrace{\frac{\partial}{\partial x_j}\left(\alpha_g\rho_g\frac{\nu_g^t}{\sigma_\varepsilon}\frac{\partial \varepsilon}{\partial x_j}\right)}_{\text{Diffusion}} \\ &- \underbrace{\alpha_g\rho_g\frac{\varepsilon}{k}C_{\varepsilon_1} < u'_{g,i}u'_{g,j} > \frac{\partial U_{g,i}}{\partial x_j}}_{\text{Production}} \\ &- \underbrace{\alpha_g\rho_g C_{\varepsilon_2}\varepsilon}_{\text{Dissipation}} \\ &+ \underbrace{\sum_p \Pi^\varepsilon_{p\to g}}_{\text{Two-way coupling}}\end{aligned} \tag{2.8}$$

with $\Pi^\varepsilon_{p\to g}$ representing the influence of the fluctuating motion of particles on the turbulence of the fluid in ε transport equation.

$$\Pi^\varepsilon_{p\to g} = C_{\varepsilon_3}\frac{\varepsilon}{k}\Pi^k_{p\to g} \tag{2.9}$$

Due to the multi-physics nature of the studied flow, additional terms to model the mean momentum exchange between the fluctuating motions are needed (reverse coupling).

In the following Table (2.2.1) are summarized the imposed constant needed for the turbulence modeling of the fluid phase.

C_{12}	C_μ	σ_k	σ_ε	$C_{\varepsilon 1}$	$C_{\varepsilon 2}$	$C_{\varepsilon 3}$
0.34	0.09	1	1.3	1.44	1.92	1.2

Figure 2.3: Constants of the gas turbulence modeling

2.2.2 Eulerian monodisperse particle phase transport equations

In this part, we first present the description of the motion of the particles of a monodisperse solid phase. The evolution of this system is governed by a set of Boltzmann like equations (cf. Chapman and Cowling (1970)):

$$\frac{\partial f_p^{(1)}}{\partial t} + \frac{\partial}{\partial \mathbf{r}}(c_p \cdot f_p^{(1)}) + \frac{\partial}{\partial c_p}\left(\frac{\mathbf{F_p}}{m_p} \cdot f_p^{(1)}\right) = \left(\frac{\partial f_p}{\partial t}\right)_{coll} \tag{2.10}$$

where $f_p^{(1)}$ is the single phase p-particle velocity distribution function; $\mathbf{F_p}$ is the external force acting on the particle, m_p and c_p are the mass and velocity of p-particle. $\mathbf{r}$ represents the spatial coordinates. The term on the right-hand-side of the equation defines the effects of collisions between particles.
with

$$\frac{F_p}{m_p} = g_i - \frac{1}{\rho_p}\frac{\partial P}{\partial x_i} - f_{Drag} \tag{2.11}$$

The first three moments of the pdf writes:

$$n_p = \int f_p^{(1)} d\mathbf{c_p} \tag{2.12}$$

$$n_p U_p = \int \mathbf{c_p} f_p^{(1)} d\mathbf{c_p} \tag{2.13}$$

$$n_p < u'_{p,i} u'_{p,j} >= \int (\mathbf{c_{p,i}} - \mathbf{U_{p,i}})(\mathbf{c_{p,j}} - \mathbf{U_{p,j}}) f_p^{(1)} d\mathbf{c_p} \tag{2.14}$$

The averaged particle properties are derived using the following definition:

$$< \psi_p >_p = \frac{1}{n_p} \int \psi_p f_p^{(1)} d\mathbf{c_p} \tag{2.15}$$

n_p is the mean number of the p-particle centers per unit volume.

Assuming that $\alpha_p \rho_p = n_p m_p$, we can define: $\alpha_g = 1 - \alpha_p$.

Multiplying equation (2.10) by property ψ_p, integrating over the whole velocity domain using definition (2.15), the general form of the transport equations governing $< \psi_p >_p$ is written:

$$\begin{aligned} \frac{\partial}{\partial t}\left(n_p \langle \psi_p \rangle_p\right) + \nabla \cdot (n_p < \mathbf{c_p} \psi_p >_p) = n_p < \frac{\mathbf{F_p}}{m_p}\frac{\partial \psi_p}{\partial \mathbf{c_p}} >_p \\ + C_p\left(< \psi_p >_p\right) \end{aligned} \tag{2.16}$$

$C_p\left(<\psi_p>_p\right) = \int \psi_p \left(\frac{\partial f_p}{\partial t}\right)_{coll} d\mathbf{c_p}$ represents the mean change rate of ψ_p transported by p-particles due to interparticle collision and is written as an integral over all possible binary collisions. Dahler and Sather (1963) proposed to decompose this term in two contributions: a collisional source term (χ_p) and a collisional flux ($-\nabla \cdot \mathbf{\Theta_p}$) due to the transport of ψ_p due to encounters between particles. This term is developed in Patino-Palacios (2007).

Substituting ψ_p by m_p in equation 2.16, we obtain the transport equation of mass of the p-particle:

$$\frac{\partial n_p m_p}{\partial t} + \nabla \cdot n_p m_p \mathbf{U_p} = 0 \tag{2.17}$$

During any collision, there is no loss of mass. Then, the collision term is null.

Substituting ψ_p by $m_p \mathbf{c_p}$ in equation 2.16, we obtain the transport equation of the momentum of the p-particle:

$$\begin{aligned}\frac{\partial}{\partial t}\left(n_p m_p \mathbf{U_p}\right) + \nabla \cdot \left(n_p m_p \mathbf{U_p U_p}\right) = -\nabla \cdot \left[n_p m_p < \mathbf{u'_p u'_p} >_p + \sum_q \mathbf{\Theta_p}(m_p \mathbf{U_p})\right] \\ + \chi_p(m_p \mathbf{U_p}) + n_p < \mathbf{F_p} >_p\end{aligned} \tag{2.18}$$

χ_p represents the collisional source term and $\mathbf{\Theta_p}$ represents the collisional flux.

Taking $\psi_p = \frac{1}{2} m_p c_p^2$, we can derive the transport equation for the fluctuating kinetic energy of p-particles, q_p^2:

$$\begin{aligned}\frac{\partial}{\partial t}\left(n_p m_p q_p^2\right) + \nabla \cdot \left(n_p m_p \mathbf{U_p} q_p^2\right) = -\nabla \cdot \left[n_p m_p \frac{1}{2} < (\mathbf{u'_p} \cdot \mathbf{u'_p}) \mathbf{u'_p} >_p + \mathbf{\Theta_p}(m_p \mathbf{q_p^2})\right] \\ - \left[n_p m_p < (\mathbf{u'_p} \cdot \mathbf{u'_p}) >_p + \mathbf{\Theta_p}(m_p \mathbf{U_p})\right] : \nabla \mathbf{U_p} \\ + \chi_p(m_p q_p^2) + n_p < \mathbf{F_p} \cdot \mathbf{u'_p} >_p\end{aligned} \tag{2.19}$$

The first term on the right side represents the transport of energy by the velocity fluctuations and collisions (kinetic flux and collisional flux). The second term specifies that the production of turbulent kinetic energy by the mean velocity gradient. The third term represents the collisional sources and the final, the interaction with the continuous phase. The building of those Eulerian equations leads to unknown terms that need closure laws.

Closure laws for the solid phase

Particle stress tensor

The effective particle stress tensor is written as follow:

$$< u'_{p,i} u'_{p,j} >= \left[P_p - \lambda_p \frac{\partial U_{p,m}}{\partial x_m}\right] \delta_{ij} - \mu_p \left[\frac{\partial U_{p,i}}{\partial x_j} + \frac{\partial U_{p,j}}{\partial x_i} - \frac{2}{3} \frac{\partial U_{p,m}}{\partial x_m} \delta_{ij}\right] \tag{2.20}$$

where $\mu_p = \alpha_p \rho_p (\nu_p^{kin} + \nu_p^{col})$.

The kinetic viscosity ν_p^{kin} is modeled as:

$$\nu_p^{kin} = \left[\frac{1}{3} q_{gp} \tau_{gp}^t + \frac{1}{2} \tau_{gp}^F \frac{2}{3} q_p^2 (1 + \alpha_p g_0 \Phi_c)\right] \times \left[1 + \frac{\tau_{gp}^F}{2} \frac{\sigma_c}{\tau_p^c}\right]^{-1} \tag{2.21}$$

with $\Phi_c = \frac{2}{5}(1+e_c)(3e_c - 1)$ and $\sigma_c = \frac{1}{5}(1+e_c)(3-e_c)$.

The collisional viscosity ν_p^{col} is modeled as:

$$\nu_p^{col} = \frac{4}{5} \alpha_p g_0 (1+e_c) \left[\nu_p^{kin} + d_p \sqrt{\frac{2}{3}\frac{q_p^2}{\pi}}\right] \tag{2.22}$$

The granular pressure P_p and λ_p writes:

$$P_p = \alpha_p \rho_p [1 + 2\alpha_p g_0 (1+e_c)] \frac{2}{3} q_p^2 \tag{2.23}$$

The granular pressure can be seen as a particle-particle interaction force. It is expected to become very important when the volume fraction of particles increases: then the maximum random packing of particles can not be exceeded.

$$\lambda_p = \alpha_p \rho_p \frac{4}{3} \alpha_p g_0 (1+e_c) d_p \sqrt{\frac{2}{3}\frac{q_p^2}{\pi}} \tag{2.24}$$

Both the kinetic stress tensor and the collisional stress tensor are function of the particle agitation and the fluid-particle correlation. In order to close those terms, both transport equations are solved (cf. equation (2.37) and equation (2.38)).

$$\begin{aligned} \alpha_p \rho_p \frac{\partial q_p^2}{\partial t} + \alpha_p \rho_p U_{p,j} \frac{\partial q_p^2}{\partial x_j} &= \underbrace{\frac{\partial}{\partial x_j}\left(\alpha_p \rho_p K_p^t \frac{\partial q_p^2}{\partial x_j}\right)}_{\text{Turbulent transport}} \\ &- \alpha_p \rho_p \underbrace{< u'_{p,i} u'_{p,j} > \frac{\partial U_{p,i}}{\partial x_j}}_{\text{Production by mean velocity gradient}} \\ &- \underbrace{\frac{\alpha_p \rho_p}{\tau_{gp}^F}\left[2q_p^2 - q_{gp}\right]}_{\text{Transfer from gas turbulence to particle agitation}} \\ &+ \underbrace{\chi_p}_{\text{Source term due to collisions}} \end{aligned} \tag{2.25}$$

with the turbulent diffusivity coefficient $K_p^t = K_p^{kin} + K_p^{col}$.

$$K_p^{kin} = \left[\left(\frac{2}{3}\frac{C_s}{C_\mu}\tau_{gp}^t \frac{1}{3} q_{gp} + \frac{5}{9}\tau_{gp}^F \frac{2}{3} q_p^2 \left\{1 + \alpha_p g_0 \phi_c\right\}\right)\right] \left(1 + \frac{5}{9}\xi_c \frac{\tau_{gp}^F}{\tau_p^c}\right)^{-1}$$

$$K_p^{coll} = \frac{6}{5}\alpha_p g_0 \left(1+e_c\right)\left[K_p^{cin} + \frac{10}{9}d_p\sqrt{\frac{2q_p^2}{3\pi}}\right]$$

$$\begin{aligned}\left[\frac{\partial}{\partial t} + U_{p,j}\frac{\partial}{\partial x_j}\right] q_{gp} &= \underbrace{\frac{1}{\alpha_p\rho_p}\frac{\partial}{\partial x_j}\left(\alpha_p\rho_p\frac{\nu_{gp}^t}{\sigma_k}\frac{\partial q_{gp}}{\partial x_j}\right)}_{\text{Turbulent transport}} \\ &- \underbrace{< u'_{g,i}u'_{p,j} > \frac{\partial U_{p,i}}{\partial x_j}}_{\text{Production due to particle velocity gradient}} \\ &- \underbrace{< u'_{g,i}u'_{p,j} > \frac{\partial U_{g,i}}{\partial x_j}}_{\text{Production due to gas velocity gradient}} \\ &- \underbrace{\frac{q_{gp}}{\tau_{gp}^t}}_{\text{Dissipation due to friction with the fluid}} \\ &- \underbrace{\frac{1}{\tau_{gp}^F}\left[\left(1+\frac{\alpha_p\rho_p}{\alpha_g\rho_g}\right)q_{gp} - 2k - 2\frac{\alpha_p\rho_p}{\alpha_g\rho_g}q_p^2\right]}_{\text{Reverse coupling}}\end{aligned} \tag{2.26}$$

Following Fevrier et al. (2003), an eddy viscosity assumption is used to predict the fluid-particle velocity correlations tensor components:

$$\begin{aligned}< u'_{g,i}u'_{p,j} > &= \frac{1}{3}q_{gp}\delta_{ij} + \frac{\eta_r}{1+\eta_r}\left(< u'_{g,i}u'_{g,j} > -\frac{2}{3}k\delta_{ij}\right) \\ &- \frac{\nu_{gp}^t}{1+\eta_r}\left(\frac{\partial}{\partial x_i}U_{p,j} - \frac{1}{3}\frac{\partial}{\partial x_m}U_{p,m}\delta_{ij} + (1-\beta_2)\left(\frac{\partial}{\partial x_j}U_{g,i} - \frac{1}{3}\frac{\partial}{\partial x_m}U_{g,m}\delta_{ij}\right)\right)\end{aligned} \tag{2.27}$$

with $\eta_r = \dfrac{\tau_{gp}^t}{\tau_{gp}^F}$ and the particle turbulent viscosity $\nu_{gp}^t = \dfrac{1}{3}q_{gp}\tau_{gp}^t$, the constant $\beta_2 = 0.6$.

Momentum equation

In the momentum equation, for monodisperse cases, $\chi_p = 0$.

Particle agitation equation

The particle agitation exchange term during collisions between particles of the same class corresponds to a dissipation term due to the inelasticity of the collision:

$$\chi_{pp} = -m_p n_p \frac{1-e_c^2}{\tau_{pp}^c}q_p^2 \tag{2.28}$$

with $\tau_{pp}^c = \left[4d_p^2 g_{pp} n_p\sqrt{\dfrac{2\pi}{3}q_p^2}\right]^{-1}$.

2.2.3 Eulerian polydisperse modeling

For the extension of the previous model to a polydisperse system in a case where there is no change in the diameter of the particles, a term has to be added to take into account the interactions between the solid phases. Transport equations for all solid phases must be derived. This work was performed by Gourdel et al. (1998), Fede and Simonin (2005),Batrak et al. (2005),Patino-Palacios (2007).

Closure laws for the solid phase

A more precise description of the closure laws for the solid phase can be found in Gobin et al. (2003). **Particle stress tensor**
The closure for the particle stress tensor stay close to monodisperse closure by introducing modified particle volume fraction, particle collision diameter and collision time scale. Batrak et al. (2005) proposed to write the effective particle stress tensor of a binary mixture of particles as a function of the stresses and the collisional flux:

$$< u'_{p,i}u'_{p,j} >= \left[P_p - \lambda_p \frac{\partial U_{p,m}}{\partial x_m}\right]\delta_{ij} - \mu_p \left[\frac{\partial U_{p,i}}{\partial x_j} + \frac{\partial U_{p,j}}{\partial x_i} - \frac{2}{3}\frac{\partial U_{p,m}}{\partial x_m}\delta_{ij}\right] \tag{2.29}$$

where $\mu_p = \alpha_p \rho_p (\nu_p^{kin} + \nu_p^{col})$.

The kinetic viscosity ν_p^{kin} is modeled as:

$$\nu_p^{kin} = \left[\frac{1}{3}q_{gp}\tau_{gp}^t + \frac{1}{2}\tau_{gp}^F \frac{2}{3}q_p^2(1 + \widehat{\alpha_p} g_0 \Phi_c)\right] \times \left[1 + \frac{\tau_{gp}^F}{2}\frac{\sigma_c}{\widehat{\tau_p^c}}\right]^{-1} \tag{2.30}$$

with $\Phi_c = \frac{2}{5}(1+e_c)(3e_c - 1)$ and $\sigma_c = \frac{1}{5}(1+e_c)(3-e_c)$.

The collisional viscosity ν_p^{col} is modeled as:

$$\nu_p^{col} = \frac{4}{5}\widehat{\alpha_p} g_0 (1+e_c)\left[\nu_p^{kin} + \widehat{d_p}\sqrt{\frac{2}{3}\frac{q_p^2}{\pi}}\right] \tag{2.31}$$

The granular pressure P_p and λ_p writes:

$$P_p = \alpha_p \rho_p [1 + 2\widehat{\alpha_p} g_0 (1+e_c)]\frac{2}{3}q_p^2 \tag{2.32}$$

The granular pressure can be seen as a particle-particle interaction force. It is expected to become very important when the volume fraction of particles increases: then the maximum random packing of particles can not be exceeded.

$$\lambda_p = \alpha_p \rho_p \frac{4}{3}\widehat{\alpha_p} g_0 (1+e_c)\widehat{d_p}\sqrt{\frac{2}{3}\frac{q_p^2}{\pi}} \tag{2.33}$$

The modified volume fraction, the collision diameter, and the collision timescale write respectively:

$$\widehat{\alpha_p} = \sum_q \alpha_q \frac{2m_q}{m_p + m_q}\left[\frac{d_{pq}}{d_q}\right]^3 \tag{2.34}$$

$$\widehat{d_p} = \frac{1}{\widehat{\alpha_p}} \sum_q \alpha_q \frac{d_{pq}^4}{d_q^3} \frac{2m_q}{m_p + m_q} \tag{2.35}$$

$$\frac{1}{\widehat{\tau_p^c}} = \sum_q \frac{2m_q}{m_p + m_q} \frac{1}{\tau_{pq}^c} \tag{2.36}$$

Both the kinetic stress tensor and the collisional stress tensor are function of the particle agitation and the fluid-particle correlation. In order to close those terms, both transport equations are solved (cf. equation (2.37) and equation (2.38)).

$$\begin{aligned} \alpha_p \rho_p \frac{\partial q_p^2}{\partial t} + \alpha_p \rho_p U_{p,j} \frac{\partial q_p^2}{\partial x_j} &= \underbrace{\frac{\partial}{\partial x_j}\left(\alpha_p \rho_p K_p^t \frac{\partial q_p^2}{\partial x_j}\right)}_{\text{Turbulent transport}} \\ &- \alpha_p \rho_p \underbrace{< u'_{p,i} u'_{p,j} > \frac{\partial U_{p,i}}{\partial x_j}}_{\text{Production by mean velocity gradient}} \\ &- \underbrace{\frac{\alpha_p \rho_p}{\tau_{gp}^F}\left[2q_p^2 - q_{gp}\right]}_{\text{Transfer from gas turbulence to particle agitation}} \\ &+ \underbrace{\sum_q \chi_{pq}}_{\text{Source term due to collisions}} \end{aligned} \tag{2.37}$$

with the turbulent diffusivity coefficient $K_p^t = K_p^{kin} + K_p^{col}$.

$$K_p^{kin} = \left[\left(\frac{2}{3}\frac{C_s}{C_\mu}\tau_{gp}^t \frac{1}{3} q_{gp} + \frac{5}{9}\tau_{gp}^F \frac{2}{3} q_p^2 \left\{1 + \alpha_p g_0 \phi_c\right\}\right)\right]\left(1 + \frac{5}{9}\xi_c \frac{\tau_{gp}^F}{\widehat{\tau_p^c}}\right)^{-1}$$

$$K_p^{coll} = \frac{6}{5}\alpha_p g_0 \left(1 + e_c\right)\left[K_p^{cin} + \frac{10}{9} d_p \sqrt{\frac{2q_p^2}{3\pi}}\right]$$

$$\begin{aligned}\left[\frac{\partial}{\partial t}+U_{p,j}\frac{\partial}{\partial x_j}\right]q_{gp} &= \underbrace{\frac{1}{\alpha_p\rho_p}\frac{\partial}{\partial x_j}\left(\alpha_p\rho_p\frac{\nu_{gp}^t}{\sigma_k}\frac{\partial q_{gp}}{\partial x_j}\right)}_{\text{Turbulent transport}} \\ &- \underbrace{< u'_{g,i}u'_{p,j} >\frac{\partial U_{p,i}}{\partial x_j}}_{\text{Production due to particle velocity gradient}} \\ &- \underbrace{< u'_{g,i}u'_{p,j} >\frac{\partial U_{g,i}}{\partial x_j}}_{\text{Production due to gas velocity gradient}} \\ &- \underbrace{\frac{q_{gp}}{\tau_{gp}^t}}_{\text{Dissipation due to friction with the fluid}} \\ &- \underbrace{\frac{1}{\tau_{gp}^F}\left[\left(1+\frac{\alpha_p\rho_p}{\alpha_g\rho_g}\right)q_{gp}-2k-2\frac{\alpha_p\rho_p}{\alpha_g\rho_g}q_p^2\right]}_{\text{Reverse coupling}}\end{aligned} \tag{2.38}$$

Following Fevrier et al. (2003), an eddy viscosity assumption is used to predict the fluid-particle velocity correlations tensor components:

$$\begin{aligned}< u'_{g,i}u'_{p,j} > &= \frac{1}{3}q_{gp}\delta_{ij}+\frac{\eta_r}{1+\eta_r}\left(< u'_{g,i}u'_{g,j} > -\frac{2}{3}k\delta_{ij}\right) \\ &- \frac{\nu_{gp}^t}{1+\eta_r}\left(\frac{\partial}{\partial x_i}U_{p,j}-\frac{1}{3}\frac{\partial}{\partial x_m}U_{p,m}\delta_{ij}+(1-\beta_2)\left(\frac{\partial}{\partial x_j}U_{g,i}-\frac{1}{3}\frac{\partial}{\partial x_m}U_{g,m}\delta_{ij}\right)\right)\end{aligned} \tag{2.39}$$

with $\eta_r = \dfrac{\tau_{gp}^t}{\tau_{gp}^F}$ and the particle turbulent viscosity $\nu_{gp}^t = \dfrac{1}{3}q_{gp}\tau_{gp}^t$, the constant $\beta_2 = 0.6$.

Momentum equation

Gourdel et al. (1998) give the collisional source terms for an homogeneous flow by analytical integration of the exact term:

$$I_{q\to p,i} = -\alpha_p\rho_p\frac{m_q}{m_p+m_q}\frac{1+e_c}{2}\frac{H_1(Z_{pq})}{\tau_{pq}^c}(U_{p,i}-U_{q,i}) \tag{2.40}$$

- m_p and m_q represent the mass of any particle p and q respectively.
- e_c is the inelastic restitution coefficient.
- τ_{pq}^c the characteristic collision time.

$H_1(Z_{pq})$ is a theoretical function due to the adaptation of the kinetic theory of gas that can be approximated by:

$$H_1(Z_{pq}) = \frac{8+3Z_{pq}}{6+3Z_{pq}} \tag{2.41}$$

where Z_{pq} represents the ratio between the square of the mean relative velocity and the relative fluctuating velocity variance given in terms of the sum of both particles species agitation:

$$Z_{pq} = \frac{V_{pq,i}V_{pq,i}}{\frac{4}{3}(q_p^2 + q_q^2)} \tag{2.42}$$

with $V_{pq,i} = U_{p,i} - U_{q,i}$

The theoretical expression of the characteristic collision time is:

$$\frac{1}{\tau_{pq}^c} = g_{pq} n_q \pi {d_{pq}}^2 \sqrt{\frac{16}{3\pi}(q_p^2 + q_q^2)} H_0(Z_{pq}) \tag{2.43}$$

where $H_0(Z_{pq})$ can, according to Batrak et al. (2005), be approximated by:

$$H_0(Z_{pq}) = \sqrt{1 + \frac{\pi Z_{pq}}{4}} \tag{2.44}$$

The characteristic collision time is proportional to the collision frequency. It is interesting to study its dependence to Z_{pq} parameter.
If $Z_{pq} \to 0$, the collisions are governed by the particle fluctuating motion here represented by the solid particle agitations.
If $Z_{pq} \to \infty$, the collisions are due to the mean particle-particle relative velocity between the solid phases.

In equation (2.43), g_{pq} represents the radial distribution function depending on the maximum random packing of identical hard spheres α_{max} (cf. Figure 2.4). This function aims at increasing the collisional flux terms in the momentum and kinetic stress transport equations when the total volume fraction of solid reaches α_{max}. Lun et al. (1984) proposed a modeling of this function:

$$g_{pq} = \left[1 - \frac{\alpha_s}{\alpha_{max}}\right]^{-2.5\alpha_{max}} \text{ if } \alpha_s < \alpha_{max} \tag{2.45}$$

where α_s is the full solid volume fraction and α_{max} is imposed to 0.64 corresponding to the maximum solid fraction for a random packing of identical hard spheres.

Influence of Z_{pq} on the momentum exchange

In the previous section, the momentum exchange during polydisperse collisions showed that $I_{q\to p,i}$ is proportional to $\sqrt{1 + Z_{pq}} \times (U_p - U_q) \times \sqrt{q_p^2 + q_q^2}$.

If $Z_{pq} \to \infty$, it has been showed that collisions are due to the slipping velocity between particles and $I_{q\to p,i} \propto (U_p - U_q)^2$. The magnitude of the mean momentum exchange during the collisions between two particles of different phases is also guided by the slipping velocity between the two solid phases.

If $Z_{pq} \to 0$, it has been showed that collisions are due to the particles agitation and $I_{q\to p,i} \propto (U_p - U_q) \times \sqrt{q_p^2 + q_q^2}$. In this case, the magnitude of the mean momentum exchange during collisions is due to both the slipping velocity between particles and

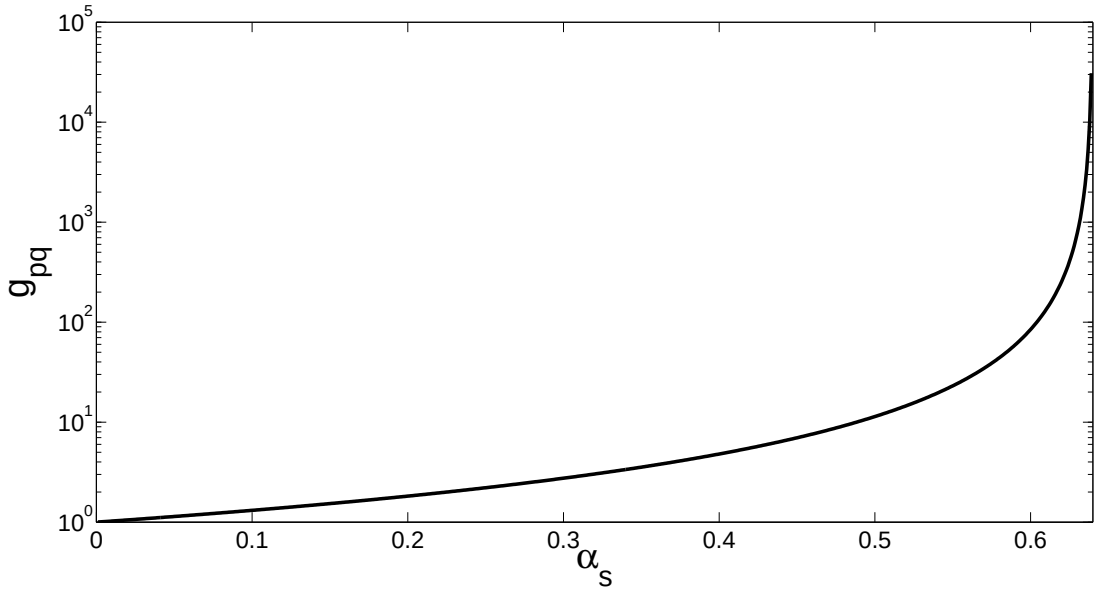

Figure 2.4: Influence of α_p on the g_{pq} function

the particle agitation.

It implies that, for example, if the particle agitation is not well resolved (due to the mesh size), the mean momentum exchange during collisions will be quite well predicted if $Z_{pq} \to \infty$ and quite badly if $Z_{pq} \to 0$.

Particle agitation equation

The collisional source term χ_{pq} in the particle agitation equation (cf. Equation (2.37)) can be divided into three contributions (cf. the following equation). The first term represents the transfer of kinetic energy to particle agitation, the second is a term characteristic from a return to the equilibrium and the last one corresponds to the dissipation due to inelastic collisions ($\propto (1 - e_c)$).

$$\begin{aligned}\chi_{pq} = &\frac{m_p m_q}{m_p + m_q}\frac{1+e_c}{2}\frac{n_p}{\tau^c_{pq}} \times \underbrace{\frac{m_q}{m_p + m_q}\frac{1+e_c}{2}(U_{p,i} - U_{q,i})^2 H_1(Z_{pq})}_{\text{Production of agitation}} \\ &- \frac{m_p m_q}{m_p + m_q}\frac{1+e_c}{2}\frac{n_p}{\tau^c_{pq}} \times \underbrace{\frac{8}{3}\frac{m_p q_p^2 - m_q q_q^2}{m_p + m_q}}_{\text{Return to equilibrium}} \\ &\underbrace{- m_p \left(\frac{2m_q}{m_p + m_q}\right)^2 \frac{1 - e_c^2}{4}\frac{n_p}{\tau^c_{pq}}\frac{2}{3}(q_p^2 + q_q^2)}_{\text{Dissipation due to inelastic collisions}}\end{aligned} \tag{2.46}$$

The particle agitation exchange term during collisions between particles of the same

class corresponds to a dissipation term due to the inelasticity of the collision:

$$\chi_{pp} = -m_p n_p \frac{1-e_c^2}{\tau_{pp}^c} q_p^2 \tag{2.47}$$

with $\tau_{pp}^c = \left[4 d_p^2 g_{pp} n_p \sqrt{\frac{2\pi}{3} q_p^2} \right]^{-1}$.

The particle agitation exchange term for the collisions between particles of different classes is depending on both the slipping velocity between particles and the agitation of each phase.

If $Z_{pq} \to 0$:

- $\varepsilon_{pq} \propto (q_p^2 + q_q^2)^{3/2}$
- χ_{pq} is the difference of two terms respectively proportional to $\sqrt{(q_p^2 + q_q^2)} \times (U_{p,i} - U_{q,i})^2$ and $\sqrt{(q_p^2 + q_q^2)} \times (m_p q_p^2 - m_q q_q^2)$

If $Z_{pq} \to \infty$:

- $\varepsilon_{pq} \propto (q_p^2 + q_q^2) \times (U_{p,i} - U_{q,i})$
- χ_{pq} is the difference of two terms respectively proportional to $(U_{p,i} - U_{q,i})^3$ and $(U_{p,i} - U_{q,i}) \times (m_p q_p^2 - m_q q_q^2)$

2.2.4 Closure laws for the fluid-particle interaction terms

The external forces applied on the particles writes:

$$< F_p >_p = I_{g \to p,i} + \alpha_p \frac{\partial P}{\partial x_i} + \alpha_p \rho_p g_i \tag{2.48}$$

Drag force

Gobin et al. (2003) proposed a closure for the drag force. According to the assumption that particles are hard spheres translating in a non-uniform flow, the drag force can be modeled in the momentum equations as a term:

$$I_{g \to p,i} = -\frac{\alpha_p \rho_p}{\tau_{gp}^F} V_{r,i} \tag{2.49}$$

where $V_{r,i}$ is the mean gas-particle relative velocity.
The momentum transfer from the particle phase to the fluid phase is defined as: $I_{p \to g,i} = -I_{g \to p,i}$.
The mean relative velocity writes:

$$\mathbf{V_r} = \mathbf{U_p} - \mathbf{U_g} - \mathbf{V_d} \tag{2.50}$$

The drift velocity V_d is due to the transport of particles by gas turbulence: the drag force is not only due to the mean velocity between the gas and the particle, there is a momentum exchange due to the gas turbulence. In industrial fluidized beds, the

particles are crossing the gas phase without "seeing" the gas turbulence ($\tau_{gp}^F >> \tau_g^t$). Then the influence of the drift velocity is expected to be negligible.
It is modeled according to the work of Simonin et al. (1993):

$$V_{d,i} = -D_{gp,ij}\left[\frac{1}{\alpha_p}\frac{\partial \alpha_p}{\partial x_j} - \frac{1}{\alpha_g}\frac{\partial \alpha_g}{\partial x_j}\right] \tag{2.51}$$

with $D_{gp,ij} = \frac{1}{3} q_{gp} \tau_{gp}^t \delta_{ij}$, τ_{gp}^t is the characteristic time from gas-particle turbulence and q_{gp} is the fluid-particle velocity correlation.

Assuming that the forces acting on the particles are reduced to the drag force, the particle relaxation time scale τ_{gp}^F represents the characteristic time of the interaction between gas and particles through the drag force and can be written:

$$\frac{1}{\tau_{gp}^F} = \frac{3}{4}\frac{\rho_g}{\rho_p}\frac{|\mathbf{V_r}|}{d_p} < C_D > \tag{2.52}$$

Gobin et al. (2003) proposed to model $< C_D >$ from the drag law of Wen & Yu limited by the one of Ergun for large solid volume fraction:

$$\begin{array}{lcl} < C_D >= & C_{D,WY} & \alpha_p \leq 0.3 \\ < C_D >= & min(C_{D,WY}, C_{D,Ergun}) & \alpha_p > 0.3 \end{array} \tag{2.53}$$

with

$$\begin{aligned} C_{D,WY} = & \quad \frac{24}{< Re_p >}\left[1 + 0.15 < Re_p >^{0.687}\right] \alpha_g^{-1.7} \quad (\text{with } \langle Re_p \rangle < 1000) \\ C_{D,Ergun} = & \quad 200\frac{\alpha_p}{< Re_p >} + \frac{7}{3} \end{aligned} \tag{2.54}$$

and the particulate Reynolds number: $< Re_p > = \alpha_g \rho_g \frac{< V_r > d_p}{\mu_g}$.

2.3 Modeling the reaction between Carbon and MeOx

In this section, a model for the reaction between coal particles and ilmenite particles is proposed. It aims at studying the decrease in the diameter of carbon particles during the reaction and the possible effect of a lack of oxygen in the ilmenite particle. The change in the density of the gas phase is also modeled. At each time step, in each cell of the domain, ρ_g is calculated as a mixture of steam and CO_2.

Nevertheless, it is assumed that the flow is **incompressible**: compressibility effects that might occur in the dense part of the bed are neglected in our study.

The purpose of this work is to study the influence of the local production of gas inside the bed, so we will consider the reaction as **isothermal**: heat transfers are neglected.

A simple reaction kinetics is chosen to model the reduction of metal oxide:

$$C_s + 2O_s \rightarrow CO_{2g} \tag{2.55}$$

The reaction is locally inhibited when there is a local lack of oxygen in the MeOx. The amount of oxygen carried by the MeOx particles has no effect on the hydrodynamical behavior of MeOx particles. There is no modeling of the change in the diameter of MeOx particles during reaction.
The density of the fluidization gas depends on its composition (concentration of CO_2). The consumption of carbon due to the reaction makes the coal particles disappear: hence the number of carbon particles is conserved. Nevertheless, a model has been developed to take into account the evolution of the diameter of carbon particles.

2.3.1 Calculation of the gas phase density

The fluidization gas is composed of steam and the reaction produces CO_2. It is therefore necessary to consider the change in the density of the gas phase.
The reference density for the gas phase is imposed to be equal to the density of steam at $T = 1243\ K$ and $P = 1\ bar$: ${\rho^0}_g = \rho_{H_2O} = 0.18\ kg/m^3$.
The gas phase is considered as a perfect gas mixture so:

$$\frac{\rho_g}{W_g} = \frac{P}{RT} \text{ where } \frac{1}{W_g} = \Sigma_\alpha \frac{Y_\alpha}{W_\alpha} \text{ and } R = 8.314\ J/mol/K.$$

$$\rho_g = \rho_0 \times \frac{W_{CO_2}}{Y_{CO_2}(W_{H_2O} - W_{CO_2}) + W_{CO_2}}$$

2.3.2 Transport equations of the reacting species

Modeling the reaction between a coal particle and a MeOx particle implies to introduce three scalars: one for the evolution of the fraction of CO_2 in the gas phase (transported by the gas phase), another one for the evolution of the fraction of oxygen in the metal oxide (transported by the MeOx phase) and one for the diameter of coal particles (transported by the coal phase). More information can be found in Flour and Simonin

(1993).

For the solid phases

Including a reaction model implies for coal particles implies a variation of the mass of coal particles during reaction. Therefore, new terms have to be introduced in the Eulerian-Eulerian approach. The transport equation of the mass fraction of the specie k is written :

$$\frac{\partial \alpha_p \rho_p Y_{k_p}}{\partial t} + \frac{\partial}{\partial x_i}[\alpha_p \rho_p (U_{p,i} + V_{k_p,i}) Y_{k_p}] = -\frac{\partial}{\partial x_i}[\alpha_p \rho_p < u"_{p,i} y"_{k_p} >] + \Gamma_{k_p} \tag{2.56}$$

with V_{k_p}, i is the i-component of the diffusion velocity V_{k_p} of the solid specie k_p and Γ_{k_p} its reaction rate. If the evolution of the mean diameter is modeled, we consider that there is no apparition or disappearing of particles due to collisions.
The conservation equation of the number of coal particles writes:

$$\frac{\partial \alpha_p \rho_p \chi_p}{\partial t} + \frac{\partial}{\partial x_i} \alpha_p \rho_p \chi_p U_{p,i} = -\frac{\partial}{\partial x_i} \alpha_p \rho_p < u"_i \chi'_p >_p + \Gamma \chi_p \tag{2.57}$$

with Γ accounts for the coalescence or dislocation of the particles. If the number of particle is conserved, $\Gamma = 0$.

χ_p represents the number of particules by unit of mass particle. Combining the equation $\alpha_p \rho_p \chi_p = n_p$ with $n_p = \dfrac{\alpha_p \pi {d_p}^3}{6}$ gives a relation between d_p and (χ_p, ρ_p).

For the gas phases

The mass conservation writes:

$$\frac{\partial}{\partial t} \alpha_g \rho_g + \frac{\partial}{\partial x_i} \alpha_g \rho_g U_{g,i} = \Gamma_g \tag{2.58}$$

It is assumed that, in the reactor, only one reaction characterized by the molar reaction rate $\dot{Q}$ occurs. The reaction rate of carbon is defined as: $\Gamma_C = \dfrac{\alpha_C \rho_C}{\tau}$ with $\tau = constant$. It is linked to the molar reaction rate through $\Gamma_C = \nu_C W_C \dot{Q}$.

The transport equation of each gaseous species by the fluid phase writes:

$$\alpha_g \rho_g \frac{\partial Y_{k,g}}{\partial t} + \frac{\partial}{\partial x_i} \alpha_g \rho_g [(U_{g,i} + V_{k,i}) Y_{k,g}] = -\frac{\partial}{\partial x_i} \alpha_g \rho_g < u"_{g,i} y"_k > + \Gamma_k \tag{2.59}$$

2.3.3 Carbon reaction model

The kinetics of consumption of the carbon particles is given by :

$$(\frac{dM_c}{dt})_{reaction} = -\frac{M_c}{\tau} \tag{2.60}$$

where M_c is the total mass of carbon in the bed, and according to ALSTOM, the reaction time τ is chosen constant and equal to 200 s.

Then, the consumption rate of carbon is: $\Gamma_c = \dfrac{-\alpha_c \rho_c}{\tau}$.

CO_2 is produced inside the bed due to the reaction between MeOx and Carbon. Then, the amount of gas produced each second when the steady state is reached can be estimated using the balance equation of the mass of carbon in the bed:

$$\frac{dM_c}{dt} = Q^c_{inlet} - Q^c_{outlet} - \frac{M_c}{\tau} \tag{2.61}$$

and

$$Q^c_{inlet} = Q^c_{outlet} + Q^{fresh}_c \tag{2.62}$$

Then it gives:

$$\frac{M_c}{\tau} = Q^{fresh}_c \quad \text{when the permanent state is reached.} \tag{2.63}$$

For a given characteristic reaction time, the mass of carbon in the bed is given by the fresh mass flow rate of carbon.

Definition of the reaction rate

Γ_c represents the reaction rate of carbon. The limitation of the reaction term is defined according the following equation:

$$\Gamma_c = Max\left(-\frac{\alpha_c \rho_c}{\tau}, -\frac{M_C}{2M_O} Y_{mO} Y_O \frac{\alpha_{MeOx}\rho_{MeOx}}{\Delta t}\right)$$

If the limiting species is Carbon, the reaction rate is $-\frac{\alpha_c \rho_c}{\tau}$. If there is a lack of oxygen in the MeOx particles, the reaction rate can be estimated using the conservation equation of Y_O.

2.4 Remarks on the main hypothesis of gas-particle flow modeling

The equations of the Eulerian-Eulerian modeling were presented. In order to close the transport equations of mass, momentum and kinetic energy, a few important hypothesis have been assumed. This section aims at presenting the most relevant.

$\mathbf{d_p/L << 1}$

The ratio between the diameter of the particles and the characteristic length of the gas phase has to be very small because the closure laws for the gas phase are based on a phase averaging performed on control volume where the size of the particle has to be smaller than the gas characteristic length scale.

The main flow is isothermal

The transport equation of the temperature of the fluid phase is not solved: variations of temperature inside the studied fluidized beds are expected to have minor influence on the hydrodynamics of cold flow models. For the first reactive simulation, the influence

of temperature is neglected.
So, the fluid properties are taken at the imposed reference pressure and temperature.

The main flow is incompressible
The density, the viscosity and the thermal diffusivity do not depend on the pressure. This assumption is acceptable in the dilute zone. In the dense zone, there could be some compressibility effects: the density of the gas phase might vary due the hydrostatic pressure in the bed.

The particles are considered hard spherical particles
The influence of the sphericity of the particles on the drag force can be modeled and introduced without changing the approach (cf. Loth (2008)). Particles are considered spherical because it is very difficult to experimentally determine its shape.

The rotation of the particles is not modeled
It might be modeled by artificially reducing the inelastic restitution coefficient. Indeed, in a fluidized bed, the effect of rotation will introduce an additional friction with the fluid.

The collisions are binary and instantaneous
It is legitimate to assume that collisions between 3 particles at the same time hardly never occurs while the flow remains dilute. In dense cases, a frictional model can be added through a frictional viscosity. Regarding the expected time step, the collision is considered instantaneous.

Uncorrelated inter-particle collision model
The velocity of the particles are not correlated during a collision: there is no effect of the turbulence on the particle impact velocity probability distribution (Simonin et al. (2002)).

The added mass force is neglected
This force is the influence of the little mass of fluid transported by the particle (it is negligible for subsonic particle velocities). Moreover, in our simulations, the ratio between the density of the fluid phase and the density of the solid phases is very small.

The history force is neglected
It is assumed that the drag force is stationary. More information on the history/Basset force can be found in Vojir and Michaelides (1994).

The surface tension force is neglected
In gas-particle flows, the surface tension can be neglected. More information can be found in Delhaye (1974).

The lift force is neglected
The lift forces are non negligible when the particles are rotating or during wall-particle collisions. If the velocity gradient in the vicinity of the wall is important, the lift force might be important. More information can be found in Oesterlé (1994).

The value of the maximum random packing is assumed
The maximum random packing of a binary mixture of spherical particles is supposed equal to the maximum random packing of identical spherical particles. If the size of the particles are too different, this is surely wrong. Nevertheless, in the case of circulating fluidized beds were $\alpha_s < \alpha_{max}$ the influence of this parameter is negligible.

2.5 Characteristic time scales in gas-particle flows

In multiphase flows, many physical phenomena occurred at different scales and it is often complicated to understand what are the predominant phenomena at stake. The estimation and ranking of the characteristic time scale of the flow is often helpful to understand the results of the simulations.
This section aims at presenting the most relevant time scales driving industrial fluidized beds flows.

2.5.1 The Stokes characteristic time: τ_p

It corresponds to the particle relaxation time of mixture of identical particles in the Stokes' regime ($Re_p << 1$):

$$\frac{1}{\tau_p} = \frac{\rho_g}{\rho_p}\frac{18\nu_g}{d_p^2} \tag{2.64}$$

2.5.2 The mean particle relaxation time: τ_{gp}^F

Also referred to as the mean characteristic time of particle entrainment by the fluid motion, τ_{gp}^F represents the characteristic time of the interaction between gas and particles through the drag force. It has been introduced by Simonin (1991). Its difference with τ_p lies in the consideration of the non-linear dependence of the drag coefficient on the instantaneous relative velocity in τ_{gp}^F:

$$\frac{1}{\tau_{gp}^F} = \frac{3}{4}\frac{\rho_g}{\rho_p}\frac{|\mathbf{V_r}|}{d_p} < C_D > \tag{2.65}$$

Regarding the Wen & Yu drag law, if $Re_p \to 0$ then $\frac{1}{\tau_{gp}^F} \to \frac{1}{\tau_p}$.

2.5.3 The fluid turbulent time scale: τ_g^t

If the turbulence of the gas phase is modeled through a $k-\varepsilon$ model, the characteristic time scale of the turbulence can be written:

$$\tau_g^t = C_\mu \frac{3}{2}\frac{k^2}{\varepsilon} \tag{2.66}$$

This timescale is linked to the relaxation time through the Stokes number: $\frac{\tau_p}{\tau_g^t} = St$.

2.5.4 The eddy particle interaction time: τ_{gp}^t

Also referred to as the fluid Lagrangian integral time scale, τ_{gp}^t is the characteristic time from the turbulence seen by the particles. The difference between τ_{gp}^t and τ_g^t states in that τ_{gp}^t takes into account the crossing trajectory effect.

$$\tau_{gp}^t = \frac{\tau_g^t}{\sqrt{1 + C_\beta \zeta_r}} \tag{2.67}$$

with $\zeta_r = \dfrac{V_{r,i} V_{r,i}}{\frac{2}{3}k}$ and $C_\beta = 1.8$.

2.5.5 The inter-particle collision time: τ_p^c

It is the mean collision characteristic coming from the kinetic theory:

$$\frac{1}{\tau_p^c} = n_p g_0 \pi d_p^2 \sqrt{\frac{16}{\pi} \frac{2}{3} q_p^2} \tag{2.68}$$

Adapted to the Eulerian modeling of a solid phase, it corresponds to the mean collision time for a mono-disperse phase. With this definition of τ_p^c, the effect of the interstitial gas on collisions is not considered.

2.5.6 The collision time scale of a binary mixture of particles: τ_{pq}^c

In the case of a poly-disperse flow, the characteristic time between the collision of a particle of phase p with any particle of phase q is defined. It is estimated according to the work of Gourdel et al. (1998).

$$\frac{1}{\tau_{pq}^c} = g_{pq} n_q \pi d_{pq}^2 \sqrt{\frac{16}{\pi} \frac{1}{3} (q_p^2 + q_q^2)} H_0(Z_{pq}) \tag{2.69}$$

2.6 General boundary conditions

2.6.1 Inlets

The inlet conditions are the Dirichlet conditions on the velocities, the volume fractions and the energies.

- Gas injectors: for the gas phase, an inlet mass flux is imposed. For the particles, it is considered as a smooth wall. So, a slip condition for particle velocity and a zero flux for random kinetic energy and flux-particle covariance are imposed.
- Gas-Particle injectors: an inlet mass flux is imposed for all phases.

2.6.2 Outlet

The outlet of the riser is a free outlet. If the flow is coming in, the volume fraction of particles is imposed equal to 10^{-12}: only gas can enter through the outlet.

2.6.3 Wall

Wall friction functions are used for the velocities and the turbulence properties of the continuous phase.
A slip condition for the velocity and zero flux for particle random kinetic energy are imposed on the dispersed phases, corresponding to elastic bouncing of spherical particle on smooth wall without friction.

2.6.4 Symmetry

The symmetry conditions are zero flux for all the variables with cancellation of the normal velocity component.

2.7 Presentation of $NEPTUNE\_CFD$ software

This section is widely inspired by the publication of Neau et al. (2010). A few years ago, three-dimensional numerical simulations of circulating fluidized beds were restricted to coarse meshes due to the limitation of computing power (CPU clock speed, memory, hard drive). The recent improvements on high performance computing overcome this limitation. For hardware, the frequencies of the processors have remained almost flat in the last years. The development of multi-core technology and the increase of memory cache size and of memory and other interconnect frequencies have led to very highly parallel and efficient computing platforms. For software, this computational power has been exploited according to the parallelization of codes (message passing). Hence, we are able to solve previously intractable problems. The strong development of HPC allows the use of finer and larger meshes and the increase of numerical simulation accuracy.
$NEPTUNE\_CFD$ is an unstructured parallelized multiphase flow software developed in the framework of the NEPTUNE project, financially supported by CEA (Commissariat l'Énergie Atomique), EDF (Électricité de France), IRSN (Institut de Radioprotection et de Sûreté Nucléaire) and AREVA NP. NEPTUNE_CFD V1.08@Tlse code

allows to take into account complex phenomena: particle mixture, particle-fluid interaction, particle-particle and particle wall collisions, heat and mass transfers and chemical reactions.

NEPTUNE_CFD V1.08@Tlse is dedicated to calculating multiphase or multi-field flows, at the local scale and in geometries that may be complex. The software has the following main characteristics and functions:

Flow systems processed

- 1 to 20 fluid fields (phases or fields)
- Processing of water/steam flows with actual thermodynamic laws

Numerical methods

- Meshes with all types of cell (element), non conforming connections
- "Cell-center" type finite volume method
- Calculation of co-localized gradients with reconstruction methods
- Distributed-memory parallelism by domain splitting

Physical models

- Interfacial momentum transfer terms
- Interfacial energy transfer terms
- Turbulence
- Head losses and porosity
- Additional scalars

Architecture

- Interfacing with the *Code_Saturne* Enveloppe module for management of the pre-processing operations on the mesh, of the parallelism and of the post-processing files
- Written in Fortran 77 (the majority) and C (ANSI 1989) (procedural programming)
- Ready for Unix and Linux platforms

The partial differential equations are discretized with a second-order centered scheme and the solution is time advanced by a first order scheme. The model and the numerical method are adapted to the handling of n-phases (in fact n-fields), including the single phase frame. Models and Eulerian transport equations represent an extension of the classical two phase flow model developed in the frame of the ESTET ASTRID Project and include water-steam closure laws and correlations.
The algorithm, based on original elliptic fractional step method (see Méchitoua et al. (2002) and Méchitoua et al. (2003)) that leads either to use linear solvers or direct $nphas \times nphas$ matrix inversion. The main interest of the method is the so-called "alpha-pressure-energy" step that ensures conservativity of mass and energy and allows strong interface source term coupling. Mass, momentum and energy equations are coupled with the help of a pressure correction equation, within the iterative "alpha-pressure-energy" step. The algorithm allows density variation according to pressure and enthalpy during the computation.

The momentum balance equations are solved with a semi-implicit method. They are split in fractional steps: explicit balance, velocity implicit increment prediction, "alpha-pressure-energy" implicit increment prediction, final velocity correction. The "Alpha-Pressure-Energy" step stops after the mass conservation sub-step, when the volume conservation holds. The user can adapt the criterion parameter ε_{vol}, but this one remains very severe as it applies to a maximum value over the whole domain. The standard value of ε_{vol} is 10^{-5}. Because of implicit formulation and three dimensional unstructured meshes, we use iterative solvers:

- For the pressure: conjugated gradient or bi-conjugate gradient stabilized (bi-cgstab),
- For volume fraction: bi-conjugate gradient stabilized or jacobi,
- For velocity: jacobi.

A time-dependent time step is used (computed from Courant and Fourier criteria), typically $\Delta t = 5 \times 10^{-4} s$. The following iterative solvers have been selected: jacobi for the velocity, conjugated gradient for the pressure and bi-cgstab for the volume fraction. The criterion parameter ε of "Alpha-Pressure" step is fixed to 10^{-6} and the maximum number of cycles into "Alpha-Pressure" step is 50.

2.7.1 Averaging

Excluding the pressure and volume fraction variables, all the time-averages are phase-averages, weighted by the volume fraction α_k. For example, the l component of the mean velocity of phase k is calculated for each cell as follows:

$$\overline{U_{k,l}} = \frac{\sum_{i=1}^{ndt} \alpha_k^i U_{k,l}^i \Delta t^i}{\sum_{i=1}^{ndt} \alpha_k^i \Delta t^i} \tag{2.70}$$

where Δt^i is the time step at iteration i.

2.7.2 Calculation information

Most of the calculations presented in this Ph.D were performed on the national computational centers. The author is grateful to:
The HPC resources of CALMIP under the allocation P0111 (Calcul en Midi-Pyrénées).
The HPC resources of CINES under the allocation 2010-026012 made by GENCI (Grand Equipement National de Calcul Intensif).

The processors used for those simulations are referenced below:
Intel Xeon Quad-Core E5472 owns 4 cores with a 3 GHz frequency
Nehalem EX owns 4 cores with a 2.8 Ghz frequency.

Résumé du Chapitre 3

Le chapitre 3 présente l'ensemble des simulations et expériences effectuées sur le pilote froid d'Alstom situé à l'Université Technologique de Compiègne.

La première partie de ce chapitre est une présentation de la géométrie du pilote et des conditions opératoires. Les études expérimentales et numériques ont été effectuées en parallèle ce qui peut expliquer certaines différences entre les conditions opératoires des simulations et des expériences.

La deuxième partie concerne l'étude de lits fluidisés circulants mono-solides. Les simulations ont permis de prédire de façon satisfaisante l'hydrodynamique du lit et ont permis d'étudier l'influence du diamètre moyen des particules ainsi que l'influence de la hauteur des injecteurs de gaz secondaires. La simulation d'un cas de LFC mono-solide polydisperse a montré l'importance de la prise en compte de la polydispersion de la phase solide sur le comportement des LFC.

La troisième partie concerne l'étude de LFC bi-solides. Des particules lourdes et grosses (ilmenite) sont mélangées à des particules légères et petites (alumine). Les études expérimentales et numériques ont toutes deux montré que l'ajout de petites particules dans un lit de grosses particules augmentait la circulation totale de solide à travers le lit. Le post-traitement des simulations avec NEPTUNE_CFD V1.08@Tlse a permis d'étudier localement l'hydrodynamique et les mécanismes physiques en jeu: les collisions entre les particules de classe différentes sont à l'origine de l'augmentation de la circulation de solide.

Ainsi, notre étude a montré que NEPTUNE_CFD V1.08@Tlse pouvait prédire quantitativement et qualitativement l'hydrodynamique de lits fluidisés circulants représentatifs de ceux utilisés dans le cadre du Chemical Looping.

Chapter 3

Application to CLC-like non-reactive poly-solid Circulating Fluidized Beds

Contents

3.1 The ALSTOM experimental setup

The Cold Flow Model (CFM) used for this study is a Circulating Fluidized Bed (CFB) based in Université Technologique de Compiègne (UTC) which works with air in cold conditions. The characteristics dimensions were calculated and validated by analogy with the real 125 MWe power plant Emile Huchet (France).
The cold flow model is used for furnace hydrodynamics tests. Picture and sketch are given by Figures 3.2 and 3.1. Solids flow comes from the furnace and goes into the cyclone 1 and returns to the furnace by loop seal 1, the cyclone 2 in series captures the smallest particles (fines) from the exhaust of cyclone 1. Solids from cyclone 2 are reintroduced into the furnace via loop seal 2. The gas coming from the cyclone 2 exhaust goes through the bag filter before being released outside (cf. Figure 3.1).

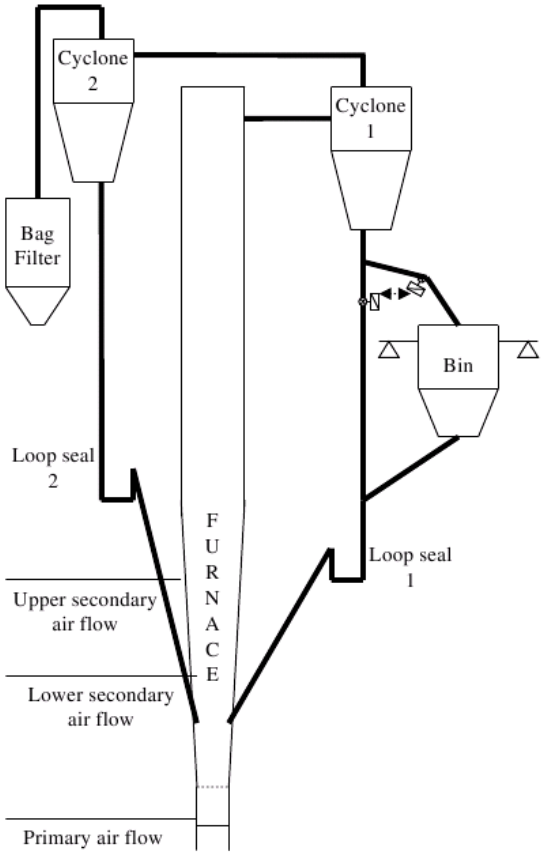

Figure 3.1: Schematic view of UTC's Cold Flow Model (CFM)

The furnace in stainless steel has a regular cross-section of 0.456 m^2 and a grate section of 0.155 m^2. The furnace widens with a conical shape. The total height of the furnace is 10 m. In the furnace, three kinds of gas injection are available. The first one introduces the gas in the furnace through the fluidization grate. This is the primary air flow. The two other levels, the secondary air flows, introduce the gas directly in the furnace. The lower and upper secondary air can be located at different levels 400 mm/800 mm/1500 mm/2000 mm from the grate.

Figure 3.2: Photo of UTC's CFM

3.1.1 Operating Conditions

For monosolid experiments, ilmenite particles (Titanium-Iron oxide) were used for the tests. According to granulometric analysis, its d_{50} is about 160 μm. The density of ilmenite, measured by using a helium Pyctometer is 4600 kg/m^3.
In bisolid experiments, a mixture of ilmenite particles and alumina particles was used. The solid mixture is introduced in the reactor in start-up phase. When the necessary amount of solids is in the reactor, the inlet air flow is adjusted to obtain the test conditions.

3.1.2 Measurement system

During an experimental campaign, multiple parameters are recorded. The acquisition starts after one hour of stabilization: the pressure and temperature in the bed reach a steady state.

Pressure

To extract the pressure, 16 probes are located at various heights along the wall of the riser (cf. Table 3.1).

Table 3.1: Pressure probes locations

z (m)	0	0.1	0.28	0.4	0.7	1.3	2	2.9	4	4.5	5.85	6.5	8.05	8.5	9.45	10.35

Pressure profile is then determined by averaging over a 5 $min.$ period of time. Then, the total solid mass in the reactor is estimated by integration of the pressure profile along the wall according to the following algorithm:

- On each part between two pressure sensors, it is assumed that the pressure gradient is constant: $P_1 - P_2 = \rho_m \cdot g \cdot (z_1 - z_2)$.
- Calculation of the mass remaining in this section of the bed: $\Delta m = \rho_m \cdot \Delta V$.
- The total inventory is the sum of all Δm.

In the following Table the calculated volume of each part of the bed are given:
This estimation of the mass of particles inside the bed is only an approximation because we do not have access to the pressure at the grid height. It might results in an underestimation of about 10 kg.

Solid mass flux

The circulating flow rate is evaluated by blowing empty method. At the end of a test, when the Cold Flow Model is getting shut-down, the storage bin, which is on a weighing gauge, is getting filled and the evolution of weight versus time is recorded. The circulating flow rate corresponds directly to the curve gradient in the first moment after the loop was stopped.
In the experiments presented, the error on the estimated circulating solid mass flux is estimated according to the following calculation:
$\frac{\Delta Q_F}{Q_F} = \frac{2\Delta m}{m} + \frac{2\Delta t}{t}$ with $t = 30$ s, $m = 200$ kg, $\Delta t = 0.25$ s and $\Delta m = 5$ kg.
The order of magnitude of the error for the ranges studied is about 7%.

Part of the bed	Heights	Calculated volume
1	0-0.1	0.016 m^3
2	0.1-0.28	0.0315 m^3
3	0.28-0.4	0.0230 m^3
4	0.4-0.7	0.0642 m^3
5	0.7-1.3	0.1574 m^3
6	1.3-2	0.2325 m^3
7	2-2.9	0.3758 m^3
8	2.9-4	0.5014 m^3
9	4-4.7	0.3191 m^3
10	4.7-5.85	0.5242 m^3
11	5.85-7	0.5242 m^3
12	7-8.05	0.4786 m^3
13	8.05-8.8	0.3418 m^3
14	8.8-9.45	0.2963 m^3
15	9.45-10.35	0.4102 m^3

Granulometry

Two methods were used to estimate the granulometry of the ilmenite and alumina used in this Cold Flow Model:
Laser granulometry where performed by R. Ansart (IMFT) at the Ecole des Mines d'Albi-Carmaux using a laser granulometer Malvern Mastersizer 2000 at a dispersion pressure set to 3.5 bars. Each test was performed 5 times to fulfill the standard NF ISO 133201.
A sieving method was used at UTC by ALSTOM.

3.1.3 Computed geometry and mesh construction

In this chapter, different geometries with multiple secondary injectors heights have been investigated.
Therefore, the number of secondary injectors and their heights can vary for each experiment.

Figure 3.3 shows a view of the LFC UTC mesh, which is formed by a layer of quadrangle. This mesh is composed of about 850 000 cells with a volume from 1 cm^3 to 10 cm^3. The smallest are placed close to the injection region of the fluidization gas while the largest are in top part of the bed.
Secondary injectors are, in the case presented by Figure 3.3, located at height 400 mm (4 injectors) and 800 mm (8 injectors).

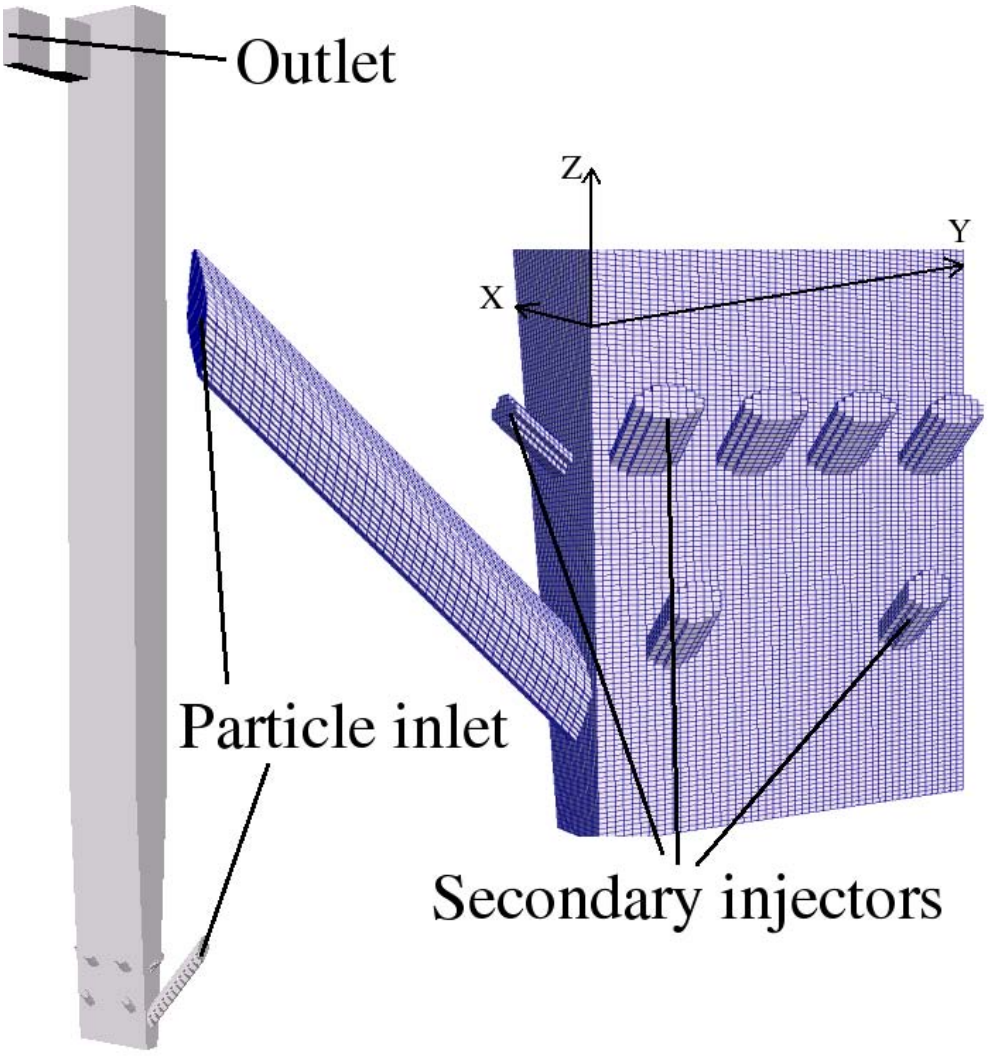

Figure 3.3: Mesh of LFC UTC Cold Flow Model

3.2 Mono-solid cases

3.2.1 Monodisperse simulations of monosolid experiments

ALSTOM participates in the construction of a pilot plant of Chemical Looping Combustion at pre-industrialization scale. To help designing this prototype, many experiments have been performed on the UTC-CFM set up mainly to study and design the carbon separation device. Data on the hydrodynamic of the circulating fluidized bed were also available. Those experiments performed in parallel with this Ph.D validated the modeling of monodisperse CFB's. Then, some parametric studies have been performed to estimate the influence of the size of the particles, the height of the secondary injectors and the fluidization velocity. Some simulations that are not presented in this study showed that the predicted circulating mass flux while performing a simulation by imposing the mass inventory in the riser gives comparable results than imposing the inlet mass flux (the inventory is well predicted).

Experimental results

Four similar experiments of a mono-solid circulating fluidized bed were performed and are presented in Table 3.2. The difference between those cases remain in the inventory of ilmenite. In this conditions, ilmenite particles are of B-type according to Geldart's classification.

Table 3.2: Monodisperse experiment and simulation

Case	Total inventory	Outlet solid mass flux
EXP 1	259 kg	5.1 kg/s
EXP 2	188 kg	6.2 kg/s
EXP 3	174 kg	5.5 kg/s
EXP 4	151 kg	6.0 kg/s
$Neptune\_CFD$	259 kg	6.5 kg/s

According to the experiment results, in the range studied, at fixed inlet gas flux, the circulation of solids is slightly linked to the total mass of solid in the bed. The circulating solid mass flux is always about 6 kg/s.

As expected, in Figure 3.4, the experiments showed that increasing the inventory of solid increases the pressure drop inside the bed.

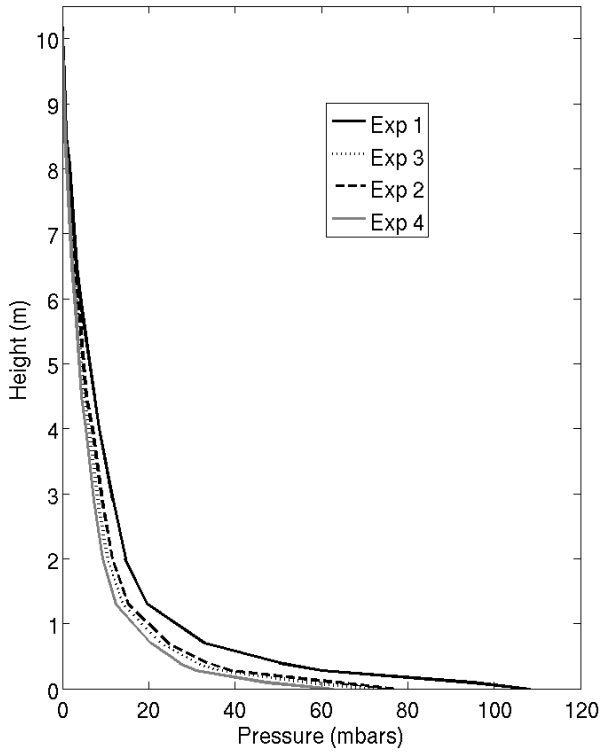

Figure 3.4: Pressure profiles of monosolid experiments

NEPTUNE_CFD results

$EXP1$ was modeled as a 3D unsteady monodisperse simulation. The simulation characteristics are summarized in the Appendix 5 in the following section: 5.2.2. In this simulation, the inventory of solid and inlet gas flux through primary and secondary injectors were imposed. The outlet mass flux of solid is reinjected through the inlet. The circulating solid mass flux is a result of the simulation.

Table 3.2 showed that the monodisperse modeling provides a good prediction of the circulating ilmenite mass flux. Nevertheless, it slightly overestimates the predicted mass flux. This can be due to the assumption that the ilmenite particles are monodispersed (the imposed d_{50} is equal to 160 μm).

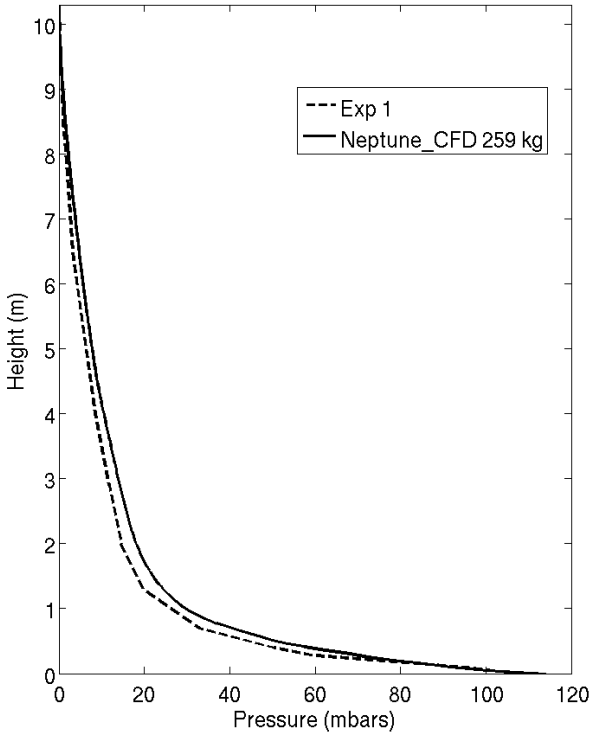

Figure 3.5: Pressure profiles of EXP 1 and simulation

Figure 3.5 shows that the experiment and simulation pressure profiles are in accordance. The simulation predicts the dense zone for $z < 1\ m$ and the dilute zone for $z > 2\ m$. The evolution of the pressure is quasi-linear in both zones.

The averaged ilmenite particles residence time can be estimated according to the ratio between the mass of ilmenite in the bed and the circulating flux of ilmenite. It goes from 25 s to 50 s for these experiments: it decreases proportionally to the decrease in the inventory of solid. Whenever possible, the simulated physical time was higher than this estimated residence time.

Parametric study of the mean diameter of the solid phase

Another 3D unsteady monosolid simulation was performed with NEPTUNE_CFD V1.08@Tlse to study the influence of the single mean diameter. The characteristics of this simulation is summarized in Appendix 5 in the following section:5.2.3. In this simulation, $d_{50} = 120\ \mu m$.

As expected, **decreasing the mean diameter significantly increases the circulating solid mass flux**.

Indeed, regarding the chosen drag law (cf. 2.2.4), in the case of a single particle in free fall, the drag force is proportional to:

- d_p for small Re_p
- $d_p^{1.7}$ for large Re_p

On the other hand, the gravity contribution is proportional to d_p^3.

In the established zone of the bed (the upper part where the slope of the pressure profile is constant), it can be assumed that $V_p \simeq V_f - V_t$. V_t represents the terminal settling velocity of the particle.
Then, for a constant fluidization velocity V_f, when d_p decreases, the particle velocity V_p increases. At the same time, for an imposed inventory, when d_p decreases, the fraction of solid in the established zone increases.
Finally, the circulating mass flux increases when d_p decreases for an imposed inventory and fluidization velocity.

Parametric study of the height of the secondary injectors

Historically, the secondary injectors are added to risers because experience showed that it reduces the emission of NOx. It also represents a security in the case of accumulation of solid at the bottom of the bed: it helps particles from flying off.

A few study dealing with the influence of secondary injectors on the hydrodynamic of the bed can be found in the literature. Wang and Gibbs (1991) concluded that for an imposed total gas velocity, increasing the secondary injector velocity increases the fraction of particles under the secondary injection zone. Kang et al. (2000) showed that the tangential injection of secondary air is more effective for the increase in the solid holdup than the radial injection.

This section aims at studying the influence of the height of the secondary injectors on the UTC geometry. Two simulations have been defined:

- The first with 6 injectors at a height of 800 mm and 8 at 2000 mm.
- The second with 4 injectors at a height of 400 mm and 6 at 1500 mm.

The main characteristics of those two cases are summarized in the Appendix 5 in the sections 5.2.4 and 5.2.5.

The total gas volume flow rate is equal to $Q_{inlet} = 1.482\ kg \cdot s^{-1}$ in both cases and is divided as shown by Table 3.3.

Those inlet boundary conditions correspond to a $V_f = 3.02\ m \cdot s^{-1}$ in the main section.

Inlet	Boundary condition	Repartition
Fluidisation grid	0.459 $kg \cdot s^{-1}$	31%
Gaz inlet at height 2000/1500	0.726 $kg \cdot s^{-1}$	49% splitted on 8/6 injectors
Gaz inlet at height 800/400	0.296 $kg \cdot s^{-1}$	20% splitted on 6/4 injectors

Table 3.3: Inlet boundary conditions

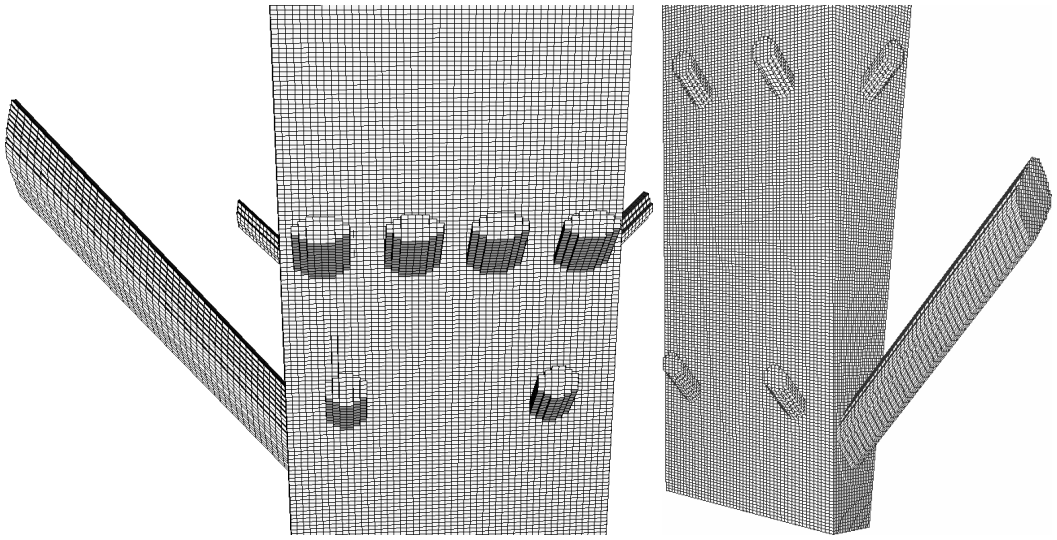

Figure 3.6: Geometries of 800/2000 (left) and 400/1500 (right) cases

The predicted circulating mass flux is 1.68 kg/s in the 400/1500 case. There is no particle circulating through the bed for the 800/2000 case.

In our case, **lowering the height of secondary injectors increases the circulation of particles**. It is due to the fact that in the 400-1500 case, injectors are blowing into the dense part of the riser: it helps the particles to fly off. In the 800-2000 case, the injectors situated at 2000 mm are blowing over the dense bed not helping ilmenite particles to fly off.

3.2.2 Polydisperse cases

This work was performed in close collaboration with ALSTOM. The experiments and the simulations were often performed at the same time. Therefore, the operating conditions sometimes happened to be a little different (cf. Table 3.4).
The following experiment and simulation were realized in order to test a new kind of ilmenite particles.

Table 3.4 clearly shows that the circulation of ilmenite in the bed is strongly underestimated by the simulation. Moreover, the small differences in the boundary conditions between experiment and simulation cannot be the source of such an underestimation. It has then been decided to perform granulometric tests on the ilmenite particles expected to have a mean diameter of $d_{50} = 120\ \mu m$: the method used for those tests was laser granulometry and sieving.

Case	$Q_{0\ mm}$ kg/h	$Q_{400\ mm}$ kg/h	$Q_{1500\ mm}$ kg/h	M_{Foyer} kg	α_s T/h
EXP 1 poly	1738	3073	2038	294	111
EXP 1 poly bis	1758	2532	2560	314	117
NEPTUNE_CFD	1827	2967	2000	260	37.8

Table 3.4: Presentation of the operating point

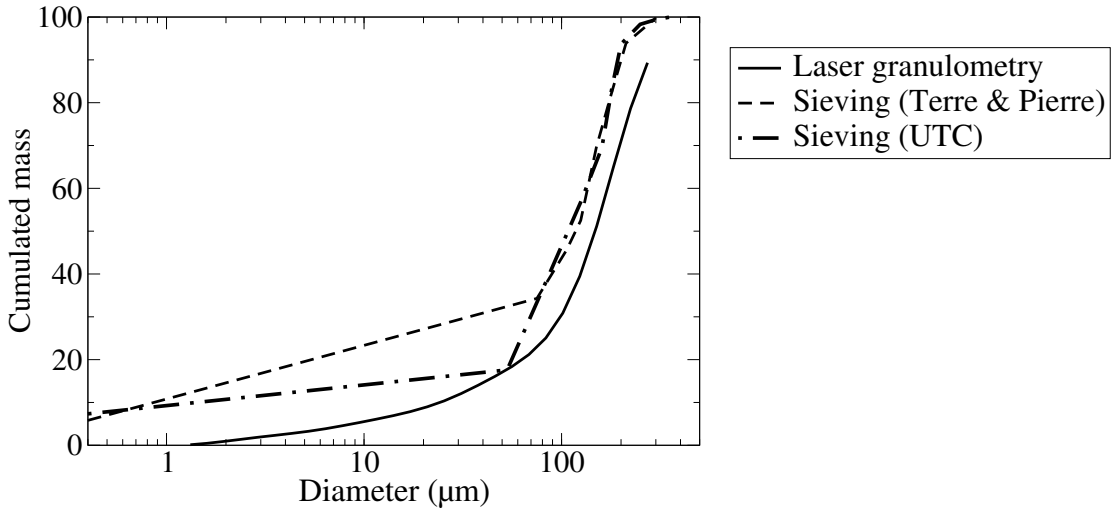

Figure 3.7: Alstom provided granulometries

The distribution of ilmenite particles plotted on Figure 3.7 does not seem to be monodispersed: the laser granulometry clearly shows an important proportion of small particles (around 40 μm). It is therefore not possible to model the ilmenite phase with a single mean diameter. It was finally decided to divide the monosolid phase into multiple classes with different mean diameter (d_{50}).

There was some significant differences between laser and sieving results. ALSTOM gives more credit to the sieving results which are closer to the provider informations than laser granulometry results. But the distribution of particles given by sieving cannot be discretized because the results stop around 50 μm diameter. Indeed, sieving on particles smaller than 50 μm cannot be performed as they agglomerate. That is why our simulation was built on the laser granulometry experimental results knowing that we might overestimate the diameter of ilmenite particles (cf. Figure 3.8).

The distribution was divided into three classes (cf. Figure 3.9).

On Figure 3.10, the modeled distribution is plotted. Because of the spreading of the distribution for the smallest particles, three classes are needed: one class for the

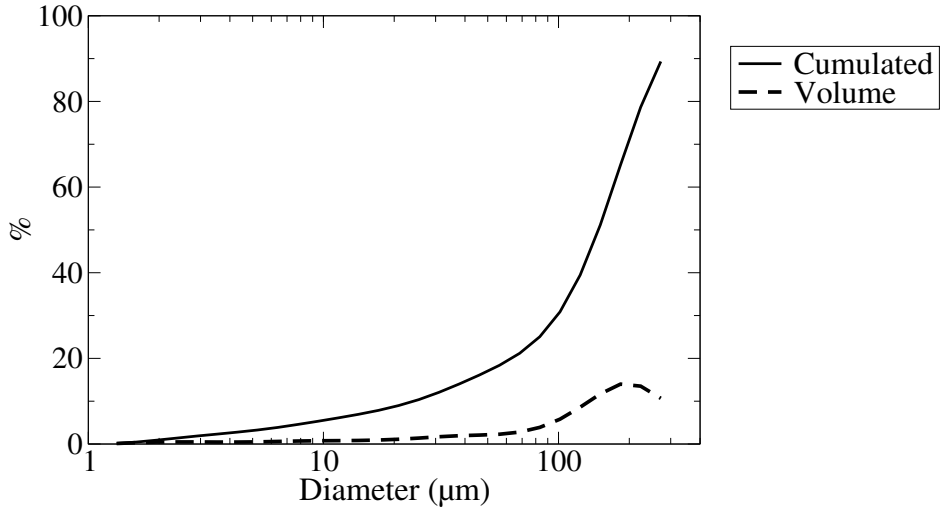

Figure 3.8: Laser granulometry of ilmenite particles

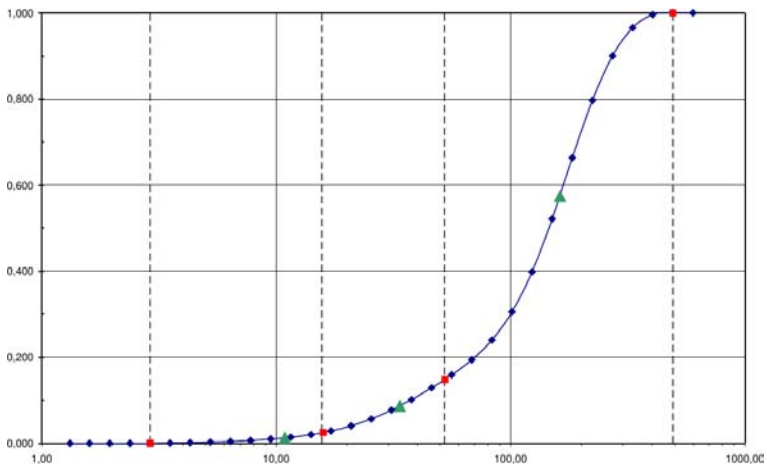

Figure 3.9: Discretized cumulated distribution function (–) d_{50} by class (△)

Classes	$d_{min}(\mu m)$	$d_{max}(\mu m)$	$Massfraction$	$d_{50}(\mu m)$
3	2.9	15.67	2.5%	10.89
2	15.87	52.47	12.3%	33.69
1	52.47	492.47	85.2%	162.75

Table 3.5: Discretization of the ilmenite solid phase

largest particles and two for the smallest.

The gas velocity imposed at the fluidization grid corresponds to 3 m/s.

In the inventory, 85% of large particles, 12.5% of medium particles and 2.5% of small particles were imposed. Table 3.7 shows that the repartition between classes is

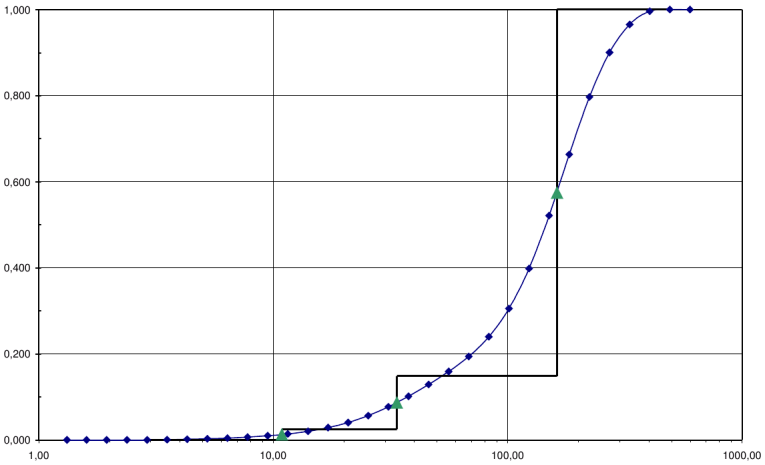

Figure 3.10: Effective cumulated distribution function (–) d_{50} by class (△)

Type of particle	**Terminal settling velocity**	d_{50}	Geldart
Ilmenite Large	$1.73\ m \cdot s^{-1}$	$165\ \mu m$	B
Ilmenite Medium	$0.14\ m \cdot s^{-1}$	$34\ \mu m$	A
Ilmenite Small	$0.015\ m \cdot s^{-1}$	$11\ \mu m$	C

Table 3.6: Terminal settling velocities

Outlet solid mass flux (kg/s)	Total	Large	Medium	Small
EXP 1p	117 T/h	-	-	-
$NEPTUNE\_CFD$: Monodisperse	37.8 T/h	-	-	-
$NEPTUNE\_CFD$: Tridisperse	85 T/h	74%	19.5%	6.5%

Table 3.7: Circulating solid mass flux for polydisperse monosolid experiments and simulations

different between the inventory and the outlet mass flux.
This study shows **the relevance of taking into account the polydispersion of the solid phase**. This can affect the predicted circulation rate of more than 100%.
It also shows that **Eulerian-Eulerian modeling can quantitatively predict the hydrodynamic of a polydisperse circulating fluidized bed**. Nevertheless, there is still a difference between simulation (85 T/h) and experiment (117 T/h). It might be due to the fact that our discretization was based on the laser granulometry which overestimates the size of the particles. Moreover, the experiment uncertainty increases when the circulating mass flux comes over 100 T/h because the siphon is undersized for such a flow.

3.2.3 Conclusion on monosolid experiments

$NEPTUNE\_CFD$ is able to predict the hydrodynamic of 3D isothermal monosolid circulating fluidized bed. All simulations of monodisperse monosolid CFB's are in good

agreement with the experiment.
In the case of a polydisperse monosolid phase, the discretization of the phase is necessary to catch the order of magnitude of the circulating mass flux. The underestimation of the predicted circulating mass flux might be due to sub-grid heterogeneities affecting of the drag force modeling. Indeed, Agrawal et al. (2001), Parmentier et al. (2011) or Benyahia (2009) showed that sub-grid models for drag are necessary to accurately predict the hydrodynamics of CFB. It is also possible that sub-grid effects affect the prediction of the exchanges of momentum and kinetic energy during collisions.
Nevertheless, the previous study showed that NEPTUNE_CFD V1.08@Tlse is an appropriate tool to predict complex multiphase flows. In order to participate in the design of the Darmstadt Chemical Looping pilot plant, it is necessary to correctly predict the hydrodynamic of a poly-solid circulating fluidized bed. The results of the previous study got us to position the secondary injectors for the next simulations and experiments at 400 mm and 800 mm.

3.3 Poly-solid cases

3.3.1 Experimental and numerical study of a poly-solid CFB with small diameter ratio and comparable fluidization and terminal settling velocities

Operating Conditions

Bi-solid experiments were performed at UTC CFB cold flow model. The solid mixture, composed of ilmenite and alumina particles, is introduced in the reactor in start-up phase. The same procedure as in the monosolid experiments is followed.
The inventory of solid in the installation and the injected gas flux are imposed. The operating point is summarized in Appendix 5.3.5 and 5.3.6.

Experiment uncertainty

In the experiment, the uncertainty on the estimated circulating mass flux is the same as in the previous experiments, about 7%.
It is difficult to estimate the proportion of alumina in the riser. The loading of alumina and ilmenite in the whole installation is known at the beginning of the campaign. But, the more cycles are performed, the less accurate is the estimation of the ratio of alumina in the installation because of particles leaving the cyclone.
Moreover, the link between the ratio of alumina in the global installation and the ratio of alumina in the riser is not easy to determine. The set-up was not made for taking samples inside the riser.
The experiment $EXP5$ was performed at the end of a campaign so it has been assumed that no more than half of the 4% of alumina initially injected has escaped from the circulating system.
The experiment $EXP6$ was performed at the beginning of a campaign so the estimation of 5% of alumina in the installation is fairly accurate.

Physical properties

The fluidization gas is air at $T = 50°C$, $P = 1\ bar$ corresponding to $\rho_g = 1.09\ kg \cdot m^{-3}$, $\mu = 1.98 \cdot 10^{-5}\ Pa \cdot s$.
The imposed diameter for the particle phases is chosen to be the d_{50} of each phase (cf. Table 3.8).

Table 3.8: Characteristics of the particle phases

Type	Density (kg/m^3)	d_{50} (μm)	Terminal settling velocity	Geldart
Alumina	1500	60	0.14 m/s	A
Ilmenite	4600	160	1.7 m/s	B

Boundary conditions of the simulation

All the simulations were performed with an imposed solid inventory (cf. Table 3.9) and fluidization velocity. Therefore, the solid circulation mass flux is a result of our simulation.

Table 3.9: Imposed inventory for each case

Case	Ilmenite	Alumina	Inventory
Alu 0%	259.0 kg	-	259.0 kg
Alu 2%	253.9 kg	5.1 kg	259.0 kg
Alu 4%	253.9 kg	10.6 kg	264.5 kg
Alu 10%	233.1 kg	25.9 kg	259.0 kg

The gas is injected as follows and corresponds to a gas velocity in the main section of 3.8 m/s:

- Fluidization grid : $Q_m = 0.4992\ kg \cdot s^{-1}$.
- Secondary inlet flow z=400 mm. For each injector (among 4): $Q_m = 0.2090\ kg \cdot s^{-1}$.
- Secondary inlet flow z=800 mm. For each injector (among 8): $Q_m = 0.0699\ kg \cdot s^{-1}$.

The solid mass flux re-injected at the inlet is imposed equal to the solid mass flux at the outlet.

The fluidization grid is considered as a smooth wall for the particle boundary conditions. So, a slip condition for particle velocity and a zero flux for random kinetic energy and flux-particle covariance are imposed. The outlet of the riser is a free outlet. If the flow is coming back, the solid volume fraction is imposed equal to 10^{-12}: only gas can enter through the outlet. Standard wall friction functions are used for the velocities and the turbulence properties of the continuous phase. A slip condition for the velocity and zero flux for particle random kinetic energy are imposed on the dispersed phases, corresponding to elastic particle bouncing on smooth wall without friction.

Numerical information

The time of calculation and averaging is summed up in Table 3.10. The processors used for those simulations are referenced below: Intel Xeon Quad-Core E5472 owns 4 cores with a 3 GHz frequency or Nehalem EX owns 4 cores with a 2.8 Ghz frequency. Whenever possible, the duration of the time averaging is about the duration of the transitory state. The transitory state is considered to be achieved when the circulating mass flux oscillates around a constant value.

Results

All presented results of $NEPTUNE\_CFD$ are time-averaged on the duration of the averaging which can be seen in Table 3.10. All the plots of a parameter along Y direction are taken in the centre of the bed: $x = 0.265\ m$.

Table 3.10: Computational time

Case	Simulation time (s)	Duration of the averaging (s)	CPU time (h) per physical s
Alu 0%	20 s	10 s	10 days, 64 proc.
Alu 2%	42 s	10 s	22 days, 64 proc.
Alu 4%	34 s	10 s	18 days, 64 proc.
Alu 10%	27 s	7 s	15 days, 64 proc.

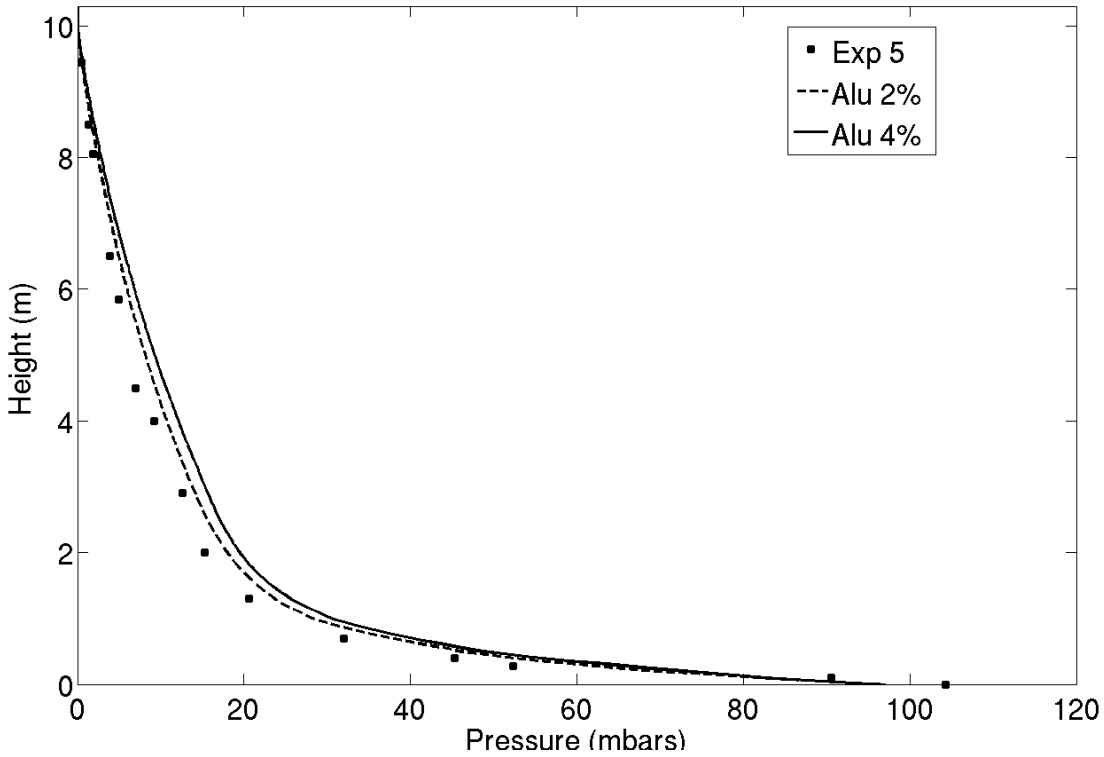

Figure 3.11: Simulation and experimental pressure profiles of bi-solid comparable cases

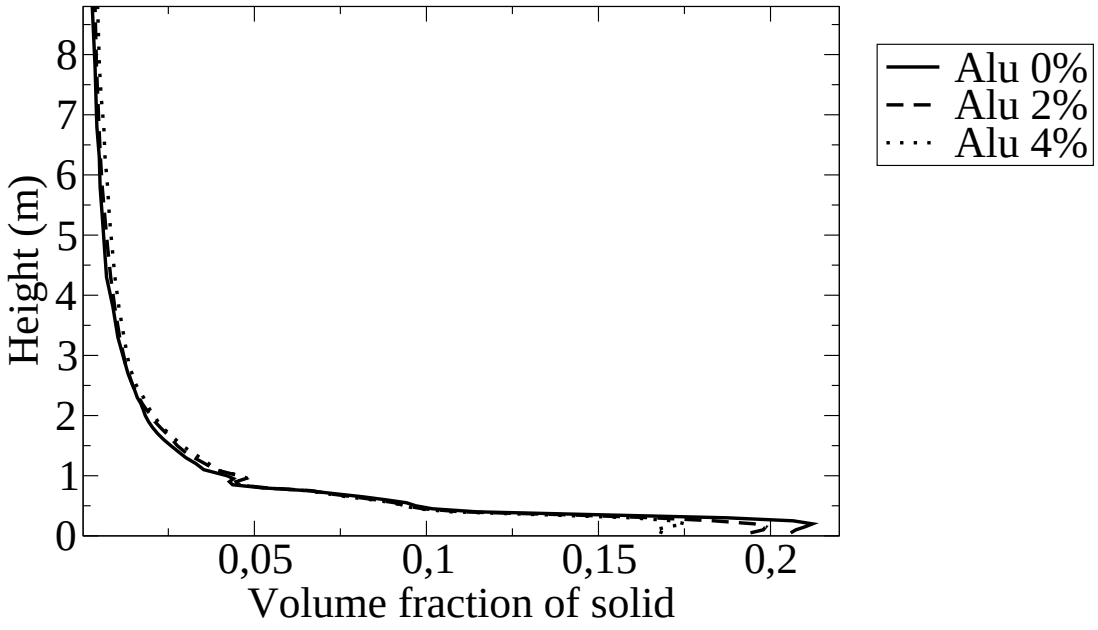

Figure 3.12: Time and space-averaged solid volume fraction ($\overline{\alpha_s}$) along the bed height

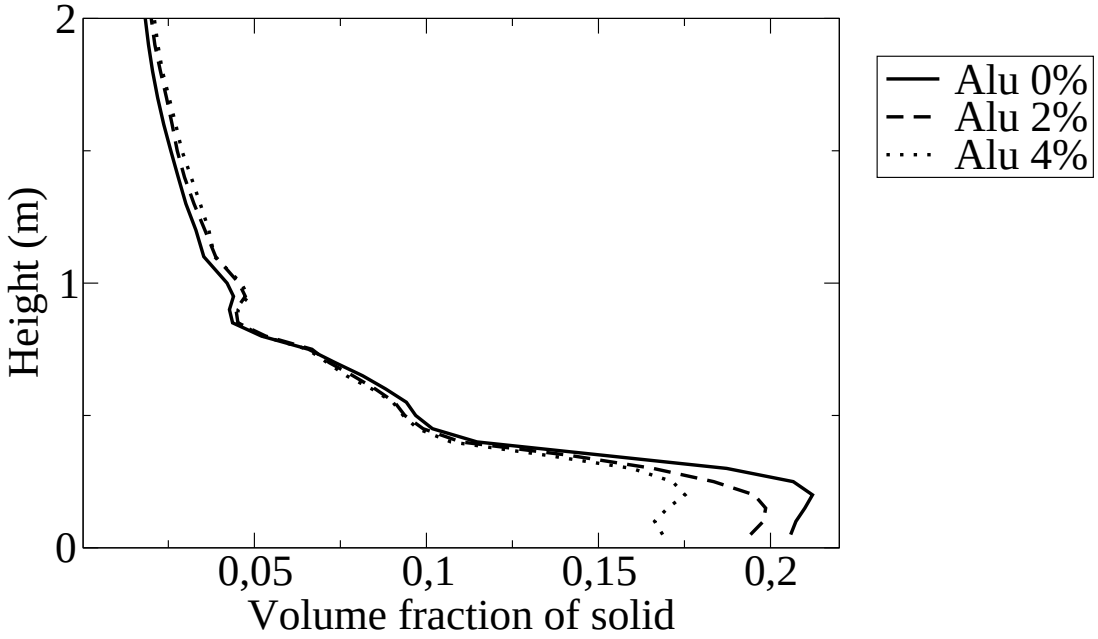

Figure 3.13: Time and space-averaged solid volume fraction ($\overline{\alpha_s}$) in the bottom part of the riser for various fraction of alumina in the bed

Experiment and simulation pressure profiles in Figure 3.11 are in accordance. The profiles are taken along the wall. The presence of alumina particles in the reactor makes the pressure profile closer to the case of a perfectly homogeneous bed. This trend is confirmed by the profiles of time and space-averaged $\overline{\alpha_s}$ along the bed (figure 3.12). The space averaging corresponds to the mean value of the time-averaged quantity at each height.
In the monosolid case, the solid volume fraction reaches 21% in the bottom part while the maximum is 17% when there is 4% of alumina in the bed. **The presence of alumina strongly decreases the averaged solid volume fraction in the dense part of the bed**. Figure 3.12 shows that the hydrodynamics is established for $z > 4\ m$. Figure 3.13 shows that adding alumina to the inventory decreases the local solid volume fraction in the dense part of the bed.

Table 3.11: Bi-solid experiment and simulation with Ilmenite and Alumina

Case	Total inventory	% of Alumina	Ilmenite mass flux	Alumina mass flux	Total mass flux
EXP 5	259 kg	2%-4%	-	-	9.6 kg/s
EXP 6	193 kg	$\simeq$ 5%	-	-	9.5 kg/s
Alu 2%	259 kg	2%	7.6 kg/s	0.48 kg/s	8.1 kg/s
Alu 4%	264.5 kg	4%	8.85 kg/s	1.04 kg/s	9.9 kg/s
Alu 10%	259 kg	10%	11.73 kg/s	2.94 kg/s	14.7 kg/s

Considering that the CFB riser is within a loop, it is hard to experimentally estimate the fraction of alumina in the inventory. Both bi-solid experiments give a circulating mass flux between 9 and 10 kg/s. The measurement uncertainty led us to perform 3 bi-solid simulations presented on Table 3.11. The predicted circulating solid mass flux is similar to the experiment results. Moreover, mono-solid and bi-solid experiment and simulations results show that there is a significant increase in the circulation of solids due to the alumina particles. Numerical modeling shows that multiplying the ratio of alumina in the bed by a factor 2 increases the circulation of ilmenite of about 16% and multiplies the circulation of alumina by a factor 2. Increasing the ratio of alumina in the inventory modifies the average estimated residence time from 33 to 20 s for ilmenite particles and from 11 to 9 s for alumina particles.

In the range studied, Figure 3.14 shows that **ilmenite and alumina mass fluxes are increasing linearly with the increase in the ratio of alumina**. The simulations with $NEPTUNE\_CFD$ give results within the range of uncertainty of the experiments for bi-solid cases and slightly overestimate the circulation of solids in the monodisperse case.

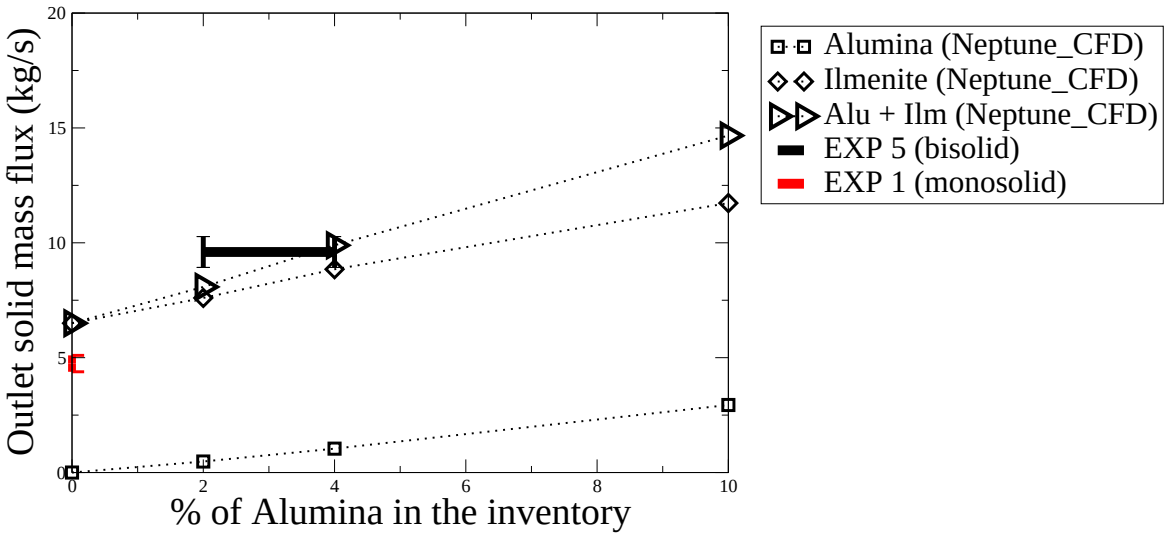

Figure 3.14: Influence of alumina on the circulating solid mass flux

Local characterization of the hydrodynamic

Flux and velocities

For all phases, in Figures 3.15 and 3.16, there is a zone in the centre of the riser where the net mass fluxes are positive and constant. This zone tends to widen with the height: for ilmenite particles this zone goes from 5 cm to 60 cm. In the lower part of the riser, there is a maximum of particles and gas mass fluxes at around 10 cm of the walls. Less than 5 cm from the walls, the particles are falling down.
The shapes of the axial mass fluxes profiles do not depend on the rate of alumina in the bed. Nevertheless, increasing the rate of alumina in the bed tends to make the solid mass flux horizontal profile in the established zone ($z > 4\ m$) more parabolic. For $z < 4\ m$, the influence of alumina particles on the solid mass flux is limited.

Figure 3.15 shows that the loading of alumina does not impact the gas mass flux, but it can strongly modify the local solid mass flux: its value in the centre of the bed goes from 30 $kg/m^2/s$ (Alu 0%) to 70 $kg/m^2/s$ (Alu 2%).
In the established zone, the maximum local solid mass flux is multiplied by a factor 2.3 while the outlet solid mass flux is multiplied by a factor 1.3.

Figure 3.16 shows that over z=4.8 m, the velocity profiles of all phases are quasi-parabolic. Both ilmenite particles and alumina particles time-averaged velocities are close.

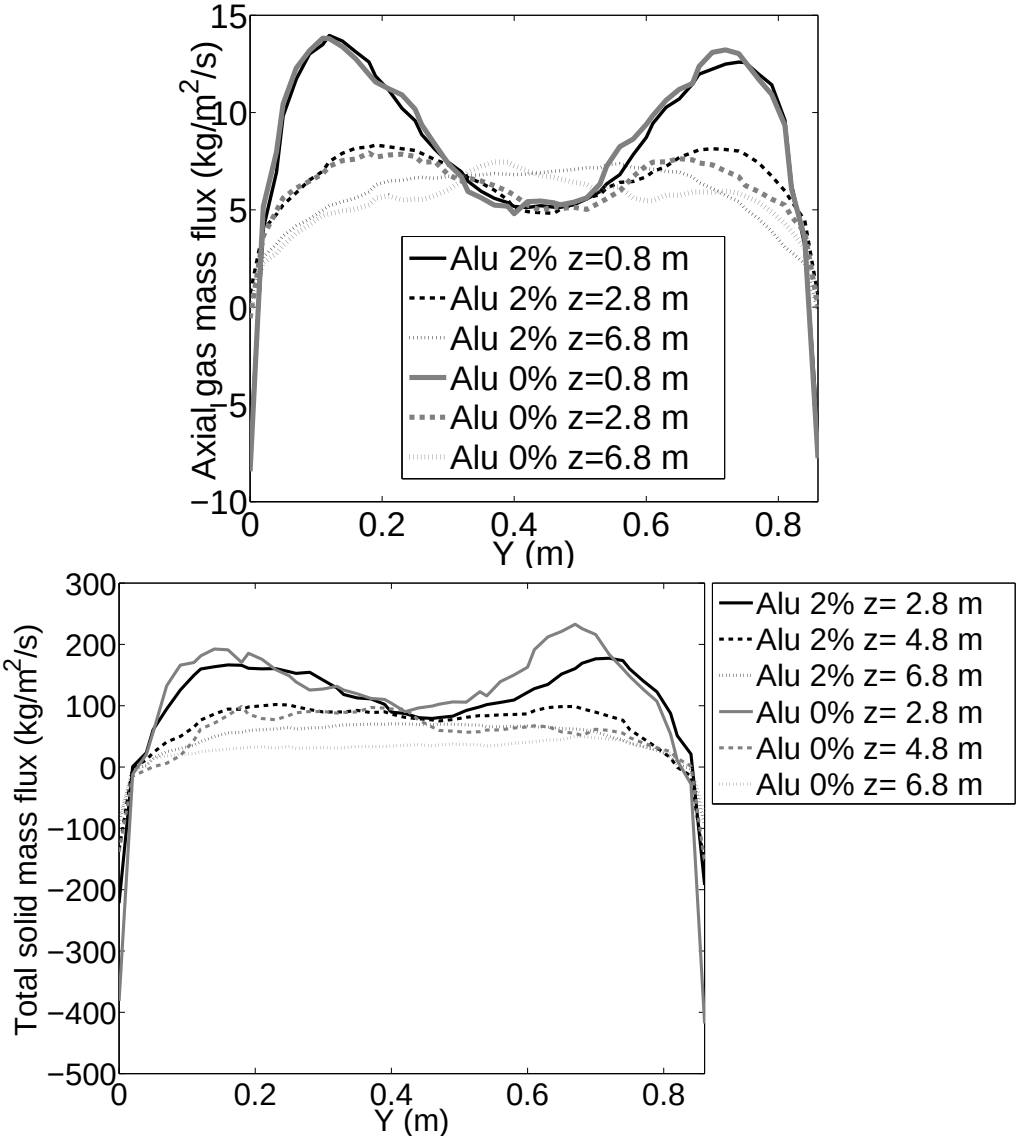

Figure 3.15: Time-averaged radial profiles of the gas mass flux (top) and solid mass flux (bottom) for mono-solid and bi-solid cases

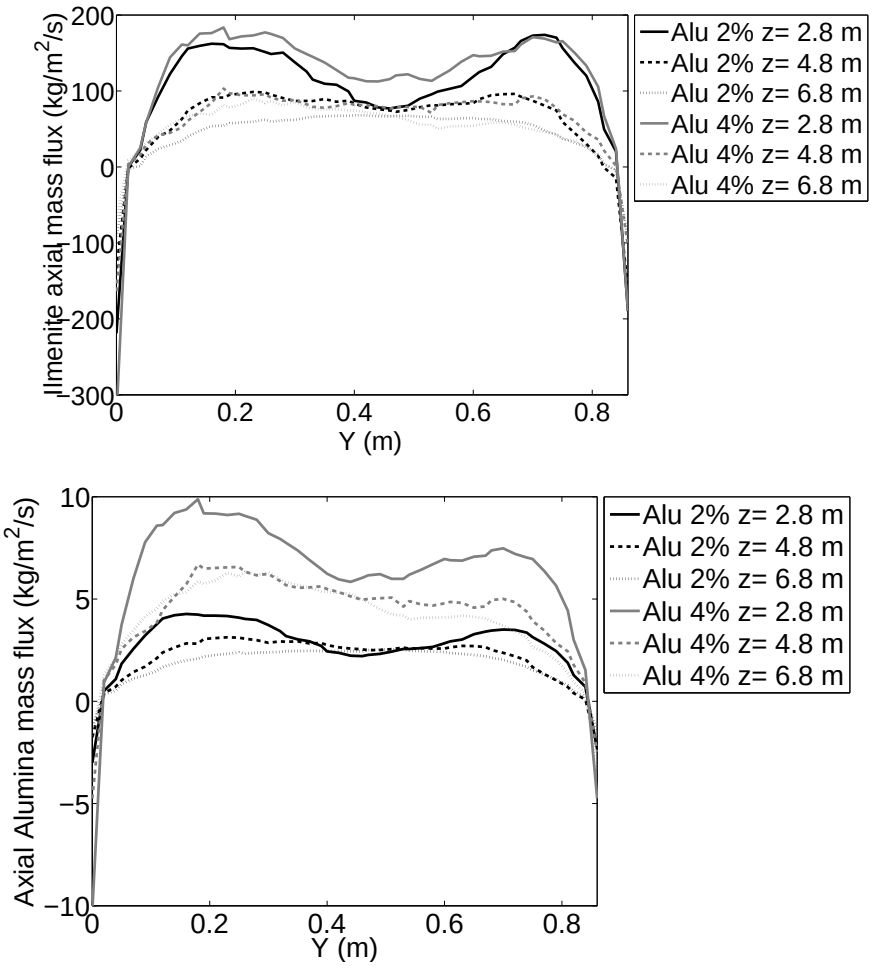

Figure 3.16: Time-averaged radial profiles of the ilmenite (top) and alumina (bottom) mass flux for bi-solid cases

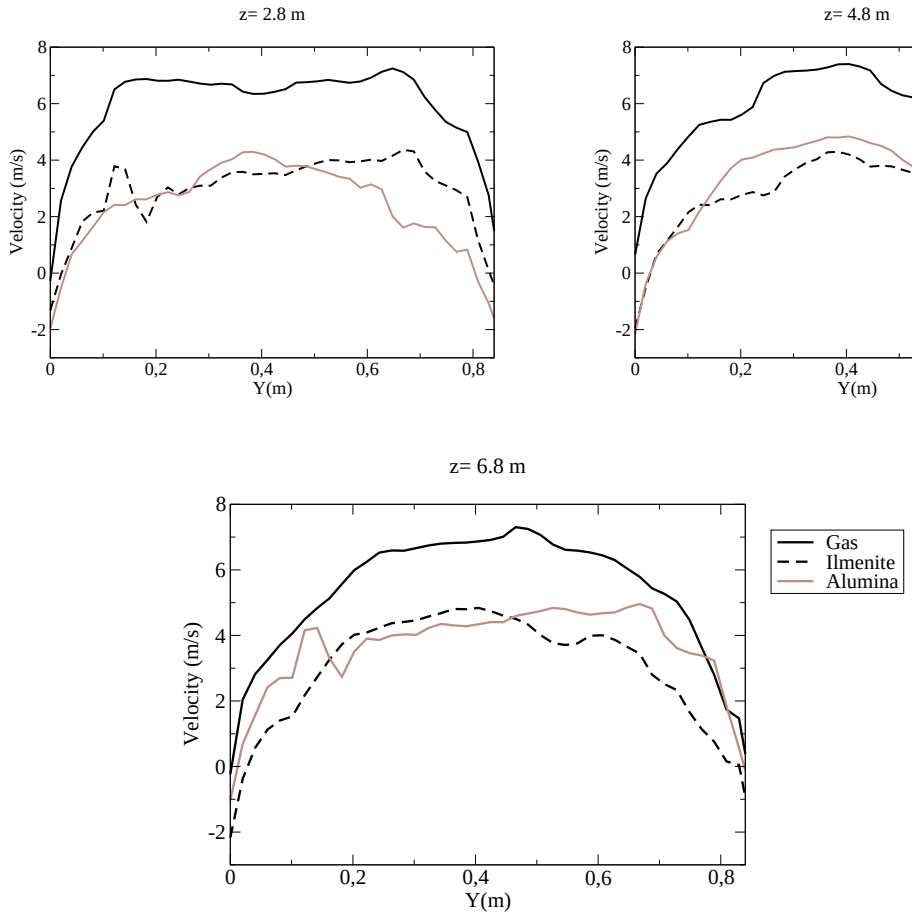

Figure 3.17: Time-averaged radial profiles of the velocities of gas and solid phases

Segregation of particles

Figure 3.18 shows that in both cases (alu 2% and alu 4%), the fraction of ilmenite in the solid decreases with the height. Increasing the alumina inventory of 2% decreases the fraction of large particle in the bed of 5% in the dense region and 8% in the upper region. Knowing that there is respectively 2% and 4% in mass of Alumina in the inventory, it corresponds to an average value of 0.94 and 0.89.

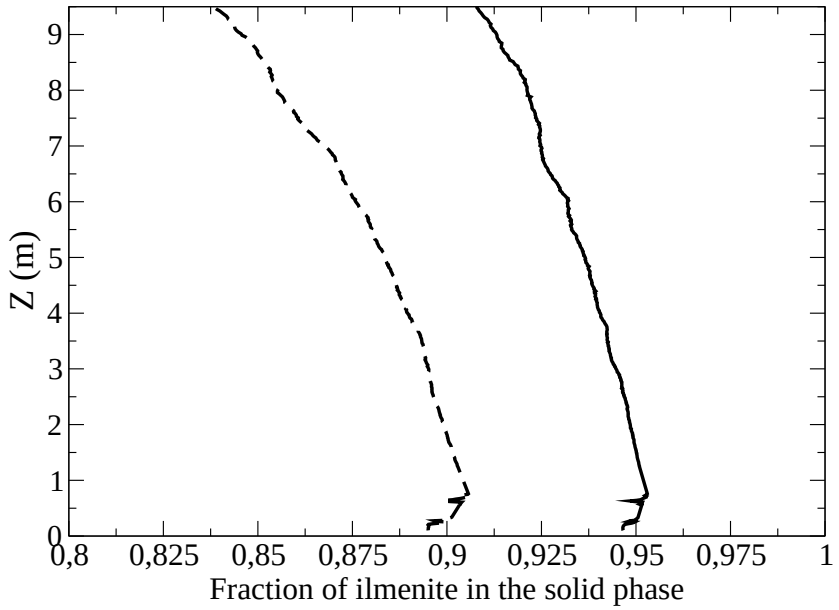

Figure 3.18: Time and space-averaged fraction of ilmenite in the solid depending on the height for Alu 2% (–) and Alu 4% (- -) cases

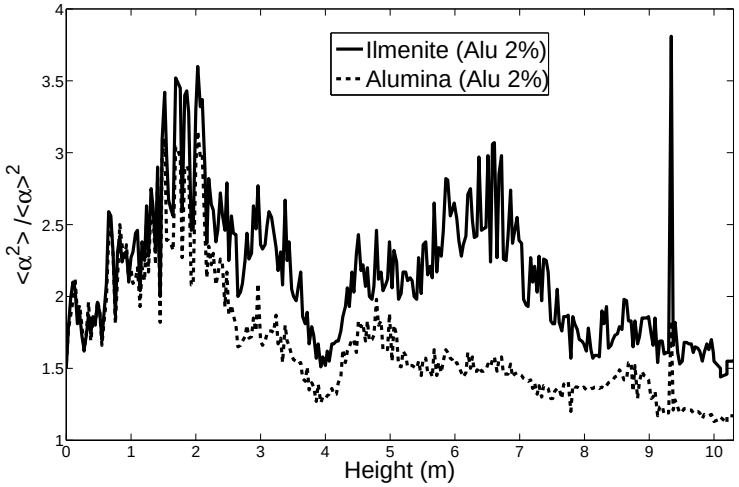

Figure 3.19: Volume fraction deviation of each solid phase in Alu 2% case

In Figure 3.19, the volume fraction of alumina is fluctuating more than the volume fraction of ilmenite. There is a maximum of deviation around z=3 m for both phases. In the dense part of the riser (between 0 and 0.6 m), $\frac{<\alpha^2>}{<\alpha>^2} \simeq 2$. It corresponds to $\sigma = E$ which means that the local solid volume fraction fluctuates along time between 7% and 23% in the dense part of the bed. $\frac{<\alpha^2>}{<\alpha>^2} > 1$ is characteristic of cluster formation: clusters are present all along the bed. Figure 3.20 show an instantaneous field of the total fraction of solid in the bed. There is some local clustering all over the bed: the solid volume fraction often reaches 5%.

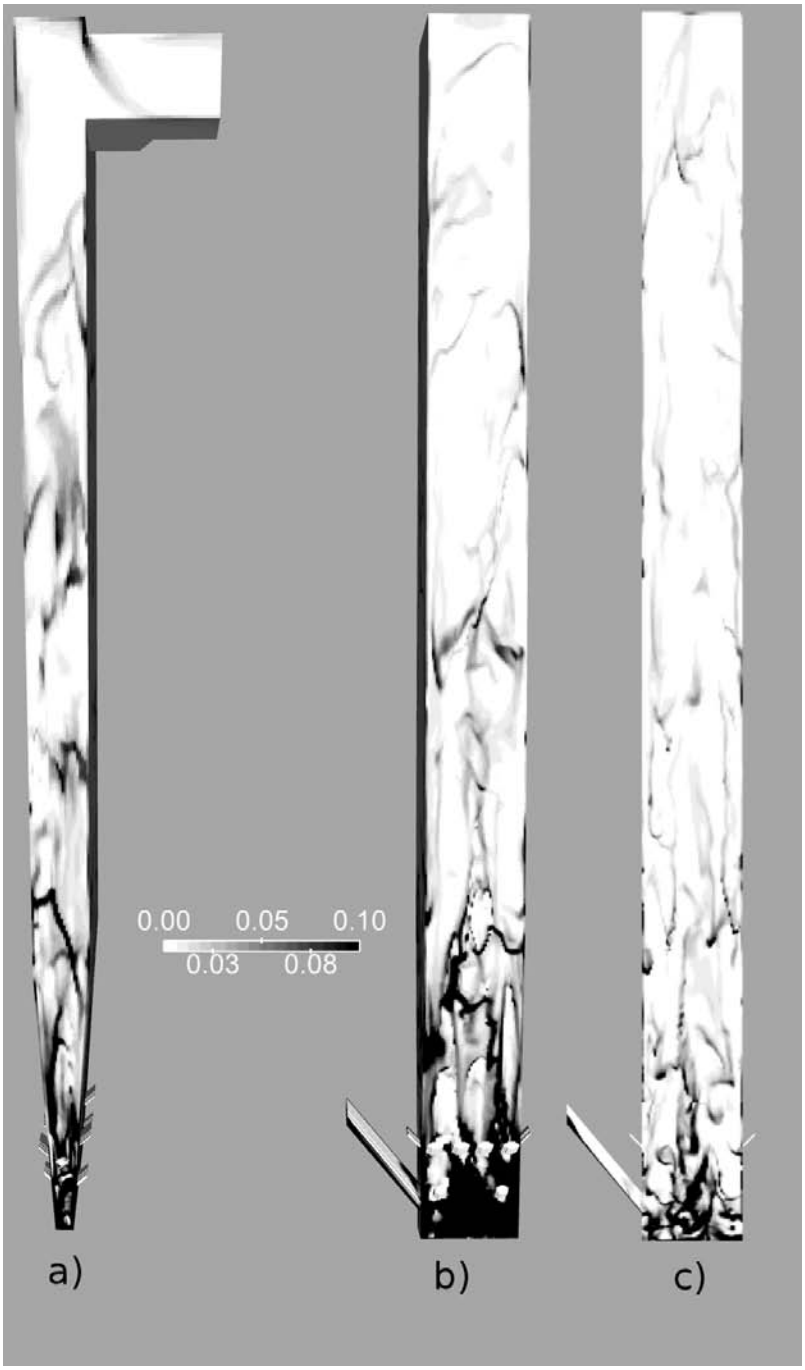

Figure 3.20: solid volume fraction in the bed. a) Wall (x-direction) b)Wall (y-direction) c) center of the bed along y

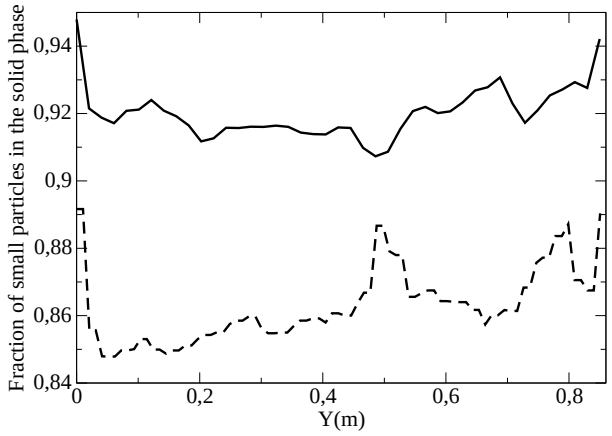

Figure 3.21: Time-averaged radial volume fraction of ilmenite in the solid phase in the center of the bed at z=6.8 m for the Alu 2% (–) and Alu 4% (- -) cases

Figure 3.21 and 3.22 show that at $z = 6.8\ m$, the radial segregation occurs between the near-wall region and the center of the bed. The fraction of ilmenite in the solid phase tends to increase from the center of the bed to the wall. The total solid volume fraction is three times higher near the wall than in the central region of the bed.

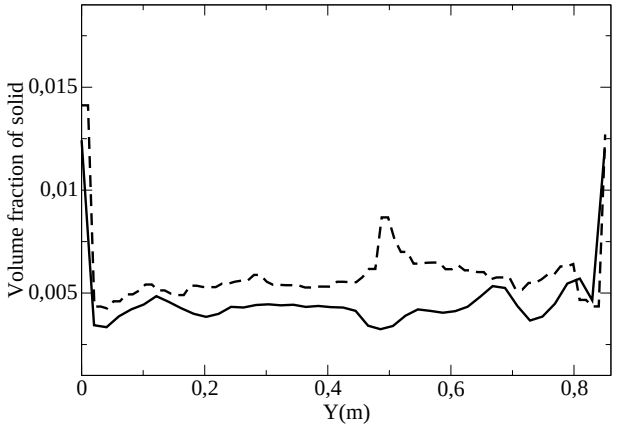

Figure 3.22: Time-averaged radial volume fraction of ilmenite in the center of the bed at z=6.8 m for the Alu 2% (–) and Alu 4% (- -) cases

Collisions influence

The time-averaged equation of momentum for particle phase writes:

$$\overline{\left[U_{p,j}\frac{\partial}{\partial x_j}\right]U_{p,i}} = -\underbrace{\overline{\alpha_p\frac{\partial P}{\partial x_i}}}_{\text{Pressure gradient}} + \underbrace{\overline{\alpha_p\rho_p g_i}}_{\text{Gravity}} + \underbrace{\overline{I_{g\to p,i}}}_{\text{Drag}} - \overline{\frac{\partial}{\partial x_j}\Sigma_{p,ij}} + \underbrace{\sum_{q\neq p}\overline{S_{pq,i}}}_{\text{Collisions}} \tag{3.1}$$

In the following post-processing, the time averaged terms of the momentum equation of the particle are plotted. The term in the legend are referred to as Drag, Collisions, Gradp, and Gravity corresponding to the previous terms.

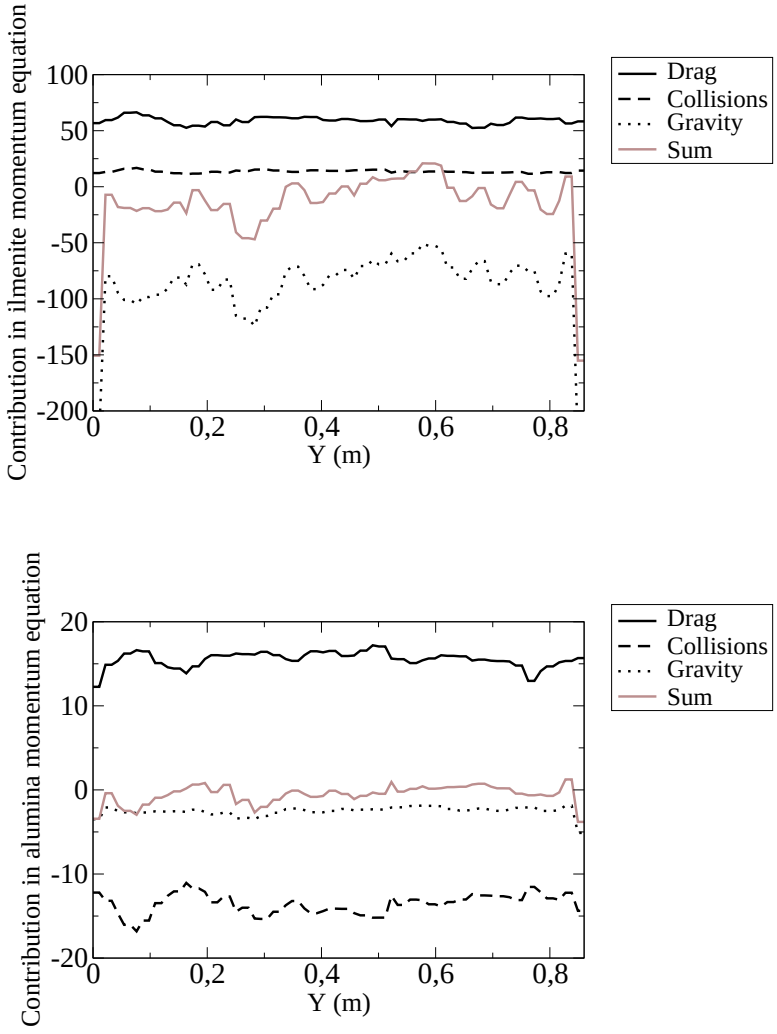

Figure 3.23: Time-averaged radial profile of the momentum equation contributions for both solid phases in Alu 2% case in the center of the bed at z=6.8 m.

In Figures 3.24 and 3.23, the contribution of drag, gravity and collisions in the momentum equation of ilmenite and alumina are plotted. For both particle species,

the collision contribution is not negligible compared to drag or gravity.
In the ilmenite momentum equation, the collisions and drag contributions are opposed to gravity, **adding alumina particles in the bed provokes collisions with ilmenite particles that helps the ilmenite particles circulation.**
In the alumina momentum equation, the drag contribution is opposed to gravity and collisions, **adding alumina particles in the bed provokes collisions with ilmenite particles that limits the alumina particles circulation.**
In the alumina momentum equation, the loss due to interclass collision is of the same order of magnitude than the drag term. According to Figure 3.23, the repartition between each of the contribution in the momentum equations is almost homogeneous. The major differences are observed along the wall, where collisions and drag contributions are negligible regarding the gravity contribution. **Along the wall, the momentum exchange is driven by gravity**.
In the momentum equation of alumina particles, the sum of those three main contributions is negligible regarding drag and collisions. For ilmenite particles, its contribution is around zero in the centre of the bed, but it is very important near the wall: ilmenite particles are falling and accelerating along the wall.

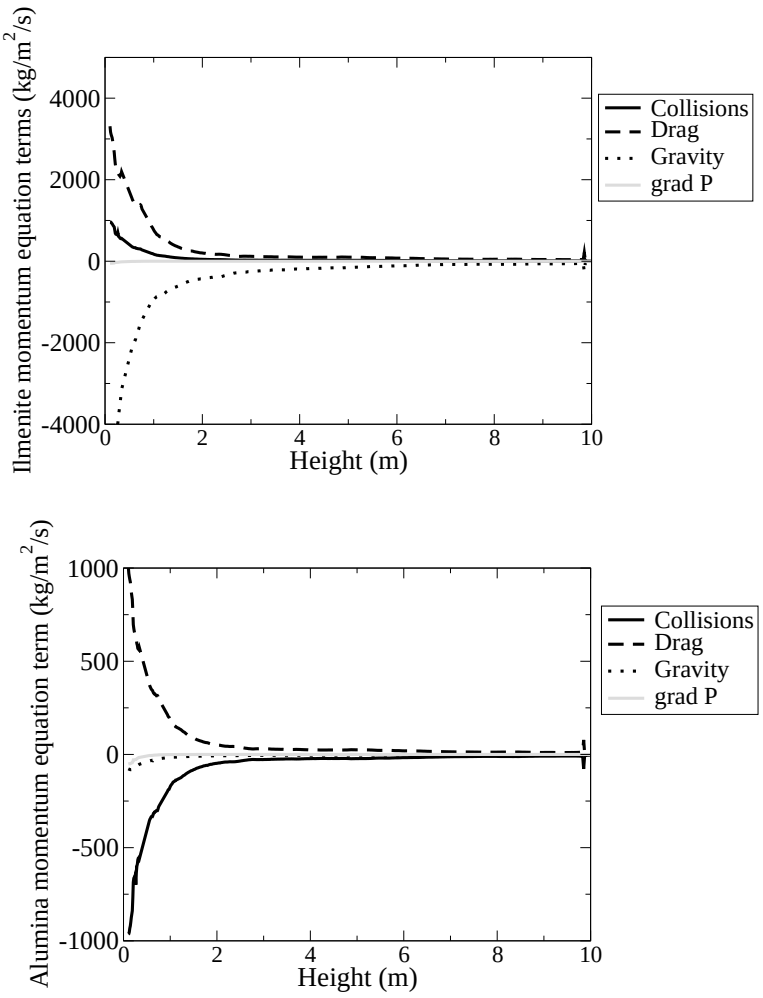

Figure 3.24: Time-averaged terms of the momentum equation of the solid phases in Alu 2% case-averaged on each z-plan.

Figure 3.25 investigates the repartition of those contributions in the established zone of the riser: between $z = 6\ m$ and $z = 9\ m$. In the established zone, the ratio corresponding to collisions and drag remain constant for the ilmenite phase. The drag contribution is 4 times larger than the collision contribution. **Even in the dilute part of the riser, collisions are not negligible regarding gravity and drag.** For the ilmenite phase, the momentum exchange during interclass collisions is compensating 17% of the gravity contribution, and drag 67%. In the momentum equation of the alumina particle, we see that **the effect of interclass collisions is equivalent to an increase in the density of the alumina particle of a factor 4 to 6**.

For the alumina particles, both ratios corresponding to collisions and drag are slightly decreasing when the height increases. The norm of the drag contribution is slightly greater than the collision contribution.

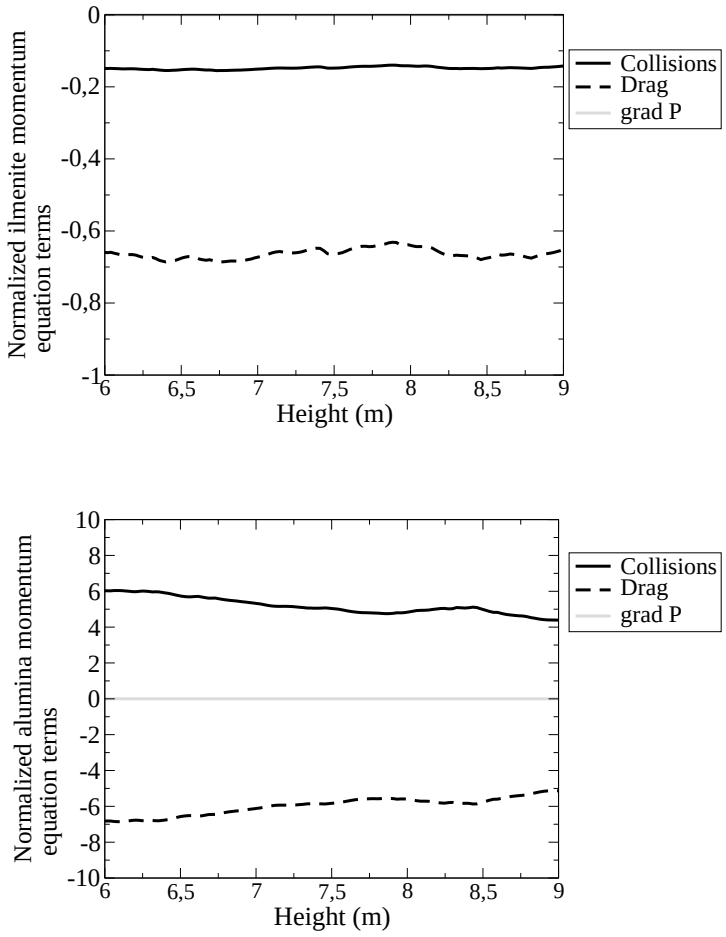

Figure 3.25: Zoom on the time-averaged terms of the momentum equation of the solid phases in Alu 2% case normalized by the gravity contribution and-averaged on each z-plan.

Figure 3.26 shows that the particle kinetic energy is maximum 5 cm to the wall and almost homogeneous in the centre of the bed.

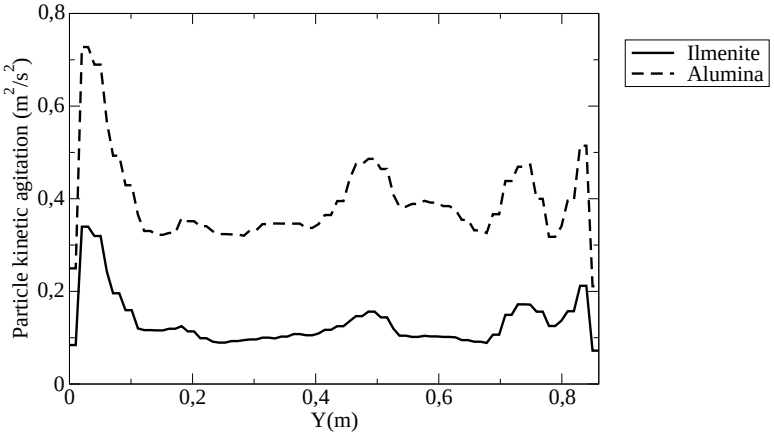

Figure 3.26: Time-averaged radial profiles of the particle random kinetic energy in Alu 2% case at z= 6.8 m.

Figure 3.27 show that for all solid phases, the q_{fp} is negligible compared to q_p^2. The influence of the turbulence of the fluid on the particles is negligible.

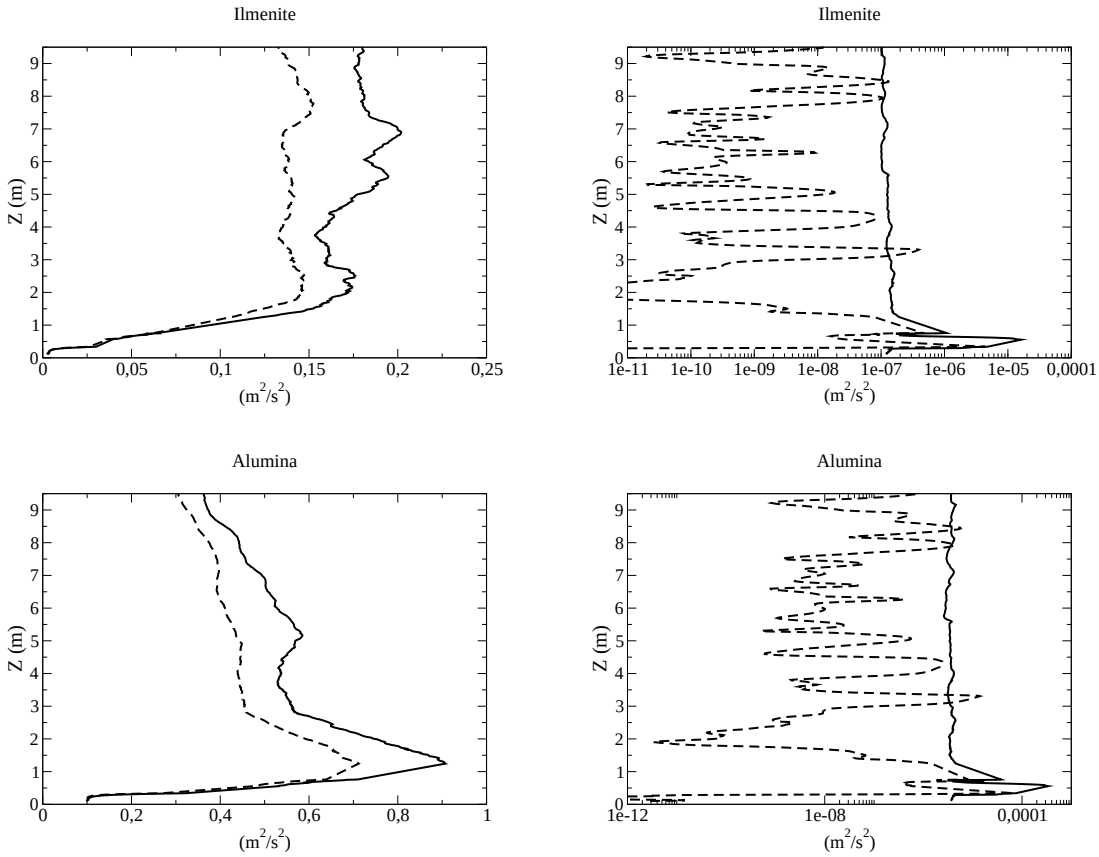

Figure 3.27: Time-averaged and space-averaged particle kinetic agitation (left) and fluid-particle velocity correlation (right) in Alu 2% (–) and Alu 4% (- -) cases

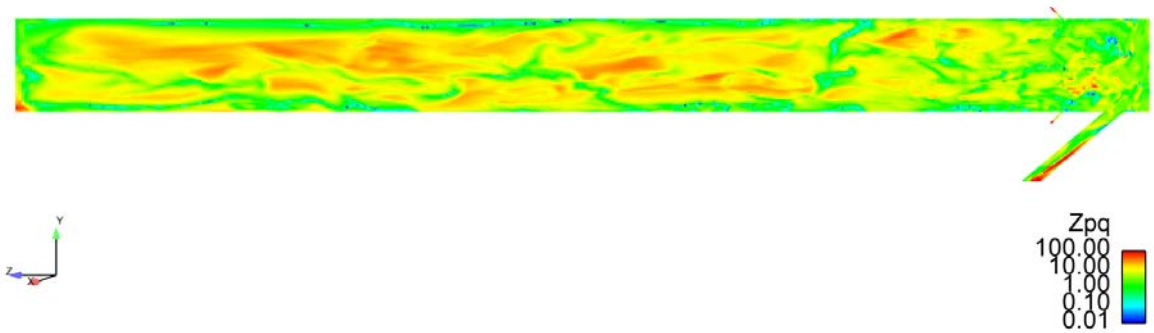

Figure 3.28: Instantaneous field of Z_{pq} in the centre of the bed

Figure 3.28 shows that $Z_{pq} > 1$ almost everywhere in the riser. It means that **the momentum exchange due to collisions is mostly driven by the relative velocity between particles**. Nevertheless, Z_{pq} is higher in the dilute zone than in the dense zone where $Z_{pq} \simeq 1$ locally. Z_{pq} is also close to 1 near the walls.

3.4 Conclusion on mono-solid and bi-solid experiment on UTC CFB cold flow model

The collaboration between ALSTOM and IMFT results in the setting of experiments and simulations of mono-solid and bi-solid circulating fluidized bed. This study showed the ability of NEPTUNE_CFD V1.08@Tlse to predict the hydrodynamics of a laboratory scale CFB cold flow model.
Experimental and simulation pressure profiles are in accordance for mono-solid (monodisperse and polydisperse) and bi-solid experiments. The circulating solid mass flux predicted by NEPTUNE_CFD V1.08@Tlse is satisfactory. The influence of the ratio of fine particles (alumina) in the bed on the circulation of solids has been quantified and found in the same proportion in both experiment and simulations. The simulation showed that multiplying the ratio of alumina:

- by a factor 2 increases the circulation of ilmenite of 16%
- by a factor 5 increases the circulation of ilmenite of 54%.

A local characterization of the hydrodynamics of the riser was performed:

- increasing the ratio of alumina in the bed decreases the maximum volume fraction in the bed
- ilmenite and alumina mass fluxes are both increasing linearly with the increase in the fraction of alumina in the inventory
- in the upper part of the riser, the velocity profiles of all phases are quasi-parabolic
- in the center of the bed, the time-averaged particle velocities are close
- the more alumina in the bed, the more the fraction of ilmenite in the solid phase decreases with height.
- clusters are formed in all areas of the CFB
- the larger and heavier particles tends to concentrate to the wall
- adding alumina particles in the bed provokes collisions that helps ilmenite particles to circulate and limits the circulation of alumina
- along the wall, the momentum exchange is mostly due to gravity
- even in the dilute part of the riser, interclass collisions are not negligible regarding gravity and drag.

This study pointed out that collisions are non negligible regarding the drag force and are responsible for an increase in the circulating solid mass flux.

Résumé du Chapitre 4

Le chapitre 4 présente une étude de l'expérience menée sur le banc du CERCHAR à l'Université Technologique de Compiègne par Fabre en 1995. L'expérience réalisée consistait à étudier un lit fluidisé circulant d'un mélange binaire de particules de même densité mais de diamètres très différents: 260 μm *vs.* 1300 μm. De plus, la vitesse de fluidisation tait deux fois moins élevée que la vitesse terminale de chute des grosses particules. Fabre a observé la circulation des deux classes de solides pour des fractions de grosses particules dans l'inventaire allant de 9% à 45%.

La première partie de ce chapitre consiste en une présentation de l'expérience menée par Fabre. Dans la deuxième partie, la modélisation d'un point de fonctionnement avec NEPTUNE_CFD V1.08@Tlse est décrite. La simulation de l'expérience de Fabre n'a pas permis d'atteindre un régime stationnaire. En effet, NEPTUNE_CFD V1.08@Tlse sous-estime la circulation de grosses particules à travers le lit. En revanche, nous avons pu prédire la circulation d'une quantité non négligeable de grosses particules. La comparaison de ces résultats avec l'étude menée par Batrak (2005) a montré que NEPTUNE_CFD V1.08@Tlse prédit une circulation de solide plus importante que Saturne_Polyphasique@Tlse si le temps physique de la simulation est suffisamment long. Le coût de cette simulation ne nous a pas permis d'aller au dela de 900 secondes physiques. Afin de comprendre cette sous-estimation du flux circulant, nous avons étudié l'influence de la taille des cellules du maillage. Raffiner le maillage diminue l'inventaire prédit de chaque classe de solide et augmente la circulation de solide prédite. Toutefois, en raison du cot des calculs aucune des simulations menées n'a pu atteindre un régime permanent.

C'est pourquoi, nous avons décidé d'étudier les mécanismes permettant de faire circuler les grosses particules en mettant en place des simulations périodiques de la partie supérieure du LFC. Les premières simulations périodiques réalisées concernent la modélisation d'une expérience numérique effectuée par Gourdel. L'objectif est de montrer que le modèle de prise en compte des intéractions entre classes de particules de l'approche Euler-Euler permet de prédire l'hydrodynamique d'un mélange binaire de particules. Nous avons également pu valider sur ces simulations LES-DPS l'implémentation de la condition de périodicité et de la modélisation des collisions interclasses.

Enfin, à partir d'un point de fonctionnement d'une expérience de Fabre, nous avons défini un domaine de calcul et un point de fonctionnement pour des simulations périodiques. Autour de ce point, nous avons défini d'autres cas permettant d'étudier l'influence de la fraction de grosses particules sur l'hydrodynamique du lit. Nous avons montré que les collisions interclasses accélèrent les grosses particules et ralentissent les

petites. La contribution des collisions dans l'équation de quantité de mouvement des grosses particles est trois fois plus importante que celle de la trainée. Nous avons pu étudier l'influence de la fraction de grosses particules sur la ségrégation radiale dans la zone tablie d'un CFB.

Chapter 4

Modeling of a binary mixture of particles with large diameter ratio

Contents

The previous section showed that the multifluid approach implemented in NEPTUNE_CFD V1.08@Tlse can predict the hydrodynamics of a CLC-like CFB.
It is therefore interesting to see if this approach is also efficient to predict the hydrodynamics of extreme CFBs. The CERCHAR experiment was built to study the influence of small particles on large particles, when the terminal settling velocity of large particles was twice the fluidization velocity.

4.1 The CERCHAR experimental setup

The experimental setup of CERCHAR studied by Fabre (1995) is a circulating fluidized bed cold model. On Figure 4.1, the various elements of the installation are presented. The cyclone is 4.5 m height and ensures the separation between species. The L-pipe is a solid return system insuring a stable inlet solid mass flux. The primary air flow is homogenized using a wind box divided into 6 compartments. The riser cross-section is rectangular: 0.8 m long by 1.2 m deep. The riser has a constant section until 9.4 m. Then the cross-section of the riser until 10.0 m is resized with an homethety equal to 0.5. The injector section is 0.032 m^2. The length of the particle inlet is equal to 0.4 m. According to Fabre (1995), the operating temperature does not exceed 50°C.

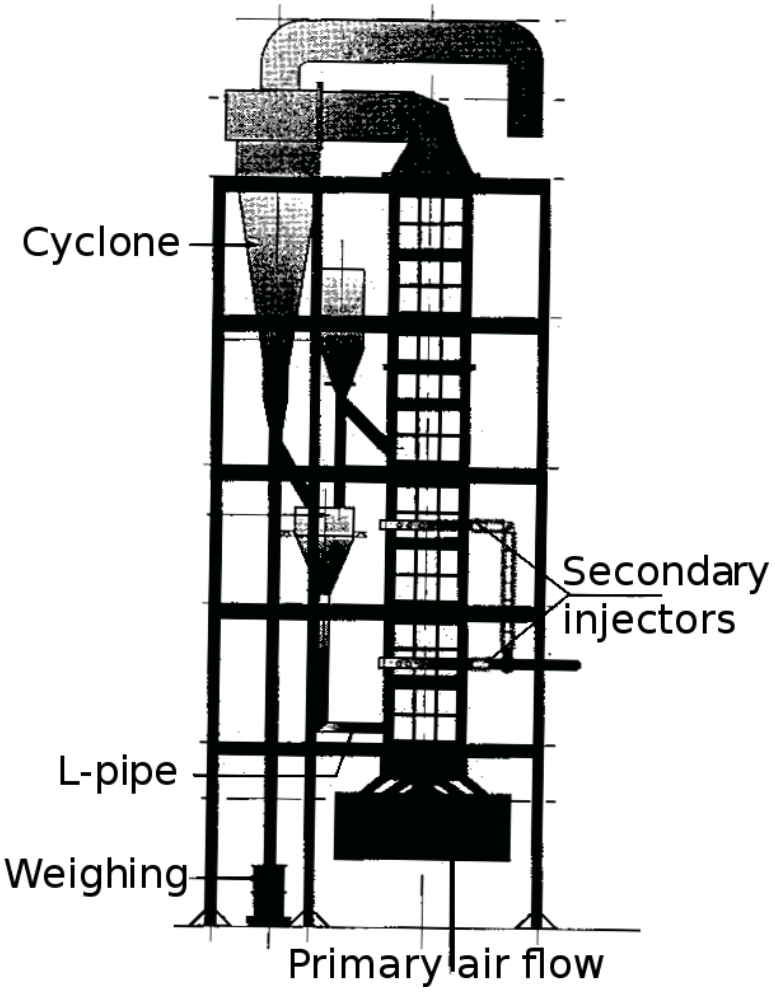

Figure 4.1: Schematic view of CERCHAR experimental set up

4.1.1 Operating conditions

The solid mixture is composed of small and large sand particles. 1000 kg of small sand are inserted into the installation. Then, the fluidization grid inlet gas flux and the inlet solid mass flux are imposed. When the circulating solid mass flux, the pressure and the temperature are stabilized in the riser, 100 kg of large sand particles are added to the installation. When the system is stabilized, the fraction of each type of sand in the outlet mass flux is estimated and the axial pressure profile is extracted. A few operating points were reported by Fabre (1995) with 100 to 1000 kg of large sand in the installation (cf. 4.2). The fluidization gas is air at 40 $°C$ and $P = 1$ atm (cf. Tables 4.1 and 4.2).

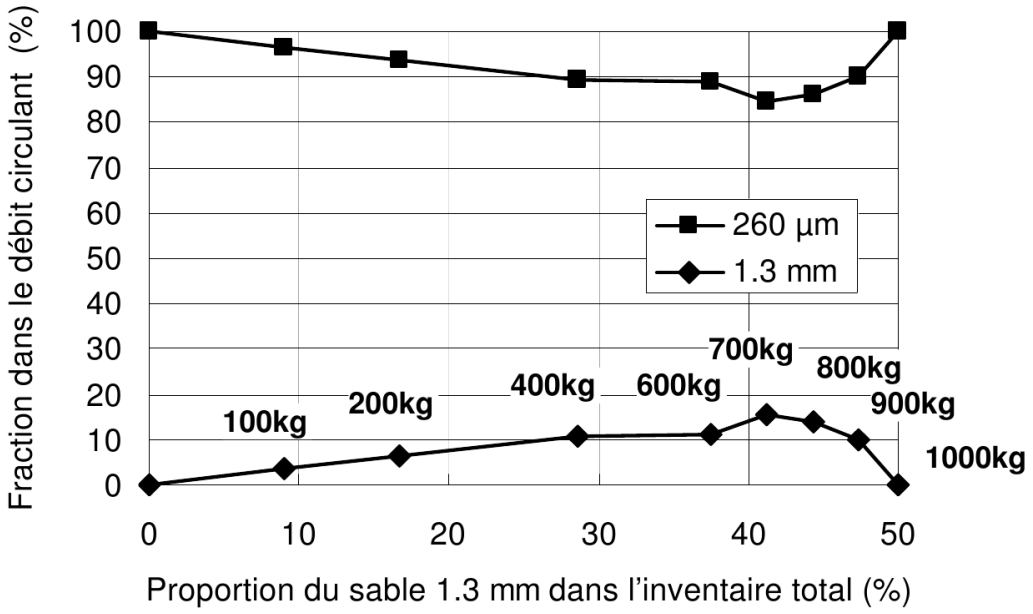

Figure 4.2: Evolution of the fraction of large sand 1.3 mm in the circulating mass flux as a function of the fraction of large sand in the inventory (cf. Fabre (1995))

Table 4.1: Characteristics of the gas phase

Density	1.123 $kg \cdot m^{-3}$
Dynamic viscosity	$1.85 \cdot 10^{-5}$ $Pa \cdot s$
Fluidization grid velocity	4 m/s

Table 4.2: Characteristics of the particle phases

Large sand particles d_{50}	1300 μm
Terminal settling velocity	9.81 m/s
Geldart type	D
Small sand particles d_{50}	260 μm
Terminal settling velocity	2.12 m/s
Geldart type	B
Sand density	2650 $kg \cdot m^{-3}$
Inlet solid mass flux	5.55 $kg \cdot m^{-2} \cdot s^{-1}$

4.1.2 Measurement system

During the experimental campaign, multiple parameters are collected.

Pressure measurement

50 probes are located at various heights along the wall of the riser. The differential pressure is averaged on 4 measurements. The resulting error on the pressure profile slope is less than 7 Pa/m.

Calculation of the mass of the bed according to the pressure profile

The same algorithm used by ALSTOM to estimate the mass remaining in the bed of the Cold Flow Model is used to estimate the total mass of solid in the bed (cf. 3.1.2).

Air mass flux

It is injected using a blower coupled with air valves. The air mass flux is estimated using the calculation of the differential pressure through a diaphragm. For each gas inlet, the gas mass flux is averaged on 4 measurements resulting in an error of less than 2%.

Solid mass flux

The circulating flow rate is evaluated by blowing empty method. At the end of a test, when the Cold Flow Model is shut-down, the storage bin, which is on a weighing gauge, is getting filled and the evolution of weight versus time is recorded. The circulating flow rate corresponds directly to the curve gradient in the first moments after the loop was stopped. Two or three measurements of the solid mass flux are performed for each

operating point resulting in an error of less than 7%.

4.2 Experimental and numerical study of a bi-solid CFB with extreme fluidization conditions

This section deals with the modeling of the hydrodynamic of a bi-solid circulating fluidized bed of particles with a high mean diameter ratio $R \simeq 5$. This case is an extreme case because the terminal settling velocity of the largest particles is twice bigger than the fluidization velocity, drag only is not sufficient to make large particle circulate through the bed. The small particles are B particles according to Geldart classification (cf. 2.1.1). The large ones are D particles (1300 μm).

The experiment was performed on the CERCHAR experimental bench by Fabre. 3D unsteady isothermal and polydisperse simulations are realized with NEPTUNE_CFD V1.08@Tlse to study the influence of interclass collisions on the circulating solid mass flux. This results are confronted with Saturne_polyphasique@Tlse (Batrak (2005)) and Fabre (1995) experimental results.

4.2.1 Computed geometry and mesh construction

The three dimensional mesh was built using SIMAIL. For the simulations, the experimental set up is simplified by removing the cyclone, tampon and return pipe. The reference mesh is made of 154 000 hexahedral cells. There are 41 nodes in the x-direction, 31 in the y-direction and 161 in the z-direction. The mesh is uniform so that $\Delta x = 0.02\ m$, $\Delta y = 0.04\ m$. Along z direction, it is uniform until $z = 0.4\ m$ with $\Delta z = 0.02\ m$, then geometric with a ratio of 1.02. The reference mesh is shown by Figure 4.3.

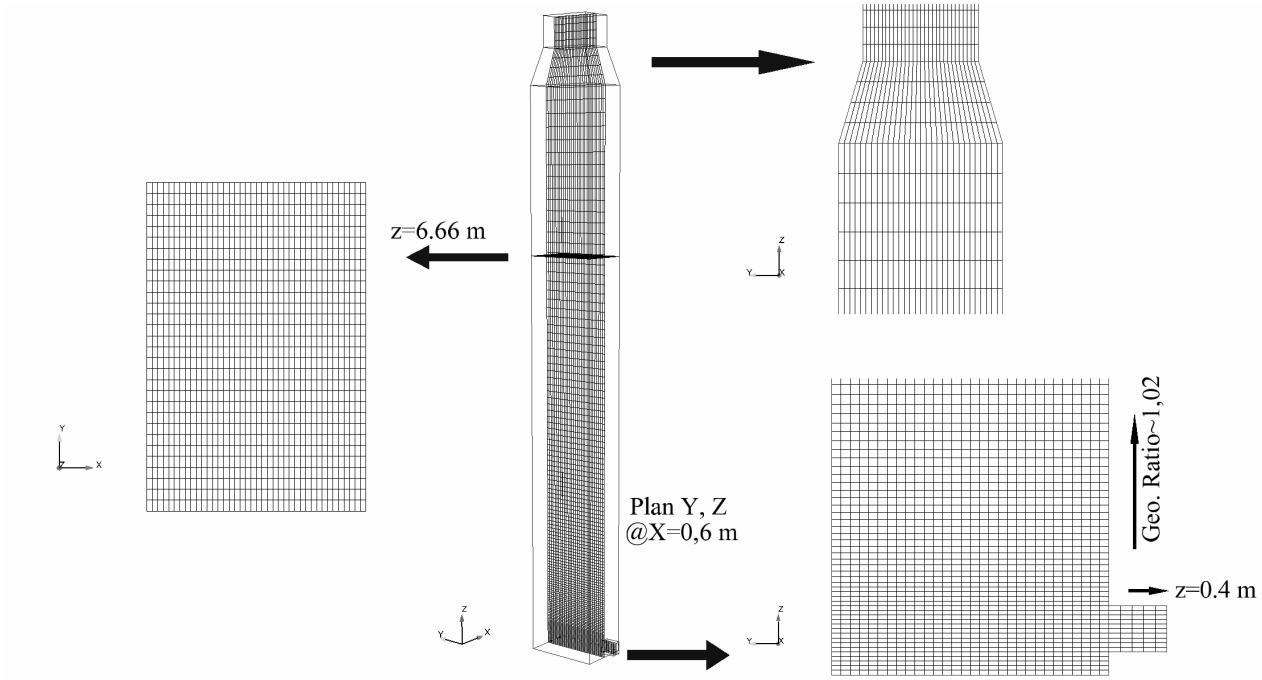

Figure 4.3: Reference mesh used to simulate the CERCHAR experiment

4.2.2 Particle and gas phase characteristics

The fluidization gas is air at 40 $°C$ and $P = 1$ atm.

Gas phase:

Density	1.123 $kg \cdot m^{-3}$
Dynamic viscosity	$1.85 \cdot 10^{-5}$ $Pa \cdot s$
Fluidization grid velocity	4 m/s
Particle inlet gas velocity	0.64 m/s

Particle phases:

Large sand particles d_{50}	1300 μm
Small sand particles d_{50}	260 μm
Sand density	2650 $kg \cdot m^{-3}$
Particle inlet particle velocity	0.64 m/s

Imposed inlet solid mass flux:	
Small sand	5.207 $kg \cdot s^{-1}$
Large sand	0.217 $kg \cdot s^{-1}$

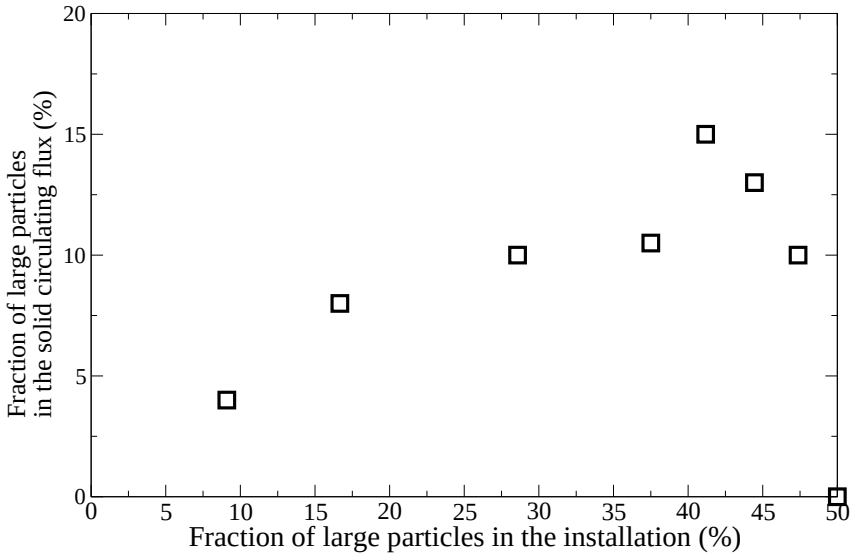

Figure 4.4: Evolution of the fraction of large sand 1.3 mm in the circulating mass flux

4.2.3 Experimental results

The figure 4.4 shows that the fraction of large particles in the circulating solid mass flux is lower than their fraction in the installation, the mixing between the two solids is not homogeneous in the installation. It means that if the inventory of the installation is representative of the inventory of the riser, there is an axial segregation between the two solid phases. The circulating mass flux of large particle first increases with the fraction of large sand in the inventory. There is a maximum of 15% of large sand in the circulating mass flux for 40% of large sand in the installation. When the mass of each class is the same in the installation, there is no circulation of large particles through the bed.

The operating point for 100 kg of large sand in the installation (cf. Figure 4.4) corresponds to $\frac{\alpha_{1.3mm}}{\alpha_{solid}} = 9\%$ in the installation. Because there is no way to estimate the fraction of each sand in the installation, this value is also considered to be the fraction of large sand in the reactor.
The fraction of large particles in the outlet mass flow is measured. It represents 4% for the 100 kg case.
Longitudinal pressure profiles measured by Fabre are given by Figure 4.5. The difference between the fluidization grid (z=0 m) and the highest pressure probe (z=9 m) is about 800 Pa in the 100 kg of large sand case. An order of magnitude of the total mass of particles in the reactor can then be estimated:

$$\frac{\Delta P}{L} \simeq \rho g \text{ with } \rho \simeq 9,06\ kg \cdot m^{-3}.$$

And $\rho = \alpha_p \rho_p + \alpha_g \rho_g$. To find an order of magnitude of the mass of particles in the bed, we can assume that $\alpha_g \rho_g = 1$.
Then, $\alpha_p \rho_p \simeq 8$, and $m_p = \alpha_p \rho_p \times \text{Volume}_{bed} \simeq 80\ kg$.

It appears that most of the particles initially placed in the installation

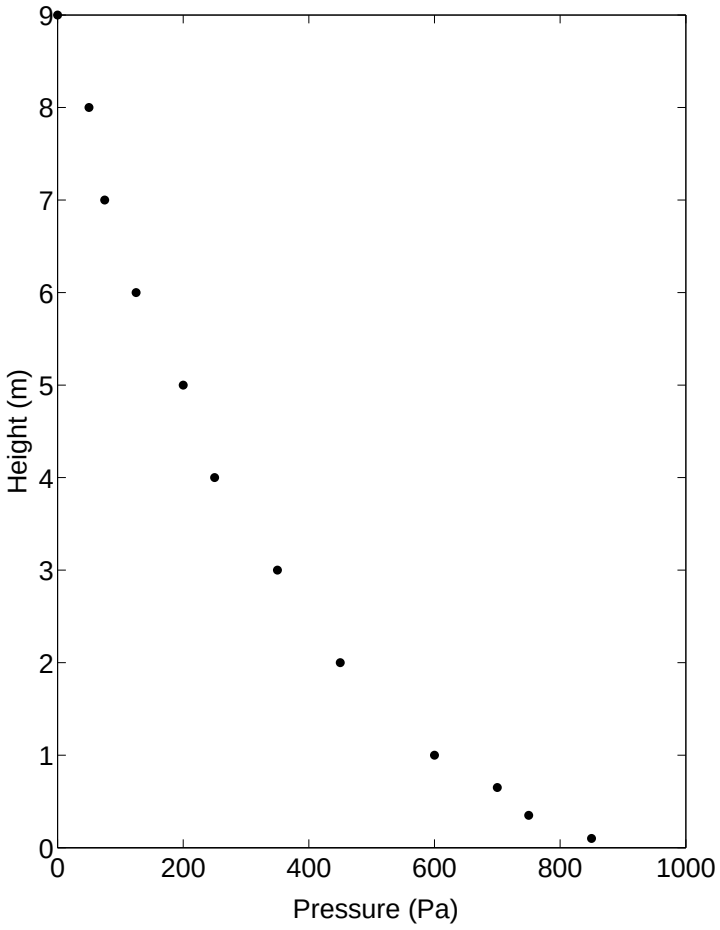

Figure 4.5: Experimental axial profile of the pressure

are not in the riser. Then, the hypothesis that the fraction of large particles in the inventory of the riser is the same as the fraction of large particles in the whole installation is strong.

4.2.4 Presentation of Batrak's work

Batrak (2005) studied the influence of polydispersion in circulating fluidized beds using the multi-fluid approach implemented in Saturne_Polyphasique@Tlse to model the CERCHAR experiment.
For the operating point where 100 kg of large particles are placed in the installation, no steady state was reached but a circulation of large particles was predicted (cf. Figure 4.6).

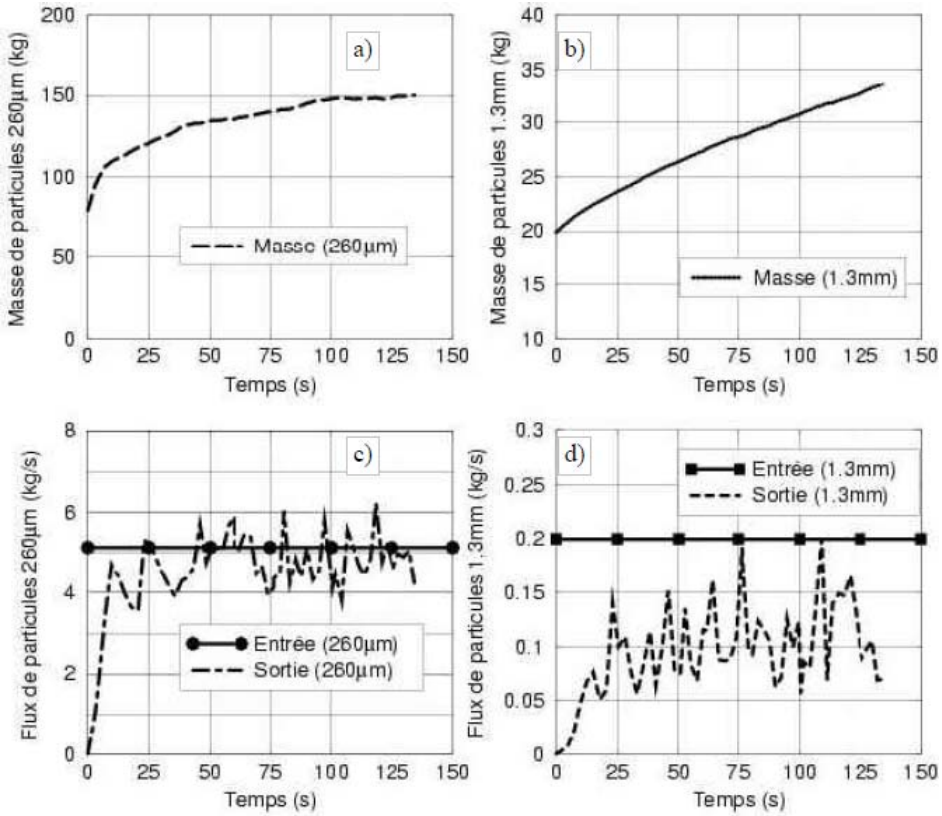

Figure 4.6: Batrak's results

The simulations with Saturne_Polyphasique@Tlse predicted the circulation of large particles, showing that the collisions between different particle species can increase the circulation of solid in a CFB. Nevertheless, the predicted solid mass flux is underestimated by a factor 2. All the operating points modeled by Batrak (2005) showed this underestimation of the large particle solid mass flux.

4.2.5 Simulation with *NEPTUNE_CFD*

Some differences exist between NEPTUNE_CFD V1.08@Tlse and Saturne_Polyphasique@Tlse. It is therefore necessary to run another calculation of the CERCHAR experiment with NEPTUNE_CFD V1.08@Tlse. In this simulation, the inlet solid mass flux is imposed. Hence, the result of the simulation is the inventory of solid in the bed and the repartition of the outlet solid mass flux. The initial and boundary conditions are summarized in the Table 4.3.

Table 4.3: Initial and boundary conditions in the simulations

	Small particles	Large particles
Inlet mass flux	5.207 kg/s	0.217 kg/s
Initial mass	80 kg	20 kg

Results

The 3D simulation of the 100 kg **of large sand experiment did not reach a steady state**. Then, the predicted inventory of solid in the bed cannot fit with experimental results: the more physical time is simulated, the more large sand particles are predicted in the bed (cf. Figure 4.8). Nevertheless, the mass of small particles seems to stabilize after 100 s (cf. Figure 4.7). Then, it slightly increases with time. This is due to the important increase in the inventory of large particles.
Figures 4.7 and 4.8 show that our simulation predicts less small particles in the inventory than Batrak's. On the other hand, we predict more large particles in the bed (cf. Table 4.4). It is due to the fact that the predicted transitory states are quite different: it takes more physical time in our simulation than Batrak's to reach a quasi-steady outlet mass flux of both solid (cf. Figures 4.9 and 4.10). But in the end, our simulation predicted an outlet mass flux of solid closer to Fabre's experiment. Table 4.5 and

Table 4.4: Inventory in the simulations

Total mass	NEPTUNE_CFD V1.08@Tlse t= 560 s/t=125 s	**Batrak** t=125 s	**Fabre** Steady state
Large particle	83 kg/40 kg	33 kg	**80 kg**
Small particle	71 kg/57 kg	150 kg	

Figures 4.9 and 4.10 show that the outlet mass flux of small particles is close to the imposed inlet mass flux. It is slightly underestimated. This is due to the increase in the mass of large particles in the bed.
The outlet mass flux of large particles is underestimated compared to experimental results. Nevertheless, NEPTUNE_CFD V1.08@Tlse predicts a circulation of large sand particles through the bed. The predicted outlet mass flux of large sand is higher than the flux predicted with Saturne_Polyphasique@Tlse by Batrak (2005).

Table 4.5: Experimental and numerical outlet solid mass flux

Total mass flux	NEPTUNE_CFD V1.08@Tlse	**Batrak**	**Fabre**
Large particle	0.16 kg/s	0.11 kg/s	0.22 kg/s
Small particle	5.15 kg/s	4.9 kg/s	5.21 kg/s

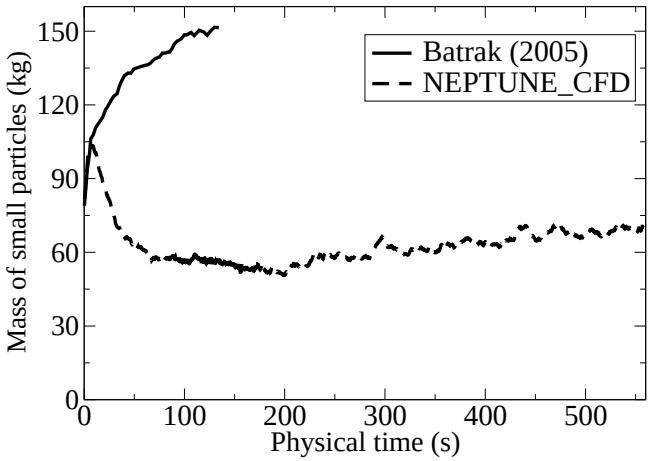

Figure 4.7: Evolution of the mass of small particles (260 μm) in the bed. Comparison between Saturne Polyphasique (Batrak) and NEPTUNE_CFD V1.08@Tlse

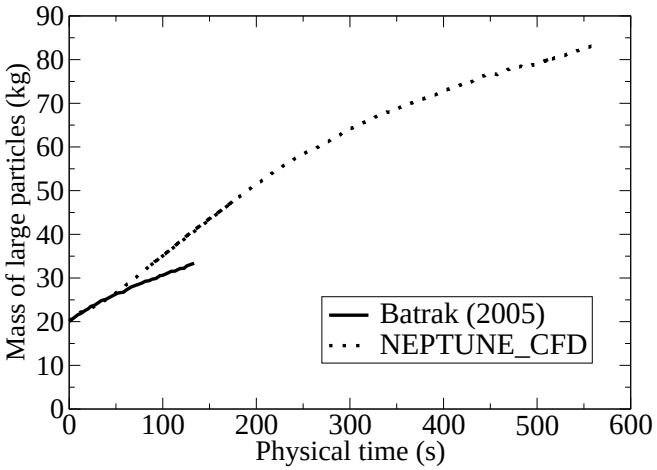

Figure 4.8: Evolution of the mass of large particles (1300 μm) in the bed. Comparison between Saturne Polyphasique (Batrak) and NEPTUNE_CFD V1.08@Tlse

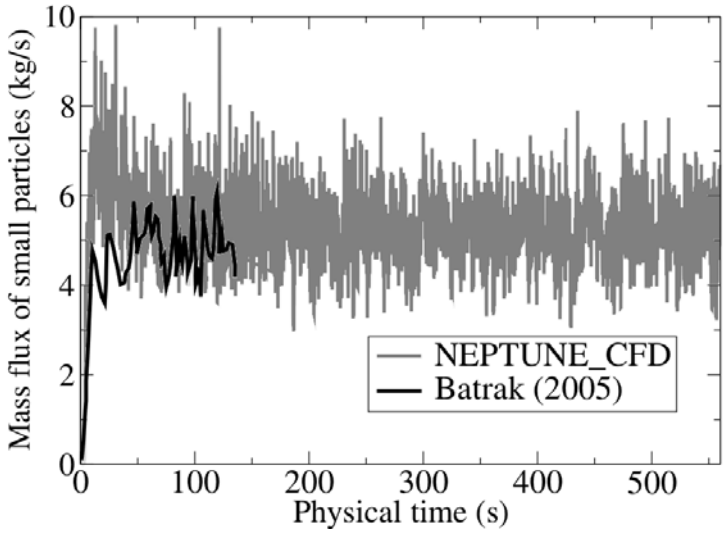

Figure 4.9: Evolution of the outlet mass flux of small particles (260 μm). Comparison between Saturne Polyphasique (Batrak) and NEPTUNE_CFD V1.08@Tlse

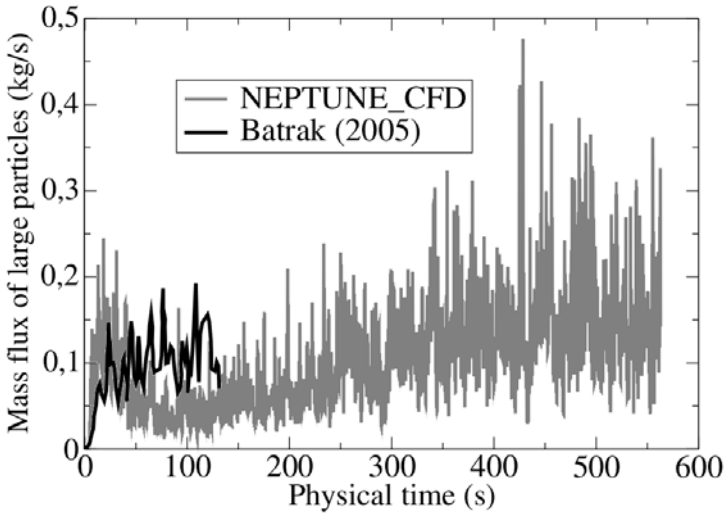

Figure 4.10: Evolution of the outlet mass flux of large particles (1300 μm). Comparison between Saturne Polyphasique (Batrak) and NEPTUNE_CFD V1.08@Tlse

4.2.6 Influence of the mesh

Presentation of the simulations

Three simulations are presented in this section. The only difference between them is the mesh refinement. These simulations are performed to determine if the predicted circulating mass flux depends on the mesh refinement. Three grids are built with one parameter - called N- to control the mesh size. In our simulations, N was equal to 6, 8 or 12. The number of cells was between 150 000 and 1 million divided as shown in Table 4.6.

Table 4.6: Mesh characteristics

	N6	N8	N12
$\Delta x \times \Delta y$ (cm^2)	2.7 × 2.9	2× 2.1	1.3 × 1.4
Δz **min (cm)**	3.3	2.5	1.7
Δz **max (cm)**	20	15	10

Results

None of the three simulations reached a steady state. Figures 4.11 and 4.12 clearly show an influence of the size of the mesh on the predicted hydrodynamics of the bed. Even if the calculations did not converge, the transitory state is different for each case, **refining the grid increases the circulation of large particles** (the values given in Table 4.7 are time-averaged between t=174 and 194 s) and thus decreases the inventory of large particles in the bed. It might be due to the effect of sub-grid structures already pointed out by Parmentier et al. (2011).

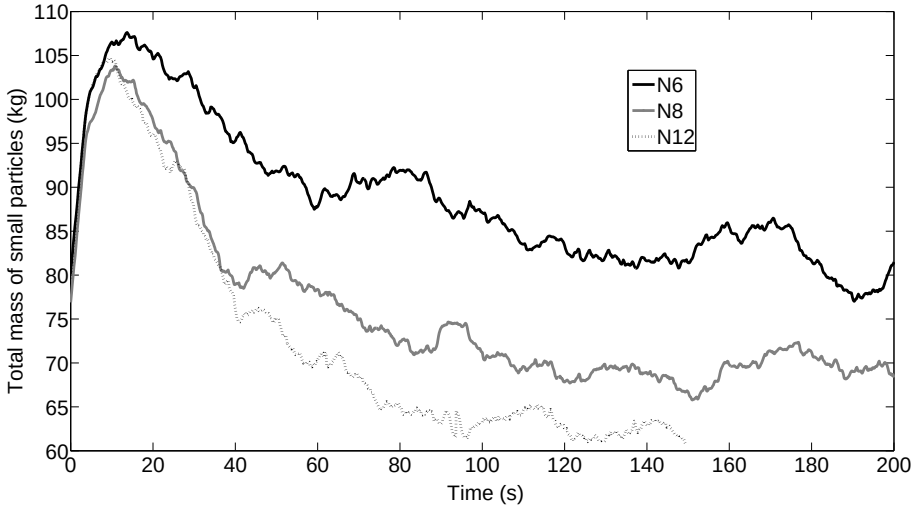

Figure 4.11: Evolution of the mass of small particles in the bed

Figure 4.13 and 4.14 show that the finer the mesh, the less particles in the bottom zone of the riser.

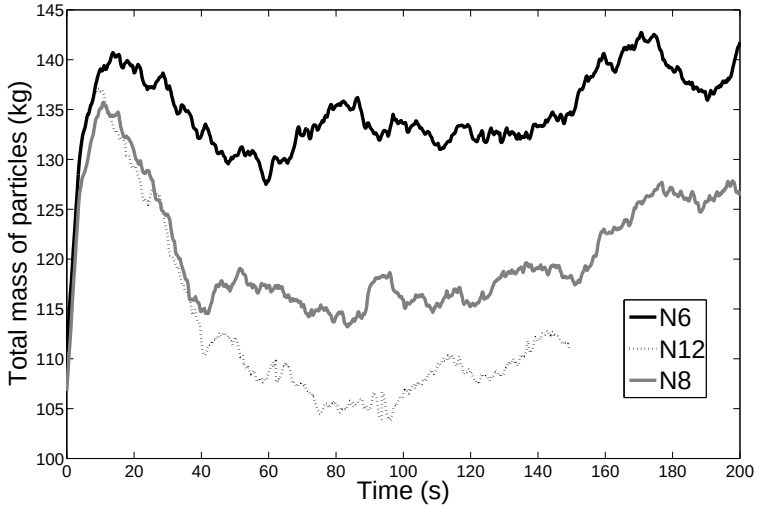

Figure 4.12: Evolution of the total mass of particles in the bed

Figure 4.15 show that the parameter $Z_{pq} \geq 1$ almost everywhere for all meshes. It means that the collisions are driven by the relative velocity between species. There is a small influence of the mesh refinement on this parameter. In N6 case, the field seems more heterogeneous than in N8 and N12.

Table 4.7: Summary of the outlet mass fluxes

Case	N6 Outlet	N8 Outlet	N12 Outlet	All Inlet
260 μm mass flux (kg/s) t = 194 s	5.1	5.08	5.25	5.2
1300 μm mass flux (kg/s) t = 194 s	0.07	0.09	0.09	0.217
$t = t_{max}$	900 s	278 s	194 s	-
1300 μm mass flux (kg/s)	0.12	0.096	0.09	0.217

These simulations show that the predicted transitory state depends on the mesh refinement. **The finer the mesh, the smaller the inventory of small particles in the bed and the greater the circulation of large particles is predicted**. It means that there are small scale heterogeneities that have a macroscopic influence on the hydrodynamic of the flow. The work of Parmentier et al. (2008) or Ozel (2011) already showed the use of sub-grid models for the drag force. This work show that it might be also very important to develop sub-grid models for the momentum and particle kinetic exchanges during collisions. The simulation with a coarse grid does not reach a steady state after 900 physical seconds. The simulations with a finer mesh are too costly to run longer, so it has been decided to perform periodic simulations in order to study the hydrodynamics of this binary mixture of particles.

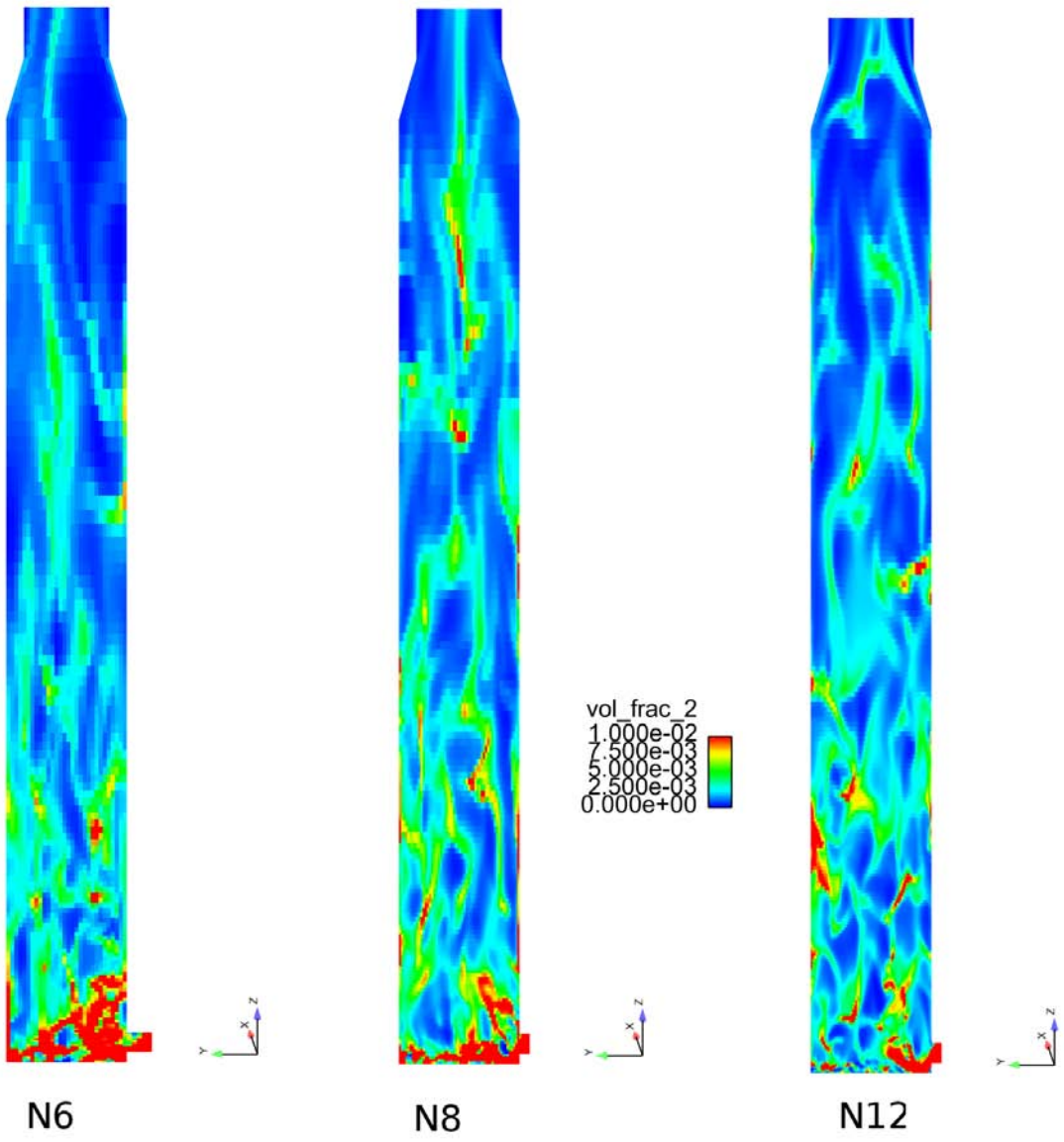

Figure 4.13: Instantaneous field of the volume fraction of small particles in the centre of the bed

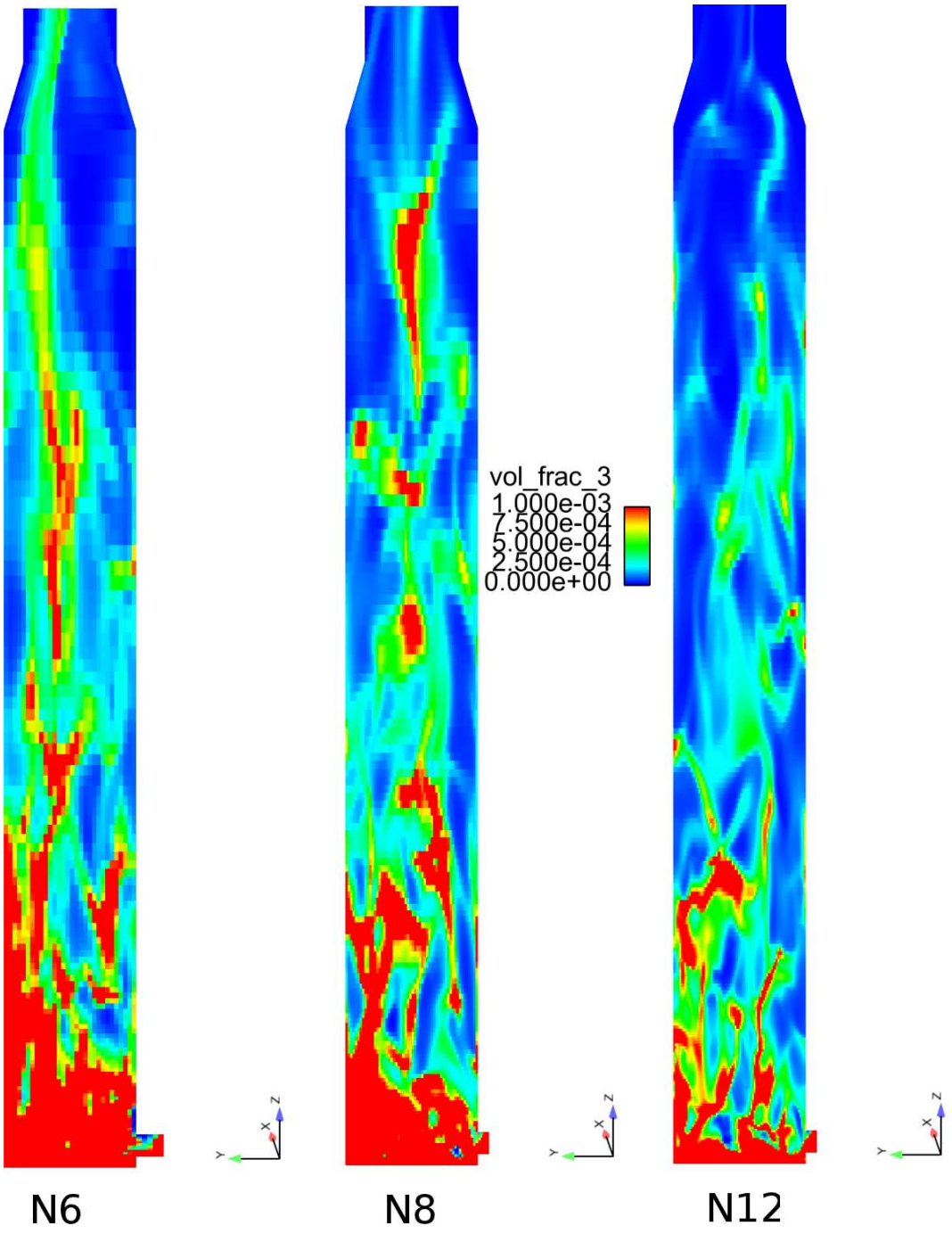

Figure 4.14: Instantaneous field of the volume fraction of large particles in the centre of the bed

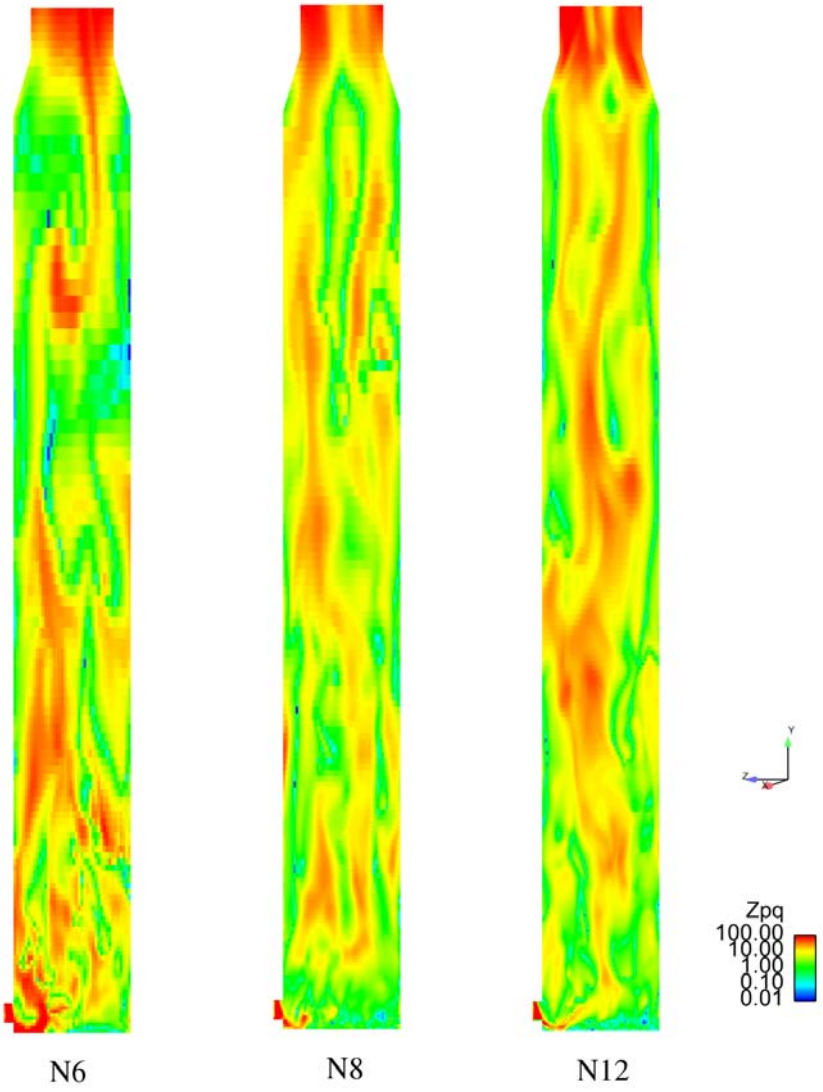

Figure 4.15: Instantaneous field of the parameter Z_{pq} in the centre of the bed

4.2.7 Conclusions on poly-solid experiments and simulations

The CERCHAR experiments showed that the particles with a terminal settling velocity twice bigger than the fluidization velocity can circulate through the bed when smaller particles are present in the installation. The 3D unsteady simulations of this experiment showed that the Eulerian-Eulerian modeling can predict the circulation of the large particles but this circulation is underestimated compared to experiments. It results in a simulation that can not reach a steady state.
Nevertheless, this study showed that NEPTUNE_CFD V1.08@Tlse predicts a more important circulation of large particles than *Saturne_Polyphasique@Tlse* did, if the simulation is long enough (900 physical seconds).
We did not reach a mesh independence but our study showed that the finer the mesh, the smaller the inventory of small particles becomes, and the greater the circulation of large particles is predicted.
Then, the underestimation of the circulating large sand mass flux can be due to:

- A too short simulation time: it takes a lot of time to reach the steady state (more than 15 minutes).
- A bad resolution of the model (interclass collisions interaction, drag...) due to sub-grid effects.

Then, in order to understand the mechanisms that lead to the circulation of large particles, it is important to investigate this experiment in a steady-state case. This is why, it was decided to perform a numerical study of the established zone of the riser of Fabre's experiment by using 3D unsteady periodic simulations.

4.3 Simulations in periodic box

The previous numerical studies did not reach a steady state. NEPTUNE_CFD V1.08@Tlse seems to underestimate the circulating mass flux of large particles in the CERCHAR experiments. In order to understand the mechanisms that trigger the circulation of large particles and cause this underestimation, periodic simulations are performed.
This parts is divided into 3 sections:

- The first section aims at presenting how the boundary conditions of the periodic simulations are implemented.
- The second presents a simulation with NEPTUNE_CFD V1.08@Tlse of Gourdel et al. (1998) numerical experiment (LES+DPS). Gourdel simulated an experiment performed by Fabre with a binary mixture of particles of same diameter but different density. The influence of the volume fraction of heavy particles for a given volume fraction of light particles is studied. Reproducing Gourdel's numerical simulation with NEPTUNE_CFD V1.08@Tlse aims at validating the interclass collision modeling. NEPTUNE_CFD V1.08@Tlse results are also compared with 0D simulation in order to check that the terms of the momentum and energy contribution due to collisions between different species are correctly implemented.
- The last section corresponds to periodic simulations of a slice of the established zone of the riser in Fabre's experiments.

4.3.1 Theoretical approach

The domain studied is a cube composed of cubical cells. A symmetric condition is imposed on the side faces and a periodic boundary condition is imposed for the upper and the lower faces.
Those boundary conditions imply that there is no mean pressure gradient between the lower and upper faces. We assume that the pressure can be split into two terms: a periodic term P^* satisfying $(P^*(z_{top}) = P^*(z_{bottom}))$ and a term that only depends on z:

$$P = P^* + \Gamma \cdot (z - z_0) \tag{4.1}$$

The axial component of the momentum equations of the gas and solid phases writes:

$$\frac{\partial \alpha_g \rho_g U_{g,z}}{\partial t} + \frac{\partial}{\partial x_j}\alpha_g \rho_g U_{g,j} U_{g,z} = -\alpha_g \frac{\partial P}{\partial z} - \alpha_g \rho_g g + I_{g\to p} + \frac{\partial}{\partial x_j}\Sigma_{g,zj} \tag{4.2}$$

$$\frac{\partial \alpha_p \rho_p U_{p,z}}{\partial t} + \frac{\partial}{\partial x_j}\alpha_p \rho_p U_{p,j} U_{p,z} = -\alpha_p \frac{\partial P}{\partial z} - \alpha_p \rho_p g + I_{p\to g} + \frac{\partial}{\partial x_j}\Sigma_{p,zj} \tag{4.3}$$

Replacing P by its expression gives:

$$\frac{\partial \alpha_g \rho_g U_{g,z}}{\partial t} + \frac{\partial}{\partial x_j}\alpha_g \rho_g U_{g,j} U_{g,z} = -\alpha_g \frac{\partial P^*}{\partial z} - \alpha_g \rho_g g + I_{g\to p} + \frac{\partial}{\partial x_j}\Sigma_{g,zj} - \alpha_g \Gamma \tag{4.4}$$

$$\frac{\partial \alpha_p \rho_p U_{p,z}}{\partial t} + \frac{\partial}{\partial x_j}\alpha_p \rho_p U_{p,j} U_{p,z} = -\alpha_p \frac{\partial P^*}{\partial z} - \alpha_p \rho_p g + I_{p\to g} + \frac{\partial}{\partial x_j}\Sigma_{p,zj} - \alpha_p \Gamma \tag{4.5}$$

Adding the previous equations for the fluid phase and $(n-1)$ particle phases gives:

$$\frac{\partial}{\partial t}\sum_{k=1}^{n}\alpha_k\rho_k U_{k,z}+\frac{\partial}{\partial x_j}\sum_{k=1}^{n}\alpha_k\rho_k U_{k,j}U_{k,z}=-\frac{\partial P^*}{\partial z}-\sum_{k=1}^{n}\alpha_k\rho_k g+\sum_{k=1}^{n}\frac{\partial}{\partial x_j}\Sigma_{k,zj}-\Gamma \quad (4.6)$$

Then, the equation (4.6) can be integrated between the two periodic faces. Assuming that a steady state is reached, the left-hand-side of the equation can be neglected. It gives:

$$0=-\int_{z=z_{bottom}}^{z_{top}}\frac{\partial P^*}{\partial z}dz-\sum_{k=1}^{n}\alpha_k\rho_k g(z_{top}-z_{bottom})+\int_{z=z_{bottom}}^{z_{top}}\frac{\partial}{\partial x_j}\Sigma_{k,zj}dz+\Gamma(z_{top}-z_{bottom}) \quad (4.7)$$

Then, the periodic contribution of the pressure is null, and we finally get:

$$\Gamma=-\sum_{k=1}^{n}\alpha_k\rho_k g+F \quad (4.8)$$

F represents the friction effect with the wall. If there is only periodic and symmetric boundary conditions in the domain, the averaged friction term on the domain is equal to zero. Then, the periodic condition corresponds to imposing the mass of gas and particles inside the box. In this case, Γ corresponds to the hydrostatic pressure.

4.3.2 Gourdel's numerical experiment

The aim of this section is to compare the results predicted by NEPTUNE_CFD V1.08@Tlse, LES/DPS simulations of Gourdel et al. (1998) and 0D simulation.

LES - DPS simulations (Gourdel et al. (1998))

Mesh and geometry

The studied geometry corresponds to a cube of characteristic length $L = 12.8$ cm.

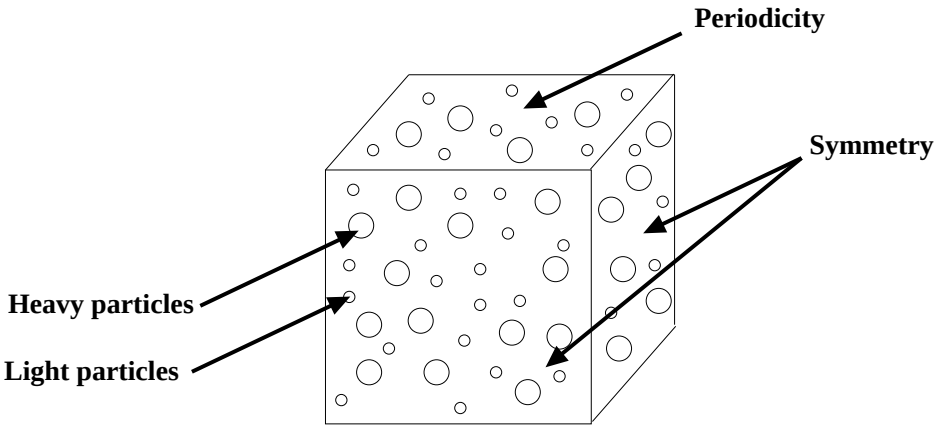

Figure 4.16: Presentation of the geometry

As shown by Figure 4.16, a symmetry condition is imposed at the wall, and a periodic condition is imposed between the upper and the lower faces. The domain is

composed of cubical cells of 2 mm width. The mesh was made of 262 144 cells.

Physical modeling

Gourdel et al. (1998) simulated a mixing of binary particles in an homogeneous isotropic turbulence. The fluid phase is modeled by LES approach. The diffusive effect of the residual field is modeled with the scale similarity closure assumption proposed by Bardina et al. (1983) completed by a sub-grid eddy-viscosity proposed by Smagorinsky Smagorinsky (1963). The particle phase is modeled using a Lagrangian approach that takes into account the collisions between particles of same size but different densities. The exchange between gas and particle phases is reduced to the drag force.
A hard sphere model is used for the collisions that are considered as elastic ($e_c = 1$). The main characteristics of the LES-DPS simulation is summarized in Table 4.8.

Table 4.8: Characteristics of the LES - DPS simulation

Gas density	$1.17\ kg \cdot m^{-3}$
Cinematic viscosity	$1.47 \cdot 10^{-5}\ m^2 \cdot s$
Mean diameter	$650\ \mu m$
Particle density	$\rho_A = 117.5\ kg \cdot m^{-3}$, $\rho_B = 235\ kg \cdot m^{-3}$
Gravity	$49.05\ m \cdot s^{-2}$
Stress tensor	$< u'_{1,i}u'_{1,j} >_1 = 8.76 \cdot 10^{-2}\delta_{i,j}\ m^2/s^2$
τ_1^t	$23 \cdot 10^{-3}\ s$
L_f^e	$7.25\ mm$
L_g^e	$3.71\ mm$
α_A	$13 \cdot 10^{-3}$
α_B	$0.66 \cdot 10^{-3}$; $1.3 \cdot 10^{-3}$; $6.6 \cdot 10^{-3}$; $13 \cdot 10^{-3}$; $37 \cdot 10^{-3}$
Number of class A particles	200 000
Number of class B particles	10 000 - 500 000
Number of cells	64^3
Characteristic size of a cell	$2\ mm$
Time step	$6.75 \cdot 10^{-4}\ s$

0D simulation of Gourdel numerical experiment

The equations of NEPTUNE_CFD V1.08@Tlse are solved in 0D considering a steady state homogeneous flow. The particle agitation is modeled according to $q_2 - q_{12}$ transport equations approach. The reverse coupling on the gas phase is neglected. The drag force is modeled according to Schiller and Naumann (1933) drag law:

$$C_d = \frac{24}{Re_p}(1 + 0.15Re_p^{0.687}) \tag{4.9}$$

with $Re_p = \dfrac{||v_{r,p}||d_p}{\nu_g}$.
Only the parallel to $V_{r,p}$ contribution in the particle-turbulence interaction time $\tau_{1,p}^t$ is modeled. Then,

$$\tau_{1,p}^t = \frac{\tau_1^t}{\sqrt{1 + 0.45\chi_p}} \tag{4.10}$$

with $\chi_p = \dfrac{3}{2}\dfrac{||v_{r,p}||^2}{k}$.
The radial distribution function is modeled by Lun et al. (1984):

$$g_0 = (1 - \frac{\alpha_s}{\alpha_{max}})^{-2.5\alpha_{max}} \text{ with } \alpha_{max} = 0.64.$$

The imposed values of k and ε are estimated as followed:

- Gas phase agitation: $k = \dfrac{1}{2} < u'_{1,i}u'_{1,i} >_1 = 0.1314\ m^2/s^2$
- Turbulent dissipation: $\varepsilon = \dfrac{1}{\beta_1}\dfrac{k}{\tau_1^t} = 2.72\ m^2/s^3 \quad \text{with} \quad \beta_1 = 2.1$

The main characteristics of the 0D simulation are summarized in Table 4.9.

Table 4.9: Characteristics of the 0D simulation

Gas density	$1.17\ kg \cdot m^{-3}$
Cinematic viscosity	$1.47 \cdot 10^{-5}\ m^2 \cdot s$
Mean diameter	$650\ \mu m$
Particle density	$\rho_A = 117.5\ kg \cdot m^{-3}$, $\rho_B = 235\ kg \cdot m^{-3}$
Gravity	$49.05\ m \cdot s^{-2}$
k	$0.1314\ m^2/s^2$
ε	$2.72\ m^2/s^3$
α_A	$13 \cdot 10^{-3}$
α_B	from 10^{-4} to 10^{-1}
Restitution coefficient	1
α_{max}	0.64

Simulations with NEPTUNE_CFD V1.08@Tlse

Mesh

The domain is a cube of 12 cm long made of 1728 cubical cells of 1 cm long.

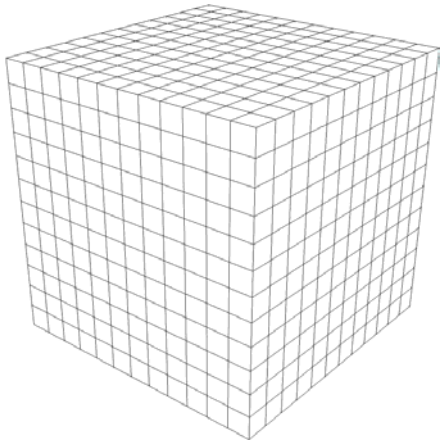

Figure 4.17: Mesh presentation

Physical modeling

The particle agitation is modeled according to $q_2 - q_{12}$ transport equations approach. The reverse coupling on the gas phase is neglected. For inter-particle interactions, granular and kinetic models (uncorrelated collisions) are used. The Wen and Yu (1966) drag law is modified imposing $\alpha_g = 1$ resulting in a Schiller and Naumann (1933) drag law.

The radial distribution function is

$$g_0 = (1 - \frac{\alpha_s}{\alpha_{max}})^{-2.5\alpha_{max}}$$

according to Lun et al. (1984) with $\alpha_{max} = 0.64$.
For the gas phase turbulence, a $(k - \varepsilon)$ model is used. The homogeneous isotropic turbulence is modeled by imposing k and ε at each time-step:

- Particle agitation: $k = \frac{1}{2} < u'_{1,i} u'_{1,i} >_1 = 0.1314\ m^2/s^2$
- Turbulent dissipation: $\varepsilon = \frac{1}{\beta_1} \frac{k}{\tau_1^t} = 2.72\ m^2/s^3 \quad \text{with} \quad \beta_1 = 2.1$

The main characteristics of the 3D simulation are summarized in Table 4.10.

Numerical parameters

The maximum Courant number is imposed at 1, the maximum Fourier number at 100. The alpha CFL is set to 10.
All simulations with NEPTUNE_CFD V1.08@Tlse run on one processor in a few minutes.
Remark on the convergence criteria: when all the fields are perfectly homogeneous and all unknown reach a steady state, the simulations are post-processed.

Table 4.10: 3D simulation characteristics

Density of the gas phase	$\rho_g = 1.17\ kg \cdot m^{-3}$
Dynamic viscosity	$1.72 \cdot 10^{-5}\ m^2 \cdot s$
Mean diameter	$650\ \mu m$
Density of the particle phase	$\rho_A = 117.5\ kg \cdot m^{-3}$, $\rho_B = 235\ kg \cdot m^{-3}$
Gravity	$49.05\ m \cdot s^{-2}$
k	$0.1314\ m^2/s^2$
ε	$2.72\ m^2/s^3$
α_A	$13 \cdot 10^{-3}$
α_B	$0.66 \cdot 10^{-3}$; $1.3 \cdot 10^{-3}$; $6.6 \cdot 10^{-3}$; $13 \cdot 10^{-3}$; $37 \cdot 10^{-3}$
Restitution coefficient	1
α_{max}	0.64
Number of cells	12^3
Size of cells	$1.0\ cm$
Time-step	time-dependent

Results

As expected, on all figures, the operating points simulated with NEPTUNE_CFD V1.08@Tlse are superimposed with the curve of points calculated by 0D code. It show that the polydisperse model is correctly implemented in NEPTUNE_CFD V1.08@Tlse.

The predicted velocities by LES+DPS and Eulerian modeling fits well (cf. Figure 4.18). Our results are similar to Gourdel's. Knowing that the terminal settling velocity of B and A particles are respectively $-2.97m/s$ and $-1.87m/s$, we see that the mean velocity of the particle species is bounded by the terminal settling velocities of A and B particles. Due to collisions, momentum transfer occurs between A and B particles resulting in the decrease in the mean velocity of the heaviest particles and in an increase in the mean velocity of the lightest ones.

In Figure 4.19, the characteristic collision times predicted with NEPTUNE_CFD V1.08@Tlse, 0D simulation and LES+DPS simulations are presented. NEPTUNE_CFD V1.08@Tlse and 0D simulations predicted identical results. Small differences are observed between the Eulerian modeling and the LES+DPS simulations. It is due to the fact that the particle spatial correlations and the particle velocity correlations for colliding particles are not used in NEPTUNE_CFD V1.08@Tlse simulations.

Nevertheless, an overestimation of the particle agitation by Eulerian-Eulerian modeling is observed, although its dependency on the fraction of heavy particles is well predicted.

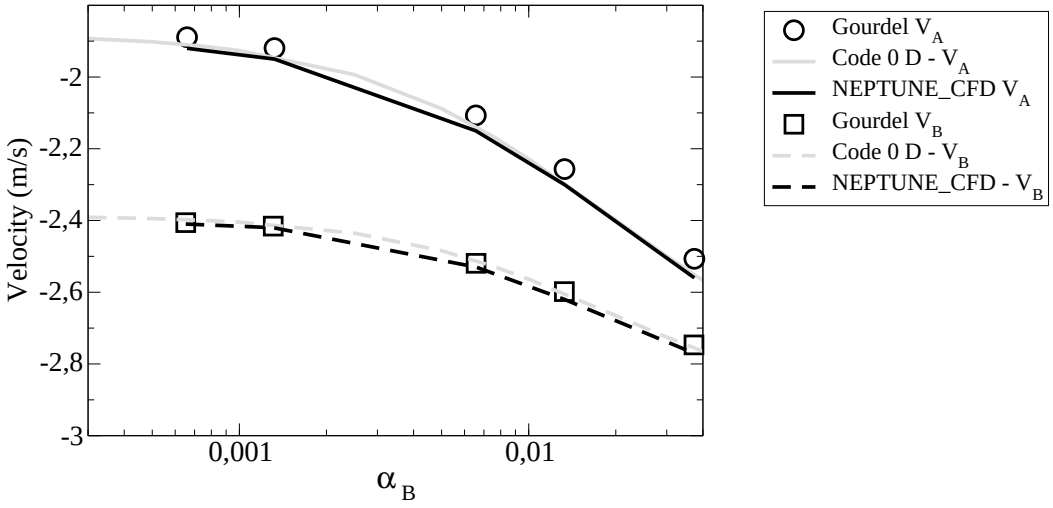

Figure 4.18: Evolution of time and domain-averaged velocities of A and B particles with the fraction of B-particles in the domain

Conclusion

These periodic simulations showed that both the polydisperse model equations and our periodic source term in the momentum equation are correctly implemented. It also showed that NEPTUNE_CFD V1.08@Tlse can predict the hydrodynamics of a binary mixture of particles. The dependency on the fraction of one particle phase can be predicted.

4.3.3 Periodic simulations of Fabre bi-solid experiment

The purpose of this section is to study the local influence of the collisions between particles of different classes in the upper part of the experimental set-up of Fabre. In Fabre's experimental results, there is no information about the real fraction of each solid in the inventory. It is assumed that the inventory inside the bed is representative of the inventory of the installation. In Chapter 3, we showed that the collisions between classes are not negligible in poly-solid CFB, even in the dilute parts. It is therefore relevant to investigate the influence of small particles on the fluidization of large ones in a case where the effect of interclass collisions is heightened: the CERCHAR experiment.

Reference experiment

In Figure 4.21, 9 operating points corresponding to the bi-solid experiments performed by Fabre at CERCHAR are presented. According to the experimental pressure profiles, there is a zone at the top of the bed where the fraction of solid in the riser is established. A slice of this upper part of the riser is considered as our periodic reference domain (cf. Figure 4.22). This physical domain is 1 m height and has a cross section of 1.2×0.8 m^2.
In a periodic simulation, the height of the domain is of paramount importance. Indeed, if it is too small, the result might not be physical because a structure can be interact-

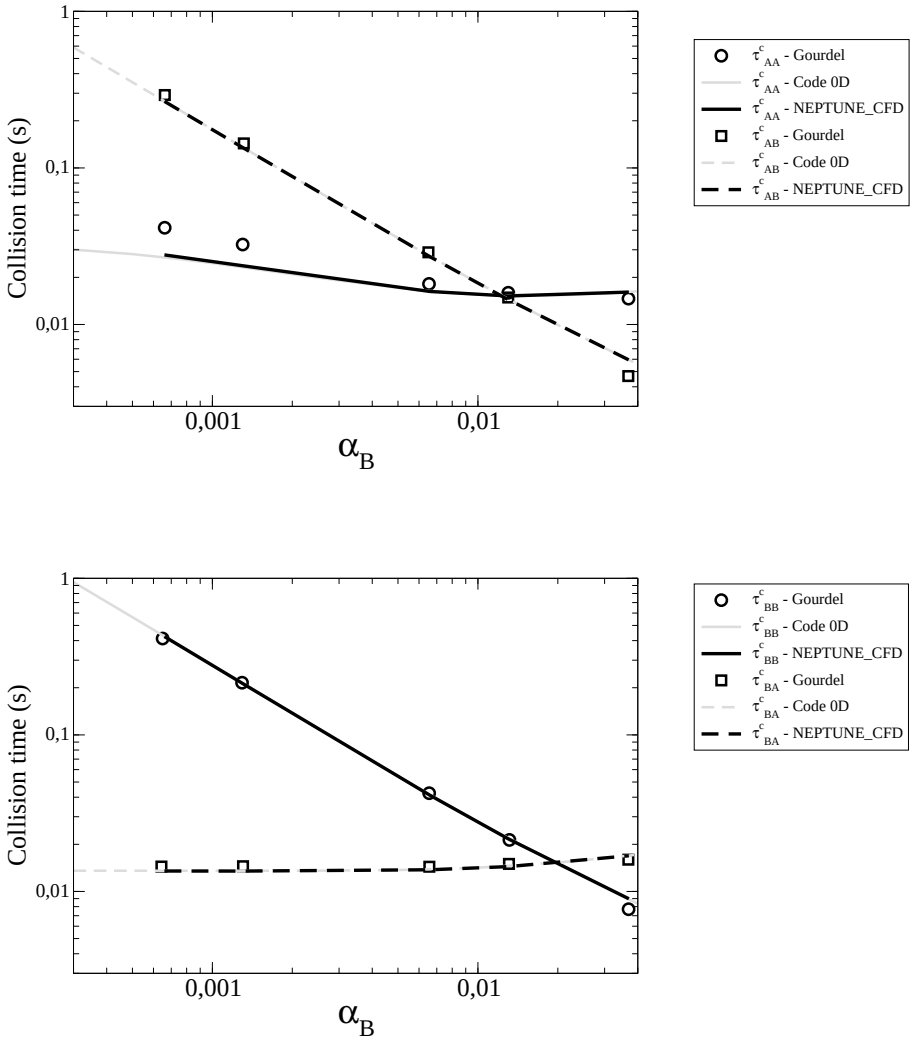

Figure 4.19: Particles characteristic collision time

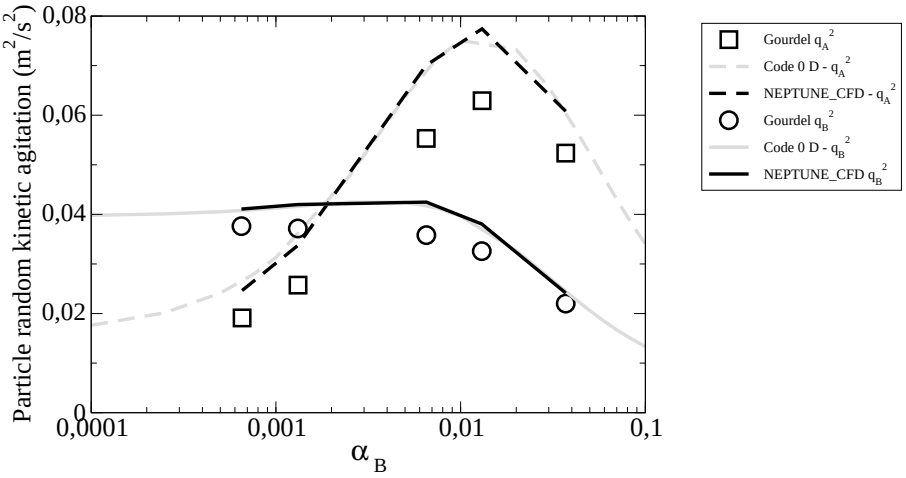

Figure 4.20: Evolution of time and domain-averaged particle agitation of A and B particles with the fraction of B-particles in the domain

ing with itself (a particle with its own wake...). Therefore, it is difficult to define the domain's characteristics for a periodic simulation. In order to compare experimental and numerical results, it is necessary to keep the same cross section: $1.2 \times 0.8\ m^2$. The height of the domain is chosen to be about five times the characteristic length leading to a 5 m height periodic domain.
The reference mesh is composed of cubic cells : $\Delta x = \Delta y = \Delta z = 2\ cm$.

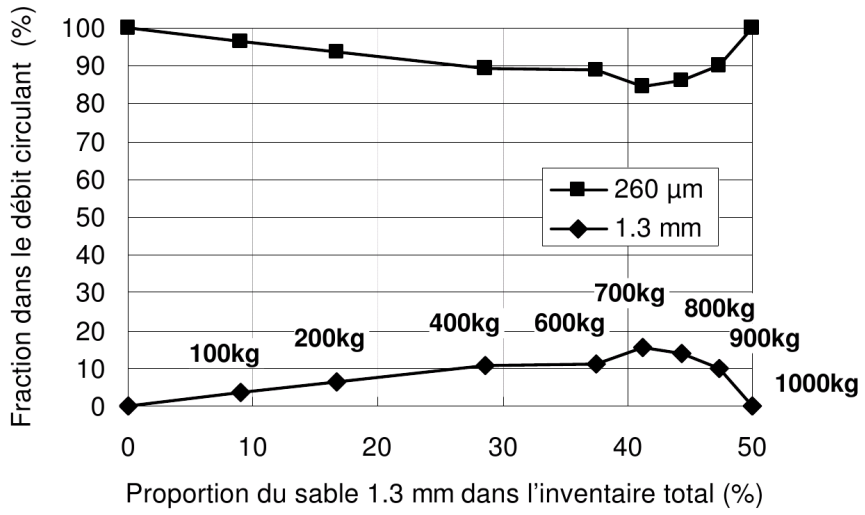

Figure 4.21: Evolution of the fraction of large sand $1,3\ mm$ in the circulating mass flux

In order to determine the inventory to impose in the periodic domain, it was decided to take the 100 kg of large sand experiment of Fabre's work as the reference case. It corresponds to 90.5% of 0.260 mm particles and 9.5% of 1.3 mm particles. Then the averaged density in the established zone is:

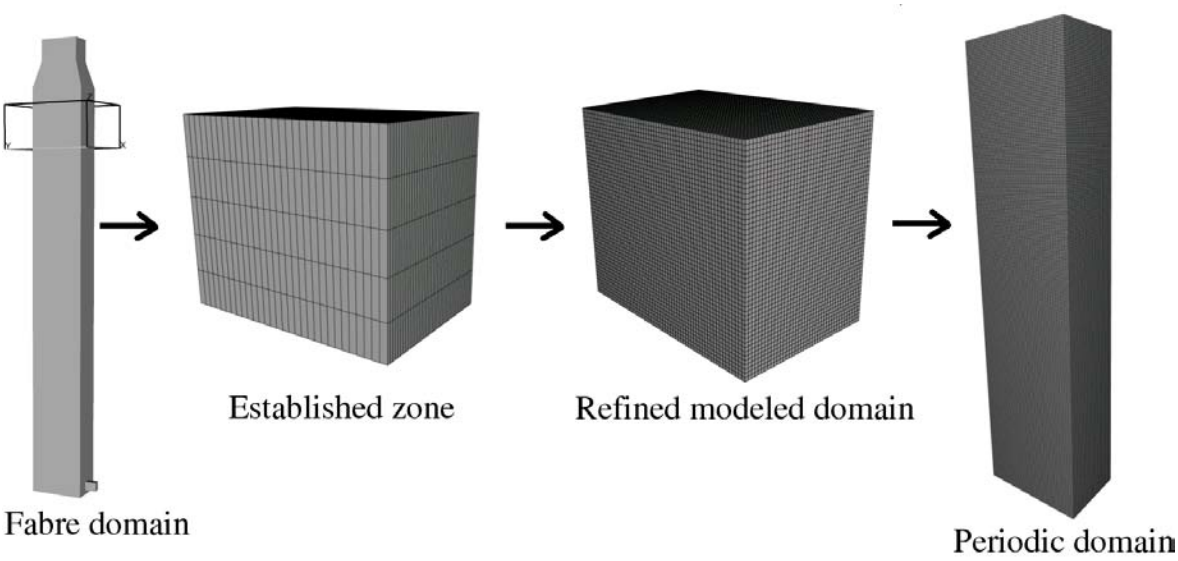

Figure 4.22: Building of the periodic domain

$$\rho_m = \alpha_g \rho_g + (\alpha_{0.26} + \alpha_{1.3})\rho_p$$
$$\rho_m = \alpha_g \rho_g + \alpha_{1.3}(\tfrac{\alpha_{0.26}}{\alpha 1.3} + 1)\rho_p$$

The established zone is dilute so we can assume that $\alpha_g \simeq 1$. Then it comes:

$$\alpha_{1.3} = \frac{\rho_m - \rho_g}{\rho_p \times \frac{\alpha_{0.26}}{\alpha 1.3}}$$

$$\alpha_{1.3} = 2.15 \cdot 10^{-4}$$
$$\alpha_{0.26} = 2.15 \cdot 10^{-3}$$

The gas volume fraction can be calculated: $\alpha_g = 1 - \alpha_{0.26} - \alpha_{1.3} = 0.9976$.

Finally, the fraction of small sand particles is equal to $2.15{\cdot}10^{-3}$ in all the simulations presented. The fraction of large sand particles vary from $2.15{\cdot}10^{-4}$ to $1.76{\cdot}10^{-3}$. Then, the ratio between small sand and large sand in the inventory vary between 9% and 45%. Five of the nine operating points have been simulated. These main characteristics of this points are summarized in Table 4.11:

Table 4.11: Operating points

$\alpha_{1.3mm}$	$2.15 \cdot 10^{-4}$	$4.3 \cdot 10^{-4}$	$8.79 \cdot 10^{-4}$	$1.495 \cdot 10^{-3}$	$1.76 \cdot 10^{-3}$
$\frac{\alpha_{1.3mm}}{\alpha_s}$	9%	17%	29%	41%	45%
$\frac{n_p^{small}}{n_p^{large}}$	1250	625	306	180	153

Boundary conditions

In these simulations, a wall condition is imposed for all faces but the periodic ones (upper and lower faces). A friction boundary condition is imposed for the gas phase.

This friction generates a momentum loss. Combined to the periodic condition, this loss results in a constant increase in the total momentum of the system. Therefore, it is compensated by adding a source term into the momentum equation at every time-step. This source term corresponds to:

$$\Gamma_{friction} = \frac{\sum_{k=1}^{n} \alpha_i \rho_i W_i}{\Delta t}$$

$\Gamma_{friction}$ is expected to remain small compared with the periodic source term added because of the periodic condition.
In this section, the total added momentum term writes:

$$\Gamma = (\alpha_g \rho_g + \alpha_p \rho_p) g + \sum_{k=1}^{n} \frac{(\alpha_i \rho_i W_i)^t}{\Delta t} \tag{4.11}$$

For the particle phase, a free-slip condition is imposed.

Convergence criteria

The periodic simulation is assumed to converge when the domain-averaged $\alpha_i V_i$ for each phase i oscillates around a constant value. The presented time-averaged results are post-processed after an averaging time of more than 5 periods of the $\alpha_i V_i$ oscillations. Unfortunately, the averaging time was not always sufficient to obtain smooth and symmetrical profiles.

Results

Figures 4.23 and 4.24 show that the particles are concentrated along the walls. Depending on the physical time of post-processing, the particles are concentrated along one or two side walls, meaning that the simulations are not stationary: particles are moving from one wall to another.

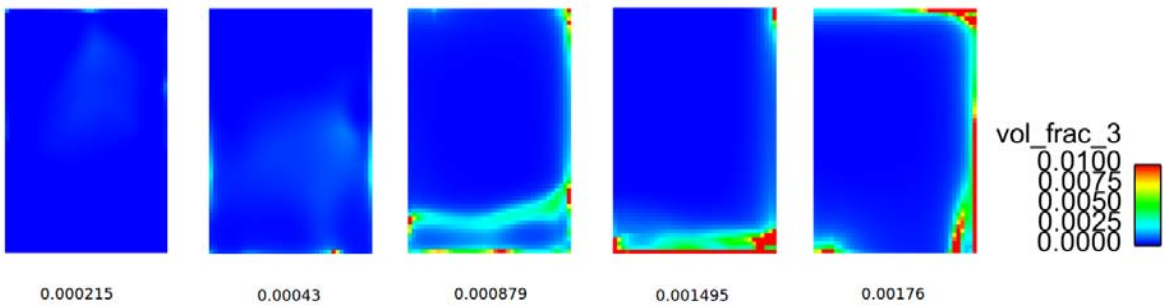

Figure 4.23: Instantaneous fields of the fraction of large particles in z plan for different fraction of large particles in the bed

Figure 4.25 shows that there is a maximum of both solid phases volume fraction to the wall. Increasing the fraction of large particles in the bed increases the fraction of large particles to the wall and decreases the fraction of small particles in all the bed. The shape of the radial profile of the small sand volume fraction is not changed by the

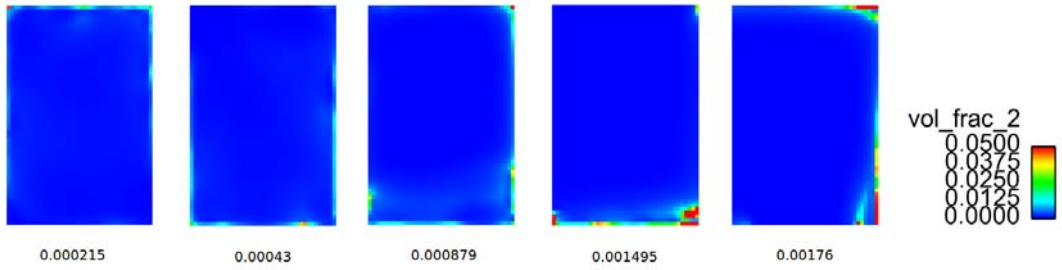

Figure 4.24: Instantaneous field of the fraction of small particles in z plan for different fraction of large particles in the bed

increase of large particles in the inventory. On the other hand, the evolution of the fraction of large particle with its inventory in the bed is more complicated to study. From 9% to 17%, the $\overline{\alpha_{large}}$ increases everywhere. The profile remains flat except on the wall. When the fraction of large sand reaches 29%, $\overline{\alpha_{large}}$ decreases in the centre and strongly increases in the area located 20 cm from the wall. **Between 29% and 41%, a significant change occurs: a local maximum appears in the center of the bed and there is a decrease in the area located 20 cm away from the wall**. The local concentration of particle in the center of the bed was already noticed by Weinstein et al. (1984).

Figure 4.26 shows that increasing the fraction of large particles from 9% to 45% in the bed increases the fraction of large sand in the riser.
Between 17% and 29%, the radial segregation profile changes: the maximum fraction of large particles goes from the centre of the bed to the wall. In the 29% case, the repartition between large and small sand is almost homogeneous. Then, the shape of the profile changes for the 41% and the 45% cases. The fraction of large sand keeps increasing in the center of the bed.
The radial segregation between species strongly depends on the fraction of large particles in the domain.

Chew et al. (2011) or Mathiesen et al. (2000a) studied the radial segregation of a size-difference binary mixture of particles where the fraction of each solid was equal to 50%. It was found that, in the upper zone of the riser, the larger particles preferentially segregated to the wall. Figure 4.26 also shows that there is a maximum of large particles to the wall for equal fraction of both solid.
Our work points out a difference with previous works: we predict **a local maximum of large particles volume fraction in the center of the bed**. Nevertheless, in Chew et al. (2011), a local maximum can be observed in the center of the domain for the more dilute cases with smaller gas superficial velocity of size-difference binary mixture.

Figure 4.27 shows that the variance of solid volume fraction normalized by the solid volume fraction is maximal to the wall for both small and large particles. For the 41% and 45% cases, there is a maximum in the center of the bed for both solid phases. There are clusters of each particle species near the wall.

Figure 4.28 shows that increasing the fraction of large particles in the domain from 9% to 41% increases the random kinetic energy for both particle phases. The near

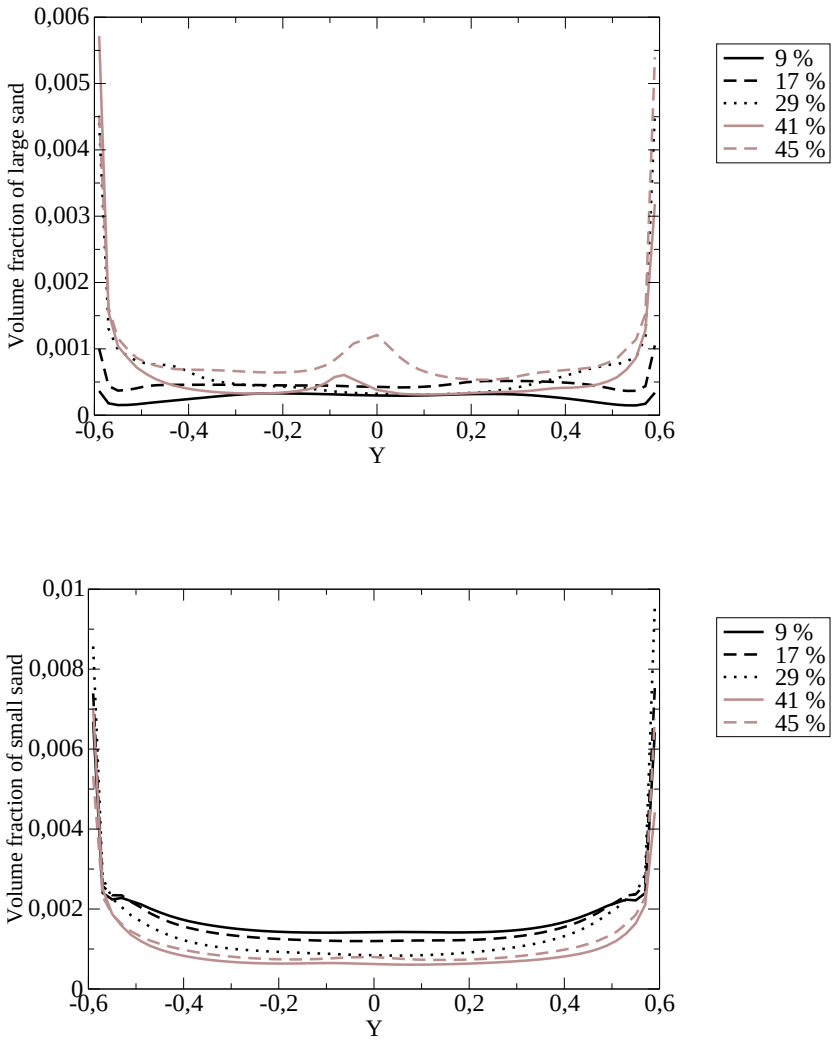

Figure 4.25: Time-averaged radial profile of the fraction of large (top) and small (bottom) particles for Y=0

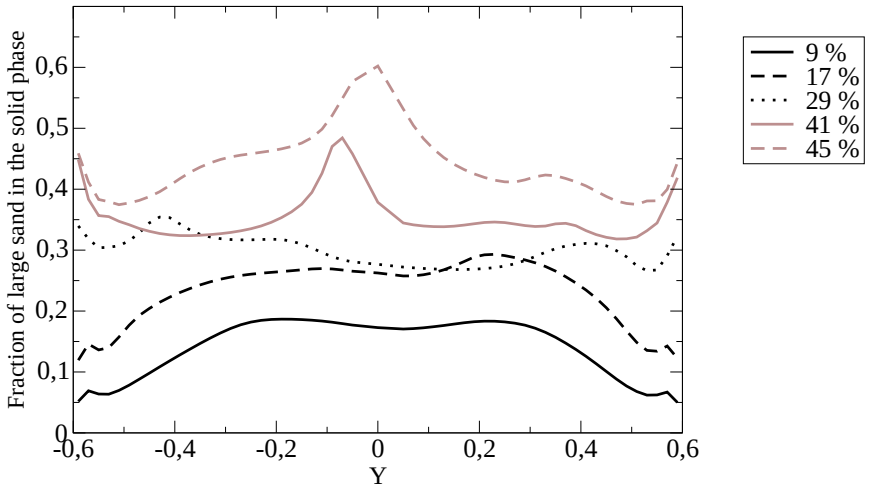

Figure 4.26: Time-averaged radial profile of the fraction of large particles Y=0

wall particle agitation does not change significantly. The increase occurs mostly in the central zone of the riser. Between 29% and 41%, there is a change in the profiles shape: two local maximum appear 35 cm from the wall. For 45% of large particle in the solid phase, there is a significant decrease in the particle agitation compared to the 41% case.

Figure 4.29 shows that $Z_{pq} > 1$ almost everywhere for all cases. Collisions are therefore driven by the relative velocity between the solid phases.

Figures 4.30 and 4.31 present the time-averaged contribution of drag, collisions and gravity in the momentum equations of each solid phase. The sum of those three contributions is plotted, representing the kinetic stress contribution.
Figure 4.30 shows that for all cases, **the interclass collisions slow down the small sand particles**. For the densest cases, the collision contribution is as important as the gravity contribution.
In the centre of the riser, the sum of all three contributions is homogeneous, but greater than zero. Near the walls this sum is lower than zero. It shows that the kinetic stress is not negligible, especially in the near wall zone.

Figure 4.31 shows that for all cases, the collision contribution is about three times the drag contribution and that **the interclass collisions accelerates the large sand particles**. For the large sand particles, the stress tensor is also very important near the wall. It is also important regarding the drag force in the center of the bed. For the 29% case, the stress tensor contribution is as important as the collision contribution in the zone located between -0.4 and 0.4.

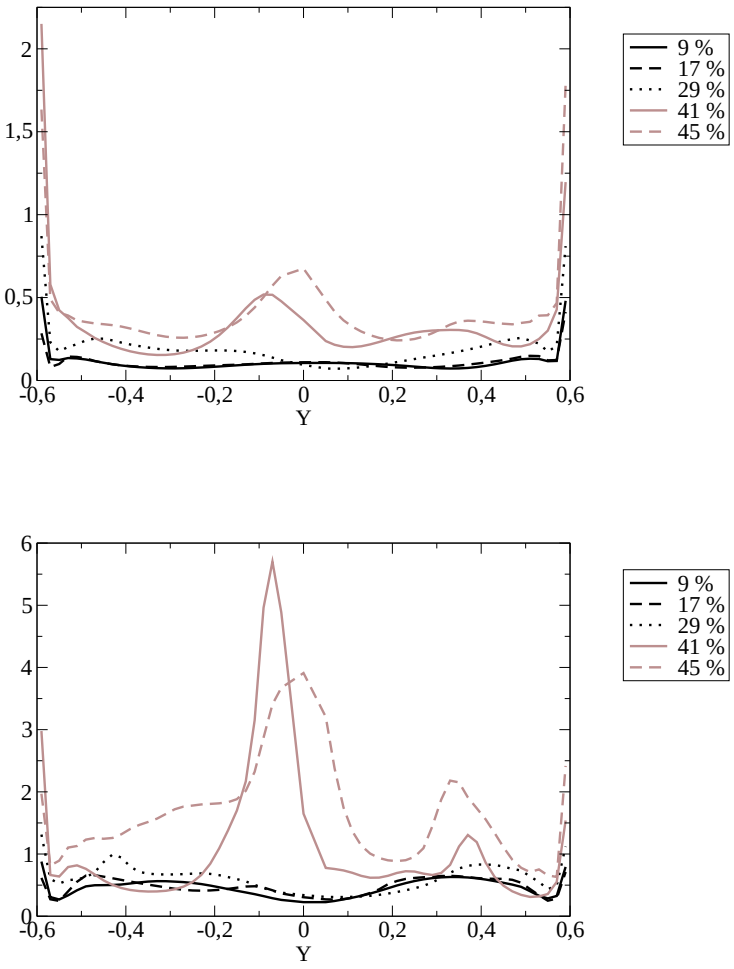

Figure 4.27: Time-averaged variance of solid volume fraction normalized by the time-averaged solid volume fraction: $\frac{<\alpha_p'^2>}{<\alpha_p^2>}$ for small sand (top), large sand (left) along the radial direction

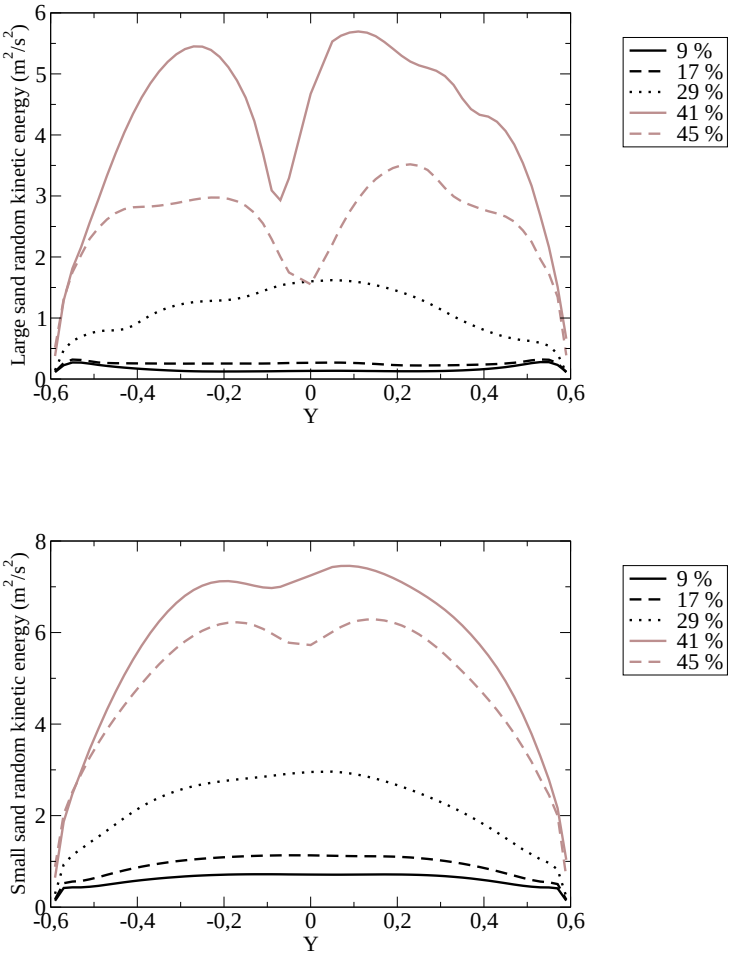

Figure 4.28: Time-averaged radial profile of kinetic agitation of large (top) and small (bottom) particles at X=0

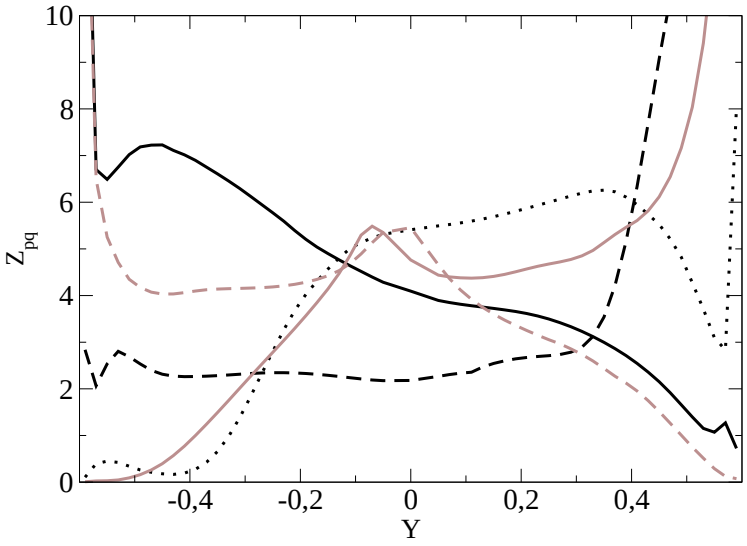

Figure 4.29: Instantaneous radial profile of Z_{pq} at X=0

Figures 4.32 and 4.33 show that every contribution in the momentum equation of the large sand particles increases when the fraction of large particles increases: from 9% to 29% it increases near the walls. For denser cases, those contributions increase in the center of the bed, and stabilize near the walls.

Figure 4.34 shows that **increasing the mass of large particles in the domain significantly increases the drag contribution in small particles momentum equation**. There is a competition between collisions that slow down the small particles and drag that accelerates it. When the fraction of large particles increases, both collisions and drag contributions get more important.

Figures 4.35 and 4.36 show the time-averaged relative velocity between phases at y=0.

Increasing the fraction of large particles in the domain increases the relative velocity between both solid phases with the gas phase near the wall. In the centre of the bed, the maximum relative velocity between gas and particles is found for the 41 % case.

The maximum relative velocity between both particle species in the centre of the bed is also found for the 41 % case (cf. Figure 4.36). This might be due to the fact that the fraction of small particles in the center of the bed increases between the 41% and the 45% case.

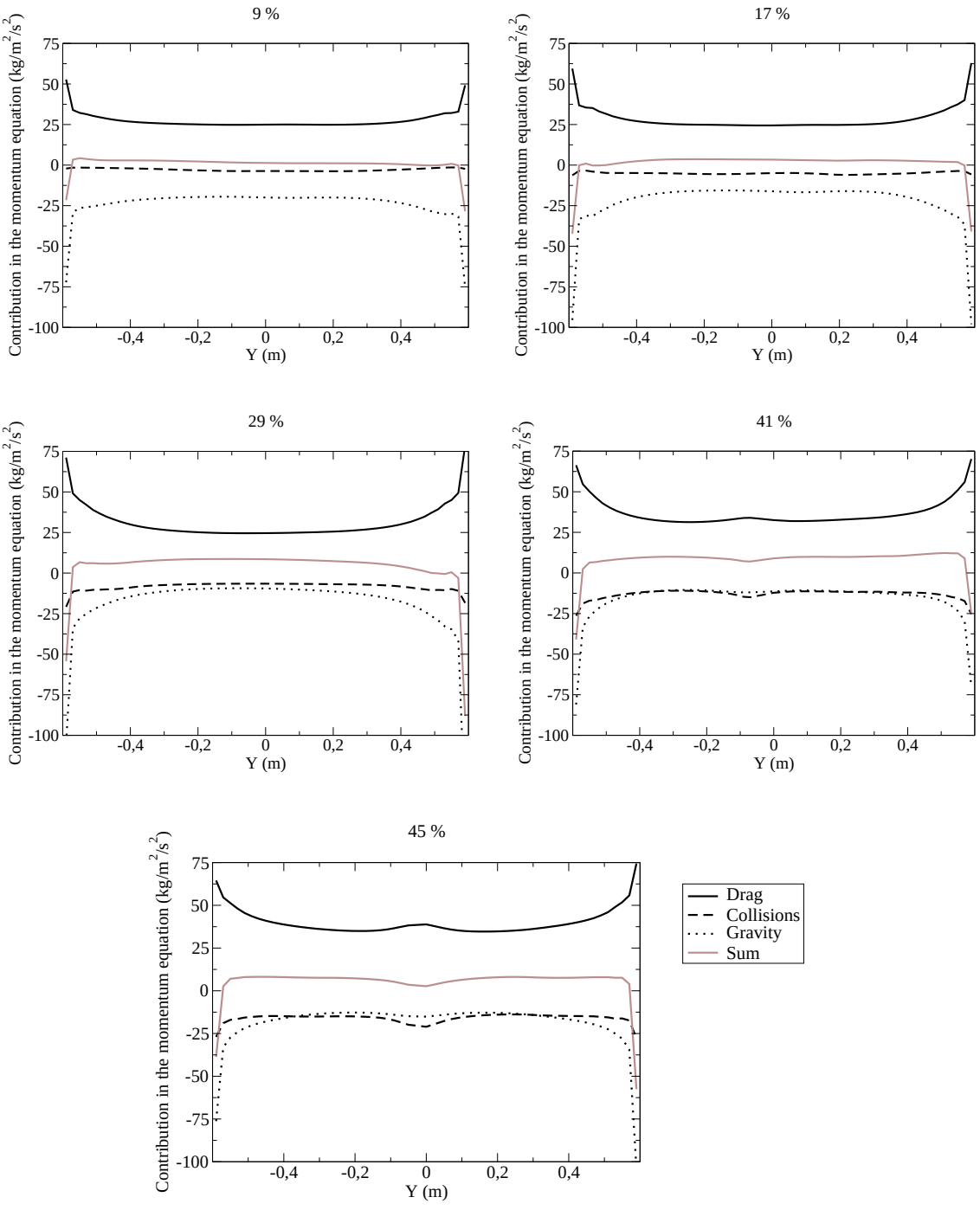

Figure 4.30: Time-averaged radial profiles of the main contributions in the momentum equation of small particles for various mass of large sand in the domain

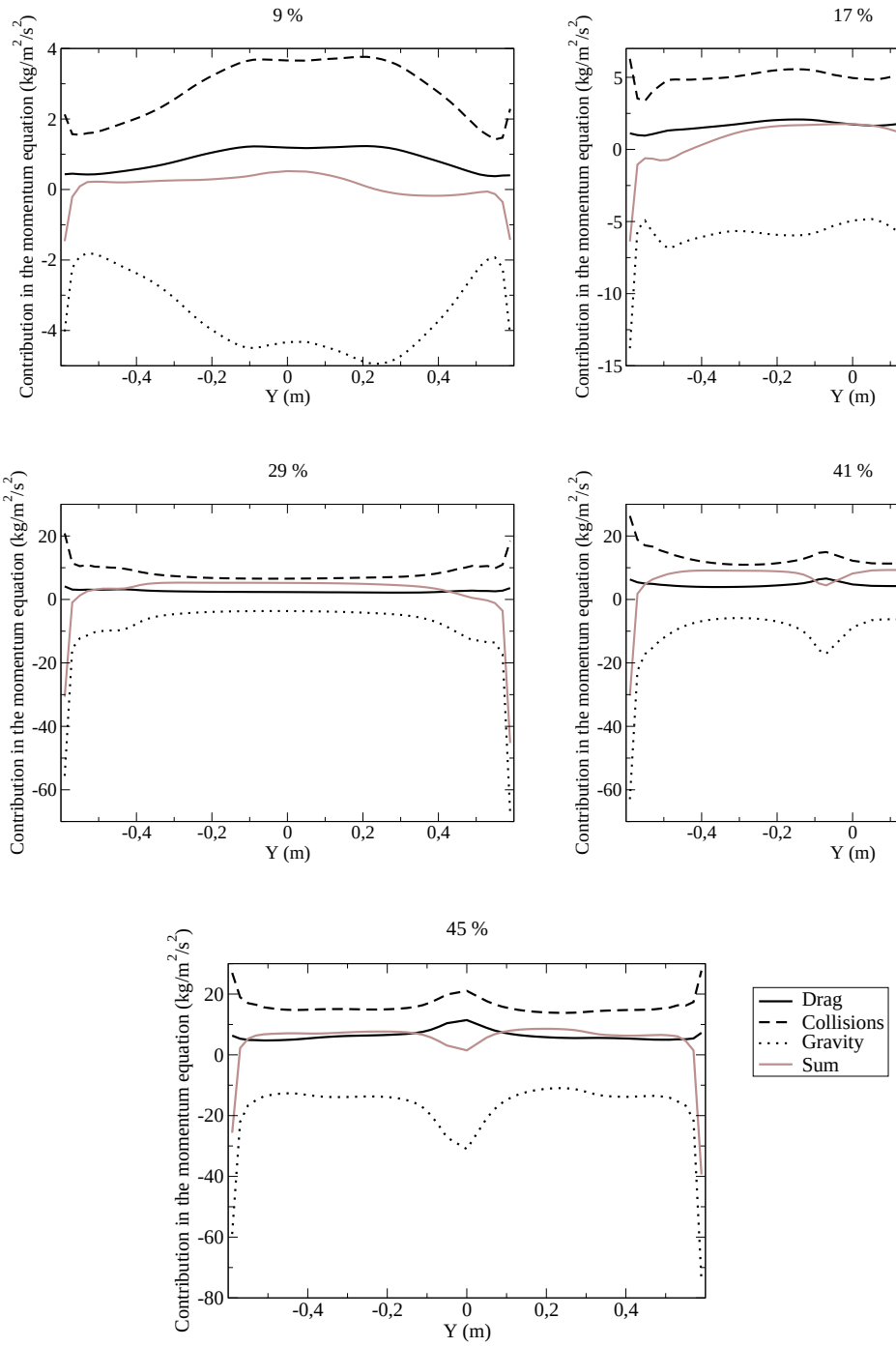

Figure 4.31: Time-averaged radial profiles of the main contributions in the momentum equation of large particles for various mass of large sand in the domain

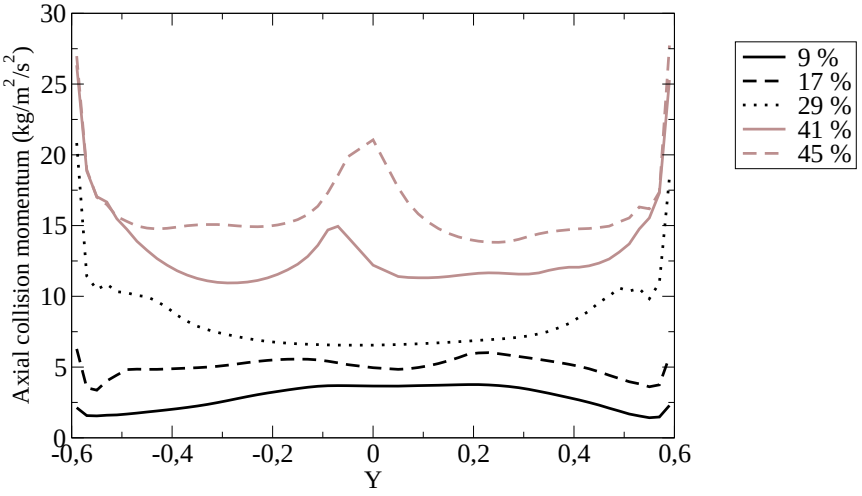

Figure 4.32: Time-averaged radial profile of the collision contribution in 1300 μm particles momentum equation at X=0

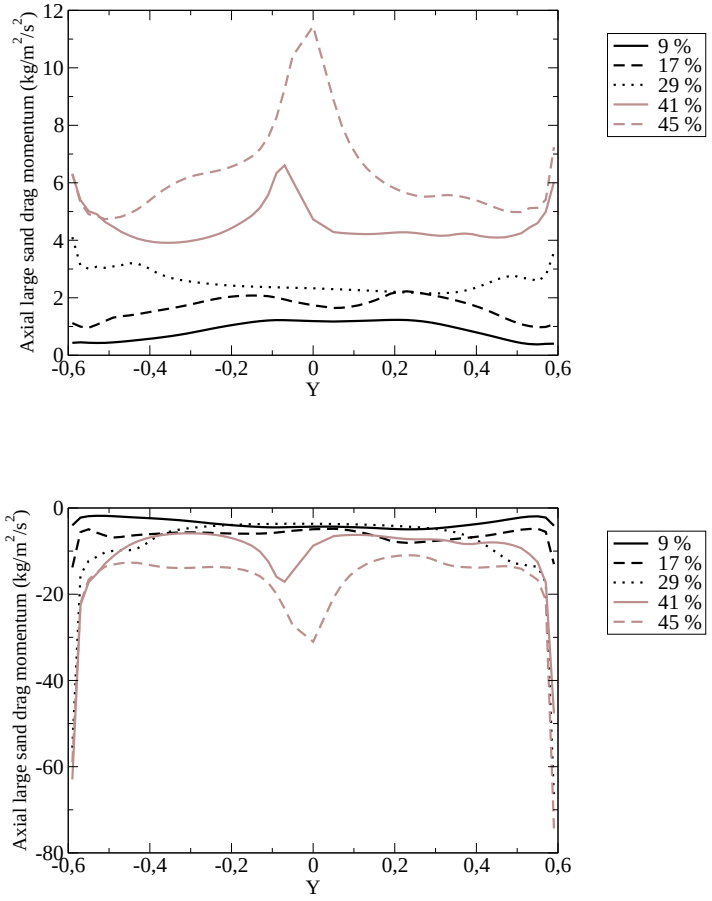

Figure 4.33: Time-averaged radial profile of the drag (top) and the gravity (bottom) contribution in 1300 μm particles momentum equation at X=0

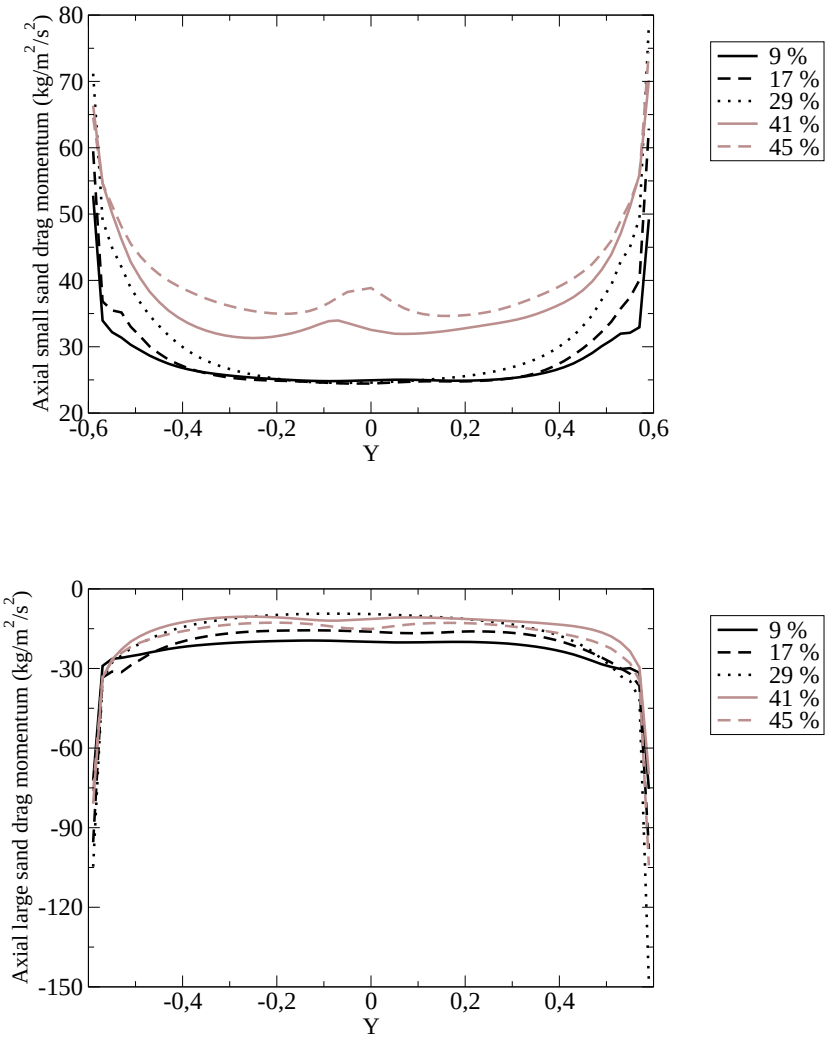

Figure 4.34: Time-averaged radial profile of the drag (top) and gravity (bottom) contribution in 260 μm particles momentum equation at X=0

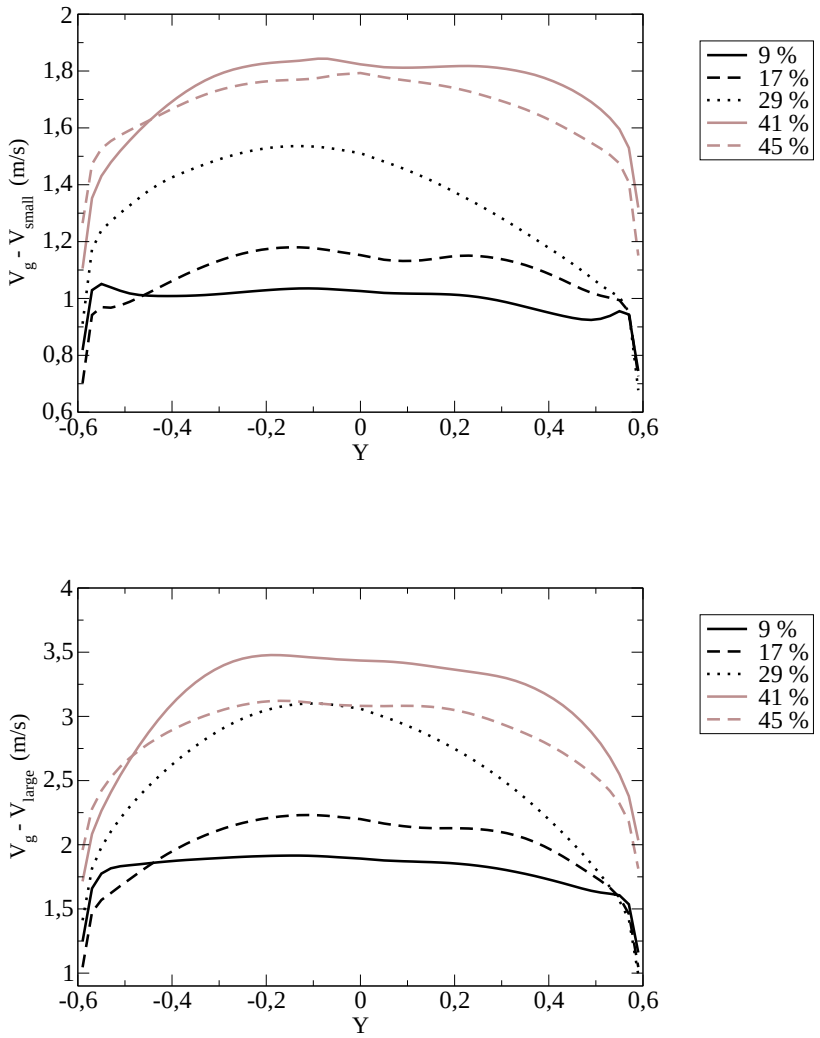

Figure 4.35: Time-averaged radial profile of $(V_g - V_{small})$ (top) and $(V_g - V_{large})$ (bottom) at X=0

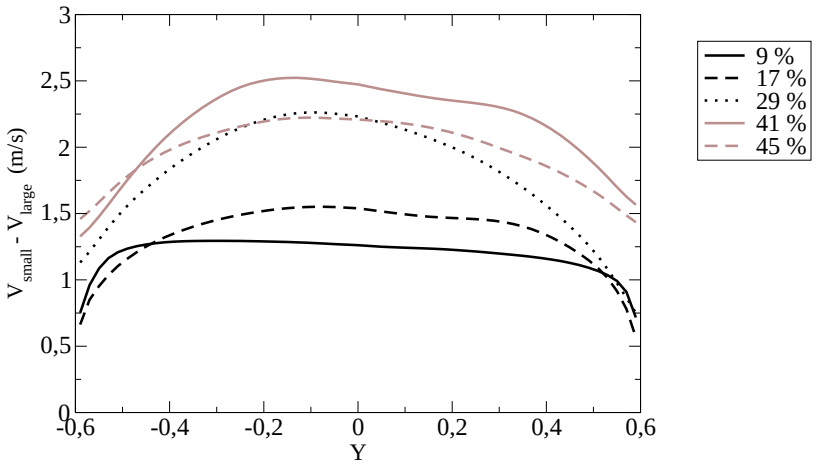

Figure 4.36: Time-averaged radial profile of $(V_{small} - V_{large})$ at X=0

Figure 4.37 shows that for the large particles, in all the periodic simulations, the absolute value of each contribution increases with the fraction of 1.3 *mm* particles. Figure 4.38 shows that the ratio between collisions and drag is almost constant when the fraction of large particles increases: the collision contribution is always between 3 and 3.5 times higher than the drag contribution. As expected, the sum of those three contributions is equal to zero.

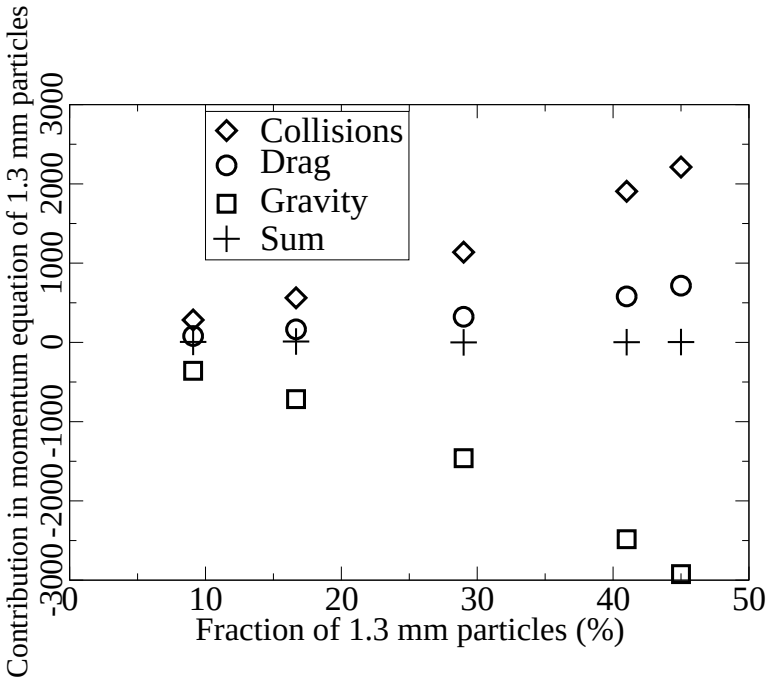

Figure 4.37: Domain and time-averaged contribution of gravity, drag and collisions in the momentum equation of the 1.3 *mm* particle phase

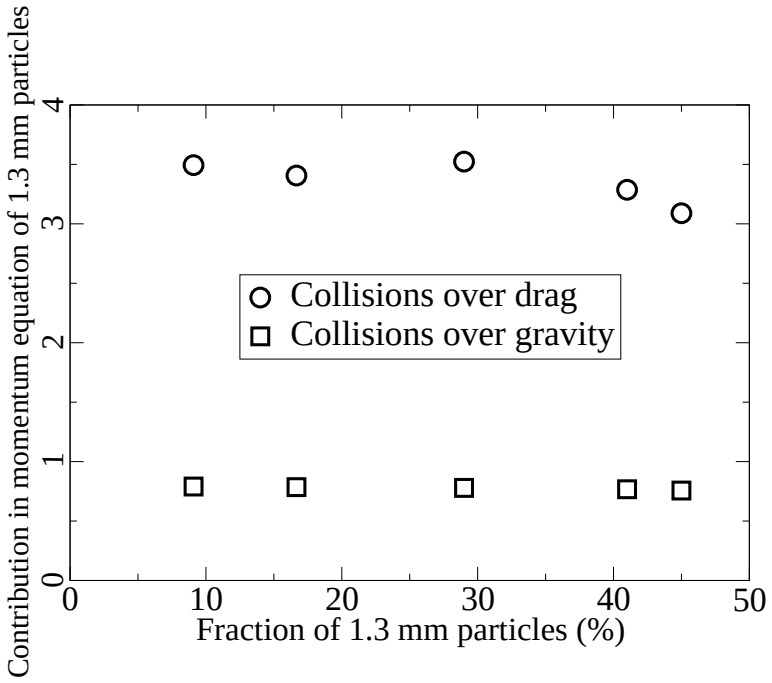

Figure 4.38: Domain and time-averaged contribution of gravity, drag and collisions in the momentum equation of the 1.3 mm particle phase

Figure 4.39 shows that for small particles, the absolute values of both drag and collision contributions are increasing. The gravity contribution remains constant while the fraction of 260 μm particles remains constant. As expected, the sum of those three contributions is equal to zero.

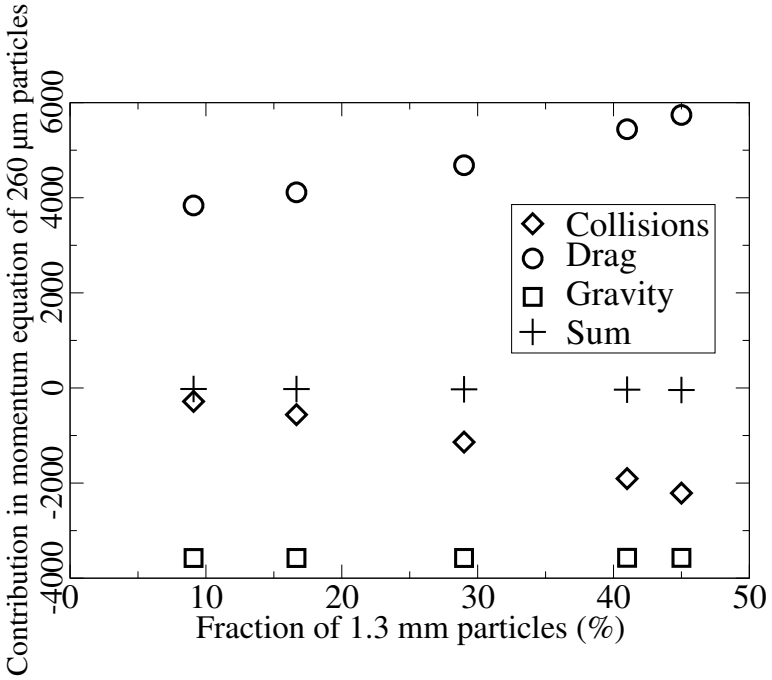

Figure 4.39: Domain and time-averaged contribution of gravity, drag and collisions in the momentum equation of the 260 μm particle phase

Figure 4.40 shows that the characteristic collision times are both decreasing with the increase in the fraction of large particles: the more particles there are in the domain, the less time there is between a collision of one class with another. If there is a lot of small particles and a few large ones, a given large particle collides with any small particle more often than a given small particle collides with any large particle. The ratio between τ_{23}^c and τ_{32}^c decreases when the fraction of large particles increases in the domain.

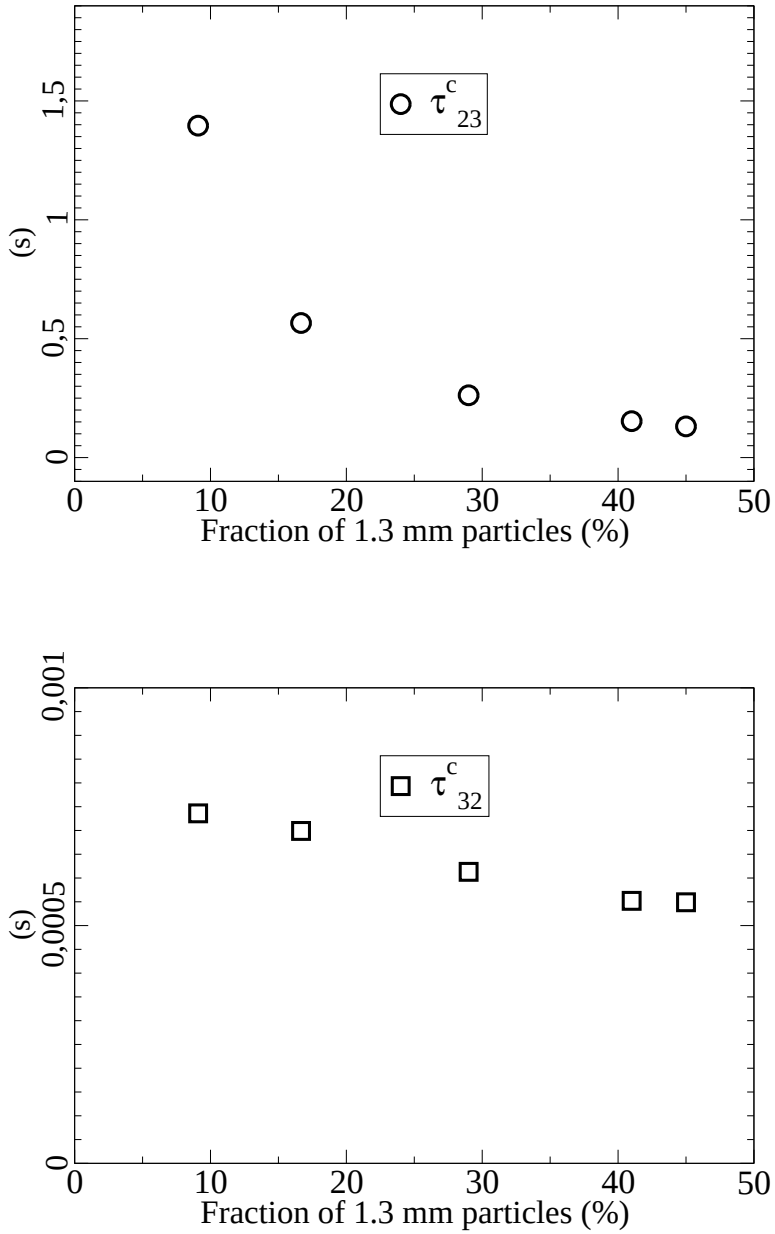

Figure 4.40: Domain and time-averaged characteristic collision time between different particle phases

Comparing periodic simulations and Fabre experiments

All the previous post-processings have been performed without any rescaling due to the periodic modeling. Indeed, at each time-step for each simulation, we imposed $\sum_{k=1}^{n} \alpha_k \rho_k W_k = 0$. Then, if we increase the α_{solid}, the gas phase axial velocity will increase to keep the balance. It is therefore useful to choose a reference to post-process the velocity and circulating mass flux of the periodic simulations. In order to compare our results with the experiment performed by Fabre in CERCHAR (cf. Figure 4.4), we chose the velocity of gas ($\overline{V_g^{Fabre}}$) equal to 4 m/s as the reference. To do so, the time and volume-averaged gas velocity in the periodic simulation is calculated: $V_g^{calc} = \widetilde{V_g} = \dfrac{\overline{\alpha_g \rho_g V_g}}{\overline{\alpha_g \rho_g}}$.
Then, a translation velocity V^{trans} is defined:

$$\overline{\alpha_g \rho_g} \overline{V_g^{Fabre}} = \overline{\alpha_g \rho_g V_g} + \overline{\alpha_g \rho_g} \overline{V^{trans}} \tag{4.12}$$

Then,

$$\overline{V^{trans}} = \underbrace{\overline{V_g^{Fabre}}}_{4\ m/s} - \widetilde{V_g} \tag{4.13}$$

Knowing $\overline{V^{trans}}$, we estimate the axial velocity of the solid phases corresponding to Fabre case:

$$\overline{\alpha_p \rho_p} \overline{V_p^{Fabre}} = \overline{\alpha_p \rho_p V_p} + \overline{\alpha_p \rho_p} \overline{V^{trans}} \tag{4.14}$$

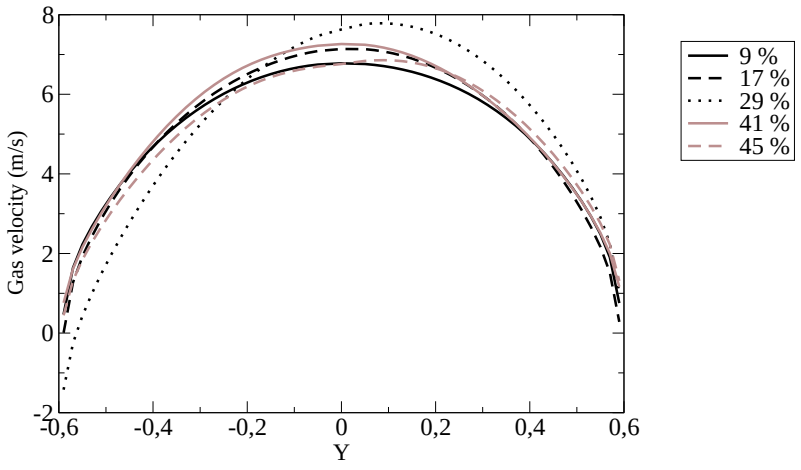

Figure 4.41: Time-averaged radial profile of the modified gas axial velocity at X=0

The gas velocity profile is parabolic and comparable for all cases (cf. Figure 4.41). The maximum gas velocity is in the centre of the bed. It goes from 6 to 7 m/s depending on the case. Nevertheless, in all cases, it remains below the terminal settling velocity of the large sand particles.

Figure 4.42 shows that the velocity profiles of both species have similar shape: parabolic for a fraction of large sand from 9% to 29%. For the denser cases, the profile tends to flatten. A local minimum is found in the centre of the bed for the larger

fraction of solid in the bed. It is consistent with Mathiesen et al. (2000a) experiment. It consisted in an experimental study of a binary mixture of particles of same density and a mean diameter of respectively 120 and 185 μm. There was 50% of each class in the bed. It was found that in the upper region of the riser, the velocity profiles of the particles tend to flatten, and even to have a local minimum in the centre of the bed.

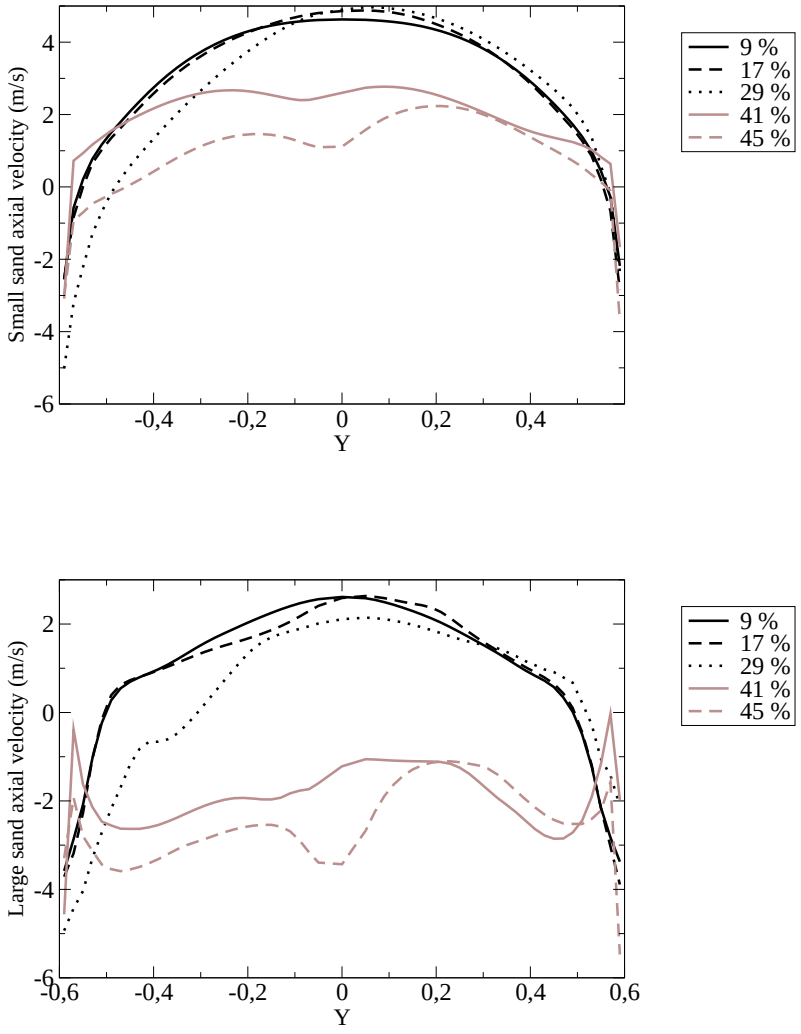

Figure 4.42: Time-averaged radial profile of the modified small (top) and large (bottom) particles axial velocity at X=0

Figure 4.43 shows that, for small fractions of large sand in the bed, the shape of radial profiles of all axial velocity phases are quasi parabolic. The more large particles in the domain, the more the shape of the profile of the solid phases gets modified. The small sand profiles tend to get homogeneous and the large sand profiles come from parabolic to homogeneous everywhere but at 0.55 and -0.55 where there is a maximum. This trend to become homogeneous is due to the influence of the non negligible kinetic stresses that tend to exchange momentum laterally (cf. Figures 4.30 and 4.31).

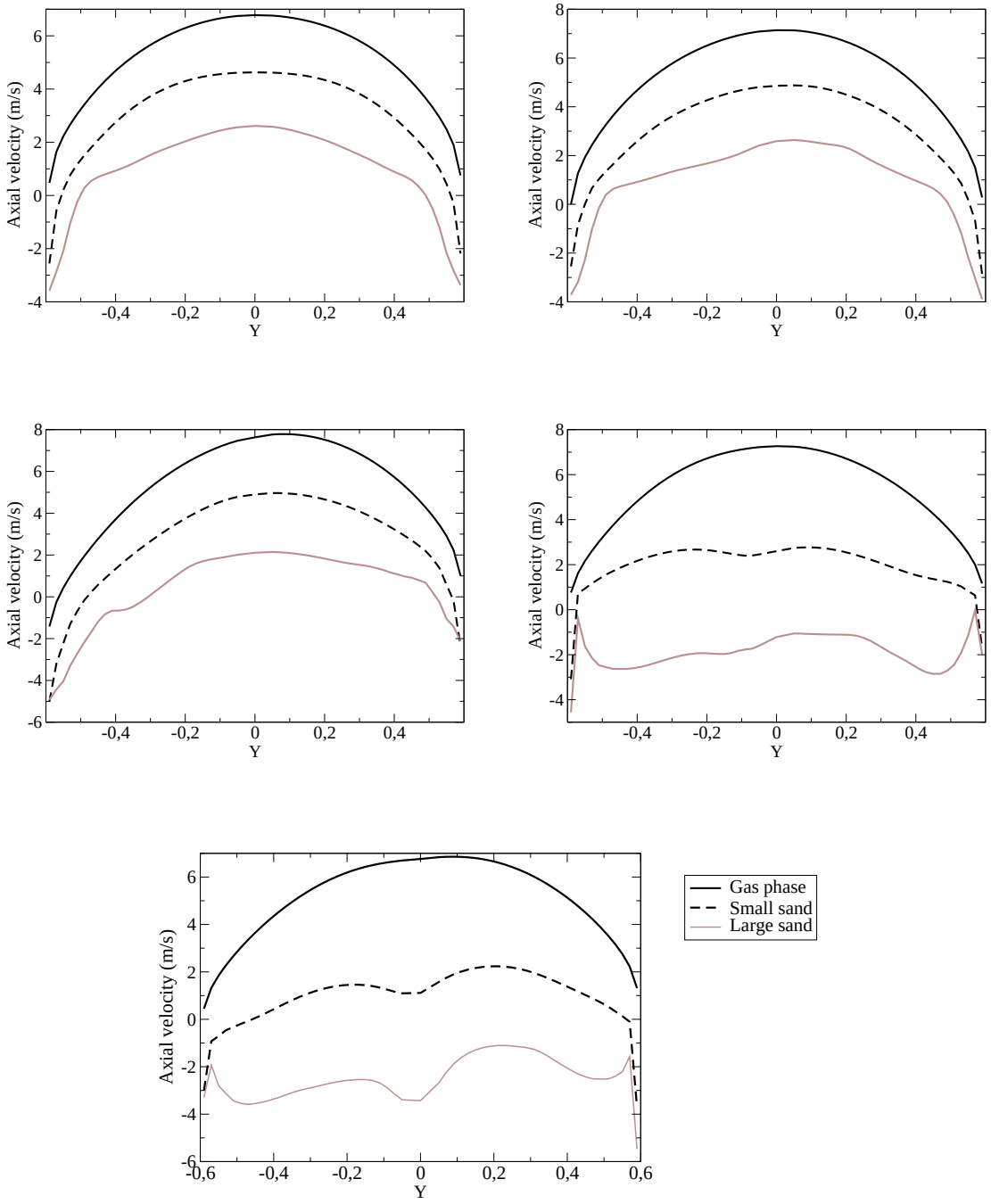

Figure 4.43: Time-averaged radial profile of the modified axial velocities of all phases at X=0 with a fraction of large sand varying from 9% to 45%

On Figure 4.44, the net flux of small particles decreases in the center of the riser when the fraction of large particle increases in the domain. **The maximum net flux of small particles is for the 9% case**. It reaches 18 $kg/m^2/s$. A large amount of small sand particles falls along the wall.

Figure 4.45 shows that **the maximum net flux of large particles is for the 17% case**: it reaches 6 $kg/m^2/s$. The net flux is negative near the wall and decreases when the fraction of large particles increases.

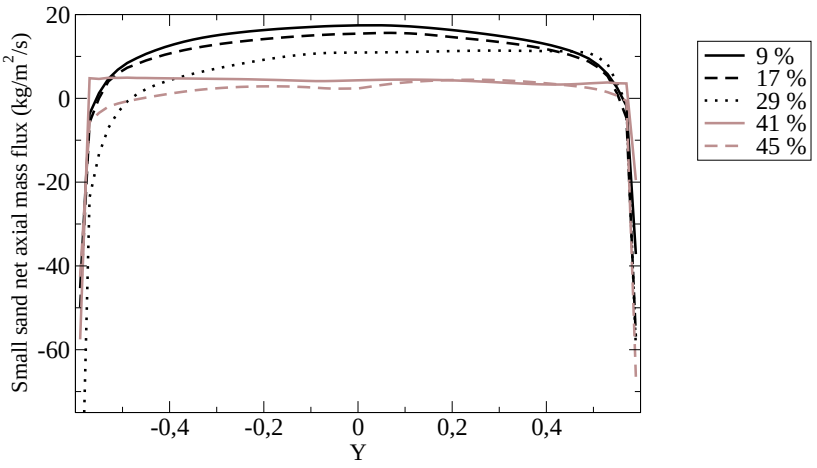

Figure 4.44: Time-averaged radial profile of the modified circulating flux of small particles at X=0

NEPTUNE_CFD V1.08@Tlse only predicted a circulation of large particles for the 9% case (cf. Figure 4.46). The circulation of small particles decreases with the increase in the fraction of large sand: over 17% of large particles in the domain, no circulation of solid is predicted. This result differs with the result of Fabre's experiment.
The circulating mass flux of solid in Fabre's experiment was imposed in all simulation to 5.55 $kg/m/s$. Our periodic simulations were based on the 100 kg of large sand case corresponding to 9% of large particles in the domain. For this case (cf. Table 4.12), experiment and simulation fit well. **By imposing only the fraction of solid in the domain and the fluidization gas velocity, simulations in a periodic box can predict the right circulating mass flux of solid and its repartition.**

Table 4.12: Experimental and simulation results for the 9% case

Circulating mass flux	Total	Small sand	Large sand	Fraction of large sand
Fabre	5.55 $kg/m^2/s$	5.328 $kg/m^2/s$	0.222 $kg/m^2/s$	4%
$NEPTUNE\_CFD$	5.78 $kg/m^2/s$	5.46 $kg/m^2/s$	0.32 $kg/m^2/s$	5.5%

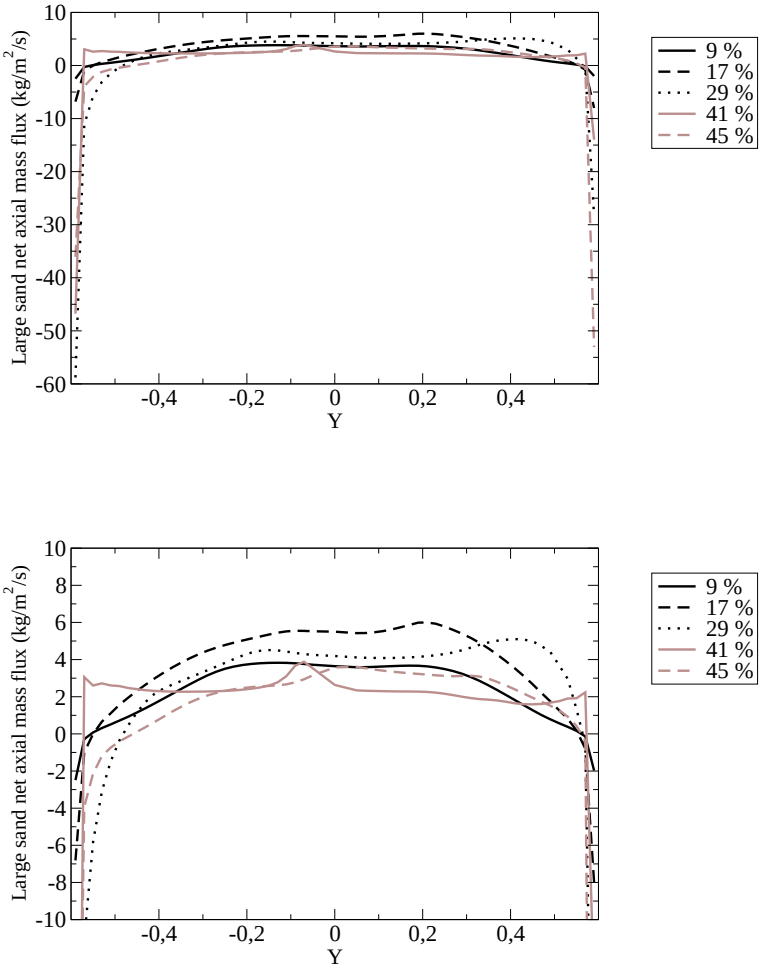

Figure 4.45: Time-averaged radial profile of the modified circulating flux of large particles at X=0

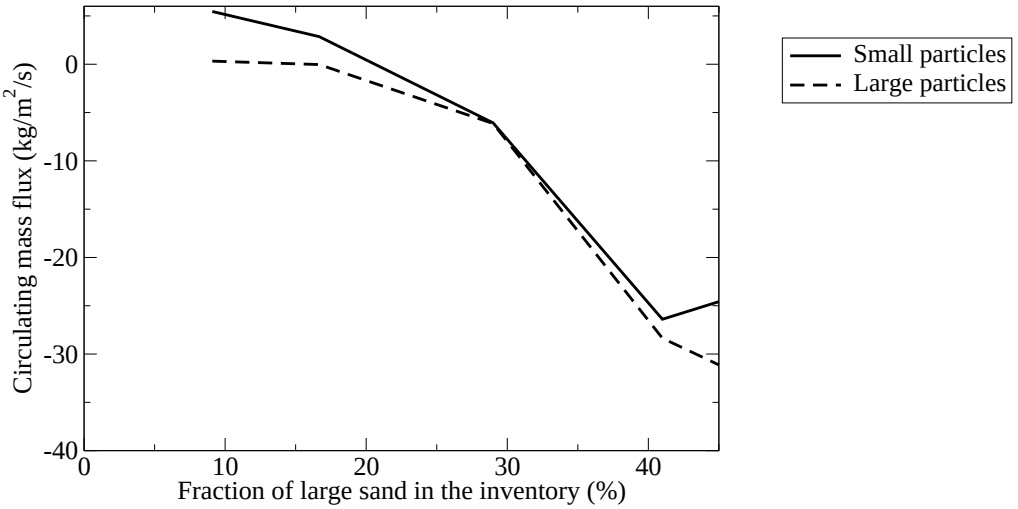

Figure 4.46: Time and volume-averaged circulating mass flux of each particle species

The other operating points can not be directly compared to the experimental results knowing that we did not impose the same boundary conditions. In Figure 4.46, the circulating mass flux of small particles is decreasing quicker than the circulating mass flux of large particles from 9% to 29%. Then, this trend reversed and the difference between both circulating mass flux keeps increasing.

Influence of the polydisperse model

In order to understand the influence of polydispersion on the gas flow, we performed another simulation without activating the polysdisperse model. The operating point is the 9% case:

$$\alpha_{260\ \mu m} = 2.15 \cdot 10^{-3} \tag{4.15}$$

$$\alpha_{1.3\ mm} = 2.15 \cdot 10^{-4} \tag{4.16}$$

Table 4.13: Results

Polydisperse model	Drag* Large	Drag* Small	Circulating flux Large	Circulating flux small
	-	-	kg/s	
ON	-0.226	-1.073	0.32	5.46
OFF	-0.995	-1.003	-2.6	7.54

* Normalized by the gravity contribution

Table 4.13 presents the time and space-averaged contributions of the drag and gravity force in both simulations. As the gravity force remains equal for each phase in both simulations, we normalized each drag contribution by the corresponding gravity.

This study shows that modeling the collisions has an effect on the fluid phase. Deactivating the interclass collisions modeling multiplies the drag force on large particles by a factor 4. It is due to an increase in the slipping velocity between the gas phase and the particle phase.
For the small particles, deactivating the polydisperse model slightly decreases the drag force on small particles.
If we use the previous post-processing method, we can estimate a circulating mass flux of each solid by imposing the fluidization velocity at 4 m/s. Our simulations show that without the polydisperse model, there is no circulation of large particles through the bed. Moreover, as expected, activating the collisions slightly decreases the circulation of small particles.

Figure 4.47 shows that activating the polydisperse model does not significantly change the shape of the profile of the volume fraction of small particles. It slightly decreases the fraction of small sand in the centre of the riser and slightly increases the fraction of small particles near the walls. Without interclass collisions, the fraction of small particle slightly increases from the centre of the bed to the wall (from $2 \cdot 10^{-4}$ to $2.75 \cdot 10^{-4}$) (cf. Figure 4.47). Taking into account the momentum and kinetic agitation exchanges between solid phases changes the radial profile of the large particles volume fraction. It increases in the centre of the bed from from $2 \cdot 10^{-4}$ to $3 \cdot 10^{-4}$. Then, it decreases between 0.55 and 0.3 m. It finally increases significantly in the near wall zone.

Then, as showed by Figure 4.48, without interclass collisions, the repartition of both solid is homogeneous everywhere but in the near wall area. **The interclass collisions tend to increase the segregation between species.** The momentum and/or the kinetic agitation exchanges between the two solid species make large particles go from the near wall region to the wall and the center of the bed.

The circulating mass flux of small particles is not significantly modified by the interclass collisions. On the other hand, **the momentum and kinetic energy exchange between particle phases increases the net flux of large particle in the centre of the bed**. There is an ascendant mass flux of large particles in the centre of the bed.

Figure 4.50 shows that **the collisions dissipate the particle agitation in the large particle equation while the collisions produce particle agitation for small particles**.

Figure 4.51 shows that the radial profile of the gas phase and the small sand velocities are not significantly changed by the interclass collisions. The large sand velocity profile goes from homogeneous (without interclass collisions) to quasi-parabolic (with collisions).

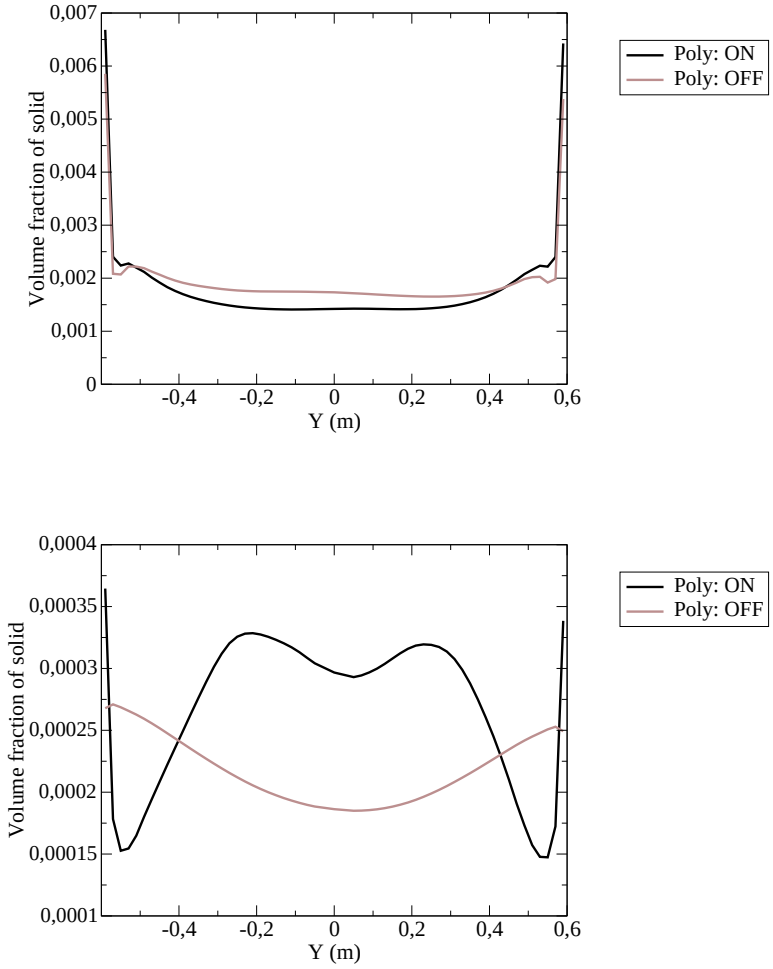

Figure 4.47: Time-averaged radial profile of the volume fraction of small (top) and large (bottom) particles at X=0

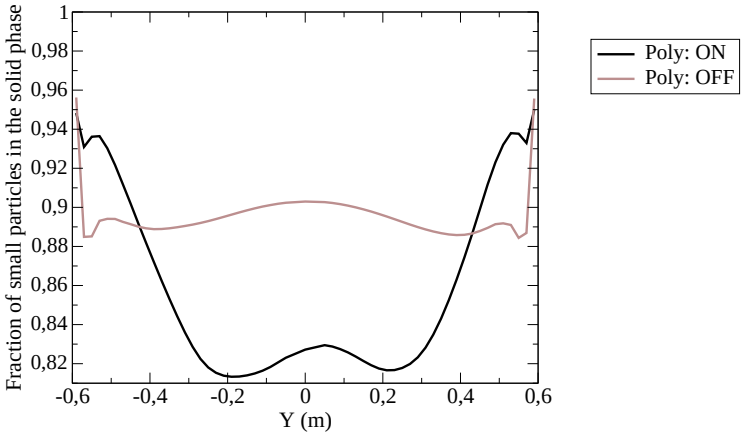

Figure 4.48: Time-averaged radial profile of the fraction of small particles in the solid phase at X=0

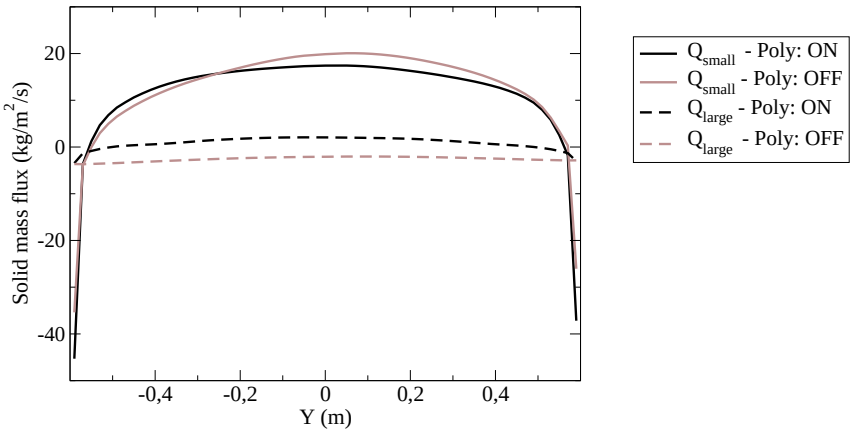

Figure 4.49: Time-averaged radial profile of the modified circulating flux of large particles at X=0

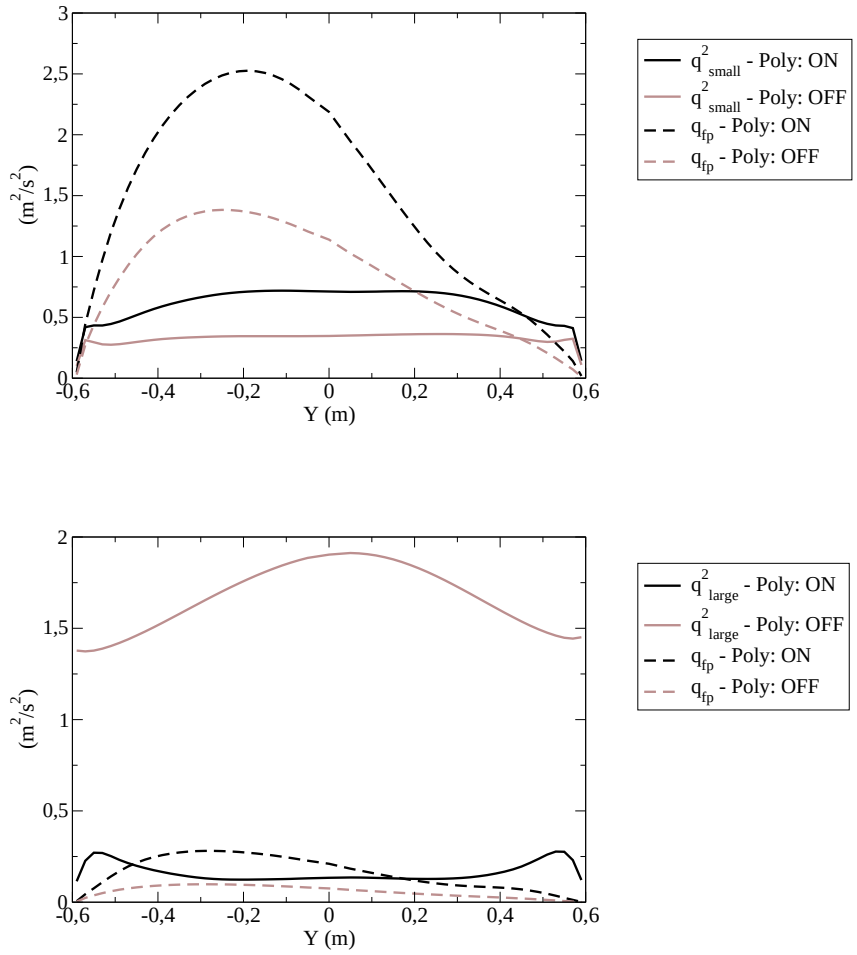

Figure 4.50: Time-averaged radial profile of the random kinetic energy of small (top) and large (bottom) particles and fluid particle velocity correlation at X=0

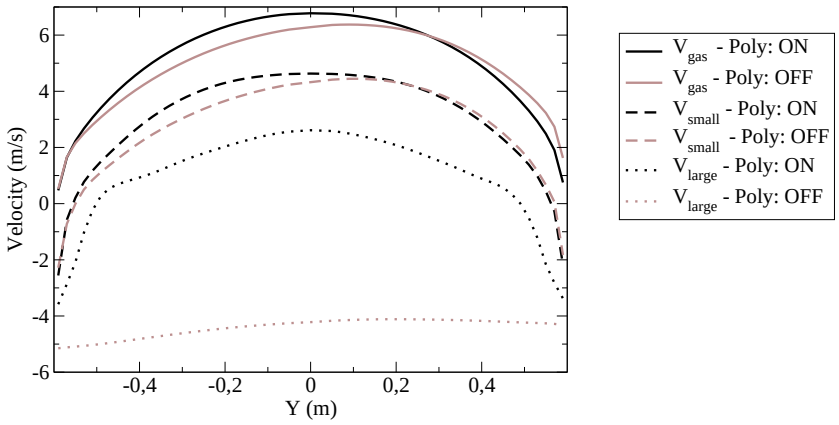

Figure 4.51: Time-averaged radial profile of the modified velocity of all phases at X=0

4.3.4 Conclusion

The first periodic simulations based on Gourdel's work showed that both the polydisperse model and the periodic source term was correctly implemented in NEPTUNE_CFD V1.08@Tlse. It also showed that the dependency of the hydrodynamics of a binary mixture of particles on the fraction of one particle phase can be predicted by NEPTUNE_CFD V1.08@Tlse.
The periodic simulation of the upper region of Fabre's bi-solid CFB experiments highlighted the specificity of this binary mixture hydrodynamics. The post-processing of the periodic simulation showed that:

- The radial segregation between species strongly depends on the fraction of large sand in the domain.
- The interclass collisions slow down the small sand particles and accelerate the large ones.
- Increasing the mass of large particles in the domain significantly increases the drag contribution in small particles momentum equation.
- The collision contribution in the large particle momentum equation is three times more important than the drag contribution.
- Around 41% of large particles in the domain, there is a change in the hydrodynamics: the kinetic stresses in the large particles momentum equation became as important as drag and a local maximum of the fraction of large particles appears in the center of the bed, resulting in a change in the radial segregation profiles.

Then, after imposing the gas velocity imposed by Fabre in its experiment in every periodic simulation, we were able to quantitatively compare the predicted circulating mass flux, velocities... It showed that:

- Imposing only the fraction of solid in the domain (9%) and the fluidization gas velocity (4 m/s) in a periodic simulation is sufficient to predict quite accurately the circulating mass flux of solid and its repartition.

- The radial profile of the circulating mass flux showed that there is a maximum in the centre of the bed for the 17% case.
- For all cases, there is a positive contribution of the circulating mass flux for both solids.

In the last section of this chapter, we investigated the specific influence of the interclass collisions term in the momentum and kinetic agitation of particles equations. It turns out that the interclass collisions:

- increase the radial segregation between species.
- increase the circulating mass flux in the center of the bed.
- dissipate the particle agitation of large particles and produce agitation for small particles.
- slightly increase the drag contribution in the momentum equation of small particles and severely decrease the drag on large particles.

It also show that the circulation of large particles in the 9% case was due to the modeling of the interclass collisions.

This study pointed out that the collisions are responsible for the circulation of large particles in the bed. Then, it would be necessary to perform a mesh dependence study on those cases, in order to determine if a sub-grid model for the momentum and particle kinetic energy exchange is necessary for the modeling of pilot scale extreme CFBs.

Résumé des conclusions et perspectives

L'objectif de ce travail était de valider l'approche Euler-Euler sur des configurations de lits fluidisés circulants polysolides non réactives à l'échelle du pilote industriel afin de participer à la définition d'un point de fonctionnement à chaud du pilote CLC en construction à Darmstadt (Allemagne). Cette étude est complétée par une étude locale de l'écoulement polysolide afin de comprendre l'influence des collisions interparticulaires sur l'écoulement.

Le troisième chapitre valide l'approche Euler-Euler sur des expériences menées par Alstom à l'Université Technologique de Compiègne (France). Nous avons montré que le code NEPTUNE_CFD V1.08@Tlse pouvait prédire le flux circulant de solide ainsi que le profil de pression dans le lit pour différentes géométries et différentes caractéristiques de particules. Comme attendu, nous avons retrouvé que diminuer la taille des particules du LFC augmentait la circulation de solide dans le lit. Une étude de l'influence de la position des injecteurs secondaires a montré que si ceux-ci étaient placés trop haut, ils empêchaient les particules de s'élever. Un cas de LFC monosolide polydisperse a été simulé. Il a montré qu'il est essentiel de prendre en compte la polydispersion éventuelle au sein d'un LFC afin de prédire correctement son hydrodynamique.
Après avoir validé notre modélisation sur une configuration monosolide, des expériences bisolides représentatives de configurations de type CLC ont permis de valider des simulations de LFC bisolides non réactives. Nous avons ainsi caractérisé l'influence de l'ajout de fines dans un lit de particules de grandes tailles et lourdes: ajouter des fines (2% en masse) permet d'augmenter sensiblement la circulation de grandes particules dans le lit. Ainsi, ajouter des fines diminue la fraction volumique de solide dans la zone dense du lit et provoque des collisions qui aident les grosses particules à s'envoler et qui ralentissent les fines. Les termes d'échanges de quantité de mouvement entre classes de particules ne sont pas négligeables devant le poids et la trainée, et ce même dans la zone diluée du riser. Nous avons montré que dans les cas étudiés, les flux circulants de chaque solide augmentaient linéairement avec la fraction de fines dans l'inventaire du lit.

Dans le Chapitre 4, on s'intéresse à l'expérience menée par Fabre au CERCHAR: un LFC bisolide où un mélange de deux sables de même densité mais de diamètres très différents (1300 μm et 260 μm) sont fluidisés par un gaz dont la vitesse dans la section principale est deux fois inférieures à la vitese terminale de chute des particules de 1300 μm. Fabre a montré l'existence d'un flux circulant de grosses particules pouvant atteindre 15% du flux total pour certaines fractions de sable 1300 μm dans l'installation. Notre simulation 3D bi-solide prédit un flux circulant de particules 1300 μm. Néanmoins, celui-ci est sous-estimé comparé aux résultats de l'expérience. Le flux circulant de par-

ticules 1300 μm oscillant autour d'une valeur constante après 500 secondes physiques, nous avons tenté de déterminer si cette sous-estimation pouvait être dûe à des effets de sous-maille. Une étude comparative des résultats donnés par des simulations comparables sur des maillages de plus en plus raffinés a montré que plus le maillage était raffiné, plus le flux circulant de solide prédit était grand, et plus l'inventaire de solide diminuait: il y a un effet des structures à petite échelle sur l'hydrodynamique du lit. Malheureusement, en raison du coût de ces simulations, nous n'avons pu atteindre un régime stationnaire.
Ainsi, afin d'étudier localement les mécanismes en jeu dans la partie haute du LFC du CERCHAR, nous avons réalisé des simulations de la partie haute du riser sur un domaine périodique. 5 simulations ont été réalisées permettant de faire varier la fraction de sable 1300 μm dans le domaine. Nous avons montré que la circulation de sable 1300 μm est dûe à un échange de quantité de mouvement entre les différentes classes de solides au cours des collisions qui accélère le sable 1300 μm et ralentit le sable 260 μm. La contribution des collisions dans l'équation de quantité de mouvement des particules de 1300 μm est trois fois supérieure à celle de la trainée. De plus, augmenter la fraction de sable 1300 μm tend à augmenter la ségrégation radiale entre espèces. Nous avons montré qu'en imposant uniquement la vitesse de fluidisation et la fraction de chaque solide dans la partie haute, nous pouvions prédire correctement la circulation de solide à travers le lit.

Le dernier chapitre est une étude du Fuel Reactor: lit fluidisé circulant bisolide et réactif. Le Chapitre 3 a montré que l'approche Euler-Euler prédisait correctement l'hydrodynamique de tels lits fluidisés circulants bisolides en configuration froide non reactive. L'objectif de ce chapitre est d'étudier l'influence de la production locale de gaz sur l'hydrodynamique du LFC. Nous avons montré qu'une étude du type injection pariétale ne pouvait pas simuler les effets de la production locale de gaz. En vue de l'établissement d'un point de fonctionnement pour le pilote en construction à Darmstadt, nous avons réalisé des simulations 3D instationnaires réactives bisolides du Fuel Reactor. Nous avons montré que la position de l'injecteur de particule permettait de contrôler l'inventaire de solide dans le lit. La connaissance du diamètre moyen des particules de charbon en régime stationnaire s'est révélé être un paramètre essentiel pour définir un point de fonctionnement stable.

Ce travail montre que l'approche Euler-Euler prédit correctement l'hydrodynamique complexe de LFC polysolides. Nous avons montré que dans des cas extrêmes, l'influence des petites structures n'était pas négligeable: il sera donc essentiel d'utiliser les modèles de sous-mailles pour modéliser la trainée des particules dans des cas où le maillage est peu raffiné. Sur l'expérience du CERCHAR, il est possible que les hétérogénéités locales aient également une influence sur le calcul des termes d'échanges de qdm ou d'énergie cinétique entre espèces de solides durant les collisions: une étude de convergence en maillage sur des simulations périodiques seront alors nécessaires pour proposer une modelisation des effets de sous-maille sur la prédiction des collisions.
Les simulations réactives ont montré l'importance du diamètre des particules de charbon sur la définition d'un point de fonctionnement stable. A l'avenir, à l'aide de la distribution de taille du charbon frais et de la fréquence de coupure des cyclones, il sera intéressant de réaliser une simulation permettant de prédire le diamètre moyen des particules de charbon en régime stationnaire. Enfin, la comparaison des résultats des

simulations avec les expériences à venir permettra de valider l'influence de la production de gaz sur l'écoulement.

Conclusion

In this work, we performed 3D unsteady polysolid reactive simulations of pilot scale circulating fluidized beds using the Eulerian-Eulerian modeling. We were able to validate our modeling on monosolid (monodisperse and polydisperse) and polysolid experiments performed by Alstom at the Université Technologique de Compiègne (France). Some limitations have been found in the modeling of extreme polysolid cases (CERCHAR experiments) leading us to investigate the influence of the mesh size on the predicted hydrodynamics. Local studies of the effect of interclass collisions in such flows were performed. Finally, we performed 3D reactive studies in order to predict the influence of the local production of gas on the hydrodynamics of a bisolid flow inside a coal fired chemical looping pilot plant.

The third chapter validates the Eulerian-Eulerian modeling on experiments performed at the Université Technologique de Compiègne by Alstom. Some parametric studies based on a monosolid experiment were performed. As expected, we showed that decreasing the mean diameter of the particles significantly increases the circulation solid mass flux. It was also found that lowering the height of the secondary injectors increases the circulation of particles. It is due to the fact that when the secondary injectors are located over the dense part of the bed, they do not help particles to circulate. The last monosolid simulation showed the relevance to take into account the polydispersion of the solid phase in some cases. Indeed, we can underestimate the circulation of particles of a factor 3 by simplifying too much the discretization of the size distribution function of the particles.
Then, some polysolid experiments composed of more than 90% of large and heavy particles and between 2 and 10% of small and light particles were simulated. In those cases, the fluidization velocity wass greater than the terminal settling velocities of both particle classes. These conditions were chosen to be as close as possible to the expected characteristics of Coal and MeOx particles in CLC applications.
Experiments and simulations fitted well: NEPTUNE_CFD V1.08@Tlse can predict the hydrodynamics of a pilot scale polysolid circulating fluidized bed. Our study showed that

- increasing the inventory of small particles strongly decreases the averaged volume fraction of solid in the dense part of the bed.
- both large and small particles mass fluxes increase linearly with the increase of the fraction of small particles in the bed.
- adding small and light particles in a CFB of large and dense particles results in collisions that helps the large particles to circulate and that limits the circulation of small ones.

- the collisions between different classes are not negligible regarding gravity and drag, even in the dilute part of the riser.

- the momentum exchange due to collisions is mostly driven by the relative velocity between particles.

In Chapter 4, another polysolid CFB composed of 10% of large particles and 90% of small particles was studied. This case is extreme because the fluidization velocity is twice time lower than the terminal settling velocity of the large particles. It means that without small particles, no large particle would circulate.
The simulations of this experiment showed that NEPTUNE_CFD V1.08@Tlse can predict a circulation of large particles through the bed. Our simulation did not reach a steady state: we underestimate the circulation of large particles through the bed. Nevertheless, our predictions are closer to the experiment than Batrak's using *Saturne_Polyphasique@Tlse*. Recent studies showed that the small scale heterogeneities characteristic from CFBs might lead to a bad resolution of the drag force acting on particles. We decided then to study the influence of our mesh size on our simulation. We showed that there is a strong mesh dependence: the finer the mesh, the higher the predicted solid circulating mass flux gets. Unfortunately, due to the cost of those calculations, we did not reach the mesh independence.
In order to investigate the influence of those small particles on the circulation of the large particles, we performed Eulerian-Eulerian simulations in a periodic box of the established zone of the previous CFB. Five operating points were defined to study the influence of the fraction of large particles in the bed (from 9 to 45%) on the hydrodynamics of the CFB. We showed that:

- the circulation of large particles is due to the momentum exchange with small particles during collisions: the collision contribution is three times higher than the drag contribution in the range studied.

- the radial segregation between species strongly depends on the fraction of large particles in the domain. The interclass collisions increase the segregation between species.

- the interclass collisions slow down the small sand particles and accelerates the large ones.

- the drag contribution in small particles momentum equation significantly increases with the fraction of large particle in the bed.

The simulation of the established zone of the bi-solid CFB in a periodic box only imposing the volume fraction of each solid and the fluidization velocity leads to results close to the experiment.

This work showed how promising CFD is to predict operating points of pilot scale polysolid reactive circulating fluidized beds. A few limitations were highlighted: in extreme case, the Eulerian-Eulerian modeling underestimates the solid circulating mass flux. In the future, it will be interesting to test the influence of sub-grid models taking into account the local heterogeneities in the drag force calculation (cf. Parmentier et al. (2011) or Özel et al. (2010)). If this correction is not sufficient to predict the right circulating mass flux of solid, it might be necessary to study and model the influence of small scale structures on the collision exchanges: a mesh refinement study on a bi-solid

flow in a periodic box can be used.

Chapter 5

Appendix

5.1 Presentation of the cases

This appendix consists in a summary of the boundary conditions of the experiments and the numerical cases presented in this thesis.

5.2 Monosolid simulations

5.2.1 Numerical informations

For the monosolid simulations, it took — days on 32 processors to simulate 50 physical seconds.

5.2.2 Secondary injectors : 400/800, $d_{50} = 160\mu$m

Fluidization gas:

- T = 50 °C and P = 1 atm,
- Density $\rho_{gas} = 1.09 \text{ kg} \cdot \text{m}^{-3}$,
- Dynamic viscosity $\mu_{gas} = 1.98.10^{-5} \text{ Pa} \cdot \text{s}$.

Particles:

- Ilmenite $\rho_I = 4600 \text{ kg} \cdot \text{m}^{-3}$
- $d_{50} = 160 \ \mu$m
- Fluidization grid
  Gas: $Q_m = 0.5075 \text{ kg} \cdot \text{s}^{-1}$
- Secondary inlet flow Z=400 mm: value for one injector
  Gas: $Q_m = 0.2061 \text{ kg} \cdot \text{s}^{-1}$
- Secondary inlet flow Z=800 mm: value for one injector
  Gas: $Q_m = 0.0698 \text{ kg} \cdot \text{s}^{-1}$

- Particle inlet flow
  Ilmenite: α_p at the inlet pipe is calculated at time-step (n) to be equal to the volumic fraction at time-step $(n-1)$ at the outlet.
  Gas: α_{gas} at the gas-particle inlet pipe is deduced from α_p.

Inlet	**Boundary coundition**	**Repartition**
Fluidisation grid	$0.5075\ \mathrm{kg \cdot s^{-1}}$	27%
Gaz inlet at height 400	$0.824\ \mathrm{kg \cdot s^{-1}}$	43.5% splitted on 4 injectors
Gaz inlet at height 800	$0.558\ \mathrm{kg \cdot s^{-1}}$	29.5% splitted on 8 injectors

Table 5.1: Inlet boundary conditions

Those inlet boundary conditions correspond to a $V_f = 3.8\ \mathrm{m \cdot s^{-1}}$ in the main section.

Initialization At the beginning of the simulation, the riser is filled with 260 kg of 160 μm Ilmenite particles.

5.2.3 Secondary injectors : 400/800, $d_{50} = 120\mu$m

Fluidization gas:

- T = 50 °C and P = 1 atm,
- Density $\rho_{gas} = 1.09\ \mathrm{kg \cdot m^{-3}}$,
- Dynamic viscosity $\mu_{gas} = 1.98.10^{-5}\ \mathrm{Pa \cdot s}$.

Particles:

- Ilmenite $\rho_I = 4600\ \mathrm{kg \cdot m^{-3}}$
- $d_{50} = 120\ \mu$m
- Fluidization grid
  Gas: $Q_m = 0.5075\ \mathrm{kg \cdot s^{-1}}$
- Secondary inlet flow Z=400 mm: value for one injector
  Gas: $Q_m = 0.2061\ \mathrm{kg \cdot s^{-1}}$
- Secondary inlet flow Z=800 mm: value for one injector
  Gas: $Q_m = 0.0698\ \mathrm{kg \cdot s^{-1}}$
- Particle inlet flow
  Ilmenite: α_p at the inlet pipe is calculated at time-step (n) to be equal to the volumic fraction at time-step $(n-1)$ at the outlet.
  Gas: α_{gas} at the gas-particle inlet pipe is deduced from α_p.

Those inlet boundary conditions correspond to a $V_f = 3.8\ \mathrm{m \cdot s^{-1}}$ in the main section.

Inlet	Boundary coundition	Repartition
Fluidisation grid	0.5075 $kg \cdot s^{-1}$	27%
Gaz inlet at height 400	0.824 $kg \cdot s^{-1}$	43.5% splitted on 4 injectors
Gaz inlet at height 800	0.558 $kg \cdot s^{-1}$	29.5% splitted on 8 injectors

Table 5.2: Inlet boundary conditions

Initialization At the beginning of the simulation, the riser is filled with 260 kg of 120 μm Ilmenite particles.

5.2.4 Secondary injectors : 400/1500, $d_{50} = 160\mu$m

Fluidization gas:

- T = 50 °C and P = 1 atm,
- Density $\rho_{gas} = 1.09\ kg \cdot m^{-3}$,
- Dynamic viscosity $\mu_{gas} = 1.98.10^{-5}\ Pa \cdot s$.

Particles:

- Ilmenite $\rho_I = 4600\ kg \cdot m^{-3}$
- $d_{50} = 160\ \mu$m

The total gas volume flow rate is equal to $Q_{inlet} = 1.482\ kg \cdot s^{-1}$ and is divided as shown by table 5.3.

Inlet	Boundary coundition	Repartition
Fluidisation grid	0.459 $kg \cdot s^{-1}$	31%
Gaz inlet at height 1500	0.726 $kg \cdot s^{-1}$	49% splitted on 6 injectors
Gaz inlet at height 400	0.296 $kg \cdot s^{-1}$	20% splitted on 4 injectors

Table 5.3: Inlet boundary conditions

Those inlet boundary conditions correspond to a $V_f = 3.02\ m \cdot s^{-1}$ in the main section.

Initialization At the beginning of the simulation, the riser is filled with 200 kg of 160 μm ilmenite particles.

5.2.5 Secondary injectors : 800/2000, $d_{50} = 160\mu$m

Fluidization gas:

- T = 50 °C and P = 1 atm,

- Density $\rho_{gas} = 1.09\ \mathrm{kg \cdot m^{-3}}$,
- Dynamic viscosity $\mu_{gas} = 1.98.10^{-5}\ \mathrm{Pa \cdot s}$.

Particles:

- Ilmenite $\rho_I = 4600\ \mathrm{kg \cdot m^{-3}}$
- $d_{50} = 160\ \mu\mathrm{m}$

The total gas volume flow rate is equal to $Q_{inlet} = 1.482\ \mathrm{kg \cdot s^{-1}}$ and is divided as shown by table 5.4.

Inlet	**Boundary coundition**	**Repartition**
Fluidisation grid	$0.459\ \mathrm{kg \cdot s^{-1}}$	31%
Gaz inlet at height 2000	$0.726\ \mathrm{kg \cdot s^{-1}}$	49% splitted on 8 injectors
Gaz inlet at height 800	$0.296\ \mathrm{kg \cdot s^{-1}}$	20% splitted on 6 injectors

Table 5.4: Inlet boundary conditions

Those inlet boundary conditions correspond to a $V_f = 3.02\ \mathrm{m \cdot s^{-1}}$ in the main section.

Initialization At the beginning of the simulation, the riser is filled with 200 kg of 160 μm Ilmenite particles.

5.3 Monosolid experiments

5.3.1 EXP 1

Essai :	1
Date :	9 juin 2009
Nom :	CS10
Objet :	LFC froid UTC
Détail :	foyer : test ilmenite

VITESSE FOYER :	3.86	m/s
Repartition air secondaire	Inferieur	59.6%
	superieur	40.4%

Masse solides introduite :	
1792	kg
4500	kg/m3

Masse solides réacteur	
288	kg

S. foyer m2 :	0.4558
P. atmo. mbar:	1000
T °C sortie :	47
Ro air kg/m3 :	1.093

Pressions foyer	
niveau m	P mbars
0	118.8
0.1	105.6
0.28	70.6
0.4	60.8
0.7	43.5
1.3	30.3
2	25.1
2.9	22.3
4	19.1
4.7	17.1
5.85	15.1
7	13.8
8.05	12.2
8.8	11.5
9.45	10.8
10.35	10.5

Pressions brutes boucle	
Localisation	P mbars
Boîte à vent :	148
Sortie foyer :	10.54
Aval Filtre à manche	-74

Remarques
Injection secondaire : ASI : 400 mm : 4 Piquages ASS : 800 mm : 8 Piquages

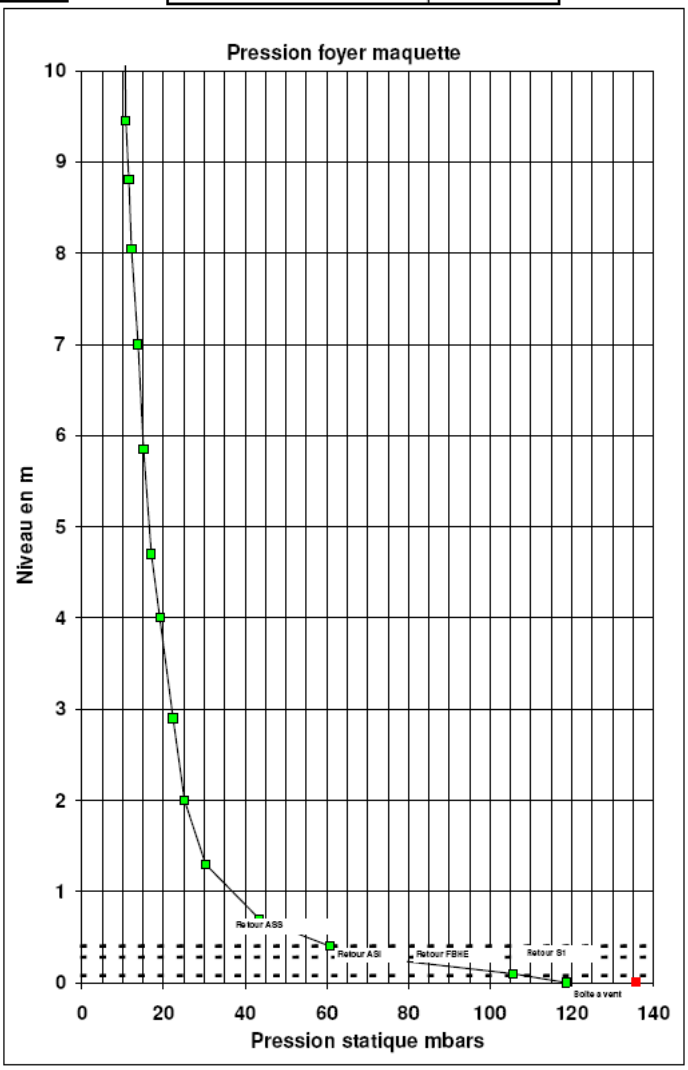

	T° venturi °C	ΔH Venturi mmCE	P venturi mbar	Débit kg/h	Repartition
Air primaire :	54.6	9.1	166.83	1827	26%
Air sec. Inf. :	54.4	80.1	213.69	2968	43%
Air sec. sup. :		36.7	214.69	2010	29%
Air surpresseur :	105.2	35.1	391.52	120	2%
Total air :				6927	
Air sort maq :	50.71	16.62	0.75	7239	

Débit mesuré (rempotage)	18.3	t/h

5.3.2 EXP 2

Essai :	2
Date :	26/11/09
Nom :	ASHS2
Objet :	LFC froid UTC
Détail :	foyer : test ilmenite

VITESSE FOYER :	3.95	m/s
Repartition air secondaire	Inferieur	60.8%
	superieur	39.2%

Masse solides introduite :	
2189	kg
4500	kg/m3

Masse solides réacteur	
188	kg

S. foyer m2 :	0.4558
P. atmo. mbar:	1000
T °C sortie :	47
Ro air kg/m3 :	1.103

Pressions foyer		
niveau m	P mbars	Prel mBars
0	97.9	77.5
0.1	84.3	63.9
0.28	59.4	39.1
0.4	54.3	33.9
0.7	44.9	24.6
1.3	35.8	15.4
2	32.0	11.7
2.9	29.6	9.3
4	27.3	7.0
4.5	25.9	5.6
5.85	24.3	4.0
6.5	23.3	2.9
8.05	21.8	1.5
8.5	21.3	1.0
9.45	20.8	0.4
10.35	20.4	0.0

Pressions brutes boucle	
Localisation	P mbars
Boîte à vent :	134
Sortie foyer :	20.36
Aval Filtre à manche	-63

Remarques
Alumine purgée
Cyclone standard
Modifications cyclone 2
Manches neuves
Siphon 2 réparé
Mode CS
+385kg ilménite
+194kg cendres
Injection secondaire :
ASI : 400 mm : 4 Piquages
ASS : 800 mm : 8 Piquages

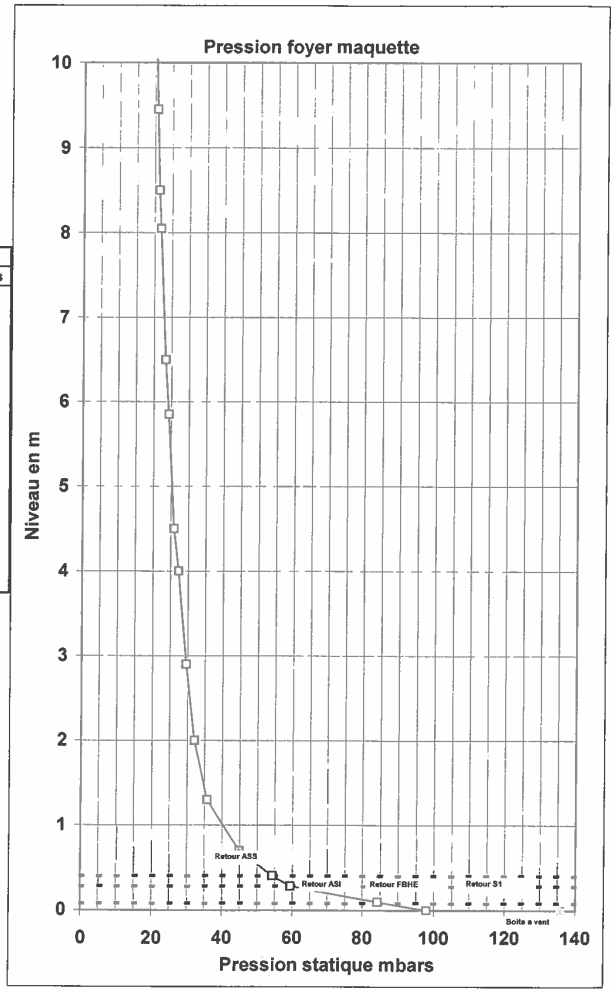

	T° venturi °C	ΔH Venturi mmCE	P venturi mbar	Débit kg/h	Repartition
Air primaire :	52.5	11.5	153.42	2052	29%
Air sec. inf. :	50.7	78.5	200.70	2939	41%
Air sec. sup. :		32.7	200.61	1898	27%
Air surpresseur :	101.1	48.4	376.77	263	4%
Total air :				7152	
Air sort mag :	48.23	17.67	0.80	7495	

Calcul sortie foyer :		
Concentration sortie :	5.007	kg/m3
Taux de vide sortie foyer :	0.9989	
Coefficient réducteur :	1.00	
Vitesse de glissement :	1.5	m/s
Débit théorique calculé :	20.14	t/h
Débit théorique (dp/dh)		t/h
Débit mesuré (rempotage)	22.4	t/h

5.3.3 EXP 3

~~Essai~~ :	1
Date :	26/11/09
Nom :	ASHS1
Objet :	LFC froid UTC
Détail :	foyer : test ilmenite

VITESSE FOYER :	3.92	m/s
Repartition air secondaire	inferieur	60.6%
	superieur	39.4%

Masse solides introduite :	
2188	kg
4500	kg/m3

Masse solides réacteur	
174	kg

S. foyer m2 :	0.4558
P. atmo. mbar:	1001
T °C sortie :	41
Ro air kg/m3 :	1.121

Pressions foyer		
niveau m	P mbars	Prel mBars
0	87.4	72.0
0.1	72.5	57.0
0.28	51.8	36.4
0.4	46.7	31.3
0.7	38.4	23.0
1.3	29.6	14.1
2	26.0	10.5
2.9	23.7	8.3
4	21.6	6.2
4.5	20.5	5.1
5.85	18.9	3.5
6.5	18.0	2.6
8.05	16.7	1.3
8.5	16.2	0.8
9.45	15.8	0.4
10.35	15.4	0.0

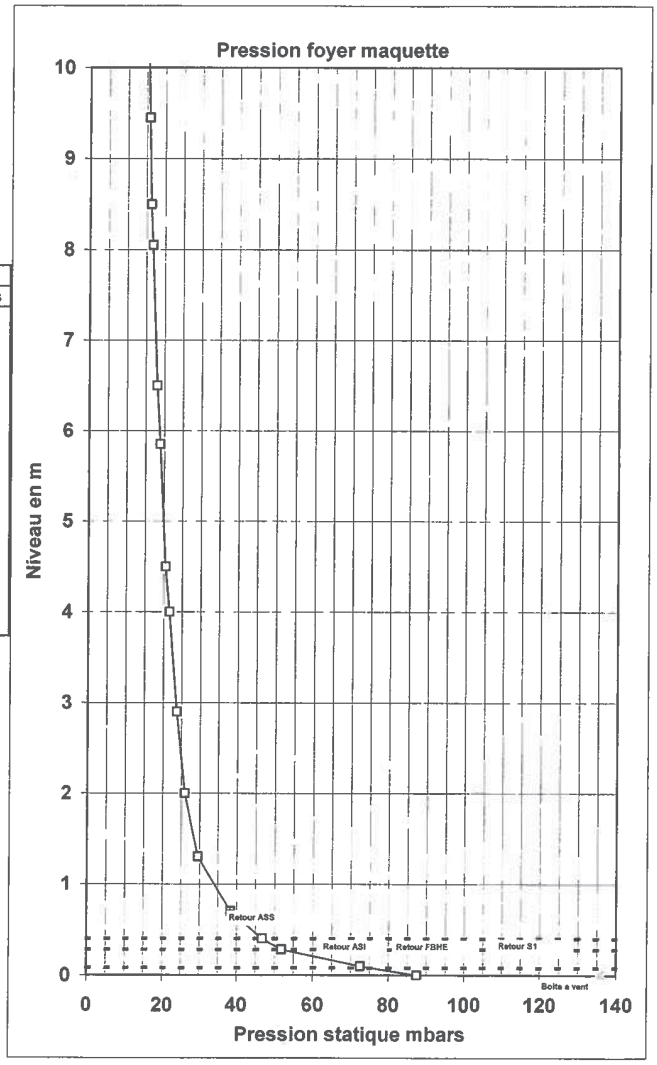

Pressions brutes boucle	
Localisation	P mbars
Boite à vent :	133
Sortie foyer :	15.42
Aval Filtre à manche	-66

Remarques
~~Alumine : 255kg (6%)~~
Cyclone standard
Modifications cyclone 2
Manches neuves
Siphon 2 réparé
Mode CS
+385kg Ilménite
Alumine Pugée (0%)
Injection secondaire :
ASI : 400 mm : 4 Piquages
ASS : 800 mm : 8 Piquages

	T° venturi °C	ΔH Venturi mmCE	P venturi mbar	Débit kg/h	Repartition
Air primaire :	50.0	12.6	149.17	2155	30%
Air sec. Inf. :	47.4	76.4	189.35	2903	40%
Air sec. sup. :		32.4	189.47	1888	26%
Air surpresseur :	95.2	51.1	360.07	263	4%
Total air :				7210	
Air sort maq :	44.00	17.63	0.81	7541	

Calcul sortie foyer :		
Concentration sortie :	4.238	kg/m3
Taux de vide sortie foyer :	0.9991	
Coefficient réducteur :	1.00	
Vitesse de glissement :	1.5	m/s
Débit théorique calculé :	16.84	t/h
Débit théorique (dp/dh)		t/h
Débit mesuré (rempotage)	19.7	t/h

5.3.4 EXP 4

Essai :	**1**
Date :	**9 novembre 2009**
Nom :	**CSII1**
Objet :	LFC froid UTC
Détail :	**foyer : test ilmenite**

VITESSE FOYER :	**3.92**	**m/s**
Repartition air secondaire	Inferieur	59.5%
	superieur	40.5%

Masse solides introduite :	
1890	kg
4500	kg/m3

Masse solides réacteur	
151	kg

S. foyer m2 :	**0.4558**
P. atmo. mbar:	1007
T °C sortie :	42
Ro air kg/m3 :	1.127

Pressions foyer	
niveau m	**P mbars**
0	82.3
0.1	67.0
0.28	50.6
0.4	46.8
0.7	40.2
1.3	32.1
2	29.0
2.9	26.9
4	25.1
4.5	24.1
5.85	22.7
6.5	21.9
8.05	20.7
8.5	20.3
9.45	20.0
10.35	19.6

Pressions brutes boucle	
Localisation	**P mbars**
Boîte à vent :	125
Sortie foyer :	19.61
Aval Filtre à manche	-59

Remarques
Alumine : 117kg
Cyclone standard
Modifications cyclone 2
Manches neuves
Siphon 2 réparé
Mode CS
+40 kg ilménite
Injection secondaire :
ASI : 400 mm : 4 Piquages
ASS : 800 mm : 8 Piquages

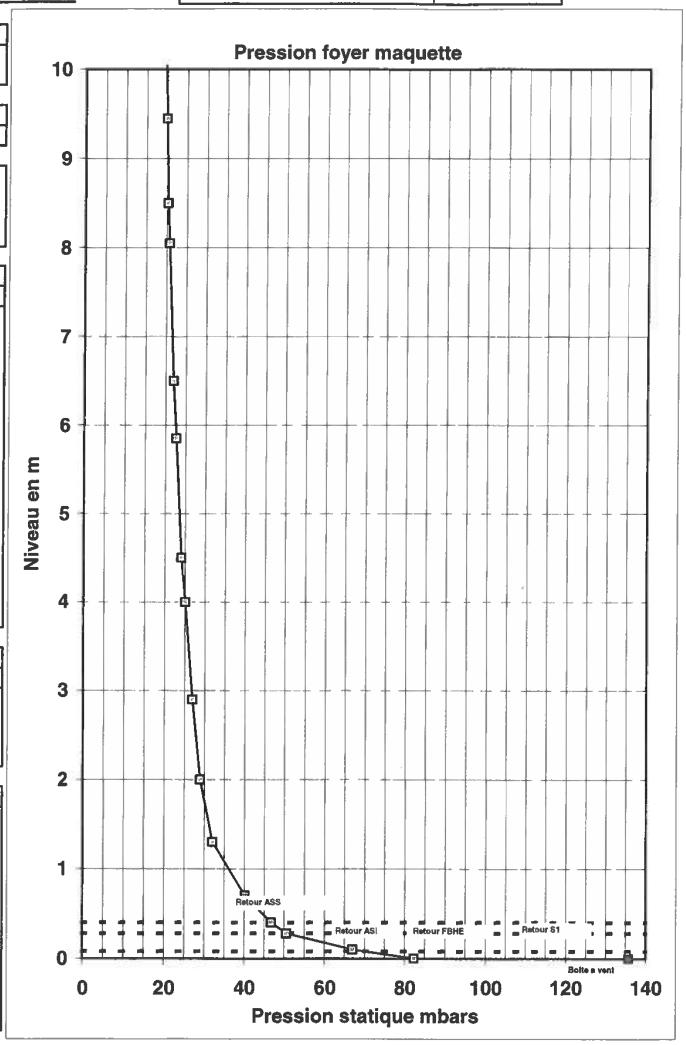

	T° venturi °C	**ΔH Venturi mmCE**	**P venturi mbar**	**Débit kg/h**	**Repartition**
Air primaire :	50.3	13.1	145.77	2196	30%
Air sec. Inf. :	47.9	74.9	187.23	2875	40%
Air sec. sup. :		34.8	187.03	1959	27%
Air surpresseur :	96.7	34.9	361.71	215	3%
Total air :				**7244**	
Air sort maq :	44.36	18.01	0.85	**7636**	

Calcul sortie foyer :		
Concentration sortie :	3.263	kg/m3
Taux de vide sortie foyer :	0.9993	
Coefficient réducteur :	1.00	
Vitesse de glissement :	1.5	m/s
Débit théorique calculé :	**12.94**	t/h
Débit théorique (dp/dh)		t/h
Débit mesuré (rempotage)	**21.5**	t/h

5.3.5 EXP 5

Essai : 1
Date : 25 juin 2009
Nom : CS18
Objet : LFC froid UTC
Détail : foyer : test ilmenite

VITESSE FOYER :	3.87	m/s
Repartition air secondaire	Inferieur	60.0%
	superieur	40.0%

Masse solides introduite :	
1799	kg
4500	kg/m3

Masse solides réacteur	
259	kg

S. foyer m2 :	0.4558
P. atmo. mbar:	1002
T °C sortie :	51
Ro air kg/m3 :	1.091

Pressions foyer	
niveau m	P mbars
0	124.6
0.1	110.9
0.28	72.6
0.4	65.6
0.7	52.3
1.3	40.9
2	35.6
2.9	32.9
4	29.5
4.5	27.3
5.85	25.3
6.5	24.2
8.05	22.2
8.5	21.6
9.45	20.8
10.35	20.3

Pressions brutes boucle	
Localisation	P mbars
Boîte à vent :	145
Sortie foyer :	20.32
Aval Filtre à manche	-75

Humide : 4%

Remarques
Agr. trou nourrices sec.
Amélioration étanchéité FAM
50 manches en moins
Events CS reliés cheminée
Rallonge CS2
TCS/PF1300/PCSCM/ P10350 remplacés
BAV CS recalibrée
Injection secondaire :
ASI : 400 mm : 4 Piquages
ASS : 800 mm : 8 Piquages

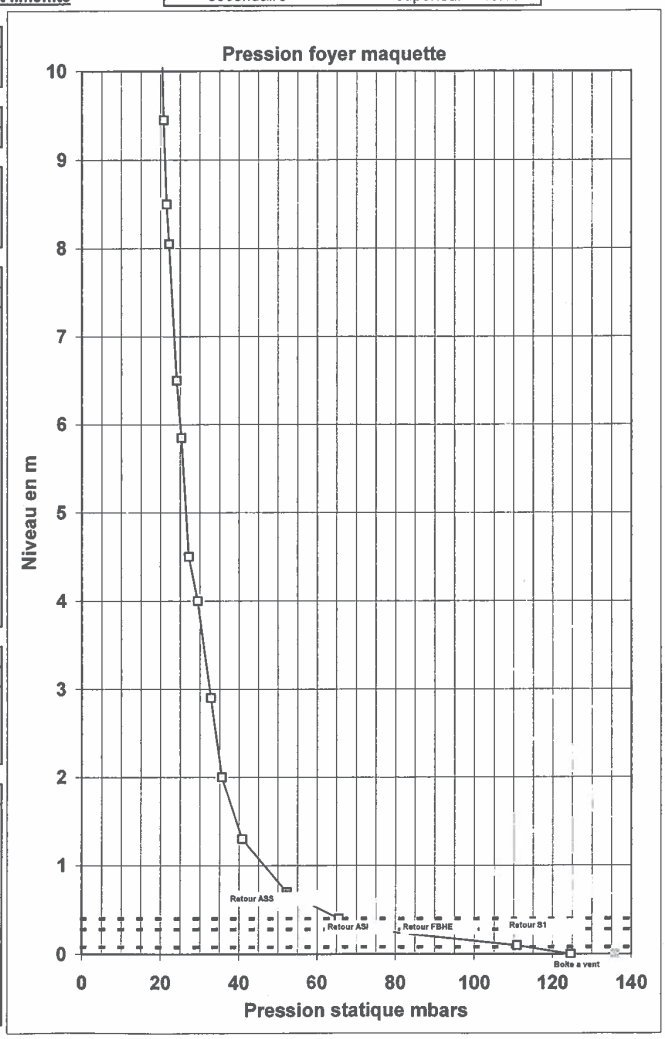

	T° venturi °C	ΔH Venturi mmCE	P venturi mbar	Débit kg/h	Repartition
Air primaire :	58.6	8.9	165.13	1797	26%
Air sec. inf. :	60.4	83.3	221.09	3010	43%
Air sec. sup. :		37.0	221.39	2007	29%
Air surpresseur :	107.5	22.6	394.46	120	2%
Total air :				6935	
Air sort maq :	55.26	16.99	0.81	7277	

Calcul sortie foyer :		
Concentration sortie :	7.218	kg/m3
Taux de vide sortie foyer :	0.9984	
Coefficient réducteur :	1.00	
Vitesse de glissement :	1.5	m/s
Débit théorique calculé :	28.12	t/h
Débit théorique (dp/dh)		t/h
Débit mesuré (rempotage)	34.4	t/h

5.3.6 EXP 6

Essai :	1
Date :	12/11/09
Nom :	CSII4
Objet :	LFC froid UTC
Détail :	foyer : test Ilmenite

VITESSE FOYER :	3.91	m/s
Repartition air secondaire	Inferieur	59.7%
	superieur	40.3%

Masse solides introduite :	
2270	kg
4500	kg/m3

Masse solides réacteur	
193	kg

S. foyer m2 :	0.4558
P. atmo. mbar:	1000
T °C sortie :	44
Ro air kg/m3 :	1.117

Pressions foyer		
niveau m	P mbars	Prel mBars
0	97.6	73.4
0.1	85.3	61.1
0.28	68.5	44.4
0.4	62.3	38.1
0.7	55.1	31.0
1.3	44.7	20.5
2	38.2	14.1
2.9	36.9	12.7
4	34.1	9.9
4.5	32.3	8.1
5.85	29.9	5.7
6.5	28.6	4.5
8.05	26.4	2.2
8.5	25.6	1.5
9.45	24.9	0.7
10.35	24.2	0.0

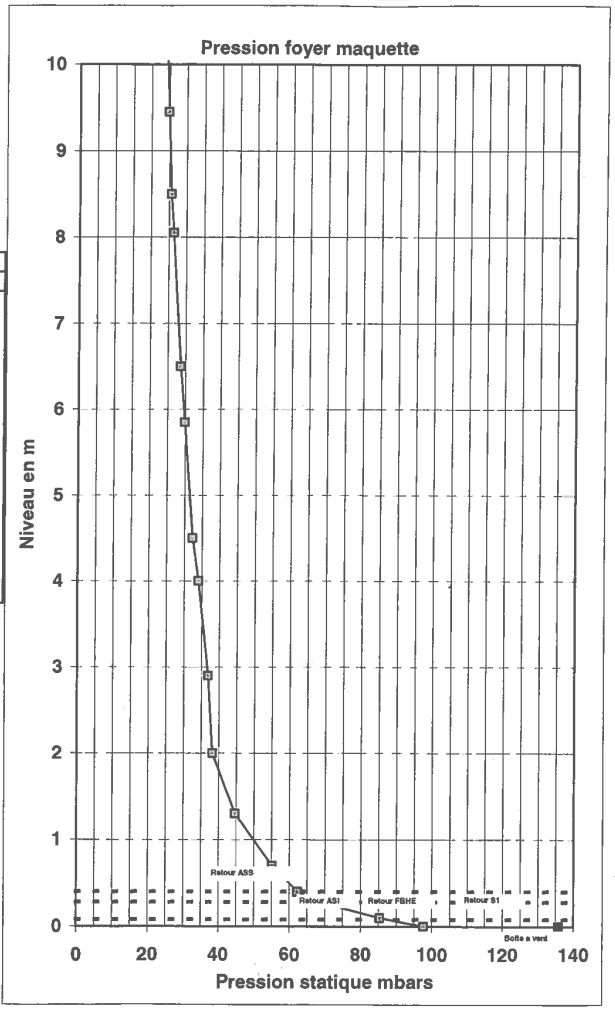

Pressions brutes boucle	
Localisation	P mbars
Boîte à vent :	132
Sortie foyer :	24.17
Aval Filtre à manche	-61

Remarques
Alumine : 238kg (5%)
Cyclone standard
Modifications cyclone 2
Manches neuves
Siphon 2 réparé
Mode CS
+240 kg Ilménite
Injection secondaire :
ASI : 400 mm : 4 Piquages
ASS : 800 mm : 8 Piquages

	T° venturi °C	ΔH Venturi mmCE	P venturi mbar	Débit kg/h	Repartition
Air primaire :	52.7	11.4	155.63	2045	29%
Air sec. Inf. :	51.6	77.8	207.69	2931	41%
Air sec. sup. :		35.5	207.48	1979	28%
Air surpresseur :	103.1	40.5	386.66	215	3%
Total air :				7170	
Air sort maq :	47.07	17.95	0.73	7565	

Calcul sortie foyer :		
Concentration sortie :	7.914	kg/m3
Taux de vide sortie foyer :	0.9982	
Coefficient réducteur :	1.00	
Vitesse de glissement :	1.5	m/s
Débit théorique calculé :	31.32	t/h
Débit théorique (dp/dh)		t/h
Débit mesuré (rempotage)	34.2	t/h

Bibliography

Adanez, J., De Diego, L., Garcia-Labiano, F., Gayan, P., Abad, A., and Palacios, J. (2004). Selection of oxygen carriers for chemical-looping combustion. *Energy Fuels*, 18(2):371–377.

Adanez, J., Dueso, C., de Diego, L., Garcia Labiano, F., Gayan, P., and Abad, A. (2008). Methane combustion in a 500 wth chemical-looping combustion system using an impregnated ni-based oxygen carrier. *Energy & Fuels*, 23(1):130–142.

Adanez, J., Gayan, P., Celaya, J., Luis, F., Garcia-Labiano, F., and Abad, A. (2006). Chemical looping combustion in a 10 kwth prototype using a cuo/al2o3 oxygen carrier: effect of operating conditions on methane combustion. *Ind. Eng. Chem. Res*, 45(17):6075–6080.

Agrawal, K., Loezos, P., Syamlal, M., and Sundaresan, S. (2001). The role of meso-scale structures in rapid gas-solid flows. *Journal of Fluid Mechanics*, 445:151–186.

Andreux, R., Hemati, M., Simonin, O., and Ferschneider, G. (2003). Hydrodynamic investigation of a cfb: numerical study and experimental validation. *Proc. of the 7th Int. Conference on Circulating Fluidized Beds*.

Andrews IV, A., Loezos, P., and Sundaresan, S. (2005). Coarse-grid simulation of gas-particle flows in vertical risers. *Industrial & engineering chemistry research*, 44(16):6022–6037.

Balaji, S., Ilic, J., Ydstie, B., and Krogh, B. (2010). Control-based modeling and simulation of the chemical-looping combustion process. *Industrial & Engineering Chemistry Research*, 49(10):4566–4575.

Balzer, G. and Simonin, O. (1994). Extension of eulerian gas-solid flow modelling to dense fluidized bed.

Bardina, J., Ferziger, J., and Reynolds, W. (1983). Improved turbulence models based on large eddy simulation of homogeneous, incompressible. Technical report, turbulent flows. Tech. Rep. TF-19, Department of Mechanical Engineering, Stanford University.

Batrak, O. (2005). *Etude numerique experimentale de l'hydrodynamique des lits fluidises Gaz-Particules avec prise en compte de la polydispersion granulometrique*. PhD thesis, INP Toulouse.

Batrak, O., Patino, G., Simonin, O., Flour, I., Le Guevel, T., and Perez, E. (2005). Unlike particles size collision model in 3d unsteady polydispersed simulation of circulating fluidised bed. In *8th Int. Conf. on Circulating Fluidized Beds*.

Benyahia, S. (2008). Verification and validation study of some polydisperse kinetic theories. *Chemical Engineering Science*, 63(23):5672–5680.

Benyahia, S. (2009). On the effect of subgrid drag closures. *Industrial & Engineering Chemistry Research*, 49(11):5122–5131.

Berguerand, N. and Lyngfelt, A. (2008). Design and operation of a 10 kwth chemical-looping combustor for solid fuels-testing with south african coal. *Fuel*, 87(12):2713–2726.

Berthiaux, H. and Dodds, J. (1999). Modelling fine grinding in a fluidized bed opposed jet mill:: Part i: Batch grinding kinetics. *Powder Technology*, 106(1-2):78–87.

Bouillard, J., Gidaspow, D., and Lyczkowski, R. (1991). Hydrodynamics of fluidization: fast-bubble simulation in a two-dimensional fluidized bed. *Powder technology*, 66(2):107–118.

Cao, Y., Liu, K., Riley, J., and Pan, W. (2004). Application of a circulating fluidized bed process for the chemical looping combustion of solid fuels. *Prepr. Pap.- Am. Chem. Soc., Div. Fuel Chem*, 49(2):815–816.

Chandel, M., Hoteit, A., and Delebarre, A. (2009). Experimental investigation of some metal oxides for chemical looping combustion in a fluidized bed reactor. *Fuel*, 88(5):898–908.

Chapman, S. and Cowling, T. (1970). The mathematical theory of. *Non-Uniform Gases*.

Chen, C. and Wood, P. (1986). Turbulence closure modeling of the dilute gas-particle axisymmetric jet. *AIChE journal*, 32(1):163–166.

Chew, J., Hays, R., Findlay, J., Karri, S., Knowlton, T., Cocco, R., and Hrenya, C. (2011). Species segregation of binary mixtures and a continuous size distribution of group b particles in riser flow. *Chemical Engineering Science*.

Chiba, S., Nienow, A., Chiba, T., and Kobayashi, H. (1980). Fluidised binary mixtures in which the denser component may be flotsam. *Powder Technology*, 26(1):1 – 10.

Ciborowski, J. and Wlodarski, A. (1962). On electrostatic effects in fluidized beds. *Chemical Engineering Science*, 17(1):23–32.

Cui, Z., Liu, Q., and Etsell, T. (2002). Magnetic properties of ilmenite, hematite and oilsand minerals after roasting. *Minerals Engineering*, 15(12):1121–1129.

Dahler, J. and Sather, N. (1963). Transport properties of polyatomic fluids, a dilute gas of perfectly rough spheres. *J. Chem. Physics*, 38:2363–2382.

Delhaye, J. (1974). Jump conditions and entropy sources in two-phase systems. local instant formulation. *International Journal of Multiphase Flow*, 1(3):395 – 409.

Delhaye, J., Giot, M., and Riethmuller, M. (1981). *Thermohydraulics of two-phase systems for industrial design and nuclear engineering*. Hemisphere Pub. Corp.

Deng, Z., Xiao, R., Jin, B., Song, Q., and Huang, H. (2008). Multiphase cfd modeling for a chemical looping combustion process (fuel reactor). *Chemical Engineering & Technology*, 31(12):1754–1766.

Dennis, J., Scott, S., and Hayhurst, A. (2006). In situ gasification of coal using steam with chemical looping: a technique for isolating co2 from burning a solid fuel. *Journal of the Energy Institute*, 79(3):187–190.

Derevich, I. and Zaichik, L. (1990). An equation for the probability density, velocity, and temperature of particles in a turbulent flow modelled by a random gaussian field. *Journal of Applied Mathematics and Mechanics*, 54(5):631–637.

Ding, J. and Gidaspow, D. (1990). A bubbling fluidization model using kinetic theory of granular flow. *AIChE Journal*, 36(4):523–538.

Elghobashi, S. and Abou-Arab, T. (1983). A two-equation turbulence model for two-phase flows. *Physics of Fluids*, 26:931.

Enwald, H., Peirano, E., Almstedt, A., and Leckner, B. (1999). Simulation of the fluid dynamics of a bubbling fluidized bed. experimental validation of the two-fluid model and evaluation of a parallel multiblock solver. *Chemical Engineering Science*, 54(3):311–328.

EWG (2007). Coal: Resources and future production. Technical report, Energy Watch Group.

Eyring, E., Konya, G., Lighty, J., Sahir, A., Sarofim, A., and Whitty, K. (2011). Chemical looping with copper oxide as carrier and coal as fuel. *Oil & Gas Science and Technology–Revue dIFP Energies nouvelles*, 66(2):209–221.

Fabre, A. (1995). *Etude de l'hydrodynamique sur un lit fluidisé circulant d'échelle industrielle*. PhD thesis, Université Technologique de Compiègne.

Fede, P. and Simonin, O. (2005). Application of a perturbated two-maxwellian approach for the modelling of kinetic stress transfer by collision in non-equilibrium binary mixture of inelastic particles. In *ASME*. ASME.

Ferschneider, G. and Mege, P. (1996). Eulerian simulation of dense phase fluidized beds. *Oil & Gas Science and Technology*, 51(2):301–307.

Fevrier, P., Simonin, O., and Legendre, D. (2003). Particle dispersion and preferential concentration dependance on turbulent reynolds number from direct and large eddy simulations of isotropic homogeneous turbulence.

Flour, I. and Simonin, O. (1993). Modélisation numérique d'un jet de gouttes avec évaporation et comparaison avec des résultats de mesure. Technical report, Laboratoire National d'Hydraulique (EDF).

Formisani, B. (1991). Packing and fluidization properties of binary mixtures of spherical particles. *Powder Technology,*, 66:259–264.

Geldart, D. (1973). Types of gas fluidization. *Powder Technology*, 7(5):285 – 292.

Gobin, A., Neau, H., Simonin, O., Llinas, J., Reiling, V., and Sélo, J. (2003). Fluid dynamic numerical simulation of a gas phase polymerization reactor. volume 43, pages 1199–1220. Wiley Online Library.

Gourdel, C., Simonin, O., and Brunier, E. (1998). Modelling and simulation of gas-solid turbulent flows with a binary mixture of particles. In *Third International Conference on Multiphase Flow*.

Gourdel, C., Simonin, O., and Brunier, E. (1999). Two-maxwellian equilibrium distribution function for the modelling of a binary mixture of particles. In *Circulating Fluidized Bed Technology VI, Frankfurt am Main, Germany*.

He, Y., Deen, N., Annaland, M., and Kuipers, J. (2009). Gas- solid turbulent flow in a circulating fluidized bed riser: Numerical study of binary particle systems. *Industrial & Engineering Chemistry Research*, 48(17):8098–8108.

Hirschberg, B. and Werther, J. (1998). Factors affecting solids segregation in circulating fluidized-bed riser. *AIChE journal*, 44(1):25–34.

Hossain, M. and de Lasa, H. (2008). Chemical-looping combustion (clc) for inherent co2 separations–a review. *Chemical Engineering Science*, 63(18):4433–4451.

Hu, H. (1996). Direct simulation of flows of solid-liquid mixtures. *International Journal of Multiphase Flow*, 22(2):335–352.

Huilin, L. and Gidaspow, D. (2003). Hydrodynamics of binary fluidization in a riser: Cfd simulation using two granular temperatures. *Chemical engineering science*, 58(16):3777–3792.

Igci, Y., Andrews IV, A., Sundaresan, S., Pannala, S., and O'Brien, T. (2008). Filtered two-fluid models for fluidized gas-particle suspensions. *AIChE Journal*, 54(6):1431–1448.

Ishida, M. and Jin, H. (1994). A new advanced power-generation system using chemical-looping combustion. *Energy*, 19(4):415–422.

Jenkins, J. and Mancini, F. (1989). Kinetic theory for binary mixtures of smooth, nearly elastic spheres. *Physics of Fluids A: Fluid Dynamics*, 1:2050.

Jenkins, J. and Richman, M. (1985). Kinetic theory for plane flows of a dense gas of identical, rough, inelastic, circular disks. *Physics of Fluids*, 28:3485.

Jin, H. and Ishida, M. (2002). Reactivity study on natural-gas-fueled chemical-looping combustion by a fixed-bed reactor. *Ind. Eng. Chem. Res*, 41(16):4004–4007.

Johansson, E., Mattisson, T., Lyngfelt, A., and Thunman, H. (2006). Combustion of syngas and natural gas in a 300 w chemical-looping combustor. *Chemical Engineering Research and Design*, 84(9):819–827.

Jung, J. and Gamwo, I. (2008). Multiphase cfd-based models for chemical looping combustion process: Fuel reactor modeling. *Powder Technology*, 183(3):401–409.

Kang, Y., Pyung, S., Jong, S., Jeong, Y., and Sang, D. (2000). Effects of secondary air injection on gas-solid flow behavior in circulating fluidized beds. *Chemical Engineering Communications*, 177(1):31–47.

Kolbitsch, P., Proll, T., Bolhar-Nordenkampf, J., and Hofbauer, H. (2009). Operating experience with chemical looping combustion in a 120 kw dual circulating fluidized bed (dcfb) unit. *Energy Procedia*, 1(1):1465–1472.

Kronberger, B., Beal, C., Morin, J., and Hofbauer, H. (2004). Design, hydrodynamic testing and scale-up recommendations of a conceptual large-scale chemical-looping combustion power plant.

Kronberger, B., Lyngfelt, A., Loffler, G., and Hofbauer, H. (2005). Design and fluid dynamic analysis of a bench-scale combustion system with co2 separation- chemical-looping combustion. *Ind. Eng. Chem. Res*, 44(3):546–556.

Kruggel-Emden, H., Stepanek, F., and Munjiza, A. (2011). A study on the role of reaction modeling in multi-phase cfd-based simulations of chemical looping combustion. *Oil & Gas Science and Technology–Revue dIFP Energies nouvelles*.

Ksepko, E., Siriwardane, R., Tian, H., and Simonyi. (2010). Comparative investigation on chemical looping combustion of coal-derived synthesis gas containing h2s over supported nio oxygen carriers. *Energy & Fuels*, pages 71–85.

Kunii, D. and Levenspiel, O. (1991). *Fluidization engineering*. Butterworth-Heinemann.

Lathouwers, D. and Bellan, J. (2000). Modeling and simulation of bubbling fluidized beds containing particle mixtures.

Lee, L., Madou, M., Koelling, K., Daunert, S., Lai, S., Koh, C., Juang, Y., Lu, Y., and Yu, L. (2001). Design and fabrication of cd-like microfluidic platforms for diagnostics: polymer-based microfabrication. *Biomedical Microdevices*, 3(4):339–351.

Lewis and Gilliland (1954). Production of pure carbon dioxide. US Patent 2,665,972.

Loth, E. (2008). Drag of non-spherical solid particles of regular and irregular shape. *Powder Technology*, 182:342–353.

Lun, C., Savage, S., Jeffrey, D., and Chepurniy, N. (1984). Kinetic theories for granular flow: inelastic particles in couette flow and slightly inelastic particles in a general flowfield. *Journal of fluid mechanics*, 140(-1):223–256.

Lyngfelt, A., Johansson, M., and Mattisson, T. (2004). Chemical-looping combustion. In *Chalmers part I COlNet Project Meeting, Utrecht*.

Lyngfelt, A., Leckner, B., and Mattisson, T. (2001). A fluidized-bed combustion process with inherent co2 separation; application of chemical-looping combustion. *Chemical Engineering Science*, 56(10):3101–3113.

Lyngfelt, A. and Thunman, H. (2005). Construction and 100 h of operational experience of a 10-kw chemical-looping combustor. *Carbon Dioxide Capture for Storage in Deep Geologic Formations-Results from the CO2 Capture Project*, 1:625–645.

Mahalatkar, K., Kuhlman, J., Huckaby, E., and O'Brien, T. (2011). Computational fluid dynamic simulations of chemical looping fuel reactors utilizing gaseous fuels. *Chemical Engineering Science*, 66(3):469 – 479.

Mathiesen, V., Solberg, T., Arastoopour, H., and Hjertager, B. (1999). Experimental and computational study of multiphase gas/particle flow in a cfb riser. *AIChE journal*, 45(12):2503–2518.

Mathiesen, V., Solberg, T., and Hjertager, B. (2000a). An experimental and computational study of multiphase flow behavior in a circulating fluidized bed. *International Journal of Multiphase Flow*, 26(3):387–419.

Mathiesen, V., Solberg, T., and Hjertager, B. (2000b). Predictions of gas/particle flow with an eulerian model including a realistic particle size distribution. *Powder Technology*, 112(1-2):34–45.

McKeen, T. and Pugsley, T. (2003). Simulation and experimental validation of a freely bubbling bed of fcc catalyst. *Powder Technology*, 129(1-3):139–152.

Menendez, R. and Alvarez, R. (1989). Coal carbonization: current and future applications. *Prepr. Pap., Am. Chem. Soc., Div. Fuel Chem.;(United States)*, 34(CONF-8904170-).

Neau, H., Lavieville, J., and Simonin, O. (2010). NEPTUNE_CFD high parallel computing performances for particle-laden reactive flows. Proc. 7th Int. Conference on Multiphase Flow, ICMF 2010, Tampa, USA.

Neri, A. and Gidaspow, D. (2000). Riser hydrodynamics: simulation using kinetic theory. *AIChE Journal*, 46(1):52–67.

Oesterlé, B. (1994). Une étude de l'influence des forces transversales agissant sur les particules dans les écoulements gazsolide. *Powder Technology*, 79(1):81 – 93.

Özel, A., Fede, P., and Simonin, O. (2010). 3d numerical prediction of gas-solid flow behavior in cfb risers for geldart a and b particles. *Proceedings of the 20th International Conference on Fluidized Bed Combustion*, pages 805–811.

Parmentier, J., Simonin, O., and Delsart, O. (2008). A numerical study of fluidization behavior of geldart b, a/b and a particles using an eulerian multifluid modeling approach.

Parmentier, J., Simonin, O., and Delsart, O. (2011). A functional subgrid drift velocity model for filtered drag prediction in dense fluidized bed. *AIChE Journal*.

Patino-Palacios, G. (2007). *Modelisation numerique eulerienne des ecoulements gaz-solide avec plusieurs especes de particules.* PhD thesis, Institut National Polytechnique de Toulouse.

Patureaux, T. and Barthod, D. (2000). Usage of cfd modelling for improving an fcc riser operation. *Oil & Gas Science and Technology*, 55(2):219–225.

Pröll, T., Kolbitsch, P., Bolhàr-Nordenkampf, J., and Hofbauer, H. (2008). A Dual Circulating Fluidized Bed (DCFB) System for Chemical Looping Processes. In *Proceedings of AIChE annual meeting. Philadelphia, USA*.

Readman, J., Olafsen, A., Smith, J., and Blom, R. (2006). Chemical looping combustion using nio/nial2o4: Mechanisms and kinetics of reduction- oxidation (red-ox) reactions from in situ powder x-ray diffraction and thermogravimetry experiments. *Energy Fuels*, 20(4):1382–1387.

Reeks, M. (1991). On a kinetic equation for the transport of particles in turbulent flows. *Physics of Fluids A: Fluid Dynamics*, 3:446.

Richter, H. and Knoche, K. (1983). Reversibility of combustion processes. In *ACS Symposium series*, volume 235, pages 71–86. ACS Publications.

Rifflart, S., Hoteit, A., Yazdanpanah, M., Pelletant, W., and Surla, K. (2011). Construction and operation of a 10 kw clc unit with circulation configuration enabling independent solid flow control. *Energy Procedia*, 4:333 – 340. 10th International Conference on Greenhouse Gas Control Technologies.

Ryu, H., Jin, G., Yi, C., et al. (2004). Demonstration of inherent co2 separation and no nox emission in a 50kw chemical-looping combustor: Continuous reduction and oxidation experiment. In *Poster Presented at the 7th International Conference on Greenhouse Gas Control Technologies, Vancouver, Canada*.

Schiller, L. and Naumann, A. (1933). Uber die grundlegenden berechungen bei der schwerkraftaufbereitung. *Vereines Deutscher Ingenieure*, 7:318.

Schoenfelder, H., Werther, J., Hinderer, J., and Keil, F. (1994). A multi stage model for the circulating fluidized bed reactor. *Fluid particle technology: analysis and applications*, page 92.

Shen, L., Wu, J., Gao, Z., and Xiao, J. (2010). Characterization of chemical looping combustion of coal in a 1 kwth reactor with a nickel-based oxygen carrier. *Combustion and Flame*, 157(5):934–942.

Shuai, W., Yunchao, Y., Huilin, L., Jiaxing, W., Pengfei, X., and Guodong, L. (2010). Hydrodynamic simulation of fuel-reactor in chemical looping combustion process. *Chemical Engineering Research and Design*, In Press, Corrected Proof:–.

Simonin, O. (1991). Prediction of the dispersed phase turbulence in particle-laden jets. pages 23–26.

Simonin, O. (2000). Statistical and continuum modelling of turbulent reactive particulate flows part i: Theoretical derivation of dispersed phase eulerian modelling fromprobability density function kinetic equation. *Lecture series-van Kareman Institute for fluid dynamics*, 6:D1–D42.

Simonin, O., Deutsch, E., and Minier, J. (1993). Eulerian prediction of the fluid/particle correlated motion in turbulent two-phase flows. *Applied Scientific Research*, 51(1):275–283.

Simonin, O., Février, P., and Laviéville, J. (2002). On the spatial distribution of heavy-particle velocities in turbulent flow: from continuous field to particulate chaos. *Journal of Turbulence*, (3).

Simonin, O. and Viollet, P. (1990). Modelling of turbulent two-phase jets loaded with discrete particles. *FG Hewitt, et al., Phenomena in multiphase yow*, page 259.

Smagorinsky, J. (1963). General circulation experiments with the primitive equations. *Monthly weather review*, 91(3):99–164.

Son, S. and Kim, S. (2006). Chemical-looping combustion with nio and fe2o3 in a thermobalance and circulating fluidized bed reactor with double loops. *Ind. Eng. Chem. Res*, 45(8):2689–2696.

Song, Q., Xiao, R., Deng, Z., Shen, L., Xiao, J., and Zhang, M. (2008). Effect of temperature on reduction of caso4 oxygen carrier in chemical-looping combustion of simulated coal gas in a fluidized bed reactor. *Industrial & Engineering Chemistry Research*, 47(21):8148–8159.

Squires, A., Kwauk, M., and Avidan, A. (1985). Fluid beds: at last, challenging two entrenched practices. *Science*, 230(4732):1329.

Survey, U. G. (2006). U.s. geological survey, mineral commodity summaries. Technical report, U.S. Geological Survey.

Taghipour, F., Ellis, N., and Wong, C. (2005). Experimental and computational study of gas-solid fluidized bed hydrodynamics. *Chemical engineering science*, 60(24):6857–6867.

Vermorel, O., Bédat, B., Simonin, O., and Poinsot, T. (2003). Numerical study and modelling of turbulence modulation in a particle laden slab flow. *Journal of Turbulence*, 4(25):1–39.

Villa, R., Cristiani, C., Groppi, G., Lietti, L., Forzatti, P., Cornaro, U., and Rossini, S. (2003). Ni based mixed oxide materials for ch4 oxidation under redox cycle conditions. *Journal of Molecular Catalysis A: Chemical*, 204:637–646.

Vojir, D. and Michaelides, E. (1994). Effect of the history term on the motion of rigid spheres in a viscous fluid. *International Journal of Multiphase Flow*, 20(3):547 – 556.

Wachmann, B. and Schwarzer, S. (1998). Three-dimensional massively parallel computing of suspensions. *International Journal of Modern Physics C-Physics and Computer*, 9(5):759–776.

Wang, X. and Gibbs, B. (1991). Hydrodynamics of a circulating fluidized bed with secondary air injection. In *Circulating fluidized bed technology III: proceedings of the Third International Conference on Circulating Fluidized Beds, Nagoya, Japan, 14-18 October 1990*, page 225. Pergamon.

Weinstein, H., Shao, M., and Wasserzug, L. (1984). Radial solid density variation in a fast fluidized bed. In *AIChE symposium series*, volume 80, pages 117–121. American institute of chemical engineers.

Wen, C. Y. and Yu, Y. H. (1966). A generalized method for predicting the minimum fluidization velocity. *AIChE Journal*, 12(3):610–612.

Xu, M., Ellis, N., Ryu, H., and Lim, C. (2007). Modeling of an interconnected fluidized bed reactor for chemical looping combustion. In *The 12th International Conference on Fluidization-New Horizons in Fluidization Engineering*, page 113. bepress.

Yang, W.-C. (2007). Modification and re-interpretation of geldart's classification of powders. *Powder Technology*, 171:69–74.

Yates, J. and Newton, D. (1986). Fine particle effects in a fluidized-bed reactor. *Chemical engineering science*, 41(4):801–806.

Zimmermann, S. and Taghipour, F. (2005). Cfd modeling of the hydrodynamics and reaction kinetics of fcc fluidized-bed reactors. *Ind. Eng. Chem. Res*, 44(26):9818–9827.